A dedicated β-NMR/β-NQR setup for LISE-GANIL and study of the nuclear moments of the neutron-rich Al and Cl isotopes

Marieke DE RYDT

Examination committee:
Prof. Dr. Piet Van Duppen[1], president
Prof. Dr. Gerda Neyens[1], promotor
Dr. Stefaan Cottenier[2]
Prof. Dr. Nathal Severijns[1]
Dr. Jean-Charles Thomas[3]
Prof. Dr. Margriet Van Bael[4]

Dissertation presented in partial fulfillment of the requirements for the degree of Doctor in Science

[1] Instituut voor Kern- en Stralingsfysica, K.U. Leuven, Celestijnenlaan 200D, B-3001 Leuven, Belgium
[2] Center for Molecular Modeling, Ghent University, Technologiepark 903, B-9052 Zwijnaarde, Belgium
[3] Grand Accélérateur National d'Ions Lourds (GANIL), CEA/DSM-CNRS/IN2P3, B.P. 55027, F-14076 Caen Cedex 5, France
[4] Laboratorium voor Vaste-Stoffysica en Magnetisme, K.U. Leuven, Celestijnenlaan 200D, B-3001 Leuven, Belgium

January 2010

ISBN number 978-90-8649-310-4
D/2010/10.705/3

The most incomprehensible thing about the world is that it is comprehensible.

Albert Einstein

Acknowledgements

The most exciting phrase to hear in science, the one that heralds new discoveries, is not "Eureka!" but rather "hmm....that's funny..."

Isaac Asimov

Na vier jaar doctoraat wil ik graag iedereen bedanken, niet alleen voor de vele aanmoedigingen bij de succesvolle *"hmm....that's funny..."* ervaringen maar ook voor de talrijke helpende handen tijdens de *"hmm....that's not funny..."* momenten waarop alles compleet verkeerd ging.

Als eerste is er een welgemeend dank-je-wel voor mijn promotor Gerda. Door jouw steun en vertrouwen kon ik zelf op 'ontdekkingstocht' gaan. Je had oog voor nieuwe ideeën en ik kon altijd bij je terecht voor lastige vragen of interessante discussies. Bedankt dat de deur van je bureau altijd 'open stond'.
I would also like to thank the other members of the examination committee for carefully reading the manuscript and for the enlightening discussion during the preliminary thesis defense. Many thanks to Dr. Stefaan Cottenier, Prof. Dr. Nathal Severijns, Dr. Jean-Charles Thomas, Prof. Dr. Margriet Van Bael and Prof. Dr. Piet Van Duppen.

Touts les résultats présentés dans cette thèse ont été obtenu pendant quatre manips à GANIL. Le succès des expériences a été réalisé grâce à l'aide d' un super équipe LISE. Merci à tous pour l' atmosphère amicale et 'accueillante', pour me donner un coup de main quand c'était nécessaire et pour la compétence 'Appellation d'Origine Contrôlée' GANIL... Un peu plus spécifiquement:
Stéphane, je veux te remercier pour être toujours astreinte. Nuit et jour, je pouvais te déranger avec des questions et des problèmes. Merci qu' on pouvait toujours compter sur toi et merci d'être 'l'ambulance' de LISE!
Un grand merci aussi à Jean-Charles, mon compagnon pendant les shifts de nuit. Ton enthousiasme est vraiment contagieux! Merci pour ton intérêt, pour corriger mille 'premières versions' de mes publications, pour tant de choses...

Jean-Michel, François et Christelle, merci pour votre aide pendant les nombreux réglages du faisceau qui étaient toujours très intensifs. Merci aussi à Olivier pour toutes les solutions réfléchies et à Laurent pour les discussions intéressantes sur les noyaux autour de $N = 28$.
Je veux aussi remercier l' équipe technique de LISE. Merci à Claude, Robert et Sébastien pour m' expliquer le sens de l'expression 'mettre quelque chose au pif' et pour bien vous occuper de ne mettre rien au pif.

Dit werk kon ook niet zonder de steun en de belangstelling van de 'Nuclear Moments' collega's in het IKS. Het aantal was soms nogal wisselend maar de sfeer was altijd super! In min of meer chronologische volgorde:
Dank je wel Pieter om me via een crash-course het Franse 'savoir-vivre' aan te leren en me te laten zien hoe je 'die mannen in GANIL aanpakt'.
Een dikke merci ook aan ons Nele bij wie ik altijd terecht kon voor moeilijke en/of last-minute vragen of om een tegendraadse module aan de praat te krijgen... Bedankt dat je toch bent meegegaan op experiment, ook al kon het tijdstip voor jou soms niet slechter gekozen worden.
Thanks to Rady and Aneta for the smooth teamwork and the nice atmosphere in the Nuclear Moments group.
Also many thanks to the fabulous CERN-gang of our group, Kieran, Deyan and Mark, for the cheerful moments in Geneva and Leuven. April 1st 2008 will always remain a memorable day in the history of office 02.79...
En dan onze pi, de broodjesman, 3,14 oftewel den allerknapste vent... van den bureau. Voor hem een woordje van dank schrijven is bijna een hoofdstuk op zich. Merci pi voor de SOS Ice Cream, voor het aanleren van de Duitse nationale geschiedenis aan onze Fritz, voor het dagelijkse "Ha Marie, zo laat vandaag...", voor de Japanse etiquette handleiding 'hoe eet ik mosselen' en voor de massa's toffe herinneringen gebundeld als 'de dolle avonturen van π en MRI'. 02.79, de populairste bureau van het IKS, alleen nog een sjotterkeskas en nen toog en dat wordt big business... Pi, bedankt voor alles hé joeng!
En natuurlijk zijn er ook onze masterstudenten, 'onze kindjes'. Zij hebben me meermaals verrast door als een volwaardig teamlid mee te draaien in onze groep. Een ferme dank je wel dus aan Kwinten, Geoffrey, Maarten en Wannes.

Dank je wel ook aan de vele collega's uit de andere IKS-groepen (Nuclear Solid State Physics, WITCH&KO en Nuclear Spectroscopy) voor de toffe sfeer op het instituut, voor de leuke babbels in de gang of op de recepties en voor het gezelschap tijdens middagpauzes in de moete. Ook de Euroschool weken in Trento, Houlgate & Leuven zal ik niet snel vergeten. Thank you all!

I would also like to thank our Japanese colleagues from RIKEN. The Belgian-French-Japanese collaboration was not always very obvious (especially not when trying to connect a Japanese laptop to a French printer network) but turned out to be very successful. Thanks for the nice cooperation, the help with all the technical work and the sharing of ideas and experiences.

Graag wil ik ook Willy en de mensen van de elektronica en mechanica werkplaatsen bedanken. Vooral in het begin van mijn doctoraat, bij het ontwikkelen en testen van de nieuwe β-NMR/β-NQR setup, heb ik meermaals op hen een beroep gedaan. Lucien zal zich zeker nog het hele gedoe met de rf-amplifier herinneren, die nu trouwens zijn naam draagt. Bedankt mannen!
Wie ook zeker een bedankje verdient, zijn Nancy, Katia, Josée, Sally, Martine en Isabelle. Niet alleen omdat ze alles in goede banen leiden en op orde houden maar ook voor de geweldige steun tijdens die laatste taaie weken. Daarnaast wil ik ook graag Luc en Bert bedanken voor de nodige computer- en IT support tijdens de voorbije vier jaar.

Verder zijn er ook nog heel wat vrienden die een bloemetje verdienen. In de frontlinie: Inge, trouwe kotgenoot en Leander, trouwe lotgenoot (ook aan het schrijven dus), beiden altijd bereid om te luisteren of om eens eventjes binnen te springen. Vanop het Leuvens front en altijd bereid om nog eens af te spreken: Jonas, Julie, Karl, Steffen en Geert. Van achter de zijlijn maar toch altijd bereid om nog eens een poging te doen om iedereen samen te krijgen: Isabelle, Thomas, Helge en Veerle. Dank je wel allemaal!
Tenslotte wil ik ook graag mijn familie bedanken. Voor de vele schouderklopjes, voor de belangstelling en voor het aanmoedigende "doet da goe hej mieke". Leuven-broer Jan, onze tandem-kookavonden met wederzijdse uitwisseling van stomme-studenten-verhalen waren super. Gent-broer Pieter, bedankt voor de altijd zo vrolijke (muziek) noot in het gezin. En moeke en pap, jullie zorgen ervoor dat thuis komen nog altijd thuiskomen is. Dank je wel!

Marieke (Leuven, januari 2010)

Abstract (English)

In order to explore the origin of matter and to characterize the fundamental interactions in nature, nuclear structure is studied. Mainly among the exotic nuclei, with extreme proton to neutron ratios, changes in the conventional shell structure are observed, resulting in new magic numbers, strong configuration mixing, shape coexistence and nuclear deformation.
Excellent probes to study nuclear structure are the magnetic dipole moment, sensitive to the configuration of the valence nucleons, and the spectroscopic electric quadrupole moment, a measure of the average deviation of the nuclear charge distribution from a sphere. Experimentally, both moments can be determined using the β-Nuclear Magnetic Resonance (β-NMR) technique.
In this PhD work, the physics behind two β-NMR approaches is discussed: the Continuous RF method and the Adiabatic Fast Passage technique. Furthermore, this thesis holds a detailed description of the newly designed β-NMR setup, installed at the LISE fragment separator at GANIL. It includes a review of all components, a survey of the field-profile measurements and an evaluation of the setup performance using a dedicated GEANT4 application.
As a test experiment, the g-factors of $^{17-18}$N were remeasured. For the ^{17}N ground state, the magnetic moment $|\mu(^{17}\mathrm{N})| = 0.3551(4)\ \mu_N$ was found. This value confirms the earlier published value and illustrates the ability of the setup to perform precision measurements. For ^{18}N, the value $|\mu(^{18}\mathrm{N})| = 0.3273(4)\mu_N$ was obtained, in agreement with the magnetic moment published by Ogawa *et al.* [1]. The second value existing in literature, $|\mu(^{18}\mathrm{N})| = 0.135(15)\mu_N$ [2], could not be reproduced, leaving its origin unclarified.
The first physics case to be studied, using both β-NMR approaches and the new setup, focusses on the quadrupole moments of the neutron-rich Al-isotopes at the border of the island of inversion. This region, including several deformed Ne, Na and Mg isotopes with neutron number around $N = 20$, is characterized by the dominance of neutron excitations from the *sd* to the *pf*-orbits in the ground state. A comparison of the measured quadrupole moment $|Q(^{31}\mathrm{Al})|$ = 134.0(16) mb to large-scale shell-model calculations suggests that ^{31}Al is dominated by normal *sd*-shell configurations with a possible small contribution

of intruder states. Furthermore, a compilation of the available experimental and calculated quadrupole moments of the odd-Z even-N sd nuclei shows that $e_p = 1.1e$ is a better effective proton charge in the sd-shell than the previously established value $e_p = 1.3e$.
Structural changes have also been observed for the neutron-rich isotopes around $N = 28$. To probe the reduced $N = 28$ gap and the near degeneracy of the $\pi(s_{1/2})$ and $\pi(d_{3/2})$ levels, the g-factors of the neutron-rich Cl-isotopes are studied. A Continuous RF β-NMR measurement on ^{44}Cl, resulting in $g(^{44}\mathrm{Cl})$ = (-)0.2749(2), shows that both effects play an important role in the ground state of this nucleus. Moreover, the experimental g-factor strongly supports a 2^- spin assignment for the ^{44}Cl ground state.
By studying the nuclear moments of the neutron-rich nuclei in the vicinity of the $N = 20$ and $N = 28$ shell closures, new physical insights are added to the current nuclear structure debate. Nonetheless, further research is needed to refine our understanding of the interactions inside the atomic nucleus.

Abstract (Nederlands)

Hoe materie ontstaat en welke eigenschappen de fundamentele interacties in de natuur hebben, kan worden bestudeerd aan de hand van de structuur van de atoomkern. Een veel gebruikte methode, die een goede beschrijving geeft van de kernstructuur rond de stabiliteitslijn, is het schillenmodel. Wanneer echter meer exotische kernen worden bestudeerd[A], voldoet het conventionele schillenmodel niet langer en moet er rekening worden gehouden met bijkomende effecten zoals het ontstaan van nieuwe magische getallen, sterke configuratiemenging, vormcoëxistentie en vervorming.

Zowel het magnetisch dipoolmoment, dat gevoelig is voor de configuratie van de valentienucleonen, als het spectroscopisch elektrisch quadrupoolmoment, dat de gemiddelde afwijking geeft van de ladingsverdeling in de kern ten opzichte van een bolvorm, zijn heel geschikt om de kernstructuur te onderzoeken. Om beide grootheden experimenteel te bepalen wordt in veel gevallen de β-Nucleaire Magnetische Resonantie (β-NMR) techniek gebruikt.

In dit onderzoekswerk wordt de achterliggende fysica van twee β-NMR methodes besproken: de Continue RF techniek en de 'Adiabatic Fast Passage' benadering. Daarnaast biedt deze thesistekst ook een gedetailleerde beschrijving van de nieuwe β-NMR opstelling die werd geïnstalleerd aan de LISE fragment separator in GANIL. Dit omvat een overzicht van alle technische componenten, een samenvatting van de veldprofielmetingen en een evaluatie van de opstelling aan de hand van een speciaal daarvoor ontwikkelde GEANT4 toepassing.

Tijdens een eerste experiment, bedoeld om de nieuwe opstelling uit te testen, werden de g-factoren van $^{17-18}$N opnieuw bepaald. Voor de grondtoestand van ^{17}N werd een magnetisch moment gelijk aan $|\mu(^{17}\mathrm{N})| = 0.3551(4)\ \mu_N$ opgemeten. Deze waarde bevestigt de eerdere publicatie en illustreert heel duidelijk dat de nieuwe opstelling bijzonder geschikt is voor precisiemetingen. Voor ^{18}N werd de experimentele waarde $|\mu(^{18}\mathrm{N})| = 0.3273(4)\mu_N$ gevonden, in overeenstemming met het magnetisch moment gepubliceerd door Ogawa *et al.* in 1999 [1]. Het magnetisch moment, $|\mu(^{18}\mathrm{N})| = 0.135(15)\mu_N$, dat eerder door Neyens

[A] Exotische kernen hebben een extreme verhouding van het aantal protonen tot het aantal neutronen.

et al. [2] werd opgemeten, kon niet worden gereproduceerd. De oorsprong van dit meetresultaat blijft voorlopig onduidelijk.
Een eerste onderzoeksproject, voorgesteld in dit doctoraatswerk, richt zich op de quadrupoolmomenten van de neutronrijke Al-isotopen, gesitueerd aan de rand van het eiland van inversie. Deze regio van exotische kernen omvat meerdere vervormde Ne, Na en Mg isotopen rond $N = 20$, waarvan de grondtoestand wordt gedomineerd door neutron excitaties van de sd naar de pf schil. Een vergelijking van het gemeten quadrupoolmoment $|Q(^{31}\mathrm{Al})| = 134.0(16)$ mb met schillenmodel berekeningen laat vermoeden dat ^{31}Al hoofdzakelijk wordt bepaald door normale sd-schil configuraties. Een kleine bijdrage van indringtoestanden kan echter niet worden uitgesloten. Bovendien toont een compilatie van beschikbare experimentele en berekende quadrupoolmomenten van oneven-Z even-N sd-kernen aan dat $e_p = 1.1e$ een betere effectieve proton lading is in de sd-schil dan de aangenomen waarde $e_p = 1.3e$.
Veranderingen in de kernstructuur worden eveneens waargenomen in de neutronrijke kernen rond $N = 28$. Om de effecten van de gereduceerde $N = 28$ schillensluiting en de ontaarding van de $\pi(s_{1/2})$ en $\pi(d_{3/2})$ niveaus te onderzoeken, worden de g-factoren van de neutronrijke Cl-isotopen bestudeerd. Een Continue RF β-NMR meting, uitgevoerd op ^{44}Cl en resulterend in $g(^{44}\mathrm{Cl}) =$ (-)0.2749(2), toont aan dat beide effecten een belangrijke rol spelen in de grondtoestand van deze kern. Bovendien bevestigt de opgemeten g-factor 2^- als de meest waarschijnlijke spin voor ^{44}Cl.
Samenvattend kan gesteld worden dat de studie van de kernmomenten van de neutronrijke isotopen in de nabijheid van de $N = 20$ en $N = 28$ schillensluitingen nieuwe elementen heeft toegevoegd aan het huidige debat over de kernstructuur. Hoe dan ook is voortgezet onderzoek nodig om de interacties binnenin de atoomkern verder te modeleren.

Contents

List of Tables

List of Figures

Introduction

Atomic nuclei exhibit a rich and fascinating structural diversity in a large mass range. About 3600 nuclei are currently known, displaying an extensive variety of lifetimes, binding energies, decay modes and nuclear shapes. Some 2400 more are believed to exist, mainly at heavy masses and at small proton to neutron ratios. Studying nuclear structure therefore plays an important role in scientific research since it reveals information on the evolution of matter and on the fundamental interactions in nature. Step by step, an answer is formulated to the general question why the universe looks the way it does today.

So far, no exact solution has been found for the many-body problem created by the strong interaction between the protons and neutrons in the atomic nucleus. Consequently, various nuclear models exist, each of them applicable in a specific and limited region of the nuclear chart. One particular approach which has been proven to be very successful is the nuclear shell model. It was developed in 1949 by Mayer, Haxel, Suess and Jensen who independently showed that the combination of a central potential and a spin-orbit term could give rise to the experimentally observed magic numbers and the shell gaps known at that time. This discovery founded a completely new field of research in theoretical nuclear physics and eventually lead to the large-scale shell-model calculations, performed nowadays using various codes and residual interactions.

For several decades, the magic numbers observed near the valley of stability were considered as being generally valid across the entire nuclear chart. However, when nuclei with extreme proton to neutron ratios became available at the newly built radioactive ion beam facilities, changes in the conventional shell structure were established. Since then, it is widely believed that magic numbers may evolve far off stability. Experimental evidence of changing nuclear structure has been found for all traditional magic numbers. This PhD work, however, focusses on the neutron-rich $N \simeq 20$ isotopes, i.e. the so-called island of inversion, and the neutron-rich $N \simeq 28$ nuclei. In both regions, strong configuration mixing, shape coexistence and nuclear deformation have been found for (semi) magic nuclei which were always believed to be well described using the spherical shell model.

The nuclear magnetic dipole moment and the electric quadrupole moment are excellent probes to study nuclear structure. As the magnetic moment consists of an orbital and a spin contribution, it indicates the shell-model character of a particular nuclear state. The electric quadrupole moment provides a direct measure of the deviation of the nuclear charge distribution from a spherical symmetry and is therefore an ideal tool to study nuclear deformation.
Ground-state magnetic moments of radioactive isotopes are often determined using the β-Nuclear Magnetic Resonance (β-NMR) technique. By scanning the frequency of a radiofrequent (rf) field, a resonant destruction or inversion of the spin polarization is induced in an ensemble of nuclei subjected to hyperfine interactions with their environment. The same principle can be implemented to study quadrupole moments, changing the name of the technique into β-Nuclear Quadrupole Resonance (β-NQR). β-NMR as well as β-NQR are efficient methods to investigate β-decaying states with a lifetime between 50 μs and a few minutes, provided that these levels can be spin polarized. As both techniques are very sensitive, an accurate and reliable setup is required in which a large and homogeneous magnetic field and an extended rf-frequency range can be applied. All experiments described in this work have been performed at the LISE fragment separator at GANIL where high production yields of exotic nuclei can be obtained using the projectile-fragmentation reaction. By breaking the symmetry of the reaction, spin polarization is induced.

This PhD thesis covers the technical aspects and the physical insights acquired based on nuclear moment measurements performed in the vicinity of the $N = 20$ and $N = 28$ shell 'closures', using a newly designed β-NMR/β-NQR setup. The outcome of the experiments is extensively discussed in four scientific articles, published in or submitted to international peer-reviewed journals. They form the basis of this thesis. Beside the first two chapters which enclose an introductory theoretical background, each of the four subsequent chapters discusses a particular experimental topic and is concluded by the corresponding publication. The subjects quoted in the chapter texts must be regarded as an introduction to or an extension of the article that follows. A summary of the framework of this thesis is given below.

- Chapter 1 gives a description of the nuclear shell model and the changes induced when going to more neutron-rich nuclei.
- Chapter 2 outlines the main principles of hyperfine interactions, nuclear moments theory and β-NMR.

- Chapter 3 includes a detailed description of the new β-NMR/β-NQR setup design and a report on the GEANT4 simulations, carried out to evaluate the performance of the setup. The main conclusions on the technical development are published in Nuclear Instruments and Methods.

  A New dedicated β-NMR/β-NQR setup for LISE-GANIL,
  M. De Rydt, R. Lozeva, N. Vermeulen, F. de Oliveira Santos, S. Grévy, P. Himpe, C. Stödel, J.C. Thomas, P. Vingerhoets and G. Neyens
  Nuclear Instruments and Methods in Physics Research A ***612*** *112 (2009)*

- Chapter 4 presents the β-NMR results of the test run performed when the installation of the new β-NMR/β-NQR setup was completed. The physics outcome of this experiment is published in Physical Review C.

  g factors of ^{17}N and ^{18}N remeasured,
  M. De Rydt, D.L. Balabanski, J.M. Daugas, P. Himpe, D. Kameda, R. Lozeva, P. Morel, L. Perrot, K. Shimada, C. Stödel, T. Sugimoto, J.C. Thomas, H. Ueno, N. Vermeulen, P. Vingerhoets, A. Yoshimi and G. Neyens
  Physical Review C ***80*** *037306 (2009)*

- Chapter 5 focusses on the $N \simeq 20$ isotopes. The introductory text provides information on the island of inversion, the physics behind the 'Continuous RF' and 'Adiabatic Fast Passage' β-NMR methods and the search for the best effective proton charge in the *sd*-shell. The results of the β-NQR measurements on ^{31}Al and the interpretation of the observed quadrupole moment in terms of neutron excitations across $N = 20$ are given in the article at the end of the chapter.

  Precision measurement of the electric quadrupole moment of ^{31}Al and determination of the effective proton charge in the sd-shell,
  M. De Rydt, G. Neyens, K. Asahi, D.L. Balabanski, J.M. Daugas, M. Depuydt, L. Gaudefroy, S. Grévy, Y. Hasama, Y. Ichikawa, P. Morel, T. Nagatomo, T. Otsuka, L. Perrot, K. Shimada, C. Stödel, J.C. Thomas, H. Ueno, Y. Utsuno, W. Vanderheijden, N. Vermeulen, P. Vingerhoets, A. Yoshimi
  Physics Letters ***B 678*** *344 (2009)*

- The $N \simeq 28$ nuclei are studied in chapter 6. An extensive summary of the literature describing the weakening of the $N = 28$ shell gap and the collapse of the $Z = 16$ sub-shell closure is presented. The chapter also holds a detailed analysis of the unpublished β-NMR results on ^{41,42,43}Cl. Furthermore, an extensive discussion of the measured g-factor of ^{44}Cl is given in the Physical Review C article that concludes the chapter.

g factor of the ^{44}Cl ground state: probing the reduced $Z = 16$ and $N = 28$ gaps,
M. De Rydt, J.M. Daugas, F. de Oliveira Santos, L. Gaudefroy, S. Grévy, D. Kameda, V. Kumar, R. Lozeva, T.J. Mertzimekis, P. Morel, T. Nagatomo, G. Neyens, L. Perrot, O. Sorlin, C. Stödel, J.C. Thomas, N. Vermeulen and P. Vingerhoets
Submitted to Physical Review C

- Conclusions and outlook on this scientific work can be found in the last chapter.

Chapter 1

The nuclear shell model

As nuclear models provide a clarifying insight in nuclear structure, they are indispensable for the interpretation of new experimental results. Vice versa, the systematics of measured nuclear properties is used to improve the reliability of theoretical predictions. Experimental and theoretical nuclear physics therefore go hand in hand to reveal the complex structure of the atomic nucleus.
One of the most successful theoretical formalisms is the nuclear shell model. Starting from the relatively simple concept of a one-body central potential and a residual interaction, it accounts for many empirically observed features of the nucleus. A detailed description is given below, starting from the general nuclear Hamiltonian (section 1.1) and its simplified version in the single-particle model (section 1.2). An extension of the latter to multiparticle valence configurations results in the shell model, as shown in section 1.3. To conclude the chapter, an introduction to large-scale shell-model calculations is given.

1.1 The general nuclear Hamiltonian

In the non-relativistic approach and neglecting the Coulomb repulsion between the protons, the atomic nucleus is described by the general Hamiltonian [3]:

$$H = T + V = \sum_{i=1}^{A} \frac{\mathbf{p}_i^2}{2m_i} + \sum_{i>k=1}^{A} V_{ik}(\mathbf{r}_i - \mathbf{r}_k) \tag{1.1}$$

which is the sum of a kinetic and a potential energy term. V_{ik} corresponds to the nucleon-nucleon potential that comprises a strong repulsive core for $\mathbf{r}_i - \mathbf{r}_k < 0.5$ fm and an attractive one-pion exchange potential at larger distances. An excellent approximation of the free nucleon-nucleon potential is given by the hard-core Hamada-Johnston potential consisting of a central, tensor and spin-orbit term.

Eq. 1.1 is extremely difficult to deal with and can only be solved for the lightest nuclei. In order to access also the intermediate and heavy-mass nuclei, a simplification is needed. One approaches the problem by adding and subtracting a common nuclear one-body potential $U(\mathbf{r})$:

$$H = \underbrace{\sum_{i=1}^{A}\left[\frac{\mathbf{p}_i^2}{2m_i} + U(\mathbf{r}_i)\right]}_{H_0} + \underbrace{\sum_{i>k=1}^{A} V_{ik}(\mathbf{r}_i - \mathbf{r}_k) - \sum_{i=1}^{A} U(\mathbf{r}_i)}_{H_{res}} = H_0 + H_{res} \quad (1.2)$$

The potential $U(\mathbf{r})$ should be chosen such that the residual interaction H_{res} is only a small perturbation of the Hamiltonian H_0 which describes the nucleus as a system of independent nucleons orbiting in a common mean-field potential. A solution of the Schrödinger equation for the Hamiltonian H_0 is given by the single-particle model. This model works well for nuclei with one particle (hole) outside (inside) a closed shell. When two or more nucleons appear in the valence space, residual interactions among them should be taken into account and better results are obtained in the nuclear shell-model framework.

1.2 The single-particle model

In the single-particle model, the potential $U(r)$ generated by all nucleons is often chosen to be the harmonic oscillator potential [4]:

$$U(r) = \frac{1}{2}m\omega^2 r^2 \quad (1.3)$$

The Schrödinger equation without residual interaction is then easy to handle mathematically. The calculated eigenvalues of H_0 are $E_{nl} = (2n + l - 1/2)\hbar\omega$ with n the number of nodes of the radial wave function and l the orbital quantum number. The corresponding level structure is shown in the left section of Fig. 1.1. Note that all states having $\Delta l = -2\Delta n$ are degenerate.
When fermions are added in a potential, the Pauli principle induces a set of 'magic' numbers. In the case of the nuclear harmonic oscillator potential, these values correspond to the total number of nucleons needed to completely fill the subsequent harmonic oscillator shells. Experimentally, the magic numbers indicate a shell closure and can be determined by looking at the systematics of e.g. the one-nucleon separation energies [5]. Sharp peaks have been observed at N,Z=2, 8, 20, 28, 50, 82, 126 for nuclei near the valley of stability. Experimental data only confirm the lowest three 'harmonic oscillator' magic numbers. In order to obtain an overall reproduction of the experimental magic numbers, two terms are added to the harmonic oscillator potential. The first is an attractive term in l^2 which induces a more constant potential in the interior of the

nucleus. Due to the l^2 term the degeneracy of the harmonic oscillator is broken and the high angular momentum levels are brought down in energy, as shown in the middle panel of Fig. 1.1. The second term is the so-called spin-orbit force which is primarily a surface phenomenon:

$$V_{\mathbf{l}\cdot\mathbf{s}} = -V_{ls}\, r_0^2\, \frac{1}{r}\, \frac{\partial U(r)}{\partial r}\, \mathbf{l}\cdot\mathbf{s} \tag{1.4}$$

It splits each nl level into two orbits, $j = l + 1/2$ and $j' = l - 1/2$, favoring the parallel alignment of the orbital and intrinsic angular momentum.
The harmonic oscillator potential, combined with the l^2 term and the spin-orbit interaction defines the single-particle or 'naive' shell model. This model owes its success not only to the correct reproduction of the experimental magic numbers but also to the predictive power of the nuclear properties in closed shell and closed shell plus one nucleon configurations. The single-particle levels are given in the right panel of Fig. 1.1.

1.3 The nuclear shell model

When two or more valence particles reside outside a closed shell, residual interactions between them should be taken into account, calling for an extended and more general shell model. The single-particle model serves as a basis for this generalization.

Before considering n-particle configurations, the discussion is restricted to two valence nucleons outside a closed shell. The nucleons have their single-particle spins coupled to a total spin J. Assume that one nucleon is fixed in a single-particle orbit with spin j_1 and the other in a single-particle orbit with spin j_2. The Hamiltonian of this two-particle system is given by:

$$H = \sum_{i=1}^{2} \left[\frac{\mathbf{p}_i^2}{2m_i} + U(\mathbf{r}_i) \right] + H_{res}(\mathbf{r}_1 - \mathbf{r}_2) \tag{1.5}$$

The energy of the two-particle configuration, subjected to the Hamiltonian in Eq. 1.5, equals:

$$E(j_1, j_2, J) = \epsilon_{j_1} + \epsilon_{j_2} + < j_1 j_2; JT \mid H_{res}(\mathbf{r}_1 - \mathbf{r}_2) \mid j_1 j_2; JT > \tag{1.6}$$

It includes the single-particle energies ϵ_{j_1} and ϵ_{j_2} which are eigenvalues of H_0 and the so called two-body matrix element (TBME) which incorporates the effect of the residual interaction H_{res} on the two-particle system with spin J and isospin T. In general, TBME are responsible for the shift and the splitting in energy of the different accessible J states, $|j_1 - j_2| \leq J \leq j_1 + j_2$.

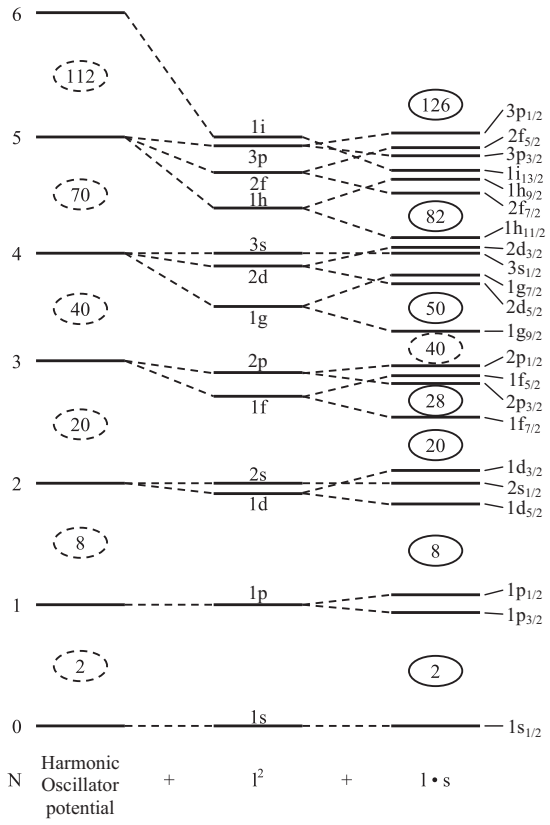

Figure 1.1: Single-particle levels, determined by the harmonic oscillator potential (left), l^2 term (middle) and spin-orbit interaction (right). Figure taken from [4]

In general, a series expansion of the residual interaction can be made. In case H_{res} is modeled as a central potential, i.e. depending on the magnitude of the separation of the two particles, a series of Legendre polynomials P_k is used:

$$H_{res}(|\mathbf{r}_1 - \mathbf{r}_2|) = \sum_{k=0}^{\infty} v_k(r_1, r_2) P_k(\cos\theta_{12}) \tag{1.7}$$

with θ_{12} the semiclassical 'angle' between the angular momentum vectors $\mathbf{j}_1$ and $\mathbf{j}_2$. The factors $v_k(r_1, r_2)$ are given by

$$v_k(r_1, r_2) = \frac{2k+1}{2} \int H_{res}(|\mathbf{r}_1 - \mathbf{r}_2|)\ P_k(\cos\theta_{12})\ d\cos\theta_{12} \tag{1.8}$$

The monopole component ($k = 0$) of the series expansion of the residual interaction corresponds to the mean energy brought to the nucleus by adding two interacting particles. It is independent of the relative orientation of $\mathbf{j}_1$ and $\mathbf{j}_2$ and it induces an overall energy shift of the entire J multiplet. In general, the monopole-energy shift can be written as [6]

$$E^m_{j_1 j_2} = \frac{\sum_J (2J+1) < j_1 j_2; JT \mid H_{res}(\mathbf{r}_1 - \mathbf{r}_2) \mid j_1 j_2; JT >}{\sum_J (2J+1)} \tag{1.9}$$

The degeneracy of the different J states is lifted by the higher order multipole components. After the monopole component, the quadrupole component ($k = 2$) usually has the highest amplitude.

So far, we have assumed that the two valence particles could only occupy the single-particle states j_1 and j_2. Let us now consider two nucleons in a valence space consisting of two or more single-particle orbits. In that case, different configurations (i.e. different combinations of the single-particle spins) can induce the same value J. This phenomenon is called configuration mixing and it can lead to a highly fragmented wave function Ψ for the created J state [7]. For each spin J and isospin T, the following Hamiltonian can be constructed:

$$H = \begin{bmatrix} H_{11} & H_{12} & \cdots \\ H_{21} & H_{22} & \cdots \\ \vdots & & \end{bmatrix} \tag{1.10}$$

The single sub-index k represents the state $|j_1 j_2; JT >_k$ in which two particular single-particle spins j_1 and j_2 are coupled to spin J. The double subindex kl used in Eq. 1.10 points to a matrix-element calculated with the states $|j_1 j_2; JT >_k$ and $|j_3 j_4; JT >_l$. Based on this convention, the elements of the Hamiltonian can be written as:

$$H_{kl} = \epsilon_{j_1}\delta_{kl} \; + \; \epsilon_{j_2}\delta_{kl} \; + \; {}_k < j_1 j_2; JT| \; H_{res}(\mathbf{r}_1 - \mathbf{r}_2) \; |j_3 j_4; JT >_l \tag{1.11}$$

The diagonal of the Hamiltonian in Eq. 1.10 comprises corrected single particle energies while the off-diagonal elements are pure TBME between the different configurations that can form spin J.

By solving the Schrödinger equation $H\Psi = E\Psi$ using the Hamiltonian in Eq. 1.10, the energy eigenvalues E and the eigenfunctions Ψ are obtained for a particular spin J and isospin T. By repeating the procedure for several values of J, the nuclear level scheme can be determined. The wave functions Ψ are used to calculate a variety of physical observables: nuclear moments, B(E2),...

As a last step, a closer look is taken at multiparticle configurations. Consider n nucleons in a single-particle state j. The matrix elements of the residual interaction between these nucleons can be written in terms of the TBME encountered earlier.

$$\left\langle j^n J \right| \sum_{i>j}^{n} H_{res}(\mathbf{r}_i - \mathbf{r}_j) \left| j^n J \right\rangle = \sum_{J_2} W(j^n J J_2) < j^2 J_2 | \, H_{res}(\mathbf{r}_1 - \mathbf{r}_2) \, | j^2 J_2 > \tag{1.12}$$

where the W coefficients are sums of the squares of the coefficients of fractional parentage (CFP), for a given J_2 over all possible values J_{n-2}.

$$W(j^n J J_2) = \sum_{J_{n-2}} \left| \left\langle j^n J \left\{ \left| j^2(J_2) j^{n-2}(J_{n-2}) J \right\rangle \right| \right|^2 \tag{1.13}$$

The CFP are a measure for the probability that a particular final state is constructed from a specific 'parent' configuration. Using the CFP formalism, the n-particle problem can be reduced to the TBME formalism which accounts for the residual interactions between two particles in the valence space. The coefficients of fractional parentage therefore hold an enormous simplification of shell-model calculations in large valence spaces.

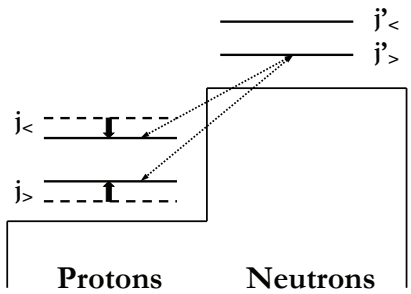

Figure 1.2: The tensor component of the residual interaction inducing a monopole shift of the single particle energies (schematic representation). Figure taken from [8]

Up to now, we have studied the total energy of a two or n-particle system, characterized by a spin J and isospin T. Let us now consider the effect of the residual interaction and its monopole component on the single-particle energies. As nucleons are added to an orbit j', the monopole term of H_{res} tends to change the single-particle energy of the orbit j. This results in the evolving shell structure and the vanishing magic numbers observed for the isotopes far off stability. For like nucleons, the monopole shift of the level j when filling the orbit j' is given by $E^m_{jj'}$ (Eq. 1.9) multiplied by the number of particles

in j'. In the case of unlike nucleons (protons filling j' and neutrons present in j or vice versa) an alternative expression for the monopole energy shift of the single-particle state j is obtained:

$$\Delta\epsilon(j) = \frac{1}{2}\left[E^m_{jj'}(T=0) + E^m_{jj'}(T=1)\right] n(j') \tag{1.14}$$

with $n(j')$ the number of j' particles. Single-particle energies including this monopole effect are called *effective* single-particle energies (ESPE).
According to Otsuka *et al.*, the large monopole shifts observed for the ESPE in exotic nuclei originate mainly from the central [9] and tensor [8] parts of the residual interaction[A]. Especially the tensor component plays an important role. It accounts for the attraction between two effective single-particle levels, one with spin $j_< = l - 1/2$ and the other with spin $j'_> = l' + 1/2$ whereas it induces a repulsion between $j_<$ and $j'_<$ (or $j_>$ and $j'_>$). The monopole shift due to the tensor interaction is depicted schematically in Fig. 1.2. The tensor force can have a large impact on the ESPE, especially when j and j' belong to a different valence sub-space[B] and when they have a large radial overlap and a high l-value. Several examples of tensor-induced changing ESPE are given in chapters 4, 5 and 6.

An extensive discussion of the nuclear shell model can be found in specialized textbooks such as [3, 10].

1.4 Large-scale shell-model calculations

In the last decades, many shell-model codes have been developed, their speed and capacity depending on the available computer technology. Most of these shell-model codes use a common calculation procedure of which the schematics is given below.

1. The number of valence particles in the configuration space is specified.

2. The model space and the configurations that span the space for each J^π value are constructed.

3. Starting from the single-particle energies and the two-body matrix elements, the Hamiltonian H is determined (see Eq. 1.10).

[A] Recall that the residual interaction H_{res} and the corresponding TBME depend on the nucleon-nucleon potential between the two valence particles. It is therefore not surprising that the monopole component of H_{res} can be split in a central, tensor and spin-orbit part.

[B] With different sub-space we mean that j is a proton state and j' is a neutron orbit or the other way around.

4. By diagonalizing H, the energy eigenvalues and the eigenfunctions are obtained. They are used to reconstruct the level scheme and to calculate the different nuclear observables, making a comparison with experiment possible.

In this very general framework, different model-space bases and diagonalization algorithms can be used and many sets of single-particle energies and TBME can be applied. This results in the large variety of shell-model codes and residual interactions that exists nowadays.

For this thesis work, large-scale shell-model calculations have been performed with the ANTOINE code [11], using the sdpf [12] and SDPF-U [13] residual interactions. The results are presented in chapters 5 and 6 that study the isotopes near the island of inversion and around $N = 28$. A description of how the ANTOINE model-space basis is calculated (the 'M-scheme') and how the Hamiltonian is diagonalized (the 'Lanczos diagonalization') is not relevant in this discussion and will be omitted.
Interesting to mention however is the method used to determine the TBME. The *sd*-part of the sdpf and SDPF-U residual interaction is based on the USD interaction developed by Wildenthal [14]. The TBME of the latter are calculated starting from the meson exchange theory of the free nucleon-nucleon potential ('G-matrix'). The pf-component of the sdpf and SDPF-U residual interaction corresponds to the set of KB' matrix elements [15] and the $\pi(sd)-\nu(pf)$ cross-shell TBME are taken from the G-matrix formalism of Kahana, Lee and Scott [16]. For the practical use in shell-model calculations, empirical corrections are added to the three sets of TBME given above. These corrections are improved when more detailed experimental data become available. In that sense, SDPF-U must be considered as 'an upgrade' of the sdpf residual interaction as it incorporates monopole changes based on recent experimental results e.g. for the ^{37}S [17] and ^{47}Ar [18] isotopes.

The nuclear shell-model has been proven to account for many experimental observations and is therefore one of the most successful and widely used techniques to interpret and simulate experimental results. Although many progressive efforts have been made, one must bear in mind that, due to the limited computational power and incomplete knowledge of the nucleon-nucleon interaction and the residual effects in the atomic nucleus, it is still very difficult to perform accurate shell-model calculations in large model spaces.

Chapter 2

Measurement of nuclear moments

Nuclear moments are excellent probes to study isotopes far from stability since they reveal direct information on the nuclear structure. Definitions and properties are presented in the first section. In the second section, the principles of the β-Nuclear Magnetic Resonance (β-NMR) technique are described. This method is often applied to determine ground-state magnetic dipole moments and electric quadrupole moments of β-decaying nuclei.

2.1 Electromagnetic moments

Nuclear moments, introduced as spherical tensor operators of rank k, represent the intrinsic properties of the nucleus when interactions with electromagnetic fields are considered. The electromagnetic fields can be applied externally but in most cases they are induced by the electrons in an atom or in a crystalline solid. This work focusses on the hyperfine interactions between nuclear spins and their electromagnetic environment in a crystal structure. It does not yield a description of the hyperfine structure of a free atom in terms of the coupled angular momentum $\mathbf{F}$.
One distinguishes between two types of nuclear moment operators, based on the nuclear properties they represent. The electric multipole moment operators $\mathbf{Q}_q^{(k)}$ are associated to the nuclear charge distribution while the magnetic multipole moment operators $\mathbf{M}_q^{(k)}$ originate from the convection and spin currents

in the nucleus. For each type, a general expression has been developed [19, 20]:

$$\mathbf{Q}_q^{(k)} = \sqrt{\frac{4\pi}{2k+1}}\, e \sum_i^A g_{l,i} r_i^k \mathbf{Y}_{q,i}^{(k)} \tag{2.1}$$

$$\mathbf{M}_q^{(k)} = \sqrt{\frac{4\pi}{2k-1}}\, \frac{\mu_N}{\hbar} \sum_i^A \sqrt{k(2k-1)}\, r_i^{k-1} \left[\frac{2g_{l,i}}{k+1} \left(\mathbf{Y}_i^{(k-1)} \mathbf{L}_i \right)_q^{(k)} + g_{s,i} \left(\mathbf{Y}_i^{(k-1)} \mathbf{S}_i \right)_q^{(k)} \right] \tag{2.2}$$

In both formulae, the contributions of all nucleons i in terms of the spherical harmonics $\mathbf{Y}_q^{(k)}(\theta, \phi)$ are summed. The orbital g-factors $g_{l,i}$ are one for a proton and zero for a neutron. The intrinsic spin g-factors $g_{s,i}$ correspond to the g-factors of a free proton and a free neutron. They have been determined experimentally and their values, $g_s^\pi = 5.585694675(57)$ and $g_s^\nu = -3.82608545(90)$, are taken from Ref. [21]. In Eq. 2.2, $\mathbf{L}_i$ denotes the orbital angular momentum of the nucleon while $\mathbf{S}_i$ is used to indicate the spin angular momentum.
For a given nuclear state $|I, m>$ with spin I, the matrix-elements of the multipole moment operators can be calculated using the procedure illustrated below. The right-hand side of Eqs. 2.3 and 2.4 is obtained by applying the Wigner-Eckart theorem, resulting in a reduced matrix element and a Wigner 3j-symbol which carries the full m-dependence [22].

$$< I, m \left| \mathbf{Q}_q^{(k)} \right| I, m >= (-1)^{I-m} \begin{pmatrix} I & k & I \\ -m & q & m \end{pmatrix} < I || \mathbf{Q}_q^{(k)} || I > \tag{2.3}$$

$$< I, m \left| \mathbf{M}_q^{(k)} \right| I, m >= (-1)^{I-m} \begin{pmatrix} I & k & I \\ -m & q & m \end{pmatrix} < I || \mathbf{M}_q^{(k)} || I > \tag{2.4}$$

From this result, two important properties of the nuclear moments and their operators can be derived:

- The spherical harmonics in Eqs. 2.1 and 2.2 determine the parity of the multipole moment operators. This implies that $\mathbf{Q}_q^{(k)}$ has parity $(-1)^k$ while the parity of $\mathbf{M}_q^{(k)}$ is $(-1)^{k-1}$. If we assume that the nuclear wave function has a well-defined spin and parity, then the matrix elements in Eq. 2.3 vanish when k is odd, giving rise to only even electric multipole moments. For the same reason, only odd magnetic moments exist.

- According to its general properties, a Wigner 3j-symbol only exists when the sum of the lower row equals 0 and when the upper row fulfills the triangle condition. For the Wigner 3j-symbols given in Eqs. 2.3 and 2.4, this implies that $q = 0$ and that $k \leq 2I$. Therefore, a nucleus with spin $I = 0$ can only have an electric monopole moment ($k = 0$) while a nucleus with spin $I = 1/2$ has an electric monopole moment and a magnetic dipole moment ($k = 1$) but no electric quadrupole moment ($k = 2$), ...

In order to determine the *observable* electric and magnetic moments, $Q^{(k)}$ and $M^{(k)}$, the expectation value of the nuclear moment operator is calculated for the state with the maximal spin projection $|I, m = I >$. Since $q = 0$, the (2k+1) coordinates of the nuclear moment operator reduce to one measurable quantity:

$$Q^{(k)} = < I, I \left| \mathbf{Q}_0^{(k)} \right| I, I >= \begin{pmatrix} I & k & I \\ -I & 0 & I \end{pmatrix} < I||\mathbf{Q}_0^{(k)}||I > \quad (2.5)$$

$$M^{(k)} = < I, I \left| \mathbf{M}_0^{(k)} \right| I, I >= \begin{pmatrix} I & k & I \\ -I & 0 & I \end{pmatrix} < I||\mathbf{M}_0^{(k)}||I > \quad (2.6)$$

2.1.1 Magnetic dipole moment

Inserting $k = 1$ in Eq. 2.2 gives the expression for the magnetic dipole moment operator $\boldsymbol{\mu}$ [23]:

$$\boldsymbol{\mu} = \frac{\mu_N}{\hbar} \left[\sum_i^A g_{l,i} \mathbf{L}_i + \sum_i^A g_{s,i} \mathbf{S}_i \right] \quad (2.7)$$

As the operator $\boldsymbol{\mu}$ consists of an orbital and a spin contribution, the magnetic dipole moment is very sensitive to the configuration of the valence nucleons and to the corresponding nuclear structure.
In a second approach, the magnetic dipole moment operator $\boldsymbol{\mu}$ can also be related to the nuclear spin operator via the nuclear g-factor g:

$$\boldsymbol{\mu} = \frac{\mu_N}{\hbar} g \mathbf{I} \quad (2.8)$$

With this expression and using Eq. 2.6, the magnetic moment μ of a nucleus with spin I can be calculated. Note that the 0^{th} component of a spherical tensor operator of rank 1 equals the z-component of the same tensor operator in its Cartesian form. Therefore, the magnetic moment is written as:

$$\mu =< I, I|\boldsymbol{\mu_z}|I, I >= gI\mu_N \quad (2.9)$$

Since $\boldsymbol{\mu}$ is a one-body operator, the magnetic moment μ of a composite nuclear state with spin I can easily be expressed in terms of the magnetic moments of its weakly bound constituents. The complete derivation can be found in [23].

$$\mu = \frac{I}{2} \left[\left(\frac{\mu_1}{I_1} + \frac{\mu_2}{I_2} \right) + \left(\frac{\mu_1}{I_1} - \frac{\mu_2}{I_2} \right) \frac{I_1(I_1+1) - I_2(I_2+1)}{I(I+1)} \right] \quad (2.10)$$

(I_1, μ_1) and (I_2, μ_2) are the nuclear spin and the magnetic moment of the two parts. A special case is encountered when one valence particle is considered outside a closed shell, which is assumed to have a zero spin and a zero magnetic moment. The orbital angular momentum $\mathbf{l}$ and the intrinsic angular momentum

s of the unpaired nucleon couple to a total spin $\mathbf{j} = \mathbf{l}+\mathbf{s}$. Applying the addition theorem (Eq. 2.10), gives two possible magnetic moments [24]:

$$\mu = \left[\left(j - \frac{1}{2}\right) g_l + \frac{1}{2} g_s\right] \mu_N \qquad \text{for } j = l + 1/2 \qquad (2.11)$$

$$\mu = \frac{j}{j+1}\left[\left(j + \frac{3}{2}\right) g_l - \frac{1}{2} g_s\right] \mu_N \qquad \text{for } j = l - 1/2 \qquad (2.12)$$

When these single particle moments are calculated with the free nucleon g-factors, they are called the Schmidt moments.
Very often in shell-model calculations, the free nucleon g-factors are replaced by effective values in order to get a better agreement between theory and experiment (examples see later). This is a direct consequence of the use of effective interactions in a limited valence space [3]. Effective nucleon g-factors are obtained from a comparison between the calculated and the measured magnetic moments and are therefore model-dependent.

2.1.2 Electric quadrupole moment

The multipole moment operator of second order is obtained by inserting $k = 2$ in Eq. 2.1:

$$\mathbf{Q}^{(2)}_q = \sqrt{\frac{4\pi}{5}} \sum_i^A e_i r_i^2 \mathbf{Y}^{(2)}_{q,i} \qquad (2.13)$$

The expression $e \cdot g_{l,i}$ in Eq. 2.1 is replaced by e_i, which takes the value $e_i = 1e$ for a proton and $e_i = 0$ for a neutron. Similar as for the magnetic dipole moment, effective values for e_i can be used in shell-model calculations to get a better agreement with experiment (examples see later).
According to Eq. 2.5, the spectroscopic quadrupole moment (in $e$mb) equals:

$$Q_s = < I, I \left| \mathbf{Q}^{(2)}_0 \right| I, I > = \sqrt{\frac{I(2I-1)}{(2I+1)(2I+3)(I+1)}} < I \,||\, \mathbf{Q}^{(2)}_0 \,||\, I > \qquad (2.14)$$

Q_s is a measurable quantity which gives the average deviation of the nuclear charge distribution from a spherical symmetry. Although nuclei with spin $I = 0$ or $I = 1/2$ have a zero spectroscopic quadrupole moment, they can have an intrinsic deformation.
Similar as for the Schmidt-moments, one can deduce a single-particle quadrupole moment for an odd nucleon in an orbit with angular momentum **j** [23]:

$$Q_{s.p.} = -e_j \frac{2j-1}{2(j+1)} \left\langle r^2 \right\rangle \qquad (2.15)$$

Here, e_j is the effective charge of the nucleon in the orbital j and $\left\langle r^2 \right\rangle$ is the mean square charge radius of the same orbital.

2.2 β-Nuclear Magnetic Resonance techniques

As illustrated in the previous section, the nuclear magnetic dipole moment and the spectroscopic electric quadrupole moment hold valuable information on the nuclear structure of the isotope under investigation. Measured values, in comparison with theoretical predictions, often reveal unexplored aspects of exotic nuclei, underlining the importance of nuclear-moment research.

A frequently used method to study ground-state nuclear moments of β-decaying nuclei is the β-Nuclear Magnetic Resonance (β-NMR) technique [25]. This technique can be used to measure nuclear g-factors as well as spectroscopic quadrupole moments. The procedure followed in both cases is the same, apart from the induced hyperfine interactions and the applied rf-frequency(ies). Before coming to the differences, the common framework in which all β-NMR measurements are performed, is described.

β-NMR requires spin-polarized nuclei. The spins of these nuclei have a preferential direction in space with respect to an axial symmetry axis (z-axis). The nuclear ensemble is called 'polarized' when the up/down symmetry along z is broken. This implies that the m and $-m$ states have a different occupation probability: $p_m \neq p_{-m}$. When the oriented nuclear ensemble is described using the formalism of the orientation tensors $\mathbf{B}^{(\lambda)}$ (see e.g. [26]), three different but equivalent definitions exist for the degree of polarization P [26, 27]:

$$P = \sum_{m=-I}^{I} \frac{m}{I}\, p_m = -\sqrt{\frac{I+1}{3I}}\mathbf{B}_0^{(1)} = \frac{< I_z >}{I} \tag{2.16}$$

For polarized nuclei, an anisotropic β-decay pattern is observed. In general, the angular distribution of radiation emitted from an oriented spin ensemble is given by [27, 28]:

$$W(\theta,\phi) = \sqrt{4\pi} \sum_{\lambda} \sqrt{\frac{1}{2\lambda+1}}\, \mathbf{B}^{(\lambda)}\, \mathbf{A}^{(\lambda)}\, \mathbf{Y}^{(\lambda)}(\theta,\phi) \tag{2.17}$$

$\mathbf{Y}^{(\lambda)}(\theta,\phi)$ stands for the spherical harmonics and $\mathbf{A}^{(\lambda)}$ are the angular distribution coefficients which describe the properties of the emitted radiation. In the case of β-decay, the general formulation of $\mathbf{A}^{(\lambda)}$ and $W(\theta,\phi)$ is very complex and can be found in specialized textbooks [28]. For a polarized ensemble and allowed β-decay however, Eq. 2.17 can be reduced to the simple expression:

$$W(\theta) = 1 + \mathbf{B}_0^{(1)}\, \mathbf{A}_0^{(1)} \cos(\theta) \tag{2.18}$$

Using Eq. 2.16 and the equality $\mathbf{A}_0^{(1)} = -\frac{v_\beta}{c}\sqrt{\frac{I+1}{3I}}A_\beta$ for allowed β-decay, $W(\theta)$ can be rewritten as the commonly known expression:

$$W(\theta) = 1 + \frac{v_\beta}{c} A_\beta P \cos(\theta) \tag{2.19}$$

v_β/c is the ratio of the velocity of the β-particles to the speed of light and is close to one for high-energy β-particles. A_β is the asymmetry parameter which depends on the spin and the decay properties of the investigated nuclei. Table 2.1 gives an overview of the A_β parameters for allowed Gamow-Teller $\beta^\mp$ transitions [27]. I_i denotes the spin of the decaying state while I_f is the spin of the daughter state. The symbol y, used in Table 2.1, equals $\frac{C_V M_F}{C_A M_{GT}}$ with C_V (C_A) the vector (axial vector) coupling constants and M_F (M_{GT}) the Fermi (Gamow-Teller) matrix elements.

Spin-polarized nuclei are implanted in a crystal which is placed in an external magnetic field $\mathbf{B_0}$ along the z-axis. This magnetic field, together with a possible electric field gradient present in the crystal, induces hyperfine interactions which cause a level splitting of the nuclear m-states.
When the implanted nuclei decay, β-rays are detected in two ΔE/E-pairs of plastic scintillators. Both pairs are situated along the polarization direction, one at 0° and the other at 180°. Using the number of coincident counts N_{up} (N_{down}) in the upper (lower) pair of scintillators, the measured β-asymmetry can be determined:

$$A = \frac{N_{up} - N_{down}}{N_{up} + N_{down}} = \frac{v_\beta}{c} A_\beta P \tag{2.20}$$

Theoretically, a non-zero β-asymmetry is observed when a polarized ensemble of decaying nuclei is considered.
Perpendicular to the external magnetic field, a rf-field is applied inside a coil placed around the implantation crystal. When the energy of the rf-field equals the energy difference between two subsequent m-states, the occupation probability of the m-states is altered. This effect leads to a different value for the polarization and therefore to a change in the experimental β-asymmetry. By

Table 2.1: Asymmetry parameter A_β for allowed Gamow-Teller $\beta^\pm$ transitions.

$I_i \longrightarrow I_f$	$A_{\beta\mp}$
I_f=I_i+1	$\pm\frac{I_i}{I_i+1}$
I_f=I_i-1	∓ 1
I_f=I_i	$\frac{\mp 1 - 2y\sqrt{I_i(I_i+1)}}{(I_i+1)(1+y^2)}$

scanning the β-asymmetry as a function of the rf-energy, a β-NMR resonance is observed from which the g-factor or the quadrupole moment can be deduced.

Based on this general principle, two β-NMR approaches are known: the Continuous RF (CRF) technique and the Adiabatic Fast Passage (AFP) method. The CRF technique combines a continuous implantation of polarized nuclei with a continuously applied rf field and a simultaneous β-detection. At resonance, the initial polarization is destroyed. AFP respects a strict time sequence of ion implantation, rf application and β-counting. When particular experimental conditions are fulfilled (see later), the spin-polarization is inverted and a double β-NMR effect is observed. This thesis work concentrates on the CRF technique as it is the experimental method used by the Leuven Nuclear Moments group. Adiabatic fast passage is described and compared to CRF in chapter 5 where the measurement of the ^{31}Al quadrupole moment is presented.

2.2.1 Measurement of nuclear g-factors

When measuring the nuclear g-factor, the isotopes of interest are implanted in a host crystal with a cubic crystal structure. As no electric field gradient is present, the magnetic field $\mathbf{B_0}$ induces an equidistant Zeeman splitting of the nuclear m-states (Fig. 2.1). The Hamiltonian describing the magnetic dipole interaction is $\mathbf{H} = -\boldsymbol{\mu} \cdot \mathbf{B_0}$ [26]. Since the magnetic field is applied along the z-axis of the chosen reference frame, only the third component of this dot product is different from zero. When using Eq. 2.8, it is found that the nuclear m-states have energies proportional to the quantum number m:

$$E_m = - < I, m \,|\boldsymbol{\mu_z}|\, I, m > B_0 = -g\frac{\mu_N}{\hbar} < I, m \,|\mathbf{I_z}|\, I, m > B_0 = -g\mu_N B_0 \, m \tag{2.21}$$

The energy difference between two subsequent levels equals

$$E_m - E_{m+1} = g\mu_N B_0 = h\nu_L \tag{2.22}$$

In this expression, ν_L denotes the Larmor frequency. When scanning the rf-frequency, different values of the rf-frequency are applied for 10 s up to a few minutes, depending on the lifetime of the nucleus. In order not to miss out on ν_L, frequency modulation is applied which covers at least one half of the interval between two subsequent rf-frequencies. Generally, the modulation takes the shape of a ramp function, being repeated at a rate of 100 Hz.
From the position of the resonance in the asymmetry versus rf-frequency curve, the experimental g-factor can be extracted. Once the spin of the state is known also the value of the magnetic moment can be determined. The β-NMR method is not sensitive to the sign of both observables.

Although β-NMR is a very general term, it is sometimes restricted to methods that exclusively study the nuclear g-factor. In that respect, the term β-Nuclear Quadrupole Resonance (β-NQR) is used when the quadrupole moment is measured. It will be clear from the context which definition of β-NMR has to be applied.

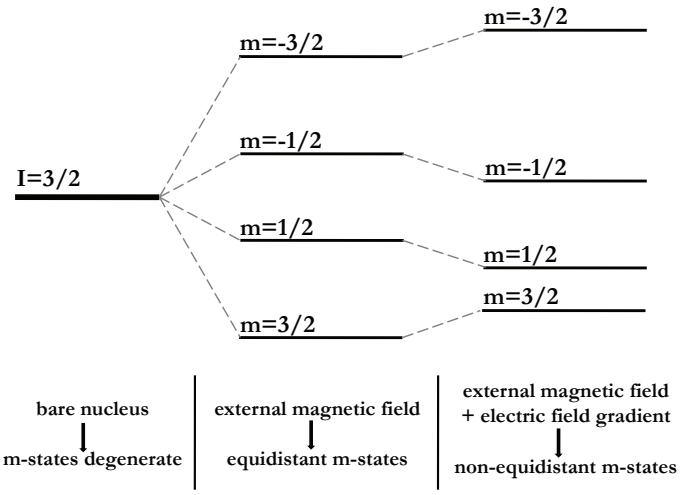

Figure 2.1: Nuclear m-states of a bare $I = 3/2$ nucleus (left). Equidistant Zeeman level splitting caused by an external magnetic field $\mathbf{B_0}$ (middle). Non-equidistant level splitting originating from the combined interaction of a magnetic field and a minor axial electric field gradient (right).

2.2.2 Measurement of spectroscopic quadrupole moments

When the spectroscopic quadrupole moment is studied, the nuclei are implanted in a crystal with an electric field gradient V_{zz}. This V_{zz} is one component of the electric-field gradient tensor at the position of the nucleus $\mathbf{x} = \mathbf{0}$, in the Cartesian axis system described by a 3×3 traceless symmetric matrix:

$$V_{ij} = \left(-\frac{\partial E_j}{\partial x_i} \right)_{\mathbf{x=0}} = \left(\frac{\partial^2 V}{\partial x_i \partial x_j} \right)_{\mathbf{x=0}} \tag{2.23}$$

E_j is the j-component of the electric field while V denotes the electrostatic potential. In addition to the Zeeman splitting caused by the external magnetic field $\mathbf{B_0}$, the energies of the m-states are also influenced by the inhomogeneous electric field at the position of the nucleus. This leads to a non-equidistant

level splitting (Fig. 2.1). The Hamiltonian of the combined interaction is [29]

$$\mathbf{H} = -\boldsymbol{\mu} \cdot \mathbf{B_0} + \frac{Q_s V_{zz}}{4I(2I-1)} \left[3\mathbf{I}_z^2 - I(I+1) + \frac{1}{2}\eta \left(\mathbf{I}_+^2 + \mathbf{I}_-^2 \right) \right] \tag{2.24}$$

The reference frame used here is the *principal axis system* (PAS) of the V_{ij} tensor, defined such that V_{ij} becomes a diagonal and traceless matrix with $|V_{zz}| \geq |V_{yy}| \geq |V_{xx}|$. The asymmetry parameter η is determined as $\frac{V_{yy}-V_{xx}}{V_{zz}}$.

Experimental conditions often simplify the complex solution of the Hamiltonian given in Eq. 2.24. The experiments presented in this work have always been performed with:

- An axial symmetric electric-field gradient and consequently $\eta = 0$.
- A dominant magnetic interaction: $\omega_L = \frac{g\mu_N B_0}{\hbar} \gg \omega_Q = \frac{Q_s V_{zz}}{4I(2I-1)\hbar}$
- An angle θ of 0° or 90° between the z-axis of the V_{ij}-PAS and $\mathbf{B_0}$.

A dominant magnetic interaction implies that the PAS of the magnetic field should be used as a reference system and that the 'quadrupole part' of the hamiltonian can be treated as a perturbation. Therefore the Hamiltonian in Eq. 2.24 is replaced by a series expansion. Based on this series expansion and respecting also the two other conditions given above, the energy difference between two subsequent m-states can be deduced [29]:

$$\begin{aligned} E_m - E_{m+1} \quad = \quad & h\nu_L - \frac{3Q_s V_{zz}}{8I(2I-1)h}(2m+1)(3\cos^2\theta - 1) - \\ & \frac{Q_s^2 V_{zz}^2}{32\nu_L h^2} \; \frac{9}{4I^2(2I-1)^2} \; [6m(m+1) - 2I(I+1) + 3] \; \sin^4\theta \end{aligned} \tag{2.25}$$

Several transition frequencies exist for one value of Q_s, depending on the nuclear spin and the m-states involved. Therefore, $2I$ transition frequencies, corresponding to one particular quadrupole moment, are applied and modulated simultaneously. In the experimental β-asymmetry pattern, a resonance is observed when Eq. 2.25 is fulfilled. From the position of the resonance, the spectroscopic quadrupole moment can be deduced, provided that the electric field gradient is known.

In literature, the term β-NQR often points to the technique which involves only an electric field gradient to determine the spectroscopic quadrupole moment. In this thesis, the term β-NQR is used for all β-NMR methods which determine Q_s, independent of the presence of an external magnetic field.

Chapter 3

Experimental setup

After having dealt with the properties of the nuclear moments and the principles of the β-Nuclear Magnetic Resonance technique, this chapter focusses on the experimental aspects of the nuclear-moment measurements performed at the LISE fragment separator at GANIL.
In November 2006, a newly designed β-NMR/β-NQR setup was installed at LISE, replacing the old setup used in earlier experiments. A technical description of all components and an overview of the corresponding GEANT4 simulations that evaluate the performance of the new setup can be found in the article that concludes this chapter. The paper was published in Nuclear Instruments and Methods in Physics Research A [30].
The following three sections concentrate on a few specific topics, which are only briefly introduced in the article. The first section describes the main beam optics used to produce and purify a polarized fragment beam at LISE-GANIL. The second section gives three arguments to motivate the installation of the new β-NMR/β-NQR setup and in the last section, the GEANT4 framework is outlined in more detail.

3.1 The GANIL facility and the LISE beamline

All β-NMR and β-NQR experiments, presented in this thesis work, are performed at the LISE fragment separator (*Ligne d' Ions Super Epluchés*) at GANIL (*Grand Accélérateur National d' Ions Lourds*, Caen, France). The LISE facility [31, 32] is well suited for β-NMR/β-NQR measurements as it provides high-purity polarized beams of exotic nuclei. The latter are produced in a projectile-fragmentation reaction, induced by a stable primary beam on a rotating target. The primary beam, with an intensity of 100 nA to 4 μA, is accelerated to intermediate energies (typically 60-80 AMeV) by two segmented

cyclotrons CSS1 and CSS2 (*Cyclotrons a Secteurs Séparés*). Before entering CSS2, the ions are stripped by a carbon foil. After passing the α-spectrometer, the primary beam is injected in the LISE beamline where it impinges on the rotating target. A ^{9}Be target is used for the experiments described in this PhD work. Projectile fragmentation and pick-up reactions are induced which create a broad spectrum of reaction products. Two dipole magnets ($B\rho 1$ and $B\rho 2$) select the isotopes under investigation. The secondary beam is purified using a wedge-shaped degrader in the intermediate dispersive plane (^{9}Be in our case), horizontal and vertical slits along the beam path and a Wien filter, positioned at the end of the LISE fragment separator. Behind the Wien filter, at the final focal point, the β-NMR/β-NQR setup is placed. A schematic of the beam optics is given in Fig. 3.1.

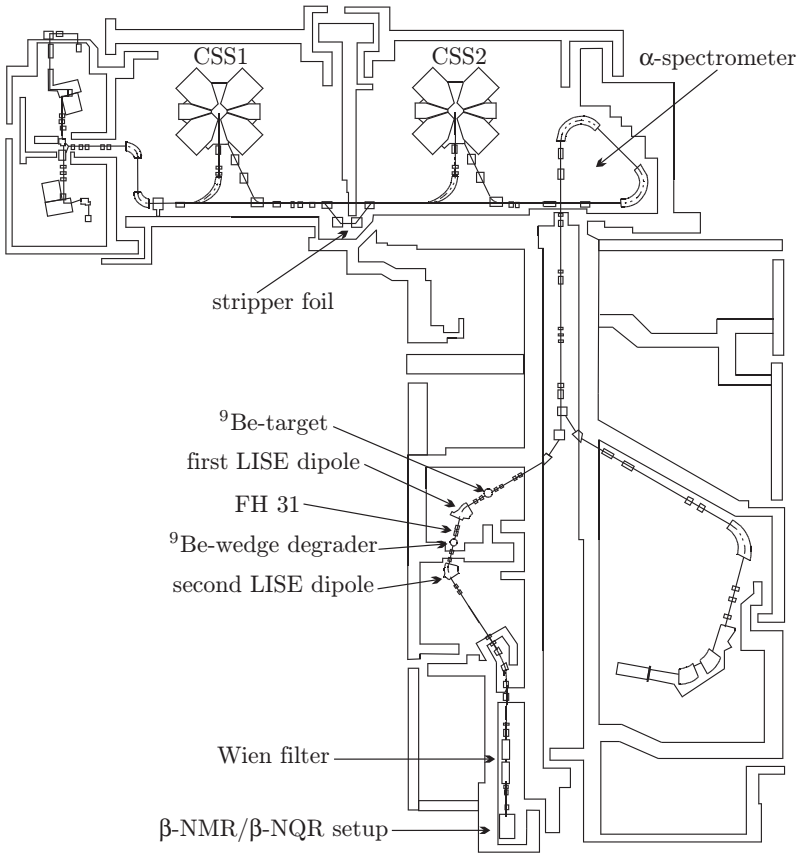

Figure 3.1: Overview of the LISE-GANIL beam line (settings according to the experiments described in this work).

In order to produce and select spin-polarized nuclei, the primary beam should make a small angle θ_L (typically 2(1)°) with respect to the entrance of the spectrometer. Moreover, a selection in the longitudinal momentum distribution of the fragments should be made, using the horizontal slits FH31, also indicated in Fig. 3.1.

The optimization of the LISE fragment separator for the selection of the proper isotope is done based on simulations with the LISE++ code [33, 34]. This program allows to determine the optimal target and wedge thicknesses, the correct $B\rho$-values, the momentum distribution of the fragments, ...

3.2 Motivation for the new β-NMR/β-NQR setup

The motivation for the development of the new setup is threefold and addresses the two main components of the β-NMR/β-NQR setup: the external magnetic field and the rf-circuit.

- **Small magnetic-field range**
  The old setup incorporated a magnet with a total range of only 0.18 T. Consequently, small g-factors (<0.1) could not be studied. The old magnet was replaced by a new type, providing magnetic fields up to 1.02 T.

- **Inhomogeneous field at the central area of the magnet**
  Field-profile measurements for the old magnet showed a rather large inhomogeneity across the volume of the implantation crystal. This is illustrated in Table 3.1 which specifies the maximum deviation of the magnetic field ΔB at a distance of 1 cm in the X, Y and Z direction from the average value in the center. Table 3.1 also presents the results of similar field-profile measurements for the new magnet, demonstrating its superior homogeneity close to the center. In all measurements, a magnetic field of 0.18 T was applied. The vertical direction defines the Z-axis while Y is oriented along the upstream beam axis.

Table 3.1: Maximum deviation of the magnetic field ΔB at a distance of 1 cm in the X, Y and Z direction from the average value in the center (±0.18 T). Identical measurements have been performed for the old and the new magnet.

Direction	ΔB for the old magnet (%)	ΔB for the new magnet (%)
X	0.87	0.02
Y	0.03	0.02
Z	1.10	0.17

Additional field-profile measurements and a description of the importance of a homogeneous magnetic field at the position of the implanted nuclei can be found in the attached paper.

- **Small rf-frequency range**
  In order to perform a successful β-NMR or β-NQR experiment, a sufficiently strong rf-field (typically more than 0.1×10^{-4} T) should be available. In the old setup, this condition was accomplished by connecting the output of the frequency generator(s) to a LRC-circuit, tuned in resonance by adjusting the value of the variable capacity. As a consequence, only frequency intervals smaller than the width of the LRC resonance (maximum 100 kHz) could be scanned, strongly limiting the possibilities of a broad β-NMR/β-NQR measurement.
  The position at which a LRC-resonance can be found is also determined by the specifications of the coil and the range of the variable capacity. For one particular coil, LRC-resonances could typically be created in a frequency region of only 1500 kHz wide. To reach a higher or lower rf-frequency region the coil had to be changed, implying another strong limitation on the g-factor range to be studied.
  Since the new setup became operational, no restrictions exist anymore. A rf-amplifier, especially designed for applications with a variable output impedance (such as the rf-coil), is now connected to the frequency generator(s), making the use of a resonant LRC-circuit no longer necessary. Technical details of the new rf-circuit are given in the NIM article.

3.3 The GEANT4 framework

In order to evaluate the performance of the new β-NMR/β-NQR setup, a GEANT4 application was developed. GEANT4 [35] is a free C++ toolkit, used to accurately describe the interaction of particles with matter in a very broad energy range. It provides a large set of geometrical building blocks and physics processes to simulate various applications in particle physics, nuclear physics, accelerator design, space engineering and medical physics.
The program implemented in the framework of this thesis is developed to study the β-detection efficiency and the sensitivity of the newly designed β-NMR/β-NQR setup to observe a resonant change in the β-asymmetry. As the program itself is far too large to be quoted to its full extent, a simple schematic is drawn explaining the course of each simulation.

1. **Initialization phase**
   At this stage, the geometry, the appropriate physics processes and the 'primary generator' are initialized.

The *geometry* is a 3D technical drawing of the experimental setup, including all information on the dimensions, materials and magnetic fields used. It contains the β-scintillators, defined as sensitive detectors, the crystal and crystal holder, the hall probe holder and the Al degrader placed in front of the crystal. A vertical magnetic field can be applied.
The *physics processes* include ionization, Bremsstrahlung, multiple scattering, Rayleigh and Compton scattering, photo-electric effects and γ-conversion for photons and electrons with energies between 250 eV and 100 GeV, using the standard low-energy GEANT4 libraries [36].
The *primary generator* controls the emission of electrons from a point-like β-source in the center of the setup. It coordinates the selection of the emission angle θ and the energy of the β-particles. θ is determined by Eq. 2.19 while the energy of the electrons is based on the formalism described in [37–41].

2. **Simulation phase**
In the second stage, a Monte Carlo simulation is made of the trajectories of two times 100 million primary events, released by the β-source according to the specific angular and energy distribution described above. The first 100 million events are processed, assuming an isotropic β-radiation pattern ($P = 0$). The second half of the simulation is performed according to Eq. 2.19, taking into account a user-defined polarization P.
After each event, the energy deposited in the different sensitive detectors is calculated and recorded. After each run, the total number of detected events is registered and the β-spectra, recorded by the scintillators, are reconstructed.

3. **Analysis phase**
Using the total number of counts per detector, a short analysis is done:

   - The detection efficiency of each detector: $\epsilon_i = \frac{N_i}{100000000}$ with N_i the number of registered events per detector for the isotropic β-pattern.
   - The experimental asymmetries, given by Eq. 2.20, for the isotropic (A_{iso}) and the anisotropic (A_{aniso}) radiation pattern.
   - The observed β-asymmetry change: $\Delta = |A_{aniso} - A_{iso}|$.
   - The observed β-asymmetry change relative to its theoretical value: $\delta = \frac{\Delta}{|A_\beta P|}$, a measure for the sensitivity of the setup to observe a resonant change in the β-asymmetry.

GEANT4 simulations have been made to study the effect of the crystal tilting angle, the crystal thickness, the Q_β-value and the applied magnetic field on ϵ_i and δ. The results can be found in the article enclosed.

The GEANT4 application presented in this work also has its limitations. So far, only a point-like β-source is included while the real beam spot has a diameter of about 16 mm. The effect of the γ-rays produced in the decay of the daughter nuclei is not taken into account, neglecting a part of the background registered by the scintillators. The influence of the rf-field is completely excluded and also the losses in the light guides, the photomultiplier tubes and the subsequent electronics chain, used to process the signals of the different detectors, are not taken into account. The figures quoted in the article should therefore be considered as upper limits for the detection efficiency and the sensitivity to observe a resonant change in the β-asymmetry.

Note
In the Nuclear Instruments and Methods article, the origin of the low-energy component arising in the simulated β-spectra of the E-detectors (Figure 7) is discussed. It is said that a significant amount of the β-particles reaches the scintillators at low energy due to scattering and absorption in the crystal and the crystal holder. A further evaluation of the GEANT4 simulations shows, however, that the low-energy component in the E-spectra is mainly caused by secondary particles created at collisions in the crystal and crystal-holder materials and not by degraded primary β-particles.

A new dedicated β-NMR/β-NQR setup for LISE-GANIL

M. De Rydt,[1] R. Lozeva*,[1] N. Vermeulen,[1] F. de Oliveira Santos,[2] S. Grévy,[2] P. Himpe,[1] C. Stödel,[2] J.C. Thomas,[2] P. Vingerhoets,[1] and G. Neyens[1]

[1] *Instituut voor Kern- en Stralingsfysica, K.U. Leuven, Celestijnenlaan 200D, B-3001 Leuven, Belgium*
[2] *Grand Accélérateur National d'Ions Lourds (GANIL), CEA/DSM-CNRS/IN2P3, B.P. 55027, F-14076 Caen Cedex 5, France*

A new β-NMR/β-NQR setup is developed to study nuclear magnetic dipole moments and electric quadrupole moments at the LISE fragment separator at GANIL. Two key elements make the new design very powerful: the homogeneous magnet and the strong radio-frequency amplifier. The combination of both makes it possible to examine a broad spectrum of magnetic dipole and electric quadrupole moments. Several factors have an influence on the detection efficiency and on the sensitivity of the setup to observe a resonant change in the β-asymmetry: the thickness and the tilting angle of the implantation crystal, the material in the vacuum chamber, the applied magnetic field and the Q_β-value of the decaying nuclei. A detailed study of these effects is made using a dedicated GEANT4 Monte Carlo simulation code.

PACS numbers: 21.10.Ky, 27.20.+n, 25.70.Mn, 07.50.-e, 07.55.-w, 29.40.Mc, 07.20.Mc, 02.70.Uu

I. INTRODUCTION

Many theoretical and experimental projects worldwide study the structure of exotic nuclei close to the drip lines. These nuclei are predicted to reveal new aspects of nuclear structure that challenge the existing models. The island of inversion ($N \simeq 20$) and the neutron rich $N \simeq 28$ isotopes, for instance, exhibit unexpected changes from the shell-model configuration. Although only two examples are given here, structural evolution occurs around all 'traditional' magic numbers. For a recent review, see Ref. [1].

Magnetic dipole moments and electric quadrupole moments provide direct information on the nuclear structure. Therefore, both observables are highly suitable to study nuclei far from stability, where changes in the shell structure appear. The magnetic dipole moment, μ, is very sensitive to the orbits occupied by the valence nucleons and it can reveal the details of the investigated nuclear configuration. The electric quadrupole moment, Q, is a direct measure of the nuclear deformation since it indicates the deviation of the nuclear charge distribution from a sphere.

* Present address: CSNSM, Université Paris-Sud 11, CNRS/IN2P3, F-91405 Orsay-Campus, France

In the past decades, remarkable progress has been made in producing high-intensity beams of exotic nuclei at various accelerator facilities. Very neutron- and proton-rich isotopes became available for nuclear structure research in general and for nuclear moment measurements in particular.
One of the most powerful methods to study ground-state magnetic dipole moments of radioactive isotopes is the β-Nuclear Magnetic Resonance (β-NMR) technique. Based on the same principle, the β-Nuclear Quadrupole Resonance (β-NQR) method was developed to study electric quadrupole moments. In literature, the term NQR usually refers to a technique which studies the quadrupole moments of stable nuclei based on the quadrupole interaction with their environment. For radioactive isotopes, however, Q is often measured through its interaction with an electric field gradient and an externally applied magnetic field. This method is called β-NQR, similar to the β-NMR technique which is used to study magnetic moments.
β-NMR as well as β-NQR require spin-polarized beams since they rely on a resonant change in the β-decay asymmetry. When the isotopes of interest are produced at an ISOL facility, the nuclear polarization can be obtained with optical laser pumping [2]. As this process strongly depends on the atomic properties of the nuclei involved, spin polarization can only be achieved for a limited amount of elements. In a projectile-fragmentation reaction, which is the production mechanism used at the LISE fragment separator at GANIL, the polarization is obtained by manipulating the reaction process. The angle put on the primary beam with respect to the entrance of the separator (typically $2(1)^\circ$) and the selection made in the longitudinal momentum distribution of the fragments result in a spin-polarized secondary beam [3–7].
As important and decisive information can be obtained from the measurement of nuclear moments, not only an accurate experimental technique but also a reliable setup is needed to study them. In the first section of this article, the β-NMR and β-NQR methods are discussed. In part two, a detailed description of the new β-NMR/β-NQR setup, used at the LISE beam line, is given. The last section presents the GEANT4 simulation code and its applications, developed to evaluate the new setup.

II. THE β-NMR AND β-NQR METHODS

The β-NMR technique is used to measure the nuclear g-factor g, which is directly linked to the magnetic dipole moment via $\mu = gI\mu_N$, with I the nuclear spin. In a β-NQR measurement, the quadrupole coupling constant $\nu_Q = \frac{eQ_sV_{zz}}{h}$ is determined, from which the spectroscopic quadrupole moment Q_s can be deduced, provided that the electric field gradient V_{zz} in the implantation crystal is known. Both techniques have been frequently used in the past and several different modes exist (e.g. the adiabatic fast passage method [8] or the continuous rf technique [9]). This work concentrates on the resonance methods that combine a constant implantation of polarized nuclei with a continuously applied radiofrequent (rf) field and a time-integrated detection of the ensemble polarization.
The β-NMR and β-NQR experiments are performed at the LISE fragment separator [10, 11]. The isotopes of interest are produced in a projectile-fragmentation reaction, induced by a stable and fully stripped primary beam (60-80 MeV/u, 1-4 eμA) on a rotating target. The secondary beam is selected by two dipole stages and transported to the D6 focal point. The beam identification is performed with three Si-detectors along

the beam path according to the standard energy loss versus time-of-flight method. A purification is done with the ^{9}Be wedge-degrader in the intermediate dispersive plane, the horizontal and vertical slits along the beam line and the Wien filter, installed in front of the β-NMR/β-NQR setup. When all components are optimized, a secondary beam purity of more than 90% can be achieved. In order to maintain the reaction-induced polarization, the fragments need to be fully stripped and the electron pick-up along the beam path has to be reduced to a minimum by adapting the thickness of the target, the wedge and the degraders. According to the simulation code GLOBAL, embedded in LISE++ package [12, 13], only fragments with $A < 80$ are completely stripped after intermediate-energy projectile-fragmentation reactions. At the end of the LISE fragment separator, the β-NMR/β-NQR setup is installed. The polarized nuclei are implanted in a crystal after being energy-degraded in two Al-foils. At 0° and 180° along the vertical polarization axis, above and below the implantation crystal, two pairs of plastic scintillators are positioned to detect the β-particles emitted when the implanted fragments decay (see Fig. 1). A spin-polarized ensemble of nuclei leads to an anisotropic β-decay pattern, given by the angular distribution function $W(\theta)$ [14]:

$$W(\theta) = 1 + \frac{v_\beta}{c} A_\beta P \cos(\theta) \tag{1}$$

A_β is the asymmetry parameter that depends on the spin and the decay properties of the investigated nuclei. P is the initial polarization of the implanted ensemble, induced by the nuclear reaction. The fraction $\frac{v_\beta}{c}$, with v_β the velocity of the β-particles and c the speed of light, is taken as 1. The measured β-asymmetry A, which is related to the polarization in the ensemble, is then defined as

$$A = \frac{N_{up} - N_{down}}{N_{up} + N_{down}} \simeq A_\beta P \tag{2}$$

where N_{up} is the number of coincident counts in the upper two detectors while N_{down} denotes the number of coincidences in the lower set of scintillators. Going from a polarized to an unpolarized ensemble induces a β-asymmetry change proportional to $A_\beta P$. This change in asymmetry is observed in a β-NMR or β-NQR measurement since both methods use hyperfine interactions to resonantly destroy the polarization at a well-defined rf-frequency.

In both techniques, the implantation crystal is situated in the center of a static magnetic field B_0, which is also the center of the setup. The external magnetic field induces a Zeeman splitting of the nuclear m-states, such that the energy difference between two subsequent levels is proportional to the g-factor and the applied magnetic field.

$$E_m - E_{m+1} = g\mu_N B_0 = h\nu_L \tag{3}$$

ν_L denotes the Larmor frequency and is typically of the order of 0.1 to 3 MHz. In β-NMR, only a Zeemann splitting of the nuclear levels is induced since an implantation crystal with a cubic lattice structure is chosen. In β-NQR, the polarized nuclei are implanted in a stopper with a non-cubic crystal structure. In that case, the quadrupole interaction with the electric field gradient causes an additional shift of the m-states which results in a non-equidistant level spacing. The energy difference between the magnetic sublevels m and m+1 under the influence of a Zeemann and

an axial symmetric quadrupole interaction can be calculated using perturbation theory. Up to the second order, the series expansion is given by expression (4), provided that the magnetic interaction (scaling with ν_L) is much stronger than the quadrupole interaction (scaling with $\frac{\nu_Q}{4I(2I-1)}$) [8].

$$E_m - E_{m+1} = h\nu_L - \frac{3h\nu_Q}{8I(2I-1)}(2m+1)\left(3\cos^2\theta - 1\right) \qquad (4)$$

$$- \frac{h\nu_Q^2}{32\nu_L}\ \frac{9}{4I^2(2I-1)^2}\ \left[6m(m+1) - 2I(I+1) + 3\right]\ \sin^4\theta$$

θ is the angle between the symmetry axis of the electric-field gradient in the crystal and the magnetic field B_0.

Perpendicular to the static magnetic field, a radio-frequent magnetic field is applied inside a coil mounted around the implantation crystal (see Fig. 1, 2 and 3). When a β-NMR measurement is performed, a particular frequency range is scanned in a number of discrete steps. For each step, the rf-frequency is continuously modulated around a central value to ensure that the resonance frequency is not missed. If the applied frequency range covers ν_L and if the rf-field strength is high enough, the occupation of all nuclear m-states is equalized and the polarization is destroyed. When the full rf-range has been scanned (typically in a few minutes), a measurement without rf-field is performed as a reference. This process is repeated until sufficient statistics are collected.

Multiple-rf β-NQR is based on the same principle, the only difference is the number of simultaneously applied frequencies. Expression 4 shows that, for a constant ν_Q, subsequent m-states have different transition frequencies. For each value of ν_Q, these correlated transition frequencies are applied simultaneously and each of them is modulated. When the quadrupole coupling constant is covered, the polarization is destroyed and a resonance is observed when the β-asymmetry is plotted as a function of the applied rf-frequency (see e.g. [15]).

III. DETAILS OF THE SET-UP

When the secondary beam enters the β-NMR/β-NQR setup, it first passes through two Al-degraders, placed at about 25 cm upstream from the implantation crystal. Behind the degraders, the fragments encounter a collimator and a Si-detector before entering the rf and detection region.

The variable degraders are two Al-foils with different thicknesses which can be inserted in the beam line and tilted with respect to the beam axis, allowing a total variable degrader thickness between 50 μm and 2600 μm. Due to the variable thickness, the implantation energy of the fragments can be precisely tuned. In case the maximum thickness of 2600 μm is not sufficient to stop the beam in the middle of the crystal (e.g. for very light nuclei), an extra Al-degrader can be mounted at a distance of a few cm from the crystal. By using an extra degrader instead of a thicker variable degrader, the angular divergence at large distances from the center is minimized.

Behind the set of variable degraders, a Pb-collimator is placed with a conical opening of 16 mm. This collimator prevents scattered particles from the degraders to get into the detection region and it limits the diameter of the beam spot to 16 mm.

Behind the collimator, the profile of the secondary beam can be measured using a position sensitive PIPS detector (Canberra, model PF20*20-500EB). This Si-detector is used during the beam tuning to check the transmission to the β-NMR/β-NQR setup and to inspect the beam spot size and position in order to realize a correct implantation in the crystal.
Behind the Si-detector, the secondary beam enters the rf and detection region. A schematic overview of this section is given in Fig. 1. The different parts, which are the magnet, the crystal holders, the rf-circuit and the β-detectors, will be further discussed in detail.

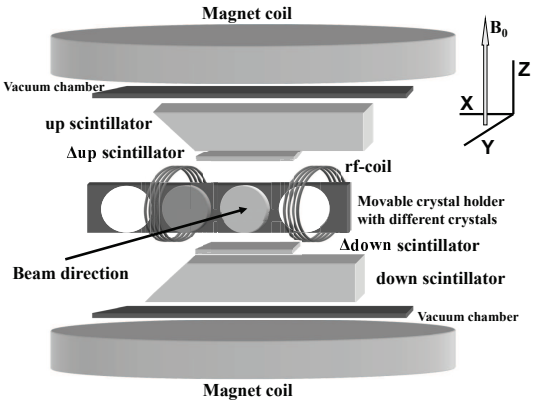

Figure 1: A schematic overview of the rf and detection region of the newly designed setup.

A. The magnet

The static magnetic field B_0 is generated by an electromagnet of the type B-E25v, manufactured by Bruker. The magnet has a variable pole gap, making it possible to achieve a central field of 2.2 T for an opening of 1 cm between the magnet poles. When the pole gap is expanded to its largest value (14.6 cm), the maximum field in the center drops to 0.87 T. The β-NMR/β-NQR application requires a 12 cm large gap since an aluminum vacuum chamber containing the rf and detection region is inserted between the magnet poles. For this configuration, a maximum field of about 1.02 T can be obtained in the center.
Not only the range of B_0 but also the homogeneity of the magnetic field over the crystal dimensions is an important aspect in β-NMR/β-NQR measurements. If the fragments experience very different field values over the implantation volume, a broadened resonance with reduced amplitude will be observed. Since the sensitivity of the method is proportional to the asymmetry change squared, a smaller amplitude due to the inhomogeneity of the magnetic field results in a less efficient technique and a significantly longer measuring time.

Extensive field profile measurements in the three spatial directions have been carried out for magnetic fields of 0.18, 0.5 and 1 T. A concise summary of these measurements is given in Table I which specifies the maximum deviation ΔB of the fields at a distance of $\pm$ 1 cm in the X,Y and Z directions from the average value in the center. X, Y and Z are defined in Fig. 1 and the center of the magnet is taken as the origin. A gradual change of the magnetic field has been observed in the X and Y directions. Going from the center to $\pm$1 cm, the field decreases by only 0.02 to 0.03%. In the Z direction, fluctuations occur, resulting in $\Delta B_z \leq 0.2\%$. These fluctuations do not reduce the accuracy of the β-NMR/β-NQR measurements since, according to the gaussian implantation profile of the fragments, most fragments are implanted close to the center ($<$ 5 mm) where ΔB_z is at most 0.05 - 0.09%.

Table I: Maximum deviation ΔB (%) of the magnetic field measured at $\pm$1 cm from the value in the center for three different magnetic fields.

Direction	ΔB for 0.18 T	ΔB for 0.5 T	ΔB for 1 T
X (Y=Z=0)	0.02%	0.02%	0.03%
Y (X=Z=0)	0.02%	0.03%	0.03%
Z (X=Y=0)	0.17%	0.11%	0.09%

During the β-NMR or β-NQR run, the field is remotely set by a Labview application. After each frequency scan (which takes 5 to 10 minutes), a measurement of the magnetic field is performed by a hall probe (HP, Group3-Danfysik model MPT-141-25s communicating with a digital tesla meter DTM141) positioned at about 7 cm behind the crystal. The accuracy of the device is 2×10^{-5} T for $B_0 < 1.2$ T. The measured magnetic field is compared to a reference value and adjusted when necessary using a feedback loop. Since the hall probe is positioned behind the crystal, an online measurement of the magnetic field in the center is not possible. However, the central value can be calculated using the field calibrations which are done before and after each experiment. During the calibration process, a complete and stable hysteresis curve is measured by varying the magnet current in steps of 0.5 A. This procedure is performed in the center as well as at the position where the hall probe is placed during the experiment, firmly establishing the relation between both.

B. The crystal holders

For the β-NMR/β-NQR experiments, two different crystal holders can be used. One operates at room temperature, the other is used to cool or heat the stopper material. On the room temperature crystal holder (Fig. 2), four different crystals can be mounted. The metal rod to which they are attached can be moved in and out the vacuum chamber, allowing another crystal to be placed in the beam path without breaking the vacuum. The holder can also be tilted with respect to the beam axis in order to minimize the path length of the β-particles inside the crystal before they reach the detectors.

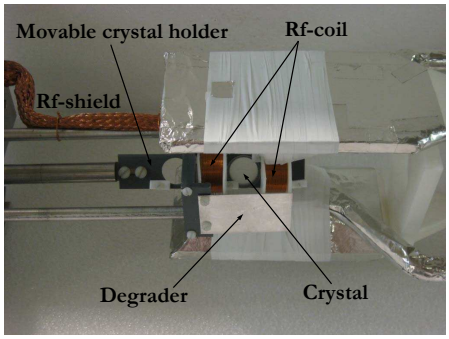

Figure 2: Downstream view of the room temperature crystal holder.

If the half life of the implanted nuclei is longer than the relaxation time, the nuclear polarization is destroyed by random spin-lattice interactions in the crystal before the β-decay takes place [8]. This effect is often caused by fluctuations in the electric field gradient due to lattice vibrations and diffusing defects or by the energy transfer to electrons. As the spin-lattice T_1-relaxation time strongly depends on the temperature [16], the problem can be solved by cooling the implantation crystal (e.g. [17] for NaCl). When cooling is applied, the cold finger crystal holder (Fig. 3) is used.

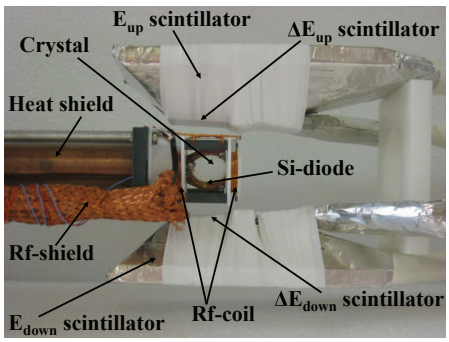

Figure 3: Upstream view of the cold finger crystal holder.

On the cold finger crystal holder, a crystal with a diameter of 2 cm is mounted in a Cu holder, the thermal contact between both is made with thermal grease (Apiezon-N). A Cu holder is used since this material has a very high thermal conductivity: 401 W/mK for 273.2 K [18] and even more for lower temperatures. The crystal holder is then attached to the cold finger, a Cu bar which is directly cooled with liquid He using a continuous flow He-cryostat (Oxford Instruments, project nr 41580). Temperatures as low as 12 K can be obtained at the end of the cold finger which is surrounded by a Cu heat shield.

The temperature on the crystal is much higher since it is placed in an unsheltered room-temperature environment. The lowest temperature obtained for a 2 mm thick NaCl-crystal is 72.4 K. The crystal temperature is measured with a Si diode sensor (LakeShore, DT-670C-SD, 0.1 K precision) which is mounted on the back side of the crystal and which can only be used in the absence of a rf-field.

C. The rf-circuit

The rf-circuit consists of a coil in which the rf-field is applied, one or more function generators, a set of resistors (in the case of β-NQR) and a rf-amplifier. A schematic overview of the rf-circuit with three generators is given in Fig. 4.

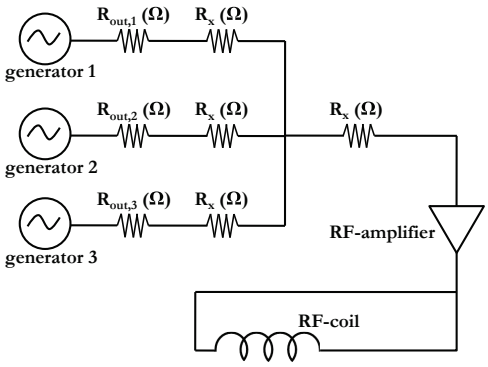

Figure 4: Schematic overview of a β-NQR rf-circuit for three signals. The circuit can be extended for an arbitrary number of frequencies using more generators, expanding the electronics scheme and adjusting the values of R_x. For β-NMR, only one generator is used.

The rf-frequency scan is controlled by the Labview application which is used to set the applied frequencies with their respective amplitude, measuring time and modulation range. An rf-signal corresponding to these specifications is produced by an Agilent arbitrary waveform generator (model 33120A) which has an output impedance (R_{out}) of 50 Ω. This type of generator cannot combine different frequencies and modulations in one signal. Therefore, several generators are used to perform a β-NQR measurement and all signals are combined into one output that is sent to a rf-amplifier with a 50 Ω input impedance. The superposition of the different signals is done according to a simple electronics scheme, illustrated for three frequencies in Fig. 4. The value of the resistors R_x is chosen as such to obtain a total resistance of 50 Ω, matching the input impedance of the rf-amplifier, over the combination of all generator output impedances R_{out} and resistors R_x. Therefore, three signals require R_x to be 25 Ω while R_x is 33.3 Ω for a set of five generators.
The output signal of the function generator(s) is too weak to induce a sufficient rf-field strength in the coil. A first option to realize the necessary amplification

would be the use of a LRC-circuit, tuned at resonance in the proper frequency range by adjusting the variable capacity. However, this implies strong limitations on the accessible g-factor region as the available rf-frequency range only covers the width of the LRC-resonance. Another option to achieve the required rf-strength, is the introduction of an rf-amplifier. As the impedance of the coil (proportional to the rf-frequency) hardly ever matches the 50 Ω output impedance of a standard amplification device, the rf-amplifier 800A3 (800 W CW, 10 kHz - 3 MHz), manufactured by AR, is installed. This amplifier model is especially designed for applications with a variable output impedance, such as an rf-circuit with coil. For a fixed gain and by changing the amplitude of the function generator signal for each individual frequency, the current in the rf-circuit and consequently the rf-field strength inside the coil can be kept constant. This avoids the use of a resonant LRC-circuit and allows very broad rf-frequency scans to be performed. An AC-current of 500 mA peak to peak (pp) in the rf-circuit is sufficient for a β-NMR/β-NQR measurement as it generates a rf-field with an amplitude between 0.1 mTpp and 1 mTpp, depending on the specifications of the coil. During the run, the current in the rf-circuit is continuously monitored by an AC current probe (Tektronix, model P6021).
The output of the amplifier is connected to the rf-coil inside the vacuum chamber via a coaxial vacuum feedthrough. Along the complete trajectory, the coaxial cable is shielded with a 1.5 mm thick Cu-layer. Since the penetration depth of eddy currents caused by rf-fields with a frequency ν is given by $\delta = 1/\sqrt{\pi\sigma\mu\nu}$ [19], Cu is chosen as a shielding material as it has a very high electric conductivity ($\sigma_{\mathrm{Cu}} = 59.77 \times 10^6$ S/m [20]). 99% of electromagnetic waves with a frequency of 100 kHz is stopped by a Cu-layer of 1.03 mm while even less material is required for higher frequencies. Measurements with a pick-up coil show that the Cu-shield around the coaxial cable reduces the rf-background by a factor of 5-8. Note that a leakage of magnetic flux spreading outwards from the coil is still present, as the coil itself cannot be shielded. However, the effect of such a rf-stray field has a negligible impact on the efficiency of the system.
In the β-NMR/β-NQR experiments, coils with a self-inductance of $L = 22.1$ μH (Fig. 2) and $L = 1.6$ μH (Fig. 3) are used. They, respectively, have 2×20 turns of Cu-wire with a diameter of 0.7 mm and 2×4 turns with a diameter of 0.8 mm. Between both halves of the coil, a space of about 2 cm is foreseen for the beam to be implanted in the crystal.

The strong 10 kHz - 3 MHz rf-signal generated in the rf-circuit in combination with the magnetic field up to 1.2 T allows to study a wide range of g-factors ($0.02<g<4.0$) and spectroscopic quadrupole moments. Both, the magnet and the rf-amplifier, make the β-NMR/β-NQR setup accurate and powerful.

D. The scintillation detectors

The β-particles are detected by two pairs of scintillation detectors along the magnetic field direction, one is situated above the crystal, the other below. Each pair consists of a thin ΔE detector, which is a rectangular prism with dimensions $30 \times 30 \times 2$ mm^3 and a 28 mm thick polyhedral E detector with bases of 80×70 mm^2 and 30×55 mm^2. A total geometric efficiency of 19% is obtained for high energetic β-particles emitted

from the center and detected in coincidence between the two upper or the two lower detectors. All detectors are polystyrene scintillators (organic scintillation material PS89) and are covered with white Teflon tape and aluminum foil to optimize internal reflection and to avoid light leakage. The detection setup is included in Fig. 3.
To avoid scattering and losses of the β-particles, the scintillators are placed close to the crystal inside the vacuum chamber. For each E-detector, the scintillation light is transported through a straight plexiglass light guide (44.2 cm long) to a photomultiplier tube (PMT) which is situated outside the vacuum chamber in an atmospheric environment. For the ΔE-detectors, the light guides are bent, allowing a more compact geometry. The curved part of each light guide is constructed with 59 optic fibers (1 mm diameter) and is attached to a straight plexiglass piece of 35.5 cm long which is used to exit from the vacuum and to make the connection with the PMT. Four 20×20 cm^2 PMT's, type R7600U manufactured by Hamamatsu, are used as readouts. The long light guides guarantee that they are placed at a distance of about 50 cm from the center in order to minimize the influence of the magnetic field B_0. At this distance, a magnetic field of less than 0.01 T remains if 1.2 T is applied in the center. Nevertheless, all photomultipliers are surrounded by a μ-metal foil, to protect them from stray fields.
To determine the β-asymmetry in a β-NMR/β-NQR measurement, coincidences between the upper two or the lower two detectors are required. This condition strongly reduces scattering and noise events in the β-spectra.

Outside the vacuum chamber, two germanium detectors are placed to register γ-rays. Each detector is positioned in front of a window where the thickness of the aluminum vacuum chamber is only 3 mm instead of the normal 2 cm. The recorded γ-spectra contain lines following the β-decay of the isotopes implanted in the crystal and are therefore very useful for the beam identification. Also γ-decaying isomeric states present in the isotopes of interest can be observed provided that these levels are populated in the projectile-fragmentation reaction.

IV. GEANT4 APPLICATION

A. Description

For the new β-NMR/β-NQR setup, a GEANT4 Monte Carlo simulation code was developed (using version GEANT4.8.1 [21]). This GEANT4 application allows us to determine the β-detection efficiency of the setup and to describe the sensitivity of the setup for the detection of a resonant change in the β-asymmetry. Simulations in various experimental conditions were made, examining the influence of magnetic fields and different Q_β-values. Also the impact of extra material in the vacuum chamber and the influence of the thickness and the tilting angle of the implantation crystal are determined.
In the GEANT4 application, two full-scale geometric configurations have been instantiated, one for each crystal holder (see section III). Both detection geometries are constructed with predefined GEANT4 building blocks inside a 'world volume' of $220 \times 230 \times 114$ mm^3 (see Fig. 5). The four β-detectors are defined as 'Sensitive Detectors' which keep track of the energies deposited in the scintillation material and

the number of interacting particles during the run. A uniform magnetic field can be applied in the Z-direction. The rf-field inside the coil is small (maximum 1 mTpp) and therefore neglected in the simulation.

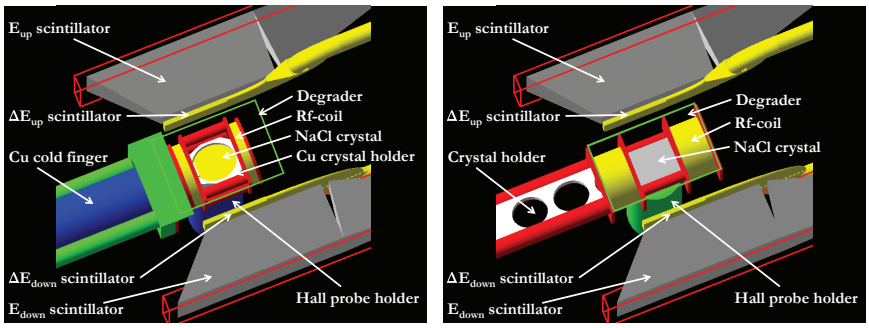

Figure 5: GEANT4 geometries for the cold finger (left) and the room temperature (right) crystal holder.

In the center of the implemented GEANT4 geometries, a point-like source is placed which simulates the β-decay of the implanted nuclei. The probability to have allowed β^--decay at a certain energy and for a particular nucleus, given by its mass A and proton number Z, is described by Wilkinson in Refs. [22–26]. The methodology outlined in that work is used here to define the β-spectrum generated by the source. The simulated β-spectrum has one particular Q_β-value and does not take into account the specific populations of the states in the daughter nucleus. Electrons are emitted under an angle θ with a probability determined by the angular distribution function W(θ) (see Eq. (1)). The implantation of the polarized beam in the crystal is not included in the simulation.

The interactions and trajectories of all primary and secondary particles are simulated using the standard low energy GEANT4 libraries [27] which include ionization, bremsstrahlung, multiple scattering, rayleigh and compton scattering, photo electric effects and γ-conversion for energies between 150 eV and 100 GeV.

In each simulation, two runs are executed, one with an anisotropic β-decay pattern, the other with an isotropic distribution of the β-radiation. In both runs, 100 million events are processed. Each event starts with a primary particle, released by the source with a particular energy and in a certain direction according to the conditions described above. A Monte Carlo simulation is made of the transport and the interactions of this particle and the created secondary particles with the material and the magnetic field in the 'world volume'. When the event interacts with one of the scintillation detectors, the deposited energy is registered. After each run, the detected β-spectra are reconstructed as shown in Fig. 6.

The number of detected particles in the different scintillators and coincidences is used to calculate the detection efficiency, the β-asymmetry, the observed β-NMR/β-NQR effect (i.e. the β-asymmetry change) and the observed fraction of the full β-NMR/β-NQR amplitude. The detection efficiency ϵ_i of a particular detector (combination) i is

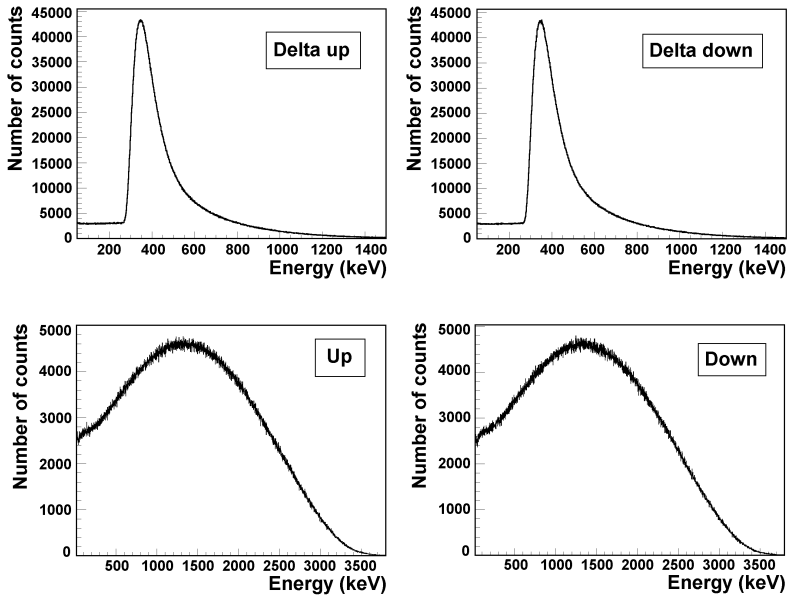

Figure 6: Simulated β-spectra for a GEANT4 geometry including only the detectors and using a ^{41}Cl β^--source ($Q_\beta = 3860$ keV) in the center of the vacuum chamber.

defined as the number of detected events N_i divided by the total number of processed events N (100 million). It is obvious that only data from the run with an isotropic radiation pattern can be used to calculate ϵ_i.

$$\epsilon_i = \frac{N_i}{N} \tag{5}$$

The β-asymmetry (Eq. 2) can be calculated for an anisotropic and an isotropic radiation pattern. According to Eq. 2, $A_{aniso} \simeq |A_\beta P|$ while theoretically, A_{iso} should be zero. To obtain the observed β-asymmetry change Δ (proportional to the observed β-NMR/β-NQR amplitude), the simulated anisotropic and isotropic β-asymmetries are subtracted.

$$\Delta = |A_{aniso} - A_{iso}| \tag{6}$$

A comparison of the simulated β-NMR/β-NQR amplitude Δ with its theoretical value $|A_\beta P|$ gives the sensitivity δ of the setup to observe a resonant change in the β-asymmetry. A perfect setup leads to $\delta = 1$ (=100%).

$$\delta = \frac{\Delta}{|A_\beta P|} \tag{7}$$

The values of ϵ_i, Δ and δ depend on several parameters: how much scattering and absorption are induced by the material present in the vacuum chamber, the density, the tilting and the thickness of the implantation crystal, the Q_β of the decaying

nuclei and the strength of the applied magnetic field B_0. The influence of these parameters on ϵ_i and δ is studied in the following four subsections.

All Geant4 simulations quoted in this work are performed for ^{41}Cl ($Z = 17$). The ground-state spin is assumed to be $I = 1/2$ and Q_β is taken as 3860 keV. The real Q_β of ^{41}Cl is 5728(65) keV but more than 80% of the β-decay proceeds to the 1868 keV level ($I = 1/2^+$) in ^{41}Ar [28], making $Q_\beta = 3860$ keV a more realistic value. The estimated A_β-parameter for a pure Gamow-Teller $1/2^+ \rightarrow 1/2^+$ transition is 2/3 [14]. An arbitrary polarization P of 10% is assumed.

B. Scattering and absorption due to extra elements in the vacuum chamber

When only the four β-detectors are present in the geometry, the detection efficiency of the E-detectors (10.3% per detector) is higher than that of the ΔE-scintillators (9.7% per detector). This is due to the significantly larger detection area of the E-detectors compared to the small ΔE-surface. As indicated in Fig. 1, β-particles emitted from the center of the geometry can reach the E-detector without passing the ΔE-scintillator first. The efficiency to detect a coincident event between the E and ΔE-detectors (7.3% per detector combination) is even more reduced since the lowest-energy β-particles are stopped in the ΔE scintillation material.
Table II shows the simulated values for the detection efficiency of the up and the down coincidence spectra, the β-asymmetry for an isotropic ensemble and the observed fraction of the full β-NMR/β-NQR amplitude for various geometric configurations. All simulations were made with the cold finger GEANT4 application and A_{iso} as well as δ were calculated using only coincident events.

Table II: Simulations performed for various geometric configurations of the cold finger setup, resulting in the efficiency for coincidence detection in the upper ($\epsilon_{coinc-up}$) and lower ($\epsilon_{coinc-down}$) detector pair, the observed asymmetry for an isotropic β-pattern (A_{iso}) and the sensitivity to observe a resonant change in the β-asymmetry (δ).

Elements included in geometry	$\epsilon_{coinc-up}$	$\epsilon_{coinc-do}$	A_{iso} (%)	δ (%)
detectors only	7.32%	7.32%	-0.0074	91.08
detectors + lightguides	7.29%	7.29%	-0.035	90.84
" + degrader + coil + hall probe	7.68%	7.67%	0.055	88.08
" + crystal holder @ 0°	4.68%	4.68%	-0.0079	83.64
" + NaCl, 1mm @ 0°	3.24%	3.24%	0.0059	67.94

As can be seen in Table II, the detection efficiency changes significantly when the crystal holder and the crystal are brought into the geometry. Other parts (e.g. the hall probe, the lightguides, the rf-coil, the degrader, ...) do not seem to have a large influence on the scattering and absorption of the β-particles and therefore on ϵ. When only the scintillators are included in the setup, the total coincidence detection

efficiency (14.6%) is smaller than the full geometric efficiency (19%). This is due to the low Q_β-value used in the calculations.
For the simulations presented in Table II, A_{iso} has values close to zero, as expected for a symmetric setup. As soon as a tilted implantation crystal or another geometric asymmetry (e.g. the β-source not exactly in the center) is brought into the system, A_{iso} starts to deviate. This induces an anisotropic radiation pattern even when no polarization is present. $A_{iso} = 0.30\%$ and $A_{iso} = 0.59\%$ have been obtained for a 1 mm thick NaCl crystal tilted by -15° and -30°, respectively, with respect to the vertical axis.
The extended solid angle of the β-detectors makes that only 91% of the full β-asymmetry change is observed for a geometry which exclusively consists of the four β-scintillators. For the complete β-NMR/β-NQR configuration including a NaCl-crystal of 1 mm, δ is reduced to about 70%. This is mostly due to scattering and absorption of β-particles.
The simulation results obtained with the cold finger and the normal crystal holder geometry are equivalent and do not show any specific differences. Although the cold finger geometry contains more material, the detection efficiency is at most 0.3% lower than the one determined with the room temperature crystal holder. The fraction of the full β-asymmetry change observed with the cold finger setup is at most 1.5% less than δ determined with the room temperature crystal holder geometry in exactly the same conditions.

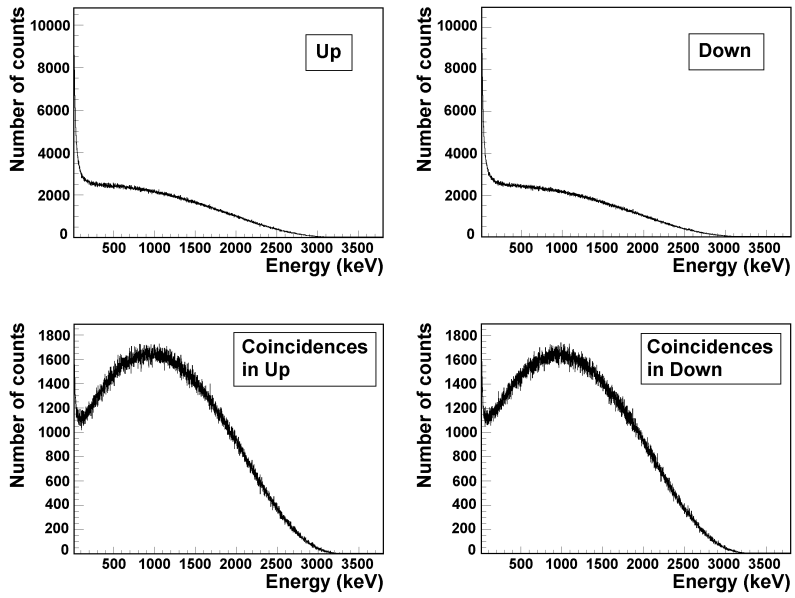

Figure 7: Simulated β-spectra of the E-up/E-down detectors, with and without the coincidence condition. The simulations were performed with the cold finger geometry using a 1 mm thick NaCl crystal (at 0°).

Including all vacuum-chamber elements in the GEANT4 geometry has an effect on the unconditioned β-spectra of both E-scintillators (see Fig. 7). They clearly show a low-energy component (< 150 keV) in the simulated signals of the E-scintillators (to be compared to Fig 6 where no such tail is present). Since the β-particles suffer from scattering and energy absorption in the implantation crystal and crystal holder, a significant fraction reaches the detectors at low energy. Most of them are stopped in the ΔE-material. However, as the ΔE-detector does not fully cover the E-surface, low-energy β-particles are also recorded in the E-detector, inducing a strong low-energy component in the unconditioned β-spectra. By requiring a coincidence with the respective ΔE-detectors, as shown in Fig. 7, the low-energy component is significantly reduced.

C. Properties of the implantation crystal

The impact of the crystal thickness and the tilting angle on ϵ and δ is shown in Fig. 8. Due to the absorption in the crystalline medium, an increase of the crystal thickness from 1 to 2 mm significantly reduces the detection efficiency and the observed asymmetry change. In both cases, tilting the implantation material yields better results since it minimizes the effective path length of the particles towards the β-detectors.

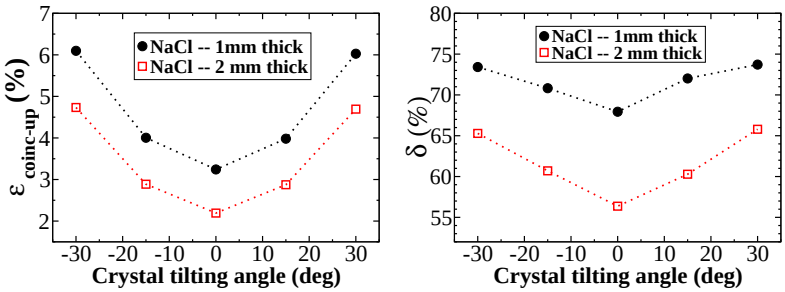

Figure 8: Efficiency of coincident detection in the upper detector pair ($\epsilon_{coinc-up}$) and sensitivity to observe a resonant change in the β-asymmetry (δ) for two different crystal thicknesses (1 and 2 mm). The simulations were made for ^{41}Cl with $Q_\beta = 3860$ keV, $P = 10\%$ and the complete cold finger setup.

All simulations shown so far are made with a NaCl-crystal. Changing the material to e.g. Si can have an influence on the detection efficiency and the observed β-asymmetry change. Table III shows a comparison between a NaCl and a Si crystal of 1 mm and tilted over -30° with respect to the vertical axis. As the density of Si (2.328 g/cm^3 [20]) is slightly higher than the density of NaCl (2.168 g/cm^3 [29]), its increased stopping power results in a reduced ϵ and δ.

Table III: Simulations performed for a NaCl and a Si-crystal in the cold finger geometry, resulting in the efficiency for coincidence detection in the upper ($\epsilon_{coinc-up}$) and lower ($\epsilon_{coinc-down}$) detector pair, the observed asymmetry for an isotropic β-pattern (A_{iso}) and the sensitivity to observe a resonant change in the β-asymmetry (δ). The simulations were made for ^{41}Cl using Q_β=3860 keV and $P = 10\%$.

Configuration	$\epsilon_{coinc-up}$	$\epsilon_{coinc-do}$	A_{iso} (%)	δ (%)
NaCl, 1mm @ $-30°$	6.10%	6.03%	0.59	73.42
Si, 1mm @ $-30°$	5.16%	5.11%	0.44	67.25

D. The effect of the Q_β-value

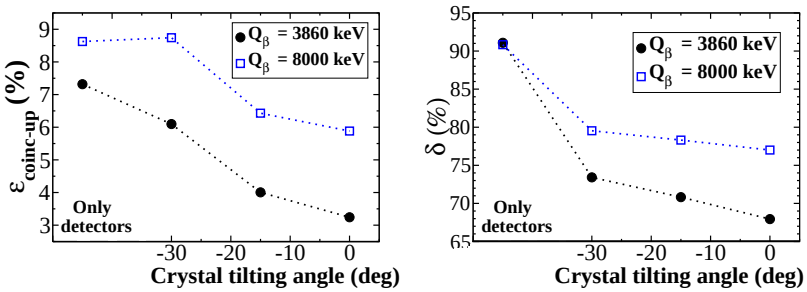

Figure 9: Efficiency of coincident detection in the upper detector pair ($\epsilon_{coinc-up}$) and sensitivity to observe a resonant change in the β-asymmetry (δ) for two different Q_β-values (3860 keV and 8000 keV). The simulations were made for ^{41}Cl, $P = 10\%$ and the complete cold finger setup, including a 1 mm thick NaCl-crystal.

Fig. 9 shows a comparison between simulations performed for ϵ and δ applying two values of the β-endpoint energy, Q_β=3860 keV and Q_β=8000 keV. The cold finger geometry was used with a NaCl-crystal of 1 mm. A higher endpoint energy results in an increased amount of β-particles passing through the ΔE-detectors. Therefore, it leads to a more efficient β-detection in the E-scintillators and a higher coincidence rate.
When only the detectors are included in the GEANT4 geometry, the efficiency δ to observe the β-asymmetry change is similar for both Q_β-values (Fig. 9). As soon as the complete setup is taken into account, δ increases with increasing endpoint energy. High-energy β-particles do not easily loose their polarization in scattering processes. For all experimental conditions, one can conclude that the detection efficiency and the observed asymmetry change improve when the β-decay has a higher Q_β-value.
High Q_β-energies also drastically change the unconditioned and the coincident β-spectra as illustrated in Fig. 10. Simulations performed for Q_β=12 MeV show a clear ΔE peak around 5.5 MeV. This peak contains the signals of high energetic electrons which pass through both detectors.

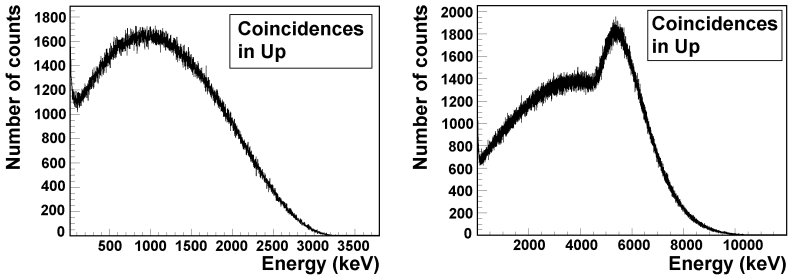

Figure 10: Coincident β-spectra of the E-up detector conditioned with ΔE-up for $Q_\beta = 3860$ keV (left) and $Q_\beta = 12$ MeV (right). The simulations were performed for the full cold finger setup with a 1 mm thick NaCl crystal.

E. The impact of magnetic fields

When a high static magnetic field is applied in the Z-direction, charged particles start spiraling around the magnetic field lines in the direction of the β-detectors. This process results in a significantly higher detection efficiency but a much lower sensitivity to the β-asymmetry change. Simulations with B_0=1 T and without magnetic field have been performed for ^{41}Cl (Q_β=3860 keV, P=10%) and the results are given in Fig. 11. Coincidence detection efficiencies as high as 14% in one detector set have been observed in a magnetic field of 1 T (NaCl-crystal of 1 mm and tilted over -30°) but they can only barely compensate for the 50% loss in the sensitivity to observe the total β-NMR/β-NQR amplitude.

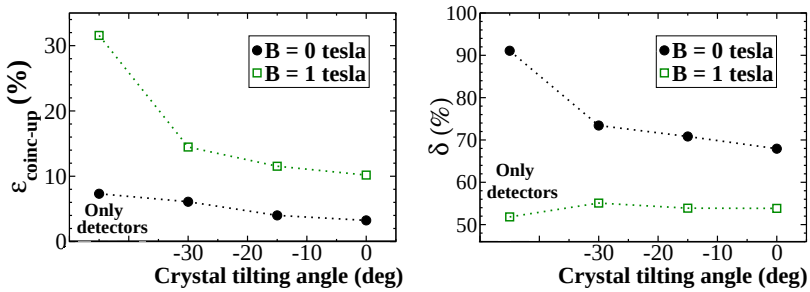

Figure 11: Efficiency of coincident detection in the upper detector pair ($\epsilon_{coinc-up}$) and sensitivity to observe a resonant change in the β-asymmetry (δ) without magnetic field and for B_0=1 T. The simulations were made for ^{41}Cl (Q_β=3860 keV, P=10%) in a NaCl-crystal of 1 mm.

V. CONCLUSIONS

The detailed description of a new β-NMR/β-NQR setup developed to be installed at the final focal point of the LISE fragment separator at GANIL demonstrates that it is now possible to measure a broad range of g-factors ($0.02<g<4.0$) and spectroscopic quadrupole moments. Two main components are responsible for this: the strong and homogeneous magnet and the rf-amplifier especially designed for variable output impedance circuits.

A theoretical description of the setup has been made using the GEANT4 toolkit. Monte Carlo simulations have been carried out, probing the influence of various elements on the detection efficiency and on the fraction of the total β-NMR/β-NQR amplitude, expected to be observed. The effects of the crystal thickness and tilting angle, the material in the vacuum chamber, the magnetic fields and the high Q_β-values have been extensively studied and a much better understanding of the experimental conditions has been obtained.

From the GEANT4 simulations, the ideal conditions to perform a β-NMR/β-NQR experiment can be deduced. Mother nuclei with a high Q_β-value induce a large detection efficiency and a good sensitivity to the β-asymmetry change. The implantation crystal must be thin and tilted as much as possible with respect to the vertical axis. Applying a magnetic field B_0 induces a high detection efficiency but it reduces the sensitivity to observe the full β-NMR/β-NQR amplitude. As both effects cancel each other, no strong influence of B_0 on the β-NMR/β-NQR measurement is observed.

So far, three experiments have been performed with the new β-NMR/β-NQR setup. The first experiment, in which the g-factors of ^{17}N and ^{18}N were remeasured, was a test run to evaluate the performance of the setup. Afterwards, several improvements were made which are included in the simulations made in this work. In the second and the third experiment, the g-factor of ^{44}Cl and the quadrupole moment of ^{31}Al were determined. The outcome of all experiments will be published elsewhere [30, 31].

Acknowledgments

We are grateful to the GANIL staff for their technical support. This work has been financed by the European Community FP6-Structuring the ERA-Integrated Infrastructure Initiative contract EURONS no. RII3-CT-2004-506065, by the FWO-Vlaanderen and by the IAP-programme of the Belgium Science Policy under Grand number P6/23.

[1] O. Sorlin and M.-G. Porquet, Prog. Part. Nucl. Phys. **61**, 602 (2008)
[2] A. Kastler, J. Phys. Radium **11**, 255 (1950)
[3] K. Asahi *et. al.*, Phys. Lett. B **251**, 488 (1990)
[4] H. Okuno *et. al.*, Phys. Lett. B **335**, 29 (1994)
[5] D. Borremans *et. al.*, Phys. Rev. C **66**, 054601 (2002)
[6] D.E. Groh *et. al.*, Phys. Rev. Lett. **90**, 202502 (2003)

[7] K. Turzo *et. al.*, Phys. Rev. C **73**, 044313 (2006)
[8] A. Abragam, The Principles of Nuclear Magnetism, Clarendon, Oxford, 1961
[9] E. Matthias *et. al.* Phys. Rev. A **4**, 1626 (1971)
[10] R. Anne *et. al.*, Nucl. Instr. and Meth. A **257**, 215 (1987)
[11] R. Anne *et. al.*, Nucl. Instr. and Meth. B **70**, 276 (1992)
[12] `http://groups.nscl.msu.edu/lise/lise.html`
[13] O.B. Tarasov and D. Bazin, Nucl. Instr. and Meth. B **266**, 4657 (2008)
[14] N.J. Stone and H. Postma (Eds.), Low-Temperature Nuclear Orientation (chapter 3), Elsevier, Amsterdam (1986)
[15] D. Borremans *et. al.*, Phys. Rev. C **72**, 044309 (2005)
[16] C.P. Slichter, Principles of Magnetic Resonance, Springer-Verlag, Berlin-Heidelberg-New York (1978)
[17] T. Yamanishi *et. al.*, J. Phys. Soc. Japan **64**, 643 (1995)
[18] Y.S. Touloukian, R.W. Pavell, C.Y. Ho and P.G. Klemens, Thermophysical properties of matter, The TPRC Data Series vol I, Thermal Conductivity Metallic Elements & Alloys, IFI/PLENUM, New York, Washington, 1970
[19] C.G. Someda, Electromagnetic Waves, Chapman & Hall, London-Weinheim-New York-Tokyo-Melbourne-Madras, 1998
[20] R.E. Bolz, G.L. Tuve (Eds.), Handbook of Tables for Applied Engineering Science, the Chemical Rubber Co., 18901 Cranwood Parkway, Cleveland, Ohio 44128, USA, 1970
[21] GEANT collaboration, Nucl. Instr. and Meth. A **506** (2003) 250
[22] D.H. Wilkinson, Nucl. Instr. and Meth. A **275** (1989) 378
[23] D.H. Wilkinson, Nucl. Instr. and Meth. A **290** (1990) 509
[24] D.H. Wilkinson, Nucl. Instr. and Meth. A **335** (1993) 305
[25] D.H. Wilkinson, Nucl. Instr. and Meth. A **365** (1995) 203
[26] D.H. Wilkinson, Nucl. Instr. and Meth. A **365** (1995) 497
[27] http://www.ge.infn.it/geant4/lowE/index.html
[28] J.A. Cameron and B. Singh, Nucl. Data Sheets **94**, 429 (2001)
[29] http://www.mateck.de/HiPuMa/e66e.asp.id.Sodium.html
[30] M. De Rydt *et. al.*, Phys. Rev. C 80 (2009) 037306
[31] M. De Rydt *et. al.*, Phys. Lett. **B 678** (2009) 344

Chapter 4

g-factors of ^{17}N and ^{18}N

In order to test the newly designed β-NMR/β-NQR setup, the g-factors of ^{17}N and ^{18}N were remeasured. ^{17}N was selected to be the first test-case because of its large production yield and the accurately known value of its magnetic moment [42]. The choice of ^{18}N as the second test case arises from a more fundamental physics argument. Two inconsistent values were published for $\mu(^{18}N)$ [1, 2], strongly encouraging a new β-NMR experiment to clarify the discrepancy between both results.

Decisive information on the g-factors of ^{17}N and ^{18}N can be found in the paper enclosed at the end of the chapter which was published as a Brief Report in Physical Review C [43]. The four sections of this chapter, preceding the paper, take a closer look at topics which are not or only briefly discussed in the article. The first section gives a short introduction to the literature study of the light neutron-rich isotopes. The second section highlights a few aspects of isomeric states and how their magnetic moments can be measured using β-NMR. The third part zooms in on the polarization curve obtained for ^{18}N, relying on the participant spectator model for projectile-fragmentation reactions. To conclude, the last section presents the unpublished ^{18}N results.

4.1 ^{17}N and ^{18}N: the physics case

Although it is not the first priority of this work, a limited literature study is performed, highlighting the structural changes happening in the light neutron-rich isotopes. The relevant region of the nuclear chart and a schematic view of the effective single particle levels, for $^{14}_{6}$C in particular, are shown in Fig. 4.1. When protons are added to the $\pi(1p_{1/2})$-orbital in the $N = 8$ isotones, a crossing between the $5/2^+$ and $1/2^+$ excited states occurs. The $5/2^+$-state

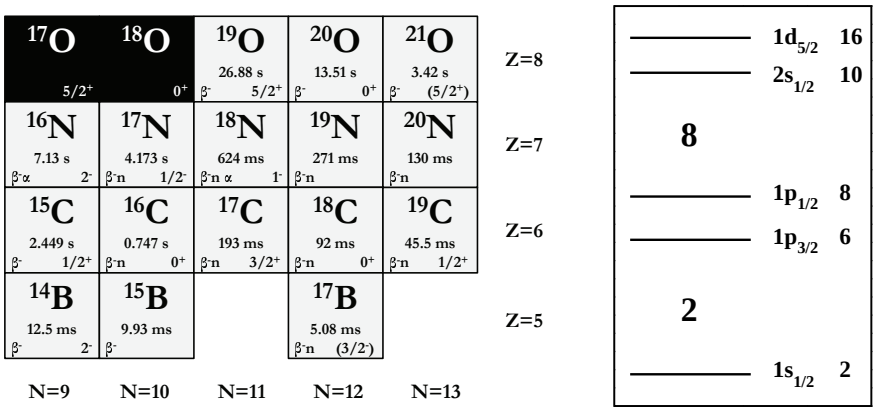

Figure 4.1: Part of the nuclear chart, depicting a selection of the light neutron-rich $_8$O, $_7$N, $_6$C and $_5$B isotopes (left). Effective single particle levels of $^{14}_6$C (right).

originates from an odd neutron in the $\nu(1d_{5/2})$ orbital while the $1/2^+$ level is dominated by $\nu(2s_{1/2})$ configurations. The transition from $^{14}_6$C, with protons occupying the $\pi(1p_{3/2})$ level, to $^{16}_8$O, characterized by a full $\pi(1p_{1/2})$ shell, activates the attractive tensor term between the $\pi(1p_{1/2})$ state and the $\nu(1d_{5/2})$ level, strongly lowering the binding energy of the $5/2^+$ state [44] as shown in Fig. 4.2. A good illustration of this effect is found in the $N = 9$ isotones. These nuclei are excellent probes to study the behavior of the $5/2^+$ and $1/2^+$ states since their ground-state spin and structure are dominated by the single valence neutron in the $\nu(sd)$-shell. $^{15}_6$C$_9$ has a $1/2^+$ ground-state spin while the spin of $^{17}_8$O$_9$ is $5/2^+$. This confirms the increasing admixture of $\nu(1d_{5/2})$ configurations in the ground state of the $N = 9$ isotones when adding protons to the $\pi(1p_{1/2})$-orbital [45, 46].

Another structural change is observed for the $N = 11$ isotones, where the transition from a paired to an unpaired neutron coupling scheme occurs [47]. In $^{19}_8$O, the paired neutron $\nu(1d_{5/2})$ configuration is favored by the $5/2^+$ ground-state while in $^{17}_6$C the $3/2^+$ ground state is dominated by unpaired seniority-3 $\nu(1d_{5/2})$ components. Wiedeking *et al.* interpreted the change in ground-state spin between $^{19}_8$O and $^{17}_6$C as a consequence of the increasing quadrupole strength relative to the pairing interaction. Unpaired $\nu(1d_{5/2})$ configurations are also needed to explain the 1^- ground state of $^{18}_7$N [1, 2], marking it as a transition nucleus. The suggestion of a pure $\nu(2s_{1/2})$ ground state for this isotope, as an alternative for the seniority-3 $\nu(1d_{5/2})$ configuration, is not supported by experiment since it would lead to a $l = 2$ forbidden transition between the 2^- and 1^- states in ^{18}N.

A third structural effect occurs for the light neutron-rich nuclei, such as ^{15}B, ^{17}B, ^{16}C and ^{16}N, where quenched effective neutron charges ($e_n \simeq 0.1$ instead of the usual $e_n = 0.5$) are required to correctly reproduce the experimental deformation parameters and the measured spectroscopic quadrupole moments [48–50]. According to Dombrádi *et al.* the small effective charges are a consequence of the decoupling of the valence neutrons from the core. As the neutrons are only loosely bound, they cannot strongly polarize the core which results in a reduction of the effective charges and the development of a neutron skin. A similar but more extreme effect was found in ^{19}C. The ground state of this isotope has a dominant $\nu(2s_{1/2})$ character and appears as a well-developed one-neutron halo [46].

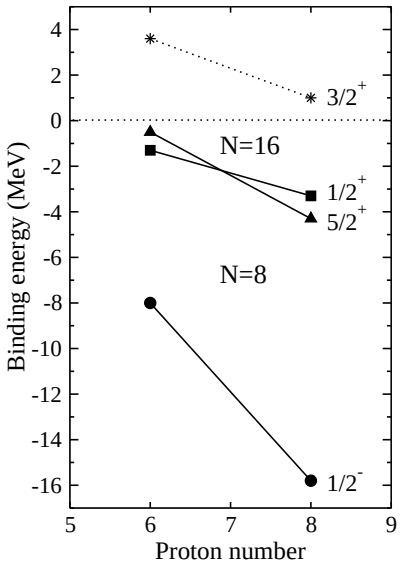

Figure 4.2: Binding energies of the $1/2^-$, $5/2^+$, $1/2^+$ and $3/2^+$ states in the $N = 8$ isotones. (Figure taken from [44])

A last structural change mentioned here is the suggested reduction of the $p-sd$ shell gap for the neutron-rich O-isotopes [51]. In $^{20}_{8}O_{12}$, five new excited states below 6 MeV are found and identified as 'intruder states'. They appear as negative-parity states which provides a strong evidence for one particle - one hole ($1p-1h$) cross-shell excitations. A good overall agreement with theory demands a weakening of the $p-sd$ shell gap when neutrons are added.

4.2 Measuring the g-factor of an isomeric state using β-NMR

In literature, two conflicting sets of nuclear moments were published for ^{18}N: $|\mu|_1 = 0.3279(13)\mu_N$, $|Q|_1 = 12.3(12)$ mb in Ref. [1] and $|\mu|_2 = 0.135(15)\mu_N$, $|Q|_2 = 27(4)$ mb in Ref. [2]. This often suggests the presence of an isomeric state in the nucleus of interest. Although the ^{18}N level scheme has been studied in three different experiments [47, 52, 53] (see article for a review) no long-lived excited state was found so far. Nevertheless, it is interesting to illustrate a few aspects of measuring isomeric g-factors using the β-NMR technique.

To induce a 'visible' β-NMR effect, the investigated (isomeric) state must have a minimum lifetime which is determined by the rf-field strength B_1. To understand this, assume a resonant rf-field $\mathbf{B}_1$ which is applied in the horizontal xy plane, perpendicular to the static field $\mathbf{B}_0$ along the vertical z direction. In such a resonant system, the magnetic moment which is initially oriented along z, will rotate about the rf-field with a frequency $\omega_1 = \frac{g\mu_N B_1}{\hbar}$, as proven in chapter 5. In order to destroy the polarization, the initial direction of the magnetic moment has to be inverted at least once before the nucleus decays. Therefore, the minimum lifetime corresponds to the time needed for the magnetic moment to rotate over 180°.

$$t_\pi = \frac{\pi}{\omega_1} = \frac{h}{2g\mu_N B_1} \tag{4.1}$$

The minimum lifetime of 50 μs, quoted in the article, is calculated with a rather high g-factor and rf-field strength. Therefore, it provides a strong lower limit for the lifetime of the states that can be studied with β-NMR.

Although not always appropriate, g-factors of β- and γ-decaying isomers can be studied with the β-NMR technique. Two conditions must be fulfilled: the isomer should be populated and polarized in the projectile-fragmentation reaction and its lifetime must respect the limit given by Eq. 4.1.

Measuring the g-factor of a purely β-decaying isomer is in all respect similar to the procedure followed when determining the g-factor of a ground state. When a composite secondary beam, consisting of an isomeric and a ground-state fraction is studied, two resonances will be observed.

The case of a γ-decaying isomer is somewhat more challenging. The β-particles, detected in a β-NMR experiment, originate from the decay of the ground state which is only linked to the isomeric state via an unobserved γ-transition. This γ-branch tends to (partly) destroy the polarization, an effect which is accounted for by inserting a de-orientation coefficient U_λ in the angular distribution of the

β-radiation. The general expression, given in Eq. 2.19, transforms into [27]:

$$W(\theta,\phi) = \sqrt{4\pi} \sum_{\lambda} \sqrt{\frac{1}{2\lambda+1}}\, U_\lambda\, \mathbf{B}^{(\lambda)}\, \mathbf{A}^{(\lambda)}\, \mathbf{Y}^{(\lambda)}(\theta,\phi) \tag{4.2}$$

The de-orientation coefficients depend on all spins and multipolarities involved in the γ-transition. In the most simple case, when a γ-ray of multipolarity L is emitted between the isomeric state with spin I_i and the ground state with spin I_f, the U_λ factors take the following values:

$$U_\lambda = (-1)^{I_i+I_f+L+\lambda}\sqrt{2I_i+1}\sqrt{2I_f+1}\begin{pmatrix} I_i & I_i & \lambda \\ I_f & I_f & L \end{pmatrix} \tag{4.3}$$

De-orientation coefficients for mixed transitions and complex γ cascades can be found in [27]. Tables displaying the calculated values of the U_1 factors (important for allowed β-transitions) and the other low-λ de-orientation coefficients are given in textbooks such as [28].
Provided that a sufficient amount of polarization remains after the γ-transition, two β-NMR resonances are observed, even for a 100% isomeric beam. Applying the Larmor frequency $\nu_{L,1}$ corresponding to the g-factor g_1 of the isomer equalizes the populations of the isomeric m-states. After the γ-transition, also the m-states of the ground-state will be equally populated, resulting in a (usually) weak β-NMR resonance. When the Larmor frequency $\nu_{L,2}$ of the ground state is encountered, the polarization of all ground-state isotopes is destroyed, no matter whether they were produced in the projectile-fragmentation reaction or fed by the γ-decay of the isomer. From the induced β-NMR resonance, the ground-state g-factor g_2 can be deduced.

4.3 Production of spin-polarized nuclei

In the Physical Review C article, the polarization of the ^{18}N fragments, produced in a one-neutron pick-up reaction, is given as a function of the selected longitudinal momentum. The observed trend can be understood in the framework of the 'participant-spectator' model, developed by Asahi *et al.* [54], Okuno *et al.* [55] and Groh *et al.* [56] for projectile-fragmentation reactions. Later, Turzó *et al.* [57] extended the concept for one-nucleon pick-up processes. In order to give a plausible explanation for the observed ^{18}N polarization versus momentum curve, the basic principles of both models are introduced.

The underlying mechanism of the participant-spectator model is based on the simple kinematics of an incoming projectile ('the participant') inducing a peripheral collision with a target nucleus, leaving a pre-fragment ('the spectator') to proceed. For projectile fragmentation reactions, the model assumes that the

nucleons of the projectile, belonging to the geometrical overlapping volume with the target nucleus are abraded without changing the motion of the remaining projectile-nucleons. In the case of pick-up, the projectile 'absorbs' one target nucleon, leaving all other nucleons undisturbed. In both cases, the spectator-part afterwards de-excites to the final fragment through random particle emission which is assumed not to change the created spin-orientation.

- **The projectile-fragmentation reaction**
  The formalism is taken from [54]. The collision of the projectile with the target results in the removal of a cluster of projectile nucleons at position $\mathbf{R}$ with momentum $\mathbf{k}$. This removal can happen at the left or at the right side of the target nucleus (illustrated in Fig. 4.3a). As $\mathbf{k}$ is very small, the reaction produces a fragment beam, focussed in the forward direction with a gaussian longitudinal momentum distribution around the projectile momentum $\mathbf{p}_p$. Applying the conservation laws of linear and angular momentum implies that:

$$\mathbf{p}_f = \mathbf{p}_p - \mathbf{k} \quad (4.4)$$
$$\mathbf{J}_f = -\mathbf{R} \times \mathbf{k} \quad (4.5)$$

  In order to obtain Eq. 4.5, the intrinsic spins of the abraded nucleons are neglected and a zero total angular momentum of the projectile is assumed. Inserting Eq. 4.4 in Eq. 4.5 shows that the polarization $P = \frac{<\mathbf{J}_{f,z}>}{\mathbf{J}_F}$ depends on the fragment momentum $\mathbf{p}_f$.
  The trajectory followed by the fragment after the reaction depends on the interplay between the attractive nucleon-nucleon interaction, trying to bend the fragment path towards the target, and the repulsive Coulomb interaction, tending to 'push' the fragment away from the target. When the nuclear attraction dominates, as for low-Z targets such as ^{9}Be, mainly 'far-side' collisions occur (as shown in Fig. 4.3a). High-Z targets give rise to 'near-side' trajectories, dominated by the Coulomb repulsion.
  The z-component of the fragment angular momentum equals $J_{f,z} = |R_y|k_x$ for pure near/far-side collisions ($R_x = 0$) taking place at the right side of the target ($\theta_R = 0°$). Similar but for the left side of the target ($\theta_R = 180°$): $J_{f,z} = -|R_y|k_x$.
  When fragments are selected under a positive angle θ_L with respect to the forward direction and when only far-side collisions are taken into account, most selected fragments are formed at the right side of the target. In that case, the polarization, proportional to $J_{f,z}$, is positive for $k_x >> 0$ and thus for the left wing of the longitudinal momentum distribution where $p_{f,x} << p_p$. Vice versa, a negative polarization is obtained for fragments with $p_{f,x} >> p_p$. If $k_x \simeq 0$, in the center of the momentum distribution,

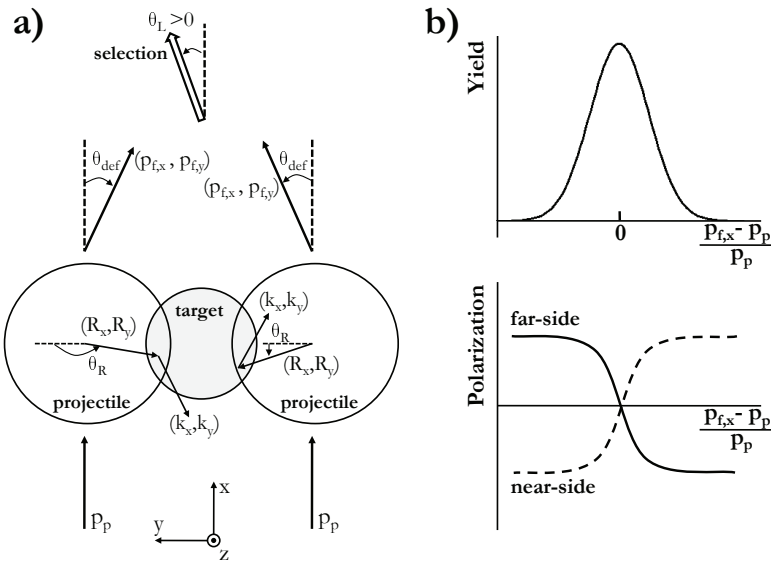

Figure 4.3: Projectile fragmentation: a) Kinematics of a projectile colliding with a target nucleus, favoring far-side trajectories. b) Yield and polarization curves as a function of the longitudinal fragment momentum, relative to p_p.

the polarization is zero. The behavior of the polarization as a function of the longitudinal fragment momentum is illustrated in Fig. 4.3b.

- **The one-nucleon pick-up reaction**
  The pick-up formalism is published in [57]. During a peripheral collision, one target nucleon is transferred to the incident projectile. The position and momentum of the added nucleon are given by **R** and **k** respectively (illustrated in Fig. 4.4a). According to Souliotis *et al.* [58] and Pfaff *et al.* [59] mainly nucleons with $\mathbf{k} = (-p_{fermi}, 0, 0)$ are picked up, giving rise to a fragment yield distribution which peaks at a lower momentum than that of the projectile.
  Applying the conservation laws of linear and angular momentum leads to similar expressions as for the projectile-fragmentation reaction, again neglecting the intrinsic spin of the absorbed nucleon and the angular momentum of the projectile.

$$\mathbf{p}_f = \mathbf{p}_p + \mathbf{k} \tag{4.6}$$
$$\mathbf{J}_f = \mathbf{R} \times \mathbf{k} \tag{4.7}$$

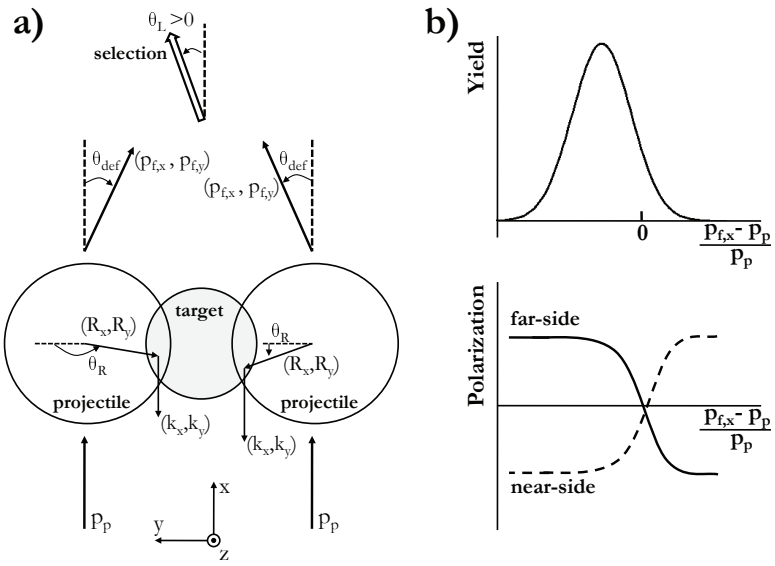

Figure 4.4: One-nucleon pick-up: a) Kinematics of a projectile colliding with a target nucleus, favoring far-side trajectories. b) Yield and polarization curves as a function of the longitudinal fragment momentum, relative to p_p.

The projectile can hit the target at the left side or at the right side. When the nuclear attraction (Coulomb repulsion) is dominant, far-side (near-side) trajectories are favored. Assume the same experimental conditions (low-Z target and selection at $\theta_L > 0$) as before. Again, mainly fragments produced at the right side of the target ($R_y > 0$) are selected.
In the center of the momentum distribution, k_x takes the value of the negative fermi momentum of the target nucleus. In this case, the obtained spin-polarization, proportional to $< J_f, z >= -k_x R_y$, is positive and different from zero. This yields a large advantage compared to projectile-fragmentation reactions which require a selection in the wing of the momentum distribution to obtain spin-polarized fragments. An overview of the yield and the polarization as a function of the longitudinal fragment momentum, relative to p_p, is given in Fig. 4.4b.

So far, a good qualitative description of the created spin-polarization as a function of the longitudinal fragment momentum is obtained for both, projectile-fragmentation and pick-up reactions. A quantitative agreement with experiment however requires a more detailed and sophisticated model to be developed.

Experimental data on ^{18}N, collected during the test-experiment, allow a qualitative comparison with the theoretical predictions based on the participant-spectator model. The ^{18}N isotopes were produced in a one-neutron pick-up reaction of a $^{18}O^{8+}$ primary beam on a rotating ^{9}Be target. The fragments were selected at $\theta_L > 0$, favoring far-side trajectories because of the low target Z value. The pick-up production yield of ^{18}N was scanned as a function of the longitudinal momentum by changing the opening of the FH31 slits. In order to probe the polarization as a function of the longitudinal momentum, the ^{18}N β-NMR was performed for three different FH31 slit openings. Each slit opening corresponds to a particular selection in longitudinal momentum and therefore to a certain secondary-beam polarization. As the β-NMR measurements were performed with similar rf-conditions, the amplitude of the resonance provides a direct measure for the amount of polarization present in the beam. The experimental yield distribution and the polarization curve are shown in Fig. 4.5. In both figures, the position and the opening of the FH31 slits is indicated with horizontal error bars.
The obtained experimental curves have to be compared to Fig. 4.4b. The experimental polarization seems to follow the theoretical trend-line which is characterized by high polarization in the left wing and a gradual decrease when going from the center to the right wing. The large error bars and broad slit openings however hinder an accurate evaluation of the data.

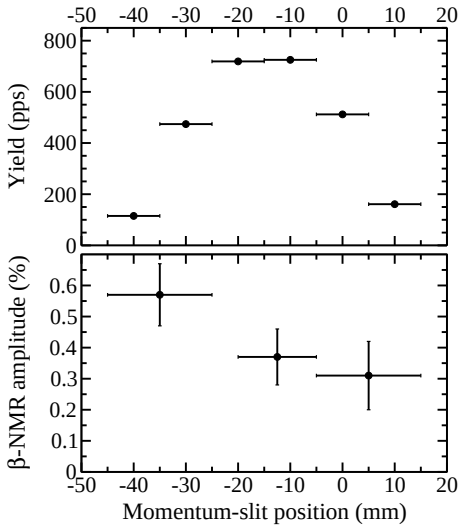

Figure 4.5: Experimental yield distribution and polarization curve for ^{18}N.

4.4 Unpublished results

As a test-experiment, the g-factors of ^{17}N ($I^\pi = 1/2^-$) and ^{18}N ($I^\pi = 1^-$) were remeasured. For ^{17}N, the obtained magnetic moment $|\mu(^{17}\mathrm{N})| = 0.3551(4)\mu_N$ is in good agreement with the published value $|\mu(^{17}\mathrm{N})|_{publ.} = 0.352(2)\mu_N$ [42]. A detailed report can be found in the Physical Review C article enclosed.
For ^{18}N, two contradictory magnetic moments exist in literature. Therefore, new β-NMR measurements were performed in both g-factor regions. Three β-NMR resonances, resulting in $|g(^{18}\mathrm{N})| = 0.3273(4)$, confirmed the literature value $|g(^{18}\mathrm{N})|_1 = 0.3279(13)$ published by Ogawa et al. [1]. An extended discussion of the results can also be found in the article.
In the g-factor range around the value $|g(^{18}\mathrm{N})|_2 = 0.135(15)$, published by Neyens et al. [2], five β-NMR scans were performed. The results of these measurements, not included in the paper, are presented here. The corresponding experimental parameters are given in Table 4.1 while the outcome of the measurements is shown in Fig. 4.6. The data sets have been analyzed with the same conditions as the measurements presented in the paper. The X-errors denote the applied rf-frequency modulation while the point on the outer right contains all data taken without rf-field. In each figure, the dotted lines represent the limits of the g-factor range, determined by the published value $|g(^{18}\mathrm{N})|_2 = 0.135(15)$. No β-NMR effect larger than one σ has been observed.
Although different experimental parameters lead to various offsets on the asymmetry axis, it is possible to put all data on the same figure. To achieve this, each data set is rescaled with respect to its own baseline, calculated as the weighted mean of all β-asymmetries in that scan. In addition, the forth and fifth data set, collected at a magnetic field of 0.5496(4) T, have a rescaled X-axis to match the frequency range of the first three measurements. When different points appear at the same frequency, they are replaced by their weighted mean. The result is shown in Fig. 4.7, again no effect larger than one σ is visible.

Table 4.1: The opening of the horizontal polarization slits FH31, the applied magnetic field B_0 (T), the scanned frequency range (kHz), the step between two central frequencies (kHz), the frequency modulation (kHz) and the obtained 1σ error for the ^{18}N β-NMR measurements around $|g| = 0.135(15)$.

Nr	FH31 (mm)	B_0 (T)	Freq.	Step	Mod.	1σ (%)
1	[-45,-25]	0.3997(3)	350-470	20	11	0.14
2	[-20,-5]	0.3996(3)	350-470	20	11	0.06
3	[-45,-20]	0.3997(3)	340-470	10	7	0.17
4	[-45,-20]	0.5496(4)	390-520	10	7	0.2
5	[-45,-20]	0.5496(4)	390-550	10	7	0.13

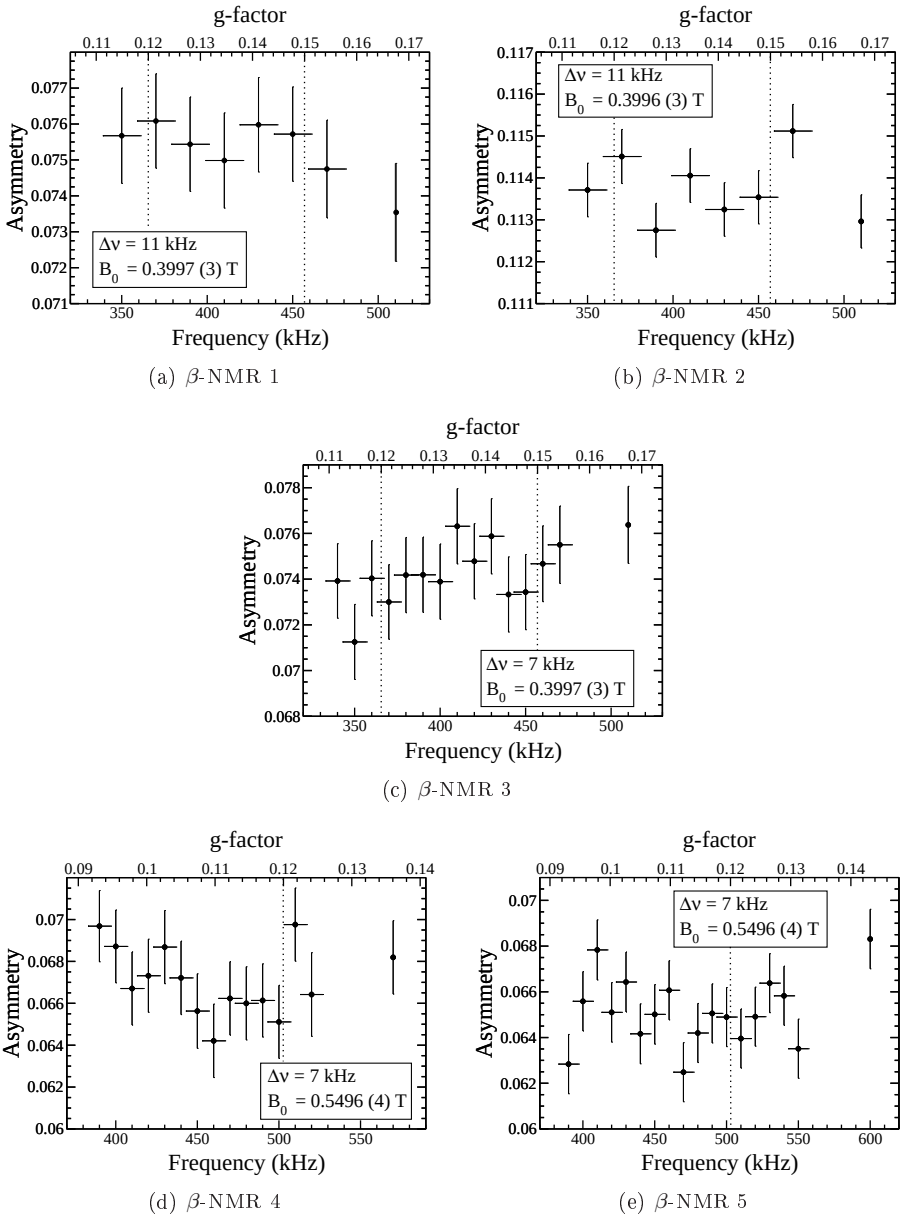

(a) β-NMR 1

(b) β-NMR 2

(c) β-NMR 3

(d) β-NMR 4

(e) β-NMR 5

Figure 4.6: Five β-NMR measurements in the $|g(^{18}\mathrm{N})|_2 = 0.135(15)$ g-factor range. The corresponding experimental parameters can be found in Table 4.1.

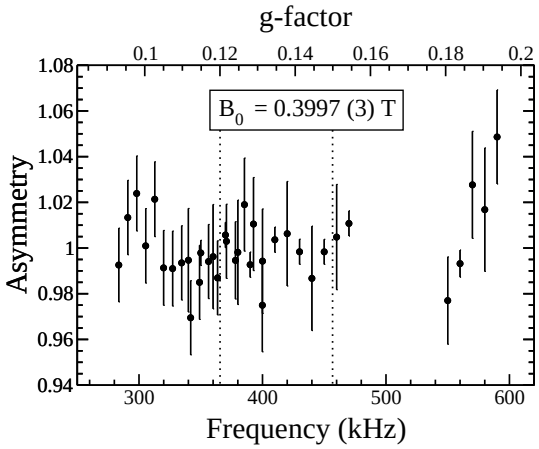

Figure 4.7: Compilation of all data taken in the $|g(^{18}\mathrm{N})| = 0.135(15)$ region. For details see text. (Indications of the applied frequency modulations are not shown.)

In conclusion, the resonance previously observed by Neyens *et al.* [2], giving rise to the g-factor $|g(^{18}\mathrm{N})| = 0.135(15)$, could not be reproduced by the present data set. The five individual β-NMR measurements did not reveal any resonance and also the compilation of the data on the same plot did not provide any g-factor indication. On the other hand, three β-NMR measurements confirmed the value $|g(^{18}\mathrm{N})| = 0.3279(13)$, published by Ogawa et al. in [1]. In order to determine the nature of the resonance observed by Neyens *et al.* [2], additional research is required taking into account the option of a (not yet observed) long-lived isomeric state[A].

[A] It is possible that an isomeric state was produced and polarized in the projectile-fragmentation reaction of a ^{22}Ne beam as described in [2] and not in the pick-up reaction with a ^{18}O beam as discussed here. This can be an explanation why the resonance observed in [2] could not be reproduced in this work. However, such an argument is very speculative and needs at least a new β-NMR measurement, using preferably a ^{22}Ne primary beam, to be verified.

g factors of ^{17}N and ^{18}N remeasured

M. De Rydt,[1] D.L. Balabanski,[2] J.M. Daugas,[3] P. Himpe,[1] D. Kameda,[4] R. Lozeva*,[1] P. Morel,[3] L. Perrot,[5] K. Shimada,[6] C. Stödel,[7] T. Sugimoto,[4] J.C. Thomas,[7] H. Ueno,[4] N. Vermeulen,[1] P. Vingerhoets,[1] A. Yoshimi,[4] and G. Neyens[1]

[1] *Instituut voor Kern- en Stralingsfysica, K.U.Leuven, Celestijnenlaan 200D B-3001 Leuven, Belgium*
[2] *Institute for Nuclear Research and Nuclear Energy, Bulgarian Academy of Sciences, BG-1784 Sofia, Bulgaria*
[3] *CEA, DAM, DIF, F-91297 Arpajon Cedex, France*
[4] *RIKEN Nishina Center, 2-1 Hirosawa, Wako, Saitama 351-0198, Japan*
[5] *IPN, 15 Rue G. Clemenceau, F-91406 Orsay, France*
[6] *CYRIC, Tohoku University, 6-3 Aoba, Aramaki, Aoba-ku, Sendai, Miyagi 6980-8578, Japan*
[7] *Grand Accélérateur National d'Ions Lourds (GANIL), CEA/DSM-CNRS/IN2P3, B.P. 55027, F-14076 Caen Cedex 5, France*

The g factors of the ^{17}N and ^{18}N ground states were remeasured using the β-nuclear magnetic resonance (β-NMR) technique on spin-polarized fragment beams at the LISE fragment separator at GANIL. Based on the g-factor results, the magnetic moments of ^{17}N ($I^\pi = 1/2^-$) and ^{18}N ($I^\pi = 1^-$) were deduced: $|\mu(^{17}\mathrm{N})| = 0.3551(4)\mu_N$ and $|\mu(^{18}\mathrm{N})| = 0.3273(4)\mu_N$. Both results are in good agreement with and more precise than the earlier observed values.

DOI: 10.1103/PhysRevC.80.037306
PACS number(s): 21.10.Ky, 21.60.Cs, 24.70.+s, 27.20.+n

Exotic nuclei close to the drip lines often exhibit different nuclear properties compared to the isotopes in the valley of stability. Therefore they are extensively studied in theoretical and experimental research, trying to understand the variation in nuclear structure that occurs all over the nuclear chart. A changing shell structure has also been found in the light neutron-rich boron ($Z = 5$), carbon ($Z = 6$), nitrogen ($Z = 7$), and oxygen ($Z = 8$) isotopes (e.g., [1–6]). For these nuclei, monopole interactions vary rapidly as the $\pi(p)$ shell and the $\nu(sd)$ orbitals are filled, giving rise to new shell gaps and vanishing magic numbers.

* Present address: CSNSM, Université Paris-Sud 11, CNRS/IN2P3, F-91405 Orsay-Campus, France

An earlier β-NMR measurement on $^{17}_{7}N_{10}$ ($I^\pi = 1/2^-$, $t_{1/2} = 4.173$ s [7]) showed that configurations with two *sd* neutrons coupled to $J^\pi = 2^+$ are present in the ground state. This induces a larger magnetic moment than the Schmidt value [8] for an odd $p_{1/2}$ proton [9]. For $^{18}_{7}N_{11}$ ($I^\pi = 1^-$ [10], $t_{1/2} = 619(2)$ ms [11]), the ground state properties and the β decay are extensively discussed in Refs. [10–19]. Large-scale shell-model calculations suggest a ground-state structure dominated by configurations with three unpaired $d_{5/2}$ neutrons coupled to $J^\pi = 3/2^+$, turning ^{18}N into a transition nucleus toward the deformed $^{17}_{6}C_{11}$ isotope [20]. Note that two contradictory magnetic and quadrupole moments have been reported: $|\mu|_1 = 0.3279(13)\mu_N$, $|Q|_1 = 12.3(12)$ mb in Ref. [14] and $|\mu|_2 = 0.135(15)\mu_N$, $|Q|_2 = 27(4)$ mb in Ref. [15]. This often suggests the presence of an isomeric state in the isotope of interest. A sufficiently long lifetime of the isomer (typically $\geq 50\mu$s) is required in order to induce a visible β-NMR resonance effect. The lower lifetime limit is determined by the applied radio-frequent-field strength.

Although a 5.25 μs isomer is observed in ^{16}N [7] and shape coexistence is predicted to occur in ^{17}C [5], no experimental evidence has been found for the presence of a long-lived ($\geq 50\mu$s) isomeric state in ^{18}N. So far, the level scheme of ^{18}N has been studied in three types of experiments, probing the charge-exchange reaction ^{18}O(^{7}Li, ^{7}Be)^{18}N [12], the β decay of ^{18}C [21] and the fusion-evaporation reaction ^{9}Be(^{11}B, $2p$)^{18}N [19]. In the charge-exchange reaction, excited states were observed with a resolution of 10 keV only, revealing two strongly populated levels around 121 keV and 747 keV, a weakly populated level at 580 keV, and two levels above 2 MeV (left panel of Fig. 1). The spin assignments, shown in Fig. 1, were made by Barker based on a weak-coupling model [22]. In the β decay of ^{18}C, states at 115 keV and 587 keV could be identified (middle panel of Fig. 1), close in energy to the lowest states observed in the charge-exchange reaction. The decay intensity of the 115 keV level to the ground state was found to be more than a factor two lower than expected from the analysis of the full data set. It was suggested that this is due to a nonobserved long-lived isomeric transition in ^{18}N. In the fusion-evaporation reaction, three levels were observed at 115 keV, 587 keV and 742 keV respectively (right panel of Fig. 1). The lifetimes of these states were measured using the recoil distance method [23]. The 115 keV level has a lifetime of 582(165) ps while the other two have lifetimes below 40 ps. The technique used in this experiment was not sensitive to long-lived isomers because of the short time window (100 ns) used for correlations between the γ-rays and the two protons. Since the presence of an isomeric state in ^{18}N has not been confirmed so far, the discrepancy between the two measured sets of nuclear moments remains unclarified.

In this Brief Report we report on a new measurement of the magnetic moments of ^{17}N and ^{18}N, performed during a test experiment which was meant to evaluate the performance of a new β-NMR setup installed at the LISE beam line [24, 25] at GANIL. A technical description of the setup will be published elsewhere [26].

Both N fragments were produced in an intermediate energy reaction, induced by a $^{18}O^{8+}$ primary beam (1 μA, 74.3A MeV) on a 1182 μm ^{9}Be target. Spin-polarization of the $^{17-18}$N-fragments was obtained by putting an angle of 2(1)° on the primary beam with respect to the entrance of the spectrometer and by making a selection in the longitudinal momentum distribution. The ^{17}N isotopes were produced by a projectile-fragmentation reaction for which the highest spin-polarization is known to occur in the wings of the momentum distribution [27–29]. For single nucleon

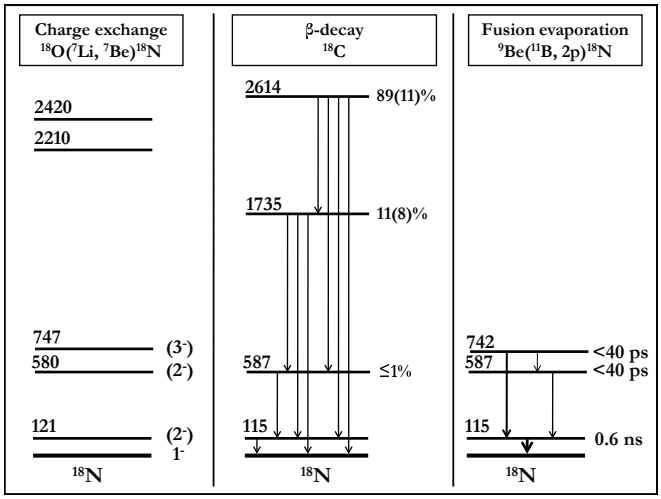

Figure 1: Level schemes of ^{18}N proposed in (left) the charge-exchange reaction ^{18}O(^{7}Li, ^{7}Be)^{18}N [12], (middle) the β decay of ^{18}C [21],(right) the fusion-evaporation reaction ^{9}Be(^{11}B, 2p)^{18}N [19].

pick-up reactions, such as the production mechanism of the ^{18}N fragments, it was demonstrated that a large amount of polarization is achieved in the left wing and in the center of the momentum distribution [30]. Selecting a momentum window according to these conditions resulted in about 2×10^5 polarized ^{17}N-ions per second and about 10^5 polarized ^{18}N-ions per second at the final focal point of the LISE fragment separator. A purity of 94% was achieved for both secondary beams, using a 1020 μm ^{9}Be wedge degrader in the intermediate dispersive plane. During the beam-tuning process, the transmission of the secondary beam was monitored on three Si detectors, using the standard energy loss versus time-of-flight technique.
In the β-NMR setup, the selected secondary beam is stopped in a 2 mm MgO crystal at room temperature. The β particles, produced by the decay of the implanted fragments, are detected in two ΔE/E pairs of plastic scintillators. Both pairs are situated along the vertical polarization direction, one above the crystal, the other below. When a polarized ensemble of nuclei decays, an anisotropic β-radiation pattern is emitted and the observed β asymmetry A is given as

$$A = \frac{N(0^\circ) - N(180^\circ)}{N(0^\circ) + N(180^\circ)} \simeq \frac{v_\beta}{c} A_\beta P \qquad (1)$$

P is the polarization of the selected ensemble and A_β is the asymmetry parameter determined by the β-decay properties (e.g., the initial and final spins) of the nuclei under investigation. The ratio of the velocity of the β particles, v_β, to the speed of light can be taken as 1 since ^{17}N and ^{18}N have high Q_β values [$Q_\beta(^{17}\mathrm{N}) = 8.68$ MeV and $Q_\beta(^{18}\mathrm{N}) = 13.9$ MeV]. When the spin polarization of the implanted ensemble is destroyed, a change in the β-asymmetry detection, proportional to $A_\beta P$, is observed.

In the case of β-NMR, the spin polarization is resonantly destroyed by hyperfine interactions between the nuclear spin ensemble and the static and radiofrequent (rf) magnetic fields. The static magnetic field B_0, applied along the polarization direction, induces an equidistant (Zeeman) splitting of the nuclear m states. The energy difference between two subsequent levels is proportional to the nuclear g factor and the magnetic field strength: $\Delta E = g\mu_N B_0$. Perpendicular to B_0, a rf field with frequency ν is generated inside a coil placed around the crystal. When the energy $h\nu$ of the rf field equals the energy difference between two quantum levels, equal populations of all m states are induced, resulting in an isotropic ensemble and a zero β asymmetry. This happens when the rf frequency corresponds to the Larmor frequency ν_L:

$$\nu_L = \frac{g\mu_N B_0}{h} \tag{2}$$

By scanning the β asymmetry as a function of the rf frequency, the nuclear g factor can be deduced from the position of the observed resonance.

While the polarized beam is implanted continuously, the rf frequency is changed in discrete steps every 10 sec to 1 min, depending on the lifetime. In order not to miss out on the resonance frequency, each applied rf frequency is modulated around its central value. The modulation range covers at least one-half of the interval between two subsequent central frequencies and is repeated at a rate of 100 Hz. After applying all frequencies in a certain scan range, data without rf field are taken as a reference. The complete cycle is repeated until enough statistics are obtained. Depending on the production rate and the detection efficiency, this takes 30 min up to a few hours.

During the β-NMR measurement, the static magnetic field B_0 is monitored by the hall probe which is positioned at about 7 cm behind the implantation crystal. From the recorded field value, the field strength at the position of the crystal can be calculated, relying on the magnet calibrations performed before and after the experiment. Using the average of both calibration curves, a field value of 0.15967(12) T was obtained for the ^{17}N measurements while B_0 was 0.39971(33) T for the β-NMR's on ^{18}N. The errors on these values consist of two contributions, added in quadrature. The statistical contribution includes the error on the field measured at the hall probe position and the errors on the slope and the intercept of the calibration function. The systematic error is given by the 0.1 mT and 0.25 mT divergence observed for repeated calibrations around 0.16 T and 0.4 T, respectively.

Three β-NMR measurements were performed on the ground state of ^{17}N. Initially, a broad frequency region was scanned in steps of 10 kHz with 6 kHz modulation (Fig.2a), revealing a 0.56(6)% NMR effect at $\nu_{L,1}$ = 864.7(20) kHz. Two fine scans around the observed resonance confirmed this result. The first fine scan was performed by scanning a narrow rf-frequency range in steps of 4 kHz with a modulation of 2.5 kHz (Fig.2b). A Larmor frequency of $\nu_{L,2}$ = 864.7(7) kHz was obtained. The same rf region was studied by a second fine scan, applying frequencies which were only 2 kHz apart and a modulation of 3 kHz. This resulted in a Larmor frequency $\nu_{L,3}$ = 863.1(15) kHz (Fig.2c). The function used to fit the three β-NMR curves includes the Lorentzian line shape and the modulation [31] with the resonance frequency, the position of the baseline, the FWHM of the Lorentz curve and the amplitude of the resonance as fit parameters. The outer right point in each β-NMR spectrum contains the data taken without rf field.

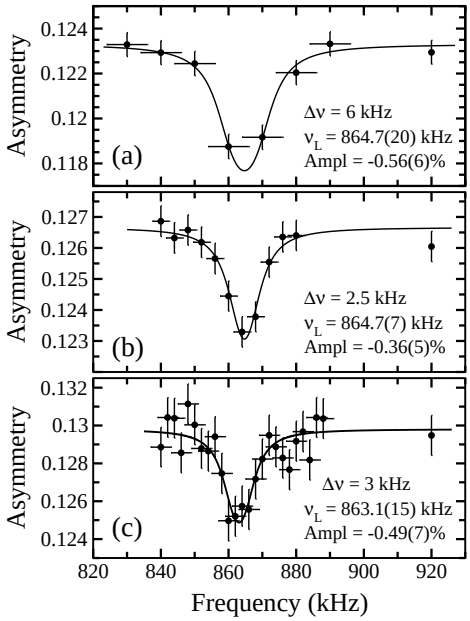

Figure 2: β-NMR results for ^{17}N. (a) Broad scan with step 10 kHz. (b) Fine scan with step 4 kHz. (c) Fine scan with step 2 kHz.

The weighted mean of the measured Larmor frequencies is calculated to be $\overline{\nu}_L(^{17}\mathrm{N}) = 864.4(6)$ kHz. Consequently, the experimental results for the g factor and the magnetic moment of ^{17}N are $|g(^{17}\mathrm{N})| = 0.7102(7)$ and $|\mu(^{17}\mathrm{N})| = |g|I\mu_N = 0.3551(4)\mu_N$ respectively. The diamagnetic correction factor for N isotopes in a MgO crystal equals $+3.55(20) \times 10^{-4}$ ([32] and references therein). Since the induced effect is smaller than the quoted error on the ^{17}N magnetic moment, no diamagnetic correction is performed. The obtained magnetic moment is in agreement with and five times more precise than the published value $|\mu(^{17}\mathrm{N})|_{\mathrm{publ}} = 0.352(2)\mu_N$ [9]. An extensive discussion and interpretation of the ^{17}N result can be found in Ref. [9].

To study the g factor(s) of ^{18}N, the region around the earlier observed value $g = 0.3279(13)$ [14] was scanned three times. In each measurement, seven central frequencies were applied in steps of 16 kHz with a modulation of 10 kHz. Three different settings of the momentum slits were used, resulting in a different initial polarization for each β-NMR measurement. A summary of the β-NMR results is given in Table I and the resonance with the highest amplitude is shown in Fig. 3.

The weighted mean of the three ^{18}N Larmor frequencies is calculated to be $\overline{\nu}_L(^{18}\mathrm{N}) = 997.3(10)$ kHz. Based on this result, the g factor of ^{18}N can be established: $|g(^{18}\mathrm{N})| = 0.3273(4)$. Assuming that this value corresponds to the g factor of the 1^- ground state, $|\mu(^{18}\mathrm{N})| = 0.3273(4)\mu_N$ is obtained, in excellent agreement with the value $|\mu(^{18}\mathrm{N})|_{\mathrm{publ}} = 0.3279(13)\mu_N$, published by Ogawa *et al.* in Ref. [14].

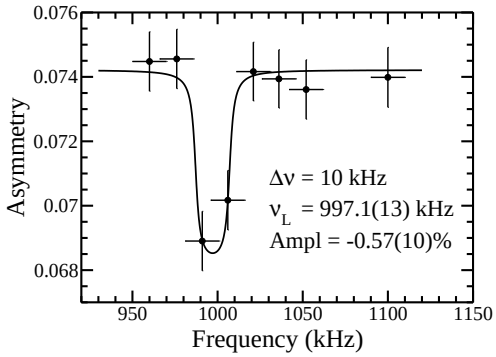

Figure 3: β-NMR result for ^{18}N

Table I: Resonance frequencies and amplitudes for the β-NMR's on ^{18}N. The measurements were performed for different momentum selections.

Momentum selection [slit positions]	ν_L (kHz)	Amplitude
left wing [-45; -25]	997.1(13)	0.57(10)%
center + right wing [-20; -5]	998.5(21)	0.37(9)%
right wing [-5; +15]	996.5(30)	0.31(11)%

The result does not include a diamagnetic correction. Due to the limited amount of beam time, the g-factor range corresponding to the result proposed by Neyens *et al.* in Ref. [15] could not be investigated in detail. A new measurement of that g-factor region would clarify the discrepancy between both experimental magnetic moments and it would confirm whether or not a long-lived isomer occurs in ^{18}N. A thorough analysis and discussion of the ^{18}N result can be found in [14] and will not be repeated here.

The upper panel of Fig. 4 gives the ^{18}N pick-up production yield for several momentum selections, applying a primary beam intensity of about 4 nA. In the lower panel, the resonance amplitudes corresponding to the momentum bins selected in the three β-NMR measurements are shown. In both figures, the position and the opening of the momentum slits are indicated with a horizontal error bar. The identical rf conditions, applied in the β-NMR measurements, allow a direct comparison of the resonance amplitudes, each proportional to the amount of destroyed polarization. Therefore, the curve in the lower panel of Fig. 4 describes the polarization of the nuclear ensemble as a function of the fragment momentum. The curve seems to follow the theoretical trend line [30], which is characterized by a high value of the polarization in the left wing and a gradual decrease when going from the center to the right wing. The large error bars on the amplitude however hinder a clear insight in the detailed behavior of the polarization as a function of the momentum selection. In conclusion, the magnetic moments of ^{17}N and ^{18}N were measured using the β-nuclear magnetic resonance technique at the LISE fragment separator at GANIL.

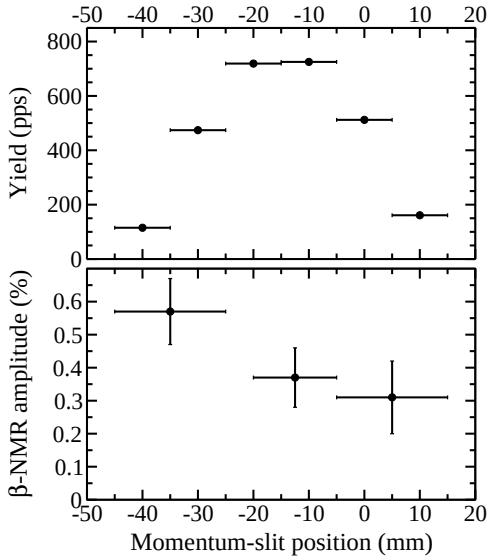

Figure 4: ^{18}N production yields (upper panel) and β-NMR amplitudes (lower panel) as a function of the momentum-slit position. The position and the opening of the slits are indicated with a horizontal error bar.

For the ^{17}N ground state, the magnetic moment $|\mu(^{17}\mathrm{N})| = 0.3551(4)\mu_N$ was found. This result is 5 times more accurate than the value published by Ueno *et al.* [9], illustrating that the newly designed β-NMR/β-NQR setup is suited for precision measurements of nuclear moments. For ^{18}N, three β-NMR measurements with different initial polarizations resulted in $|\mu(^{18}\mathrm{N})| = 0.3273(4)\mu_N$ which confirms the magnetic moment published by Ogawa *et al.* [14]. A future g factor measurement around $|g|_2 = 0.135(15)$ should examine the result obtained by Neyens *et al.* [15]. Independently, new β-decay and γ-spectroscopy experiments that allow the observation of a long-lived ($\geq 50\mu$s) isomer are needed. Also a high-precision mass measurement can reveal the presence of an isomeric state in ^{18}N, provided that its half-life is more than 1 ms.

[1] H. Okuno *et al.*, Phys. Lett. **B 354**, 41 (1995).
[2] H. Ogawa *et al.*, Eur. Phys. J. **A 13**, 81 (2002).
[3] V. Maddalena *et al.*, Phys. Rev. C **63**, 024613 (2001).
[4] M. Stanoiu *et al.*, Phys. Rev. C **78**, 034315 (2008).
[5] H. Sagawa, X.R. Zhou, T. Suzuki and N. Yoshida, Phys. Rev. C **78**, 041304 (R) (2008).
[6] T. Suzuki and T. Otsuka, Phys. Rev. C **78**, 061301 (R) (2008).

[7] D.R. Tilley, H.R. Weller and C.M. Cheves, Nucl. Phys. **A 564**, 1 (1993).
[8] G. Neyens, Rep. Prog. Phys. **66**, 633 (2003).
[9] H. Ueno *et al.*, Phys. Rev. C **53**, 2142 (1996).
[10] J.W. Olness, E.K. Warburton, D.E. Alburger, C.J. Lister and D.J. Millener, Nucl. Phys. **A 373**, 13 (1982).
[11] Z.H. Li *et al.*, Phys. Rev. C **72**, 064327 (2005).
[12] G.D. Putt, L.K. Fifield, M.A.C. Hotchkis, T.R. Ophel and D.C. Weisser, Nucl. Phys. **A 399**, 190 (1983).
[13] K.W. Scheller *et al.*, Phys. Rev. C **49**, 46 (1994).
[14] H. Ogawa *et al.*, Phys. Lett. **B 451**, 11 (1999).
[15] G. Neyens *et al.*, Phys. Rev. Lett. **82**, 497 (1999).
[16] R.H. France, Z. Zhao and M. Gai, Phys. Rev. C **68**, 057302 (2003).
[17] L. Buchmann *et al.*, Phys. Rev. C **75**, 012804(R) (2007).
[18] J.L. Lou *et al.*, Phys. Rev. C **75**, 057302(R) (2007).
[19] M. Wiedeking *et al.*, Phys. Rev. C **77**, 054305 (2008).
[20] Z. Elekes *et al.*, Phys. Lett. **B 614**, 174 (2005).
[21] M.S. Pravikoff *et al.*, Nucl. Phys. **A 528**, 225 (1991).
[22] F.C. Barker, Aust. J. Phys. **37**, 17 (1984).
[23] T. Alexander and J. Forster, *Advances in Nuclear Physics* (Plenum Press New York, 1978).
[24] R. Anne *et al.*, Nucl. Instrum. Methods A **257**, 215 (1987).
[25] R. Anne *et al.*, Nucl. Instrum. Methods B **70**, 276 (1992).
[26] M. De Rydt *et al.*, submitted to Nucl. Instrum. Methods A (2009).
[27] K. Asahi *et al.*, Phys. Lett. **B 251**, 488 (1990).
[28] H. Okuno *et al.*, Phys. Lett. **B 335**, 29 (1994).
[29] D. Borremans *et al.*, Phys. Rev. C **66**, 054601 (2002).
[30] K. Turzó *et al.*, Phys. Rev. C **73**, 044313 (2006).
[31] D. Yordanov, Ph.D. thesis, Instituut voor Kern- en Stralingsfysica, K.U.Leuven (2007), unpublished.
[32] K. Matsuta *et al.*, Phys. Rev. Lett. **86**, 3735 (2001).

Chapter 5

Quadrupole moment of ^{31}Al

In April 2008, the spectroscopic electric quadrupole moment of ^{31}Al was measured using two different β-NMR techniques: the Continuous RF (CRF) method and the Adiabatic Fast Passage (AFP) technique. A detailed presentation of the results and a discussion of the neutron-rich Al-isotopes in the shell-model framework are published in Physics Letters B [60]. The article also includes the motivation for the use of $e_p = 1.1e$ as the effective proton charge in the sd-shell. A copy of the paper can be found at the end of this chapter. In addition, the three sections below provide supplementary information on the $N \simeq 20$ isotopes, the physics behind the β-NMR methods and the search for the best effective proton charge in the sd-shell.

5.1 The island of inversion

The use of a harmonic oscillator to simulate the nuclear mean-field potential introduces the magic number 20 between the opposite-parity states $1d_{3/2}$ and $1f_{7/2}$ that originate from the $N = 2$ and $N = 3$ major oscillator shells respectively. When concentrating on the neutron $N = 20$ shell-closure, the gap between both orbitals can be estimated by comparing the one-neutron separation energies of the $N = 20$ and $N = 21$ isotones. It is found to be of the order of 7.5 MeV in the double magic nucleus $^{40}_{20}$Ca$_{20}$ [61].
When going down to lower proton numbers along the $N = 20$ isotones, several anomalies are observed for nuclei below $Z = 14$. A few examples are quoted here. When the energy of the first 2^+ state in the even-even $N = 20$ isotones is considered, a sudden drop appears for $^{32}_{12}$Mg [62] and $^{30}_{10}$Ne [63]. For the same nuclei, also a significantly larger $B(E2)$-value is measured [63, 64]. In the β-decay of $^{32}_{12}$Mg [65], two abundant transitions are observed to high-lying states in $^{32}_{13}$Al whereas the β-decay of $^{32}_{12}$Mg being a normal *sd* isotope is expected to

proceed mainly to the ground state of the daughter nucleus. Furthermore, also measured nuclear moments of the neutron-rich $_{11}$Na and $_{12}$Mg isotopes [66–69] show a significant deviation from the values put forward by the *sd* shell model. All before-mentioned effects have a common origin: the presence of 2 particle - 2 hole ($2p-2h$) neutron excitations from the *sd* to the *pf* orbits in the ground state. When these intruder configurations dominate, the nucleus belongs to the so-called island of inversion. In that region of exotic nuclei around $N = 20$, $2p-2h$ excitations are favored as the gain in correlation energy[A] exceeds the energy needed to promote two neutrons across the reduced $N = 20$ shell gap.

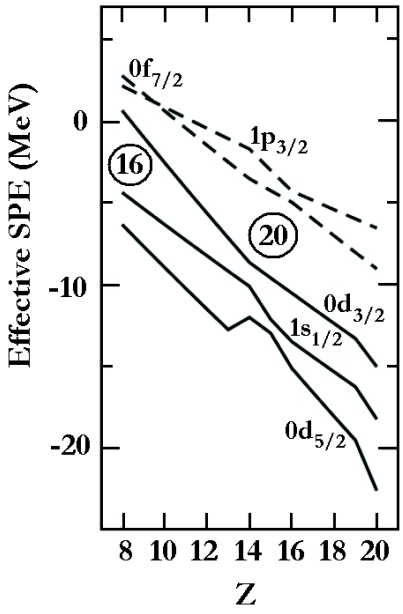

Figure 5.1: Effective single particle energies (ESPE) of the $N = 20$ isotones as a function of Z, calculated with the Monte Carlo shell model, using the SDPF-M residual interaction. (Figure taken from [71])

The growing importance of intruder configurations in the ground states of the $Z < 14$ nuclei evolves in parallel with the reduction of the $N = 20$ shell-gap. As presented in Fig. 5.1, the energy difference between the $1d_{3/2}$ and $1f_{7/2}$ levels stays almost constant when going from $^{40}_{20}$Ca$_{20}$ to $^{34}_{14}$Si$_{20}$ while a strong decrease is observed for nuclei below $^{32}_{12}$Mg$_{20}$. The driving force behind the

[A] Relying on the work by Heyde *et al.* [70], the term 'correlation energy' comprises the monopole and quadrupole terms of the effective nucleon-nucleon interaction among the valence particles in the nucleus.

changing single particle energies is the proton-neutron monopole interaction. As described in [44] the $V^{pn}_{d_{5/2}d_{3/2}}$ monopole term is significantly larger than all other monopole terms in the sd valence space due to the spin-isospin dependence of the nuclear interaction. The interaction is maximized for a proton and a neutron state with the same orbital momentum and an opposite spin orientation. Therefore, a completely filled $\pi(1d_{5/2})$ and $\nu(1d_{3/2})$ orbital strongly attract each other, creating a large $N = 20$ gap above the neutron orbital involved. When protons are removed from the $\pi(1d_{5/2})$ orbit ($Z < 14$), the attraction is reduced and the $\nu(1d_{3/2})$ level rises in energy which results in a smaller $N = 20$ shell gap. As a consequence, the $N = 16$ sub-shell closure becomes more pronounced in the Ne and O isotopes.

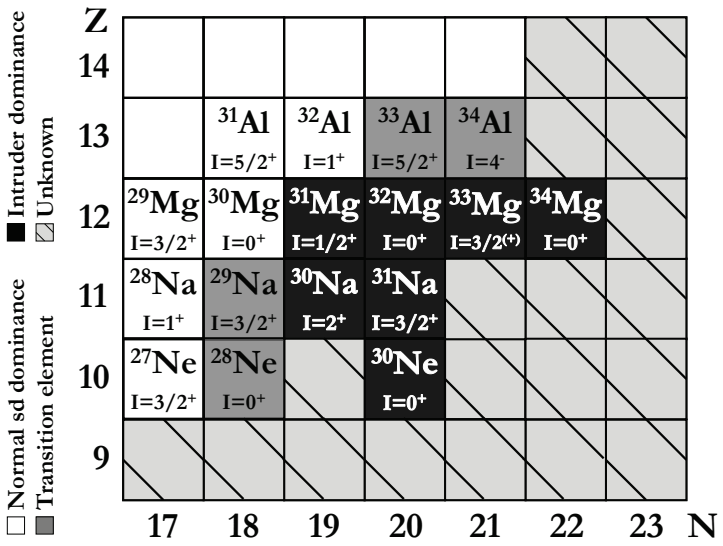

Figure 5.2: Current status of the island of inversion. Isotopes indicated on a black background have ground states dominated by intruder configurations. A white background points to nuclei with a normal $\nu(sd)$ ground state while grey indicates the transition nuclei. Regions indicated with diagonal stripes have not been explored yet.

A schematic of the island of inversion is shown in Fig. 5.2 and a complete review can be found in [44, 72]. This section further concentrates on how nuclear moments can trace the mixing of intruder configurations in the ground states of the neutron-rich $N \simeq 20$ isotopes. Note that if shell-model calculations are used, they must include the pf-shells in their configuration space in order to obtain an accurate description of the isotopes in the island of inversion.

5.1.1 The Ne and Na isotopes

No experimental values are known for the nuclear moments of the most neutron-rich Ne-isotopes. The magnetic moments have been measured up to $^{25}Ne_{15}$ while the quadrupole moments have only been determined for ^{21,23}Ne [73].
In the Na-chain, Keim *et al.* measured and discussed the nuclear moments of the $^{26-31}Na_{15-20}$ nuclei [66, 67]. For the lowest-mass isotopes $^{26-29}$Na, a good agreement is observed between the experimental magnetic moments and the calculated values, obtained in the full *sd* model space with the USD Hamiltonian of Brown and Wildenthal [74]. A significantly worse agreement appears for $\mu(^{30}\text{Na})$ and $\mu(^{31}\text{Na})$, providing a strong indication of pf-configuration mixing in the ground states of these isotopes. As the electric quadrupole moment is even more sensitive to collective properties and excitations across $N = 20$, a measurement can refine the conclusions drawn from the magnetic moment values. In addition to the intruder dominance in the ground states of ^{30}Na and ^{31}Na, the quadrupole-moment measurements revealed the presence of $2p-2h$ configurations in the ground state of ^{29}Na. Evidence for this effect was also found based on theoretical calculations performed by Utsuno *et al.* in the $sdf_{7/2}p_{3/2}$ valence space using the SDPF-M residual interaction [75].

5.1.2 The Mg isotopes

Combined laser and β-NMR spectroscopy experiments revealed the ground-state spins and magnetic moments of the odd-mass neutron-rich Mg isotopes ($Z = 12$). For $^{27}Mg_{15}$, the measured 1/2 spin and the negative magnetic moment point to a positive-parity ground state dominated by an odd $2s_{1/2}$ neutron, in agreement with older experimental results and many-particle shell-model calculations within the *sd* shell [76].
Adding two more neutrons gives $I = 3/2$ and a positive magnetic moment for $^{29}Mg_{17}$ [76], indicating a major $\nu(1d_{3/2})$ ground-state configuration. Again, a good agreement is observed with shell-model calculations confined to the *sd* valence space, placing ^{29}Mg outside the island of inversion.
The first deviation from the $\nu(sd)$ scheme appears for $^{31}Mg_{19}$. Neyens *et al.* [68] report on the measured $I = 1/2$ spin and the negative magnetic moment, suggesting a positive parity and strongly prolate deformed ground state with a pure $2p-2h$ intruder character.
For $^{33}Mg_{21}$, laser and β-NMR spectroscopy revealed a 3/2 ground-state spin and a negative magnetic moment. The interpretation of both results in the Nilsson-model picture provides strong evidence for a negative-parity ground state, dominated by $2p-2h$ intruder configurations [69]. This conclusion, however, is inconsistent with the positive-parity $1p-1h$ ground state put forward by the β-decay studies of ^{33}Na [77] and ^{33}Mg [78]. Note that $1p-1h$ excitations only support a negative magnetic moment when the pf neutrons are

coupled to spin 2, resulting in a configuration never been observed as a ground state inside the island of inversion [79]. Other available experimental results, e.g. from intermediate-energy Coulomb excitation experiments [80] and proton inelastic scattering measurements [81], can be interpreted in both frameworks. Therefore, the debate on the ground-state structure of ^{33}Mg is still ongoing.

5.1.3 The Al isotopes

For the neutron-rich Al isotopes ($Z = 13$) at the border of the island of inversion, nuclear-moment measurements expose the transition from the 'normal' Si ground states to the deformed Mg isotopes. The g-factors of $^{31-34}$Al$_{18-21}$ are measured using the β-NMR technique on polarized fragment beams [82–85]. A comparison of the experimental values with theoretical calculations shows that $^{31-32}$Al can be described as normal *sd*-shell nuclei. For ^{33}Al and ^{34}Al, an increasing amount of $2p-2h$ intruder configurations is necessary to correctly explain the measured magnetic moments.
As the nuclear quadrupole moments are even more sensitive to neutron excitations across $N = 20$ than the magnetic moments, a systematic study of Q is made for the neutron-rich Al isotopes. Before the publication of this thesis, the quadrupole moments of ^{31}Al and ^{32}Al have been measured at RIKEN with a limited accuracy [86, 87]. The Physics Letters B article and the discussion embedded in this thesis report on the precision measurement of $Q(^{31}\mathrm{Al})$, a crucial and necessary step in the description of the odd-mass Al isotopes towards the semi-magic nucleus ^{33}Al. As ^{33}Al is a transition nucleus between the semi-magic ^{34}Si and the strongly deformed ^{31}Mg, a measurement of $Q(^{33}\mathrm{Al})$ will add important information to the study of the nuclear structure at the border of the island of inversion. The accurate value of $|Q(^{31}\mathrm{Al})|$, obtained in this work, will contribute to a correct interpretation of the new result.

5.2 AFP versus CRF β-NMR

The g-factor and the spectroscopic quadrupole moment of ^{31}Al were measured using the Adiabatic Fast Passage (AFP) and the Continuous RF (CRF) β-NMR techniques [60]. In this section both methods are discussed in the classical approach - for CRF this has never been done before - which studies the evolution of the magnetization $\mathbf{M}$ as a function of time. $\mathbf{M}$ is the total magnetic moment of a nuclear ensemble and its z-component is proportional to the spin-polarization P. When no interaction is present, $\mathbf{M}$ is aligned in the z-direction as defined by the spin-orientation created in the projectile-fragmentation reaction. From the time-evolution of the magnetization, the behavior of the polarization can be deduced which is used to reconstruct the β-NMR curve.

In a β-NMR experiment, the magnetization is subjected to the influence of a static magnetic field $\mathbf{B}_0$ along the vertical z-axis and a radiofrequent field $\mathbf{B}_1(t)$, rotating at a particular angular frequency ω in the horizontal xy-plane. For the time being, frequency modulation and rf-sweeping are neglected. A schematic of the problem is given in Fig. 5.3a. In the laboratory frame S (the xyz-frame), the time-evolution of the magnetization $\mathbf{M}$ is obtained by solving the Bloch equation [88], omitting all life-time and relaxation effects:

$$\left.\frac{d\mathbf{M}}{dt}\right|_S = \mathbf{M} \times \gamma \left[\mathbf{B}_0 + \mathbf{B}_1(t)\right] \tag{5.1}$$

with $\gamma = g\frac{\mu_N}{\hbar}$ the gyromagnetic ratio. The time dependence of $\mathbf{B}_1(t)$ can be eliminated by using a coordinate system S' that rotates about the z-axis with a frequency ω. In the S'-frame, $\mathbf{B}_0$ along the $z = z'$ axis and $\mathbf{B}_1$ chosen in parallel to x' are static and the Bloch equation is reduced to [88]

$$\left.\frac{d\mathbf{M}}{dt}\right|_{S'} = \mathbf{M} \times \gamma \left[\left(B_0 - \frac{\omega}{\gamma}\right)\mathbf{e}_z + B_1 \mathbf{e}_{x'}\right] = \mathbf{M} \times \left[(\omega_0 - \omega)\,\mathbf{e}_z + \omega_1 \mathbf{e}_{x'}\right] \tag{5.2}$$

$\omega_0 = \frac{g\mu_N B_0}{\hbar}$ is called the angular Larmor frequency while $\omega_1 = \frac{g\mu_N B_1}{\hbar}$ is defined as the angular Rabi-oscillation frequency.

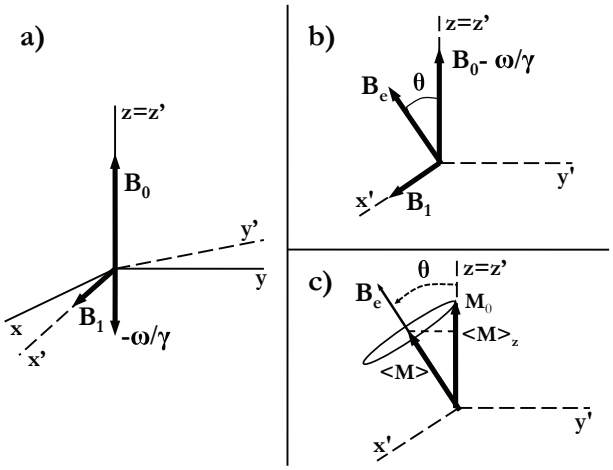

Figure 5.3: a) Static magnetic field $\mathbf{B}_0$ and rf-field $\mathbf{B}_1$ which is rotating with frequency ω in the laboratory frame S and static in the rotating frame S'. b) Effective field $\mathbf{B}_e$ making an angle θ with the $z = z'$ axis. c) Precession of the magnetization about $\mathbf{B}_e$.

In the rotating frame S', the amplitude of the effective field $\mathbf{B}_e(\omega)$, indicated in Fig 5.3b, can be calculated

$$B_e(\omega) = \sqrt{\left(B_0 - \frac{\omega}{\gamma}\right)^2 + B_1^2} \tag{5.3}$$

The effective field makes an angle $\theta(\omega)$ with the $z = z'$ axis as shown in Fig 5.3b. Simple geometry leads to the expression of $\theta(\omega)$ given below.

$$\theta(\omega) = \arccos\left(\frac{\omega_0 - \omega}{\sqrt{(\omega_0 - \omega)^2 + \omega_1^2}}\right) \tag{5.4}$$

The dependence of θ on the rf-frequency ω is outlined in Fig 5.4a. Two simulations are performed, using $\omega_0 = 1000$ kHz and two different values for the angular Rabi-oscillation frequency, $\omega_1 = 5$ kHz and $\omega_1 = 15$ kHz. From Fig 5.4a it is clear that a small rf-field strength results in a narrow resonance region, defined as the frequency interval where $|\omega_0 - \omega|$ is smaller than $|\omega_1|$ and where the transition from $\theta(\omega) = 45°$ to $\theta(\omega) = 135°$ occurs. The width of the resonance region equals $2\omega_1$.

In a system where only a static magnetic field is present, the magnetization starts precessing about the field vector. Applying this principle to the S'-frame, $\mathbf{M}$ is precessing about $\mathbf{B}_e$ with a frequency $\omega_e = \gamma B_e = \sqrt{(\omega_0 - \omega)^2 + \omega_1^2}$. A special case is encountered when the resonance condition $\omega = \omega_0$ is fulfilled. Then the magnetization in S' precesses about $\mathbf{B}_e = \mathbf{B}_1$ with a frequency ω_1.

When the production yield of the isotope of interest is very high, a β-NMR curve can be obtained by applying many subsequent rf-frequencies in an interval around the resonance frequency ω_0. For each rf-frequency, Eq. 5.2 is solved and the observed average polarization, proportional to $< M >_z = < M >_{z'}$, is plotted. As illustrated in Fig. 5.3c, the following expression for $< M >_z$ is obtained:

$$< M >_z = < M >_{z'} = < M > \cos(\theta) = [M_0 \cos(\theta)]\cos(\theta) = M_0 \cos^2(\theta) \tag{5.5}$$

Two examples of likewise simulated β-NMR curves are shown in Fig. 5.4b. The simulations were made without any frequency sweep or frequency modulation, using $\omega_0 = 1000$ kHz and two values of the angular Rabi oscillation frequency, $\omega_1 = 5$ kHz and $\omega_1 = 15$ kHz. The obtained line shapes are Lorentzian which can be proven explicitly when inserting Eq. 5.4 in Eq. 5.5.

$$< M >_z = M_0 \frac{(\omega_0 - \omega)^2}{(\omega_0 - \omega)^2 + \omega_1^2} \tag{5.6}$$

The full width at half maximum (FWHM) of a Lorentzian β-NMR curve equals $2\omega_1$ and is therefore completely determined by the applied rf-field strength, as illustrated in Fig. 5.4b.

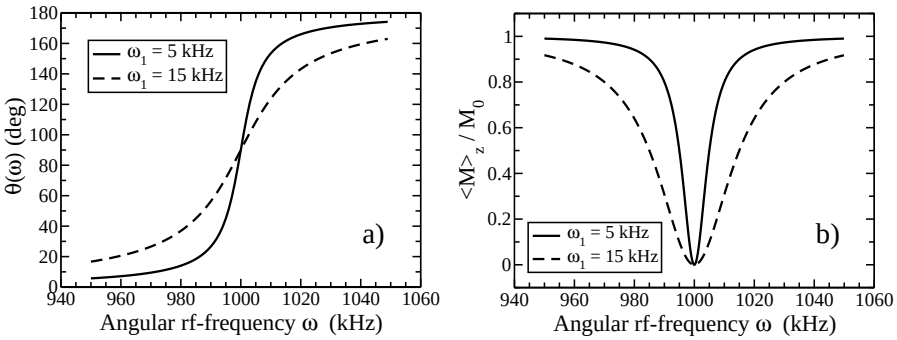

Figure 5.4: a) The angle $\theta(\omega)$ between $\mathbf{B}_e$ and the z' axis as a function of ω for $\omega_1 = 5$ kHz and $\omega_1 = 15$ kHz. b) Simulated β-NMR curves without frequency sweep or frequency modulation, using $\omega_0 = 1000$ kHz and two different Rabi oscillation frequencies, $\omega_1 = 5$ kHz and $\omega_1 = 15$ kHz.

For the β-NMR measurements presented in this work however, low production yields demand the use of a frequency sweep or frequency modulation (see section 2.2). Two approaches are possible. If well-defined sequences of ion-implantation, rf sweep and β-detection are applied in an attempt to inverse the spin polarization, the β-NMR technique is called Adiabatic Fast Passage. When continuous ion-implantation and β-detection are combined with a simultaneously applied and modulated rf signal, a destruction of the polarization is induced and the corresponding method is called Continuous RF β-NMR.

5.2.1 Adiabatic Fast Passage β-NMR

The Adiabatic Fast Passage measurement on ^{31}Al consists of subsequent cycles. All experimental details are given in the attached Phys. Lett. B article. Each cycle starts with an implantation time, followed by an rf-frequency sweep, a β-detection time and another sweep of the same rf-frequency range. Let's have a closer look at the second and the fourth part of the cycle. There, the rf-frequency is swept linearly from $\omega_i - \Delta\omega$ to $\omega_i + \Delta\omega$ around a central value ω_i. The sweep typically takes a few ms ($t_{rf} = 3$ ms for the ^{31}Al β-NMR), giving rise to a rather low sweep-frequency $\omega_r = 2\pi/t_{rf}$. As the rf-frequency is no longer constant, a revision of Eqs. 5.5 and 5.6 is needed.

As the rf-frequency is swept from $\omega_i - \Delta\omega$ to $\omega_i + \Delta\omega$, the effective field $\mathbf{B}_e$ will follow this evolution by rotating from the initial angle $\theta(\omega_i - \Delta\omega)$ to the final angle $\theta(\omega_i + \Delta\omega)$. It can be proven [88] that the component of the magnetization which is initially oriented along $\mathbf{B}_e$ will remain constant when

$$\omega_r \ll \omega_e \tag{5.7}$$

The magnetization thus follows the direction of the effective field $\mathbf{B}_e$ when the field changes sufficiently slow. This condition is generally called the *adiabatic theorem* and must be fulfilled for the majority of the data points when a β-NMR measurement is performed. The adiabatic theorem becomes more strict close to the resonance where $\omega_e = \omega_1$. In the case of ^{31}Al, ω_r is 2.094 kHz while ω_1, the minimal value of ω_e, equals 7.3 kHz (corresponding to $B_1 = 0.1$ mT). For the β-NMR on ^{31}Al, the submission to the adiabatic theorem is not optimal. However, only small deviations from the AFP line shape are expected.

In order to make a mathematical description of the resonance line shape after adiabatic spin inversion, the Bloch equation has to be solved for the appropriate experimental conditions. Therefore, the axis system S'' is introduced, rotating around $y' = y''$ with a frequency ω_r and having z'' parallel to $\mathbf{B}_e(t)$ (see Fig. 5.5). In this frame, the Bloch equation becomes:

$$\left.\frac{d\mathbf{M}}{dt}\right|_{S''} = \mathbf{M} \times [\gamma B_e(t)\mathbf{e}_{z''} - \omega_r \mathbf{e}_{y''}] \tag{5.8}$$

Although the vector $\mathbf{B}_e$ has a fixed direction in S'', its amplitude changes as a function of time. However, when the precession of $\mathbf{M}$ about $\mathbf{B}_e$ is much faster than the amplitude variation ($\omega_r \ll \omega_e$), B_e can be considered as a constant in time. Eq. 5.8 then holds the following solution for $< M >_{z''}$ in S'':

$$< M >_{z''} = M_0 \cos(\theta(\omega_i - \Delta\omega)) + M_0 \sin(\theta(\omega_i - \Delta\omega))\frac{\omega_r}{\omega_e}\sin(\omega_e t) \tag{5.9}$$

The second term can be neglected provided that the adiabatic theorem is fulfilled for all ω_e. Tracing this solution back to the S-frame gives the average z-component of the magnetization as a function of the applied frequency $\omega(t)$:

$$< M(\omega(t)) >_z = M_0 \cos(\theta(\omega_i - \Delta\omega)) \cos(\theta(\omega(t))) \tag{5.10}$$

In an AFP β-NMR measurement, the β-detection only starts after a complete rf-pulse. This means that the observed polarization is the polarization obtained at the final frequency $\omega = \omega_i + \Delta\omega$. Therefore, the line shape of an AFP β-NMR resonance applying a frequency sweep around ω_i is determined by

$$\begin{aligned} < M(\omega_i) >_z &= M_0 \cos(\theta(\omega_i - \Delta\omega)) \cos(\theta(\omega_i + \Delta\omega)) \\ &= M_0 \frac{\omega_0 - \omega_i + \Delta\omega}{\sqrt{(\omega_0 - \omega_i + \Delta\omega)^2 + \omega_1^2}} \frac{\omega_0 - \omega_i - \Delta\omega}{\sqrt{(\omega_0 - \omega_i - \Delta\omega)^2 + \omega_1^2}} \end{aligned} \tag{5.11}$$

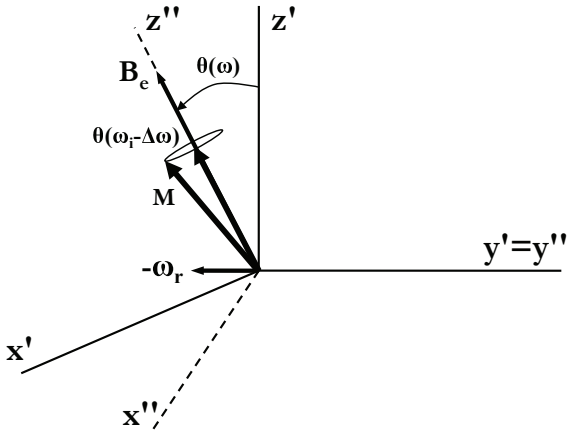

Figure 5.5: The reference frame S'', rotating with a frequency ω_r about y'. When the adiabatic condition is fulfilled, the average magnetization ($< M >_{z''} = M_0 \cos[\theta(\omega_i - \Delta\omega)]$) remains constant along the rotating effective field.

Simulations using Eq. 5.11 can probe the influence of the rf-field strength B_1 and the sweep range on the observed β-NMR line shape. Simulations are made for the experimental conditions of the β-NMR measurement on ^{31}Al described in the Physics Letters B article. Note that the experimentally applied frequencies ν and $\Delta\nu$, given in the paper, are replaced by $\omega = 2\pi\nu$ and $\Delta\omega = 2\pi\Delta\nu$, consistent with the theoretical discussion presented here.
First, the influence of B_1 is studied, keeping the sweep range fixed at $\Delta\omega = 2\pi \times 1.54 = 9.68$ kHz (angular sweep range used for the AFP β-NMR on ^{31}Al). Fig. 5.6a illustrates that a larger rf-field strength induces a broader β-NMR curve with a smaller amplitude. This can be understood based on the behavior of $\theta(\omega)$, the angle between the effective field and the z-axis, which is outlined in Fig. 5.6b for three rf-field strengths ($B_1 = 0.03$ mT, $B_1 = 0.1$ mT and $B_1 = 0.25$ mT). On either side of the resonance, a sweep interval of $\Delta\omega = 9.68$ kHz is drawn, indicating $\theta(\omega_{res} - 9.68)$ and $\theta(\omega_{res} + 9.68)$ on the three curves. As can be observed, the product of the cosines of the two angles will be smaller for $B_1 = 0.25$ mT than for $B_1 = 0.1$ mT and $B_1 = 0.03$ mT, which have a much narrower resonance region. This proves that, in order to have a full inversion of the spin polarization, the width of the resonance region, which is of the order of $2\omega_1$, should be much smaller than twice the sweep interval $\Delta\omega$. For the particular case considered here, ω_1 needs to smaller than 2.2 kHz ($B_1 < 0.03$ mT), which corresponds to about one fourth of $\Delta\omega$.

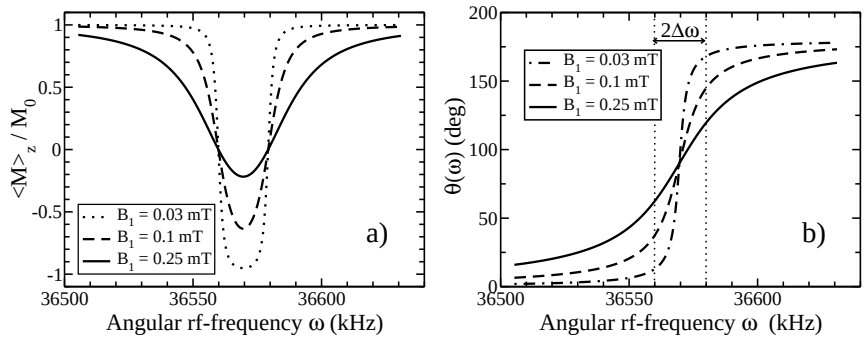

Figure 5.6: a) Simulated AFP β-NMR resonances for a sweep range $\Delta\omega = 9.68$ kHz applying B_1 =0.03, 0.1 and 0.25 mT. b) $\theta(\omega)$ curves for B_1 =0.03, 0.1 and 0.25 mT, indicating the total sweep range $2\Delta\omega = 19.4$ kHz around the resonance frequency.

The inverse effect is studied in Fig. 5.7a where simulations are shown for two sweep ranges, $\Delta\omega = 2\pi \times 1.54 = 9.68$ kHz and $\Delta\omega = 2\pi \times 3.54 = 22.24$ kHz, keeping the rf-field strength constant at 0.1 mT. A larger sweep range gives rise to a broader and deeper β-NMR curve. Again, this can be explained by looking at $\theta(\omega)$, given in Fig. 5.7b for $B_1 = 0.1$ mT. Both sweep ranges are indicated, symmetric around the resonance frequency ω_0. For the largest sweep range, the product of the cosines corresponding to the initial and final frequencies will be closer to minus one, resulting in a larger β-NMR amplitude. This confirms once more that $\omega_1 \ll \Delta\omega$ needs to be fulfilled in order to obtain a complete inversion of the spin polarization.

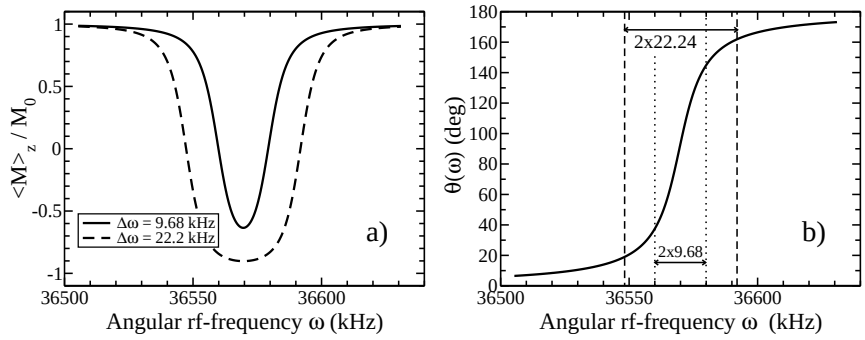

Figure 5.7: a) Simulated AFP β-NMR resonances for a rf-field strength $B_1 = 0.1$ mT, applying a sweep range of $\Delta\omega = 2\pi \times 1.54$ kHz and $\Delta\omega = 2\pi \times 3.54$ kHz. b) $\theta(\omega)$ for B_1 =0.1 mT, indicating the total sweep ranges $2\Delta\omega = 19.4$ kHz and $2\Delta\omega = 44.5$ kHz around the resonance frequency.

To conclude, a full AFP spin inversion is obtained if the adiabatic theorem $\omega_r \ll \omega_1$ AND the $\omega_1 \ll \Delta\omega$ condition are true[A]. Therefore, a fragile balance exists between the applied sweep frequency ω_r, the rf-field strength and the sweep range. For the AFP measurements performed on ^{31}Al no complete inversion of the polarization was observed as the applied B_1 (about 0.1 mT, giving rise to $\omega_1 = 7.3$ kHz) was too large for $\Delta\omega = 2\pi \times 1.54 = 9.68$ kHz.

5.2.2 Continuous RF β-NMR

For the CRF β-NMR method, which combines a continuous ion implantation and β-detection with a modulated rf signal, no models based on physical arguments are available. The only existing theoretical formalism is developed by D. Yordanov [69] and gives a purely mathematical description of the total β-NMR line profile $f(\nu;\nu_0,\Gamma,M)$:

$$f(\nu;\nu_0,\Gamma,M) \sim \int_{\nu-M}^{\nu+M} L(\xi-\nu_0;\Gamma)\left|\frac{dt}{d\xi}\right| d\xi \tag{5.12}$$

$L(\xi-\nu_0;\Gamma)$ expresses the Lorentzian line shape as a function of the rf-frequency ξ, centralized around the central value ν_0 and determined by the full width at half maximum (FWHM) Γ. The term $dt/d\xi$ gives the time needed per frequency and depends on the modulation range M. When a ramp modulation is used, Eq. 5.12 reduces to

$$f(\nu;\nu_0,\Gamma,M) \sim \arctan\frac{2(\nu-\nu_0+M)}{\Gamma} - \arctan\frac{2(\nu-\nu_0-M)}{\Gamma} \tag{5.13}$$

Being the only CRF β-NMR model for a long time, Eq. 5.12 has been used to analyse and fit all experimental β-NMR resonances in this thesis work, leaving the amplitude and the FWHM of the curves as free parameters. So far, the generated β-NMR line shape has been considered as intuitively correct. However, no experimental verification of this hypothesis has ever been performed using e.g. a β-NMR measurement applying a small frequency step size and a large frequency modulation[B].

In addition to the mathematical model given above, this thesis work introduces a new theoretical formalism containing all physical aspects of the CRF β-NMR measurement. Similar as for the AFP technique, the classical framework is used. In this case, however, two procedures can be followed, both assuming the adiabatic condition to be fulfilled and the nuclear lifetime to be infinite.

[A] The set of the two conditions, $\omega_r \ll \omega_1$ and $\omega_1 \ll \Delta\omega$, is called the 'AFP condition' in the Physics Letters B article at the end of the chapter.

[B] In most cases, frequency modulation is used to overcome low production rates. For higher yields, more data-points are taken typically with a small or no rf-modulation.

The first procedure starts from the AFP result given in Eq. 5.11. Simulations within this particular CRF approach induce the same β-NMR line shape as the mathematical model described earlier. The simulated resonance amplitudes, however, are unrealistic. Despite its unphysical character, the formalism has been added to the discussion below since it accounts for the theoretical line shapes used to fit the experimental β-NMR results. It must be stressed that the use of a possibly wrong line shape does not influence the values of the deduced g-factors[A].
The second CRF approach starts from the general expression 5.10, valid for all β-NMR measurements based on a rf-frequency changing in time. It holds the correct β-NMR amplitudes but different β-NMR line shapes compared to the first CRF approach. In order to check the reliability of the second model, a β-NMR measurement using the combination of a small frequency step size and a very large modulation range is strongly encouraged. Below, both models are discussed and evaluated in detail.

First CRF approach
The first CRF approach is a direct extension of Eq. 5.11, only replacing the concept of a single frequency sweep by that of a continuous frequency modulation. The argumentation is as follows. As the frequency modulation is a periodic function around a central frequency ω_i (a ramp function in our case), the initial and final frequencies in each period are identical. Therefore, the average z-component of the magnetization is determined by a cosine squared. Furthermore, as the β-detection is performed simultaneously with the rf-modulation, the 'start' and 'end' point are undefined and an average over all possible angles between $\theta(\omega_i - \Delta\omega)$ and $\theta(\omega_i + \Delta\omega)$ is needed. The latter can be replaced by an average over ω using Eq. 5.4, leading to the following expression for $< M >_z$:

$$< M >_z = M_0 \frac{1}{2\Delta\omega} \int_{\omega_i - \Delta\omega}^{\omega_i + \Delta\omega} \frac{(\omega_0 - \omega)^2}{(\omega_0 - \omega)^2 + \omega_1^2} \, d\omega \tag{5.14}$$

In Fig. 5.8, simulations are presented for the experimental conditions of the CRF β-NMR on ^{31}Al. Note that the rf-frequency $\nu = \omega/(2\pi)$ and not the angular frequency ω is put on the X-axis in order to make a comparison with experiment straightforward. If the modulation range $\Delta\nu = \Delta\omega/(2\pi)$ is kept constant at 1.2 kHz, an increase of the rf-field strength shows a broadening of the β-NMR curve and an increase of the amplitude (Fig. 5.8a). Vice versa, if the rf-strength B_1 is fixed at 0.1 mT, the β-NMR line shape becomes much wider and less deep when the modulation interval is expanded (Fig. 5.8b).

[A] Although its behavior for large modulation ranges is not physical, the first CRF approach predicts a correct Lorentzian β-NMR line shape when a small or zero frequency modulation is applied. As the g-factor is in most cases deduced from a fine scan with a small modulation range, the fitted line shape does not induce an extra error on the g-factor value.

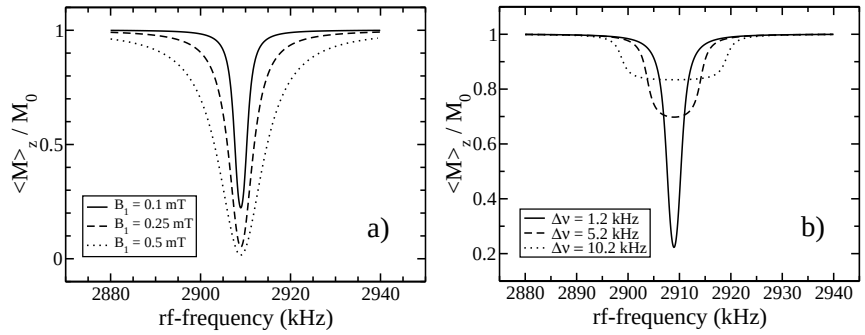

Figure 5.8: a) Simulated CRF β-NMR curves (approach 1) for a sweep range $\Delta\nu = \Delta\omega/(2\pi)$ of 1.2 kHz applying B_1 =0.1, 0.25 and 0.5 mT. b) Simulated CRF β-NMR curves (approach 1) for a rf-field strength of 0.1 mT applying $\Delta\nu = \Delta\omega/(2\pi)$ =1.2, 5.2 and 10.2 kHz.

An evaluation of the β-NMR results obtained with Eq. 5.14 and shown in Fig. 5.8 can be made. Two aspects are discussed, the β-NMR line shape and the β-NMR amplitude.
When the frequency-modulation range increases, the simulated line shape varies from a Lorentzian function to a 'rounded' step function. Exactly the same line shape is obtained with the mathematical formalism, described earlier.
Although the line shape of the resonances in Fig. 5.8 seems intuitively correct, inconsistencies arise when considering the β-NMR amplitudes of the simulations. According to Eq. 5.14, a large modulation range would drastically decrease the amplitude of the β-NMR resonance. This behavior, however, has never been observed experimentally and a counterexample was found in a series of β-NMR measurements on ^{44}Cl. As will be shown in chapter 6, five β-NMR measurements have been performed on the ^{44}Cl ground state, gradually decreasing the frequency-modulation range. Two measurements can be directly compared to each other as they were performed with the same rf-strength and using a modulation which overcomes the inhomogeneous line-broadening[A]. The amplitudes of both measurements are given in Table 5.1, relative to the amplitude obtained for $\Delta\nu = \Delta\omega/(2\pi) = 1.6$ kHz. The experimental results are compared to simulated amplitudes, using the same frequency modulations and assuming $B_1 = 0.1$ mT. Table 5.1 illustrates that Eq. 5.14 is not able to predict a realistic β-NMR amplitude for the measurement using $\Delta\nu = 17$ kHz.

[A] An inhomogeneous magnetic field and defects in the structure of the implantation crystal induce a broader β-NMR resonance with a reduced amplitude when a small or zero frequency modulation is applied. For $B_0 = 1$ T, field fluctuations of 5 to 9×10^{-4} T can be expected, requiring a frequency modulation of 1.03 to 1.85 kHz in order to overcome the inhomogeneous line broadening.

Table 5.1: Comparison of two experimental and simulated β-NMR amplitudes of ^{44}Cl for different frequency-modulation intervals. The experimental values are given relative to the amplitude obtained for $\Delta\nu = 1.6$ kHz. The simulated amplitudes are calculated using Eq. 5.14 and assuming B_1=0.1 mT.

$\Delta\nu$ (kHz)	Experimental ampl. (%)	Simulated ampl. (%)
17	74(11)	10
1.6	100(13)	100

Second CRF approach

The second CRF approach starts from the general formula 5.10 which describes the z-component of the magnetization after a time period t as the product of $\cos(\theta)$ at the start ($= t_0$) and $\cos(\theta)$ at a time $t_0 + t$. In a CRF measurement, where rf and β-detection are applied simultaneously, no end-point is reached and the average magnetization over the modulation interval is observed. This implies an integration over all t in the interval $[0, t_m]$ with t_m the modulation period. As also the starting point t_0 is not well-defined, another integration over t_0 is needed. For the CRF technique, Eq. 5.10 changes into:

$$< M >_z = M_0 \frac{1}{t_m} \int_0^{t_m} \cos(\theta(\omega(t_0))) \left(\frac{1}{t_m} \int_0^{t_m} \cos(\theta(\omega(t_0 + t))) dt \right) dt_0 \quad (5.15)$$

Since $\omega(t_0 + t)$ is a periodic function in time and using Eq. 5.4, the term between brackets can be rewritten as $\left(\frac{1}{2\Delta\omega} \int_{\omega_i - \Delta\omega}^{\omega_i + \Delta\omega} \frac{\omega_0 - \omega}{\sqrt{(\omega_0 - \omega)^2 + \omega_1^2}} \, d\omega \right)$, which is independent of the initial conditions. Therefore, expression 5.15 reduces to:

$$< M >_z = M_0 \left(\frac{1}{2\Delta\omega} \int_{\omega_i - \Delta\omega}^{\omega_i + \Delta\omega} \frac{\omega_0 - \omega}{\sqrt{(\omega_0 - \omega)^2 + \omega_1^2}} \, d\omega \right)^2 \quad (5.16)$$

Simulations have been performed based on Eq. 5.16 using the experimental conditions for ^{31}Al as presented in the Physics Letters B article. A summary of the simulations is shown in Fig. 5.9. Applying $\Delta\nu = 1.2$ kHz and $B_1 = 0.1$, 0.25 or 0.5 mT gives the curves presented in Fig. 5.9a. Changing the modulation range from $\Delta\nu = 1.2$ kHz to 10.2 kHz for a constant rf-strength of 0.1 mT results in Fig. 5.9b.

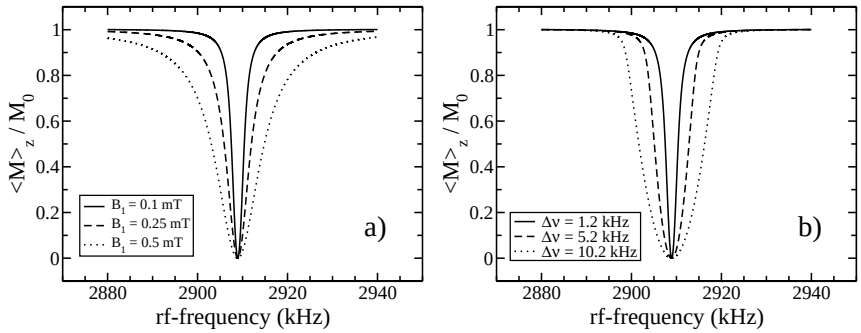

Figure 5.9: a) Simulated CRF β-NMR curves (approach 2) for a sweep range $\Delta\nu = \Delta\omega/(2\pi)$ of 1.2 kHz applying B_1 =0.1, 0.25 and 0.5 mT. b) Simulated CRF β-NMR curves (approach 2) for a rf-field strength of 0.1 mT applying $\Delta\nu = \Delta\omega/(2\pi)$ =1.2, 5.2 and 10.2 kHz.

Bearing in mind that the nuclear lifetime is not taken into account in the presented models, realistic amplitudes are obtained for the β-NMR curves simulated using Eq. 5.16. When an infinite nuclear lifetime is assumed, the full resonance effect is observed even for very low rf-field strengths and extremely small modulation intervals.
The line shapes of the β-NMR resonances calculated with Eq. 5.16 differ from the present intuitive idea of how a β-NMR curve with modulation looks like. However, it must be underlined once more that an experimental high-efficiency β-NMR has never been performed using the combination of a small frequency step size and a very large modulation range. The outcome of such an experiment would be able to judge which of both CRF approaches, presented in this work, generates the correct line shape and is therefore strongly encouraged.

5.3 Changing effective charges

As introduced in section 2.1, shell-model calculations do not account for all possible nuclear effects. When nuclear moments are calculated, meson-exchange currents (MEC) are omitted and particle configurations are neglected due to the limited valence space and the residual interactions. A general discussion of both aspects is given below [23, 26].

- Meson-exchange currents arise from the interaction between the nucleons. When this interaction is disturbed by the presence of electromagnetic fields, correction factors should be introduced. When at least two nucleons are involved, MEC corrections induce two-body terms in the, up to now, one-body multipole moment operators.

- In addition to configurations of valence particles which are explicitly prohibited by restrictions on the valence space, also particle-core polarization is often not taken into account in shell-model calculations. In general, the latter holds two contributions. The first-order particle-core polarization effect comprises the M1 particle-core coupling of valence particles to $1p-1h$ excitations between spin-orbit partners across a major shell. Magnetic dipole moments are very sensitive to this contribution. Second-order core polarization includes the coupling of valence particles to quadrupole vibrations (E2) or to $2p-2h$ excitations of the core. This effect has a strong influence on the nuclear quadrupole moment.

To take into account omitted valence particle configurations, particle-core polarization and MEC-corrections, effective nucleon g-factors and effective charges are used in shell-model calculations.

Note that the quenching of the free nucleon g-factors and charges grows stronger for heavier nuclei and larger cores. The odd-mass Bi-isotopes ($Z = 83$) for instance, have one $\pi(1h_{9/2})$ proton outside a closed Pb ($Z = 82$) core. Nevertheless, their magnetic moments are very different from the Schmidt value since first-order core-polarization effects, i.e. $1p-1h$ excitations from the $\pi(1h_{11/2})$ orbit inside the Pb core to the $\pi(1h_{9/2})$ spin-orbit partner in the configuration space, should be taken into account [26].
For the study of the *sd* nuclei, a ^{16}O core is used. M1 core polarization is not relevant since all spin-orbit partners are either included in the core or in the valence space. It is therefore not surprising that the experimental magnetic moments can be reproduced with the free nucleon g-factors. Second-order core polarization does play a role in the structure of *sd* shell nuclei. Valence particles can couple to the first 2^+ or another excited state of the ^{16}O core. As these configurations are not included in the shell-model calculations, it is expected that (small) effective charges are needed to reproduce the observed Q-moments.

In Ref. [74], Brown and Wildenthal proposed $e_p = 1.3e$ and $e_n = 0.5e$ as the effective proton and neutron charge for the *sd* shell nuclei. The values result from a comparison of the experimental quadrupole moments and E2 matrix elements, known at that time, with calculations using the USD-interaction [74] in the $\pi(sd)\nu(sd)$ shell. Since the publication of the review article in 1988, a fair number of new and more accurate experimental quadrupole moments and B(E2) values became available. These data provide a stringent test for the established effective charges $e_p = 1.3e$ and $e_n = 0.5e$.

Being 'an appendix' to the Physics Letters B article, this section focusses on the proton effective charge e_p only. Similar as in the paper, only isotopes with an odd proton number Z and an even neutron number N are considered. As their ground-states and low-lying energy levels are dominated by the proton configuration, the odd-Z even-N nuclei are excellent probes to study the effective proton charge. The approach in this work is therefore different from the one in the Ref. [74] where a fit through all available quadrupole moments and B(E2) values is used to determine e_p and e_n simultaneously.

In the first step, the updated quadrupole-moment dataset of the odd-Z even-N nuclei, including the experimental values for ^{17}F, ^{23,25,27,29}Na, ^{27,31}Al, ^{35,37}Cl and ^{39}K (see table 5.2), is compared to calculations with the neutrons restricted to the $\nu(sd)$ shell. The protons are confined to the $\pi(sd)$ orbits. All shell-model calculations quoted in this section are made with the ANTOINE code [11] using the sdpf residual interaction [12]. The *sd* part of the latter corresponds to the USD interaction and the theoretical predictions are therefore equivalent to the ones presented in the work of Brown and Wildenthal. In Fig. 5.10, the experimental quadrupole moments are plotted against their theoretical values, using $e_p = 1.1e$ (Fig. 5.10a) and $e_p = 1.3e$ (Fig. 5.10b) as effective proton charges. When a perfect agreement between experiment and theory is obtained, the data coincide with the solid line $Q_{exp} = Q_{th}$. Note that the error bars on the experimental values are smaller than the dots. In order to compare both figures, a χ^2 analysis[A] is performed using the expression [89]:

$$\chi^2 = \frac{1}{n}\sum_{i=1}^{N}\left[\frac{1}{\left[\sum_{i=1}^{N} 1/\sigma_i^2\right]}\left(\frac{y_{i,exp}-y_{i,th}}{\sigma_i}\right)^2\right] \tag{5.17}$$

with n the degrees of freedom and σ_i the errors on the experimental values $y_{i,exp}$. It is clear from the χ^2 values in Fig. 5.10 that $e_p = 1.1e$ provides a much better description of the 'recently measured' $\pi(sd)$ quadrupole moments than the previously adopted effective charge $e_p = 1.3e$.

[A] The χ^2 values calculated in the Physics Letters B article do not include the experimental error bars. Therefore, they are different from the ones mentioned in the text of this section.

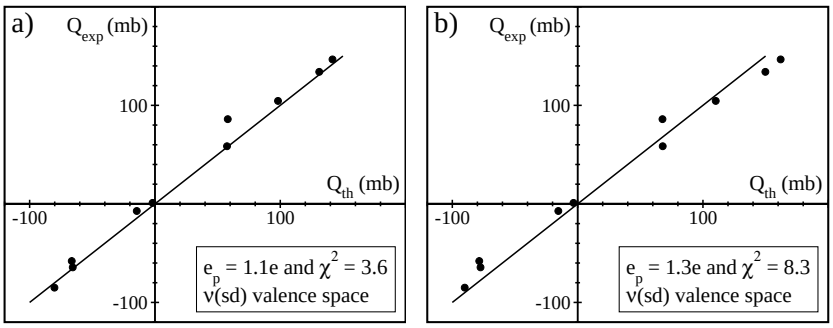

Figure 5.10: Comparison of the experimental quadrupole moments of the odd-Z even-N $\pi(sd)$ nuclei with ANTOINE calculations using the sdpf residual interaction in the $\pi(sd)\nu(sd)$ valence space. The effective charges are ($e_p = 1.1e$,$e_n = 0.5e$) for a) and ($e_p = 1.3e$,$e_n = 0.5e$) for b). The solid line indicates the $Q_{exp} = Q_{th}$ curve.

As described earlier in the text, the quadrupole moment of an odd-Z even-N nucleus is very sensitive to the proton configuration of a particular state and therefore to the effective proton charge. Although B(E2) values[A] involve two nuclear states instead of one, they provide an excellent cross-check of the effective proton charge obtained from the comparison of theoretical and measured quadrupole moments. In Fig. 5.11 and Table 5.3, experimental B(E2) values of several transitions in ^{21,23}Na, ^{27}Al, ^{31}P and ^{35,37}Cl [90, 91] are compared to shell-model calculations. All measured B(E2) values, except for the one of ^{21}Na, were determined before 1977 and have most probably[B] been included in the compilation of Brown and Wildenthal. Nevertheless, calculations using $e_p = 1.1e$ show a better agreement with experiment than the theoretical values obtained for $e_p = 1.3e$. Recall that Brown and Wildenthal used a more extended set of B(E2) values, including many $0^+ \rightarrow 2^+$ transition matrix elements of even-even nuclei, also depending on the effective neutron charge e_n, to fix the effective proton charge at $e_p = 1.3e$.

In the Physic Letters B article, ANTOINE calculations are performed in a larger valence space, which includes also the $\nu(f_{7/2}p_{3/2})$ shell. By doing so, intruder configurations can be taken into account and a better agreement between theory and experiment is obtained for the neutron-rich $\pi(sd)$ nuclei. For both effective charges ($e_p = 1.1e$ and $e_p = 1.3e$), the same study of the quadrupole moments and the B(E2) values is carried out, using $\nu(sdf_{7/2}p_{3/2})$ as the confi-

[A] The B(E2) value gives a quantitative measure for the E2 transition strength. In Ref. [23], the following definition of B(E2) can be found: $B(E2; I_i \rightarrow I_f) = \frac{1}{2I_i+1} < \Psi_f || E2 || \Psi_i >^2$.

[B] The B(E2) values used in Ref. [74] are only referred to as 'B.H. Wildenthal and J. Keikonen unpublished'.

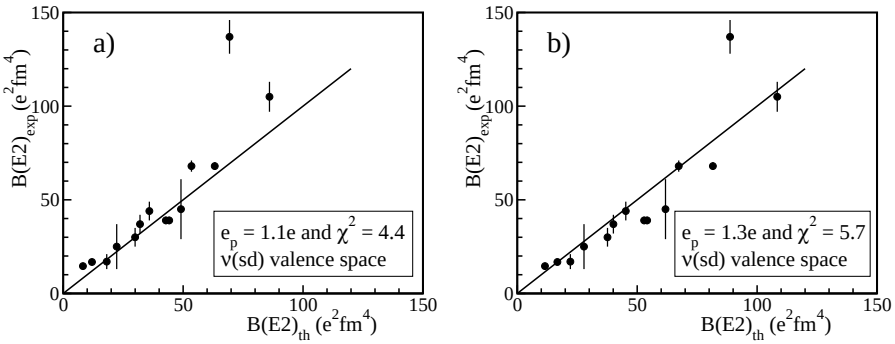

Figure 5.11: Comparison of the experimental B(E2) values of the odd-Z even-N $\pi(sd)$ nuclei with ANTOINE calculations using the sdpf residual interaction in the $\pi(sd)\nu(sd)$ valence space. The effective charges are ($e_p = 1.1e$,$e_n = 0.5e$) for a) and ($e_p = 1.3e$,$e_n = 0.5e$) for b). The solid line indicates the $B(E2)_{exp} = B(E2)_{th}$ curve.

guration space for the neutrons. Fig. 5.12a and 5.12b, also given in the article, show the comparison of the measured quadrupole moments (including $Q(^{41}\mathrm{K})$) with the theoretical predictions applying $e_p = 1.1e$ and $e_p = 1.3e$ respectively. $e_p = 1.1e$ is found to be the optimal effective proton charge for the odd-Z even-N $\pi(sd)$ nuclei, using the sdpf residual interaction in the $\pi(sd)$ $\nu(sdf_{7/2}p_{3/2})$ configuration space.

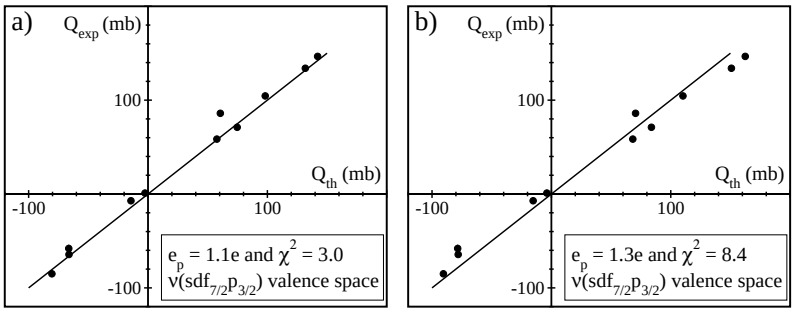

Figure 5.12: Comparison of the experimental quadrupole moments of the odd-Z even-N $\pi(sd)$ nuclei with ANTOINE calculations using the sdpf residual interaction in the $\pi(sd)\nu(sdf_{7/2}p_{3/2})$ valence space. The effective charges are ($e_p = 1.1e$,$e_n = 0.5e$) for a) and ($e_p = 1.3e$,$e_n = 0.5e$) for b). The solid line indicates the $Q_{exp} = Q_{th}$ curve.

The same conclusion is found by studying the B(E2) values, also calculated in the $\pi(sd)\nu(sdf_{7/2}p_{3/2})$ valence space using the sdpf residual interaction. An overview is given in Fig. 5.13 and Table 5.3.

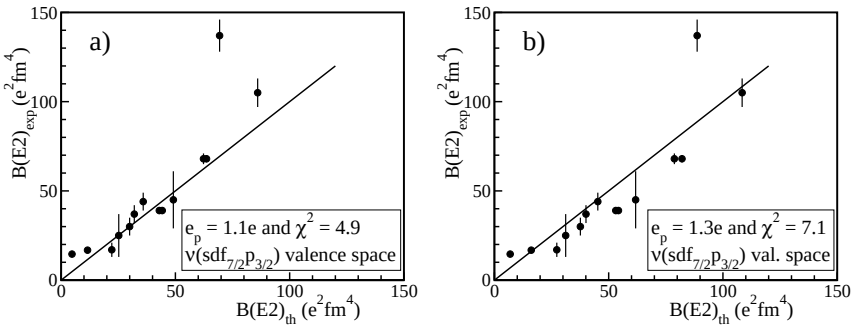

Figure 5.13: Comparison of the experimental B(E2) values of the odd-Z even-N $\pi(sd)$ nuclei with ANTOINE calculations using the sdpf residual interaction in the $\pi(sd)\nu(sdf_{7/2}p_{3/2})$ valence space. The effective charges are ($e_p = 1.1e$,$e_n = 0.5e$) for a) and ($e_p = 1.3e$,$e_n = 0.5e$) for b). The solid line indicates $B(E2)_{exp} = B(E2)_{th}$.

From the study of the quadrupole moments and the B(E2) values of the odd-Z even-N $\pi(sd)$ nuclei, it must be concluded that $e_p = 1.1e$ is a better effective proton charge than the previously established value $e_p = 1.3e$. This result, however, should be placed in the context of a much broader research project. The next step would be to study the calculated and measured quadrupole moments and B(E2) values of the even-Z odd-N nuclei in order to determine the proper effective neutron charge e_n. When both effective charges have been established separately, a general cross-check needs to be performed by comparing theoretical and experimental values of all $\pi(sd)$ shell nuclei and especially of the even-even and odd-odd isotopes.

Table 5.2: A compilation of quadrupole moment data of the odd-Z even-N sd shell nuclei, used for the evaluation of the effective proton charge e_p in the sd shell. Shell-model calculations are made with the ANTOINE code using the sdpf residual interaction in the $\pi(sd)\nu(sd)$ and $\pi(sd)\nu(sdf_{7/2}p_{3/2})$ valence spaces.

Nucl.	Q_{exp} (mb)	Ref.	$\nu(sd)$ space (mb)		$\nu(sdf_{7/2}p_{3/2})$ space (mb)	
			$e_p = 1.1e$	$e_p = 1.3e$	$e_p = 1.1e$	$e_p = 1.3e$
^{17}F	-58(4)	[92]	-66.4	-78.5	-66.4	-78.5
^{23}Na	104.5(10)	[93]	98.2	110.2	98.2	110.2
^{25}Na	1.0(4)	[94]	-1.9	-3.3	-2.5	-3.8
^{27}Na	-7.2(3)	[67]	-14.5	-15.4	-14.3	-15.3
^{29}Na	86(3)	[67]	58.1	67.7	60.6	70.5
^{27}Al	146.6(10)	[95]	141.7	162	142.1	162.4
^{31}Al	134.0(16)	[60]	131.1	149.8	131.8	150.8
^{35}Cl	-85.0(11)	[96]	-80.2	-90.1	-80.5	-90.5
^{37}Cl	-64.35(64)	[97]	-65.6	-77.5	-66.2	-78.1
^{39}K	58.5(6)	[98]	57.5	67.9	57.7	68.2
^{41}K	71.1(7)	[98]	/	/	74.7	83.8

Table 5.3: B(E2) data set (e^2fm^4) of the odd-Z even-N sd shell nuclei, used to select the best effective proton charge e_p in the sd shell. The experimental values are taken from [90, 91]. Shell-model calculations are made with the ANTOINE code using the sdpf residual interaction in the $\pi(sd)\nu(sd)$ and $\pi(sd)\nu(sdf_{7/2}p_{3/2})$ valence spaces.

Nucl.	Transition	B(E2)$_{ex}$	$\nu(sd)$ space		$\nu(sdf_{7/2}p_{3/2})$ space	
			$e_p = 1.1e$	$1.3e$	$e_p = 1.1e$	$1.3e$
^{21}Na	$5/2^+ \rightarrow 3/2^+$	137(9)	69.3	88.7	69.3	88.7
^{23}Na	$5/2^+ \rightarrow 3/2^+$	105(8)	86	108.4	86	108.4
^{23}Na	$7/2^+ \rightarrow 5/2^+$	45(16)	49.1	61.8	49.1	61.8
^{23}Na	$7/2^+ \rightarrow 3/2^+$	37(5)	32	40.1	32	40.1
^{27}Al	$1/2^+ \rightarrow 5/2^+$	39(2)	44.2	54.2	44.3	54.3
^{27}Al	$3/2^+ \rightarrow 5/2^+$	39(2)	42.8	52.9	43	53.1
^{27}Al	$7/2^+ \rightarrow 5/2^+$	68(2)	63.2	81.6	63.6	82.1
^{31}P	$3/2^+ \rightarrow 1/2^+$	30(5)	30	37.6	30	37.6
^{31}P	$5/2^+ \rightarrow 1/2^+$	44(5)	35.9	45.2	35.9	45.2
^{35}Cl	$1/2^+ \rightarrow 3/2^+$	14.6(14)	8.2	11.5	4.8	6.9
^{35}Cl	$5/2^+ \rightarrow 3/2^+$	68(3)	53.5	67.3	62.3	78.7
^{35}Cl	$7/2^+ \rightarrow 5/2^+$	25(12)	22.3	27.8	25.2	31.2
^{35}Cl	$7/2^+ \rightarrow 3/2^+$	17(4)	18.1	22.1	22.2	27.3
^{37}Cl	$1/2^+ \rightarrow 3/2^+$	16.8(10)	12	16.7	11.6	16.1

Precision measurement of the electric quadrupole moment of ^{31}Al and determination of the effective proton charge in the sd-shell

M. De Rydt,[1] G. Neyens,[1] K. Asahi,[2] D.L. Balabanski,[3] J.M. Daugas,[4] M. Depuydt,[1] L. Gaudefroy,[4] S. Grévy,[5] Y. Hasama,[2] Y. Ichikawa,[6] P. Morel,[4] T. Nagatomo,[6] T. Otsuka,[7] L. Perrot,[8] K. Shimada,[9] C. Stödel,[5] J.C. Thomas,[5] H. Ueno,[6] Y. Utsuno,[7] W. Vanderheijden,[1] N. Vermeulen,[1] P. Vingerhoets,[1] and A. Yoshimi[6]

[1] *Instituut voor Kern- en Stralingsfysica, K.U.Leuven, Celestijnenlaan 200D, B-3001 Leuven, Belgium*
[2] *Department of Physics, Tokyo Institute of Technology, 2-12-1 Oh-okayama, Meguro-ku, Tokyo 152-8551, Japan*
[3] *Institute for Nuclear Research and Nuclear Energy, Bulgarian Academy of Sciences, BG-1784 Sofia, Bulgaria*
[4] *CEA, DAM, DIF, F-91297 Arpajon Cedex, France*
[5] *Grand Accélérateur National d'Ions Lourds (GANIL), CEA/DSM-CNRS/IN2P3, B.P. 55027, F-14076 Caen Cedex 5, France*
[6] *RIKEN Nishina Center, 2-1 Hirosawa, Wako, Saitama 351-0198, Japan*
[7] *Japan Atomic Energy Agency, Tokai, Ibaraki 319-1195, Japan*
[8] *IPN, 15 Rue G. Clemenceau, F-91406 Orsay, France*
[9] *CYRIC, Tohoku University, 6-3 Aoba, Aramaki, Aoba-ku, Sendai, Miyagi 6980-8578, Japan*

The electric quadrupole coupling constant of the ^{31}Al ground state is measured to be $\nu_Q = \left|\frac{eQV_{zz}}{h}\right| = 2196(21)$kHz using two different β-NMR (Nuclear Magnetic Resonance) techniques. For the first time, a direct comparison is made between the continuous rf technique and the adiabatic fast passage method. The obtained coupling constants of both methods are in excellent agreement with each other and a precise value for the quadrupole moment of ^{31}Al has been deduced: $\left|Q(^{31}\mathrm{Al})\right| = 134.0(16)$ mb. Comparison of this value with large-scale shell-model calculations in the sd and sdpf valence spaces suggests that the ^{31}Al ground state is dominated by normal sd-shell configurations with a possible small contribution of intruder states. The obtained value for $\left|Q(^{31}\mathrm{Al})\right|$ and a compilation of measured quadrupole moments of odd-Z even-N isotopes in comparison with shell-model calculations shows that the proton effective charge $e_p = 1.1e$ provides a much better description of the nuclear properties in the sd-shell than the adopted value $e_p = 1.3e$.

PACS: 21.10.Ky, 21.60.Cs, 24.70.+s, 27.30.+t, 25.70.Mn, 29.27.Hj, 76.60.-k

I. INTRODUCTION

The electric quadrupole moment Q provides a direct measure of the deviation of the nuclear charge distribution from a sphere. As the quadrupole moment is a sensitive probe to indicate changes in the shell structure, its measurement is an important tool in studying nuclei in and near the island of inversion. This region, comprising the Ne (Z=10), Na (Z=11) and Mg (Z=12) isotopes with neutron number around N=20, is characterized by the dominance of neutron excitations from the sd to the pf-orbits (known as intruder configurations) in the ground state.

The first experimental evidence for this effect was found in the measured nuclear masses and two-neutron separation energies of the $^{26-32}$Na isotopes [1]. In the same year, Campi et al. made the first theoretical analysis of the observed experimental anomalies, performing constrained Hartree Fock calculations [2]. Later, β-decay studies revealed a low lying 2^+ state in ^{32}Mg [3, 4], pointing to a deformed ground state in that nucleus. Further evidence for the existence of the island of inversion was provided by the measurement of B(E2)-values and nuclear moments of the neutron-rich Ne, Na and Mg isotopes (e.g. [5–12]).

As new experimental results became available, shell-model calculations grew more important. Starting from the early calculations performed by Watt et al. [13] and Poves and Retamosa [14], new residual interactions in larger model spaces were developed [15, 16] taking into account particle-hole excitations of the neutrons across the reduced N=20 shell gap. For nuclei inside the island of inversion, theoretical predictions reproduce the observed nuclear properties quite well. For the neutron-rich $^{31-34}$Al isotopes (Z=13) located at the border of the island of inversion, the interpretation of experimental results by means of theoretical models contributes to a better understanding of how the transition to the region of deformed nuclei occurs. A comparison between the measured nuclear magnetic moments of $^{31-34}$Al [17–20] and shell model calculations shows that ^{31}Al and ^{32}Al can be described as normal sd-shell nuclei [17, 19]. For ^{33}Al and ^{34}Al, intruder configurations play a role in the ground state [19, 20] and in the low-energy level structure [21, 22]. This indicates a gradual transition from the Si isotopes, being normal in their ground states, to the deformed Mg isotopes inside the island of inversion.

As the nuclear quadrupole moment is even more sensitive to neutron excitations across N=20 than the magnetic moment, a measurement of Q can provide crucial and decisive information about the mixing between sd and pf configurations in the ground states of the neutron-rich Al isotopes. So far, the Q-moments of $^{31-32}$Al have been studied with a limited accuracy in Refs. [23, 24]. This letter reports on the precision measurement of the ^{31}Al ground-state quadrupole moment, which is a crucial step in describing the systematics of the odd-mass Al isotopes towards the semi-magic nucleus ^{33}Al.

The quadrupole moment of ^{31}Al was measured using two different β-Nuclear Magnetic Resonance techniques, based on a pulsed and a continuous radiofrequent field respectively. This provides a unique opportunity to directly compare both methods and results. The two techniques can be used to determine magnetic moments (then we call it a β-NMR method) or quadrupole moments (then the term β-NQR or β-Nuclear Quadrupole Resonance is adopted).

II. EXPERIMENT

Neutron-rich ^{31}Al nuclei were produced in a projectile fragmentation reaction, induced by a $^{36}S^{16+}$ primary beam (77 MeV/u) impinging on a 1212 μm thick ^{9}Be target. Selection of the secondary beam was done with the high-resolution fragment separator LISE at GANIL [25, 26]. Si-diodes have been used for the beam identification by standard energy loss versus time of flight measurements. Spin polarization of the fragments [27] was obtained by putting an angle of $2(1)^\circ$ on the primary beam with respect to the entrance of the spectrometer. To get the highest polarization, a selection in the right wing of the longitudinal momentum distribution was made, giving a polarized ^{31}Al production yield of about 10^4 pps for a primary beam intensity of 1 μA. A purity of 90% was achieved using a 1054 μm thick ^{9}Be wedge-degrader in the intermediate dispersive plane.

At the end of the LISE fragment separator, a β-Nuclear Magnetic/Quadrupole Resonance (β-NMR/β-NQR) set-up is installed. The ^{31}Al-nuclei are implanted in a cubic Si-crystal for β-NMR or in an α-Al_2O_3 (corundum) crystal for β-NQR. No crystal cooling is needed since the spin-lattice relaxation time T_1 of ^{31}Al ($t_{1/2} = 644(25)$ ms) in both crystals is sufficiently long to preserve the nuclear polarization for a few half lives. T_1 of ^{31}Al in an α-Al_2O_3 crystal is estimated to be 4.8 s, using the $T_1T^2Q^2 =$ const law [28] and the measured relaxation time of ^{27}Al [29].

The implanted nuclei are exposed to an external magnetic field B_0 which induces a Zeemann splitting of the nuclear m-states. When a non-cubic crystal (e.g. Al_2O_3) is used as a stopper material, the quadrupole interaction with the electric field gradient causes an additional shift of the magnetic substates which results in a non-equidistant level spacing. Perpendicular to the external magnetic field, a radiofrequent (rf) field is applied. This rf-field is generated inside the coil mounted around the crystal, by a function generator and rf-amplifier. The asymmetry in the β-decay of the polarized nuclei is observed in two sets of three thin plastic scintillators, one set is situated above the crystal, the other below. Scattering and noise events are reduced in this configuration by requiring a coincidence between the three detectors in each set. A schematic drawing of the β-NMR/β-NQR set-up is given in Fig. 1.

The transition frequency between the magnetic sublevels m and $m+1$ under the influence of a Zeemann and an axially symmetric quadrupole interaction can be calculated using perturbation theory, provided that the Larmor frequency ν_L is much larger than $\frac{\nu_Q}{4I(2I-1)}$. Up to the second order, this series expansion is given by [30]:

$$\nu_m - \nu_{m+1} = \nu_L - \frac{3\nu_Q}{8I(2I-1)}(2m+1)\left(3\cos^2\theta - 1\right) \tag{1}$$

$$- \frac{\nu_Q^2}{32\nu_L}\ \frac{9}{4I^2(2I-1)^2}\ \left[6m(m+1) - 2I(I+1) + 3\right]\ \sin^4\theta$$

I is the nuclear ground-state spin and θ is the angle between the electric field gradient along the c-axis of the crystal and the magnetic field B_0. The Larmor frequency ν_L equals $\frac{g\mu_N B_0}{h}$ with g the nuclear g-factor. The quadrupole coupling constant ν_Q is defined as $\frac{eQV_{zz}}{h}$. In this expression, Q is the spectroscopic quadrupole moment (in mb) and V_{zz} the axially symmetric electric field gradient.

For ^{31}Al (I=5/2$^+$), five different transition frequencies exist. In table I, these five frequencies are given in case the symmetry axis of the electric field gradient is parallel

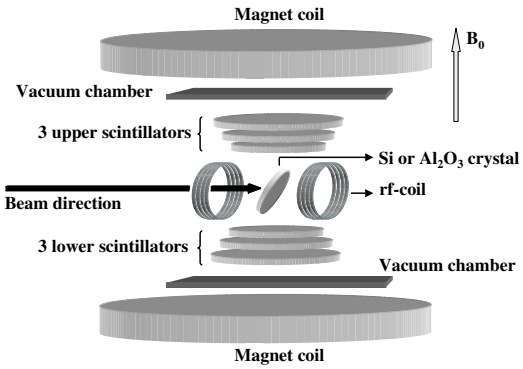

Figure 1: A schematic overview of the β-NMR/β-NQR set-up.

(θ=0°) or perpendicular (θ=90°) to the direction of B_0. For the 90° orientation, the quadrupole splitting is about two times smaller than for the 0° direction which implies that a double quadrupole moment window can be scanned with the same frequency settings.

Table I: Overview of the transition frequencies between the m-states in ^{31}Al.

Transition	$\theta = 0°$	$\theta = 90°$
$-5/2 \leftrightarrow -3/2$	$\nu_1 = \nu_L + \frac{3}{10}\nu_Q$	$\nu_1 = \nu_L - \frac{3}{20}\nu_Q + \frac{9}{1600}\left(\frac{\nu_Q^2}{\nu_L}\right)$
$-3/2 \leftrightarrow -1/2$	$\nu_2 = \nu_L + \frac{3}{20}\nu_Q$	$\nu_2 = \nu_L - \frac{3}{40}\nu_Q + \frac{9}{1280}\left(\frac{\nu_Q^2}{\nu_L}\right)$
$-1/2 \leftrightarrow 1/2$	$\nu_3 = \nu_L$	$\nu_3 = \nu_L + \frac{9}{800}\left(\frac{\nu_Q^2}{\nu_L}\right)$
$1/2 \leftrightarrow 3/2$	$\nu_4 = \nu_L - \frac{3}{20}\nu_Q$	$\nu_4 = \nu_L + \frac{3}{40}\nu_Q - \frac{9}{1280}\left(\frac{\nu_Q^2}{\nu_L}\right)$
$3/2 \leftrightarrow 5/2$	$\nu_5 = \nu_L - \frac{3}{10}\nu_Q$	$\nu_5 = \nu_L + \frac{3}{20}\nu_Q - \frac{9}{1600}\left(\frac{\nu_Q^2}{\nu_L}\right)$

When a single rf-frequency (for β-NMR) or a correlated set of frequencies (for β-NQR) are applied such that they correspond to the frequency difference between two adjacent m-states, the polarization is destroyed or reversed. This can be observed as a change in the β-decay asymmetry. The latter quantity is defined as

$$\text{Asymmetry} = \frac{N_{up} - N_{down}}{N_{up} + N_{down}} \simeq \frac{v}{c} A_\beta P \qquad (2)$$

N_{up} is the number of coincident counts detected by the upper set of detectors, while N_{down} is the number of coincident counts recorded in the lower scintillators. A_β is the asymmetry parameter and depends on the β-decay properties of the nucleus under

consideration. P is the initial polarization of the implanted ensemble, induced by the nuclear reaction.

Two techniques are commonly used: the continuous rf technique (CRF) [31, 32] and the adiabatic fast passage method (AFP) [18, 23]. Both are based on the principle of β-NMR [30]. In the CRF technique, the spin polarization is resonantly destroyed by mixing the m quantum states with a rf-field while the AFP method requires a pulsed production and rf system in order to reverse the population of the m-states. This letter describes and compares both techniques which have been applied in the same experimental conditions for the first time.

In the CRF method, ^{31}Al nuclei are continuously implanted in the stopper crystal which is exposed to one (β-NMR) or several correlated (β-NQR) rf-frequencies. At the same time, the asymmetry of the β-decay is measured. When the applied frequency (set) covers the Larmor frequency (β-NMR) or the quadrupole coupling constant (β-NQR), all m-states are equally populated. The polarization is destroyed and a resonance is observed when the β-asymmetry is plotted as a function of the rf-frequency. The resonance amplitude is proportional to the initial polarization P of the implanted ensemble.

A broad rf-region is scanned in discrete steps. In order to cover a large frequency range in one step, frequency modulation is used. In the case of β-NQR and for each value of ν_Q, all transition frequencies ν_i (Table I) are applied simultaneously and modulated over 55% of the frequency step between two subsequent values. Typically, one set of frequencies is applied during several seconds (up to minutes). After going through all frequency steps and before starting the next scan, data without rf are taken as a reference. The process is repeated for 30 minutes up to several hours until sufficient statistics are collected.

The AFP method uses a pulsed beam which is implanted in the crystal during the time 'beam on' as outlined in Fig. 2. When the beam is switched off, a single rf-frequency (β-NMR) or a set of correlated frequencies (β-NQR) is applied for a few ms (rf-time) and swept over a certain rf-range around a central value. If the sweep range, the rf-field strength and the rf-time are chosen properly, the AFP-condition is fulfilled and the population of the m-states is reversed [30]. After the rf pulse sequence, the β-counting is started, typically for one lifetime. The AFP-cycle is concluded with the same rf-sequence in order to restore the original direction of the polarization. The different β-NQR frequencies are not applied simultaneously as in the CRF-method but according to a sequence (Fig. 2).

The duty cycle of the AFP-method is in most cases slightly below 50%, compared to 100% in the CRF technique. The resonance amplitude however is proportional to $2P$ (from $+P$ to -P) when the AFP-condition is exactly met. Because the sensitivity of the method is proportional to the asymmetry change squared, the AFP-method can be up to two times more efficient than the CRF technique.

In order to prove that the measured quadrupole coupling constants are independent of the experimental conditions, both methods were applied using a different magnetic field and a different crystal orientation. The continuous rf β-NMR and β-NQR were performed in an external field of 0.25 T. The measuring time per frequency was 10 s. For the β-NQR measurement, the c-axis of the Al_2O_3 crystal was oriented parallel to the direction of B_0. The corresponding transition frequencies are given in the middle column of Table I. All AFP measurements were performed with B_0=0.5 T and θ was put to 90°. The transition frequencies are shown in the last column of Table I.

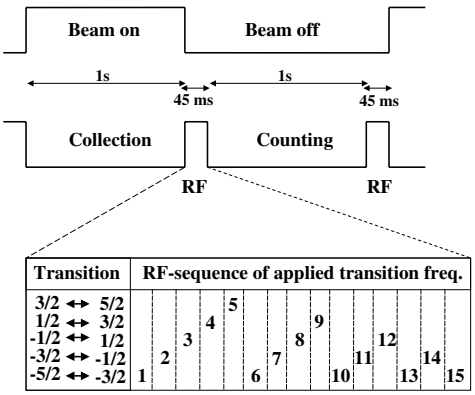

Figure 2: Structure of one AFP β-NQR cycle. A zoom is made of one rf-on period. It shows the order in which all five transition frequencies in ^{31}Al are applied.

III. RESULTS

In order to implement a successful β-NQR experiment on the ^{31}Al ground state, a precise knowledge of the Larmor frequency ν_L is required. Therefore, a β-NMR measurement (Al implanted in Si) was performed prior to each β-NQR-measurement. The results are shown in Fig. 3. The upper panel shows the continuous rf β-NMR with a frequency modulation of 1.2 kHz. Using a fitting function that includes the Lorentzian line shape and the frequency modulation resulted in $\nu_L = 2909.3(2)$ kHz. Other fit parameters were the position of the baseline, the FWHM of the curve and the amplitude (proportional to the polarization).

The lower panel of Fig. 3 displays the AFP result, obtained with 1.54 kHz frequency modulation. The same fitting procedure was applied and a Larmor frequency $\nu_L = 5820.2(3)$ kHz was found.

The slightly better relative accuracy obtained with the AFP-method, stems from the fact that the relative frequency modulation was a little smaller compared to the one applied in the continuous rf β-NMR, resulting in a narrower resonance and a more precise value of ν_L. An absolute field calibration was not performed in this experiment as the β-NQR transition frequencies ν_i (see Table I) do not directly depend on the magnetic field but only on the Larmor frequency and the unknown quadrupole coupling constant. Consequently, no magnetic moments were deduced.

The spectroscopic quadrupole moment of the ^{31}Al ground state was initially measured with the continuous rf method. Starting from a broad scan, covering a wide range of $|Q|$ and using a large frequency modulation (81.5 kHz), a resonance was found at ν_Q=2218(75) kHz (Fig. 4a). In the subsequent β-NQR, a zoom of the frequency region was made around the earlier observed resonance (Fig. 4b), applying a frequency modulation of 40.7 kHz. ν_Q=2188(25) kHz was obtained. The continuous rf results were confirmed by a measurement using the adiabatic fast passage technique with a

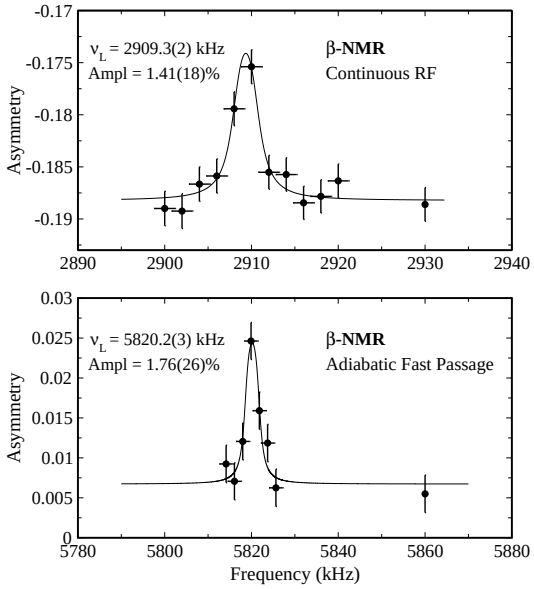

Figure 3: β-NMR resonances obtained with the continuous rf technique (upper panel) and the AFP method (lower panel).

modulation of 75.5 kHz, resulting in ν_Q=2215(47) kHz (Fig. 4c). The weighted mean of the three ν_Q's is calculated to be $\overline{\nu}_Q\left(^{31}\mathrm{Al}\right)$=2196(21) kHz. Since the quadrupole coupling constant of stable ^{27}Al was also determined in an α-Al_2O_3 crystal at room temperature, its value can be directly compared to $\overline{\nu}_Q\left(^{31}\mathrm{Al}\right)$. Using the known values $|Q(^{27}\mathrm{Al})| = 146.6(10)$ mb [33] and $\nu_Q(^{27}\mathrm{Al}) = 2402.5(17)$ kHz [34], the quadrupole moment of the ^{31}Al ground state can be calculated as follows:

$$|Q\left(^{31}\mathrm{Al}\right)| = \frac{|Q\left(^{27}\mathrm{Al}\right)|\,\overline{\nu}_Q\left(^{31}\mathrm{Al}\right)}{\nu_Q\left(^{27}\mathrm{Al}\right)} \tag{3}$$

$|Q(^{31}\mathrm{Al})| = 134.0(16)$ mb is obtained. This result is more than one order of magnitude more precise and in agreement with the earlier measured quadrupole moment of ^{31}Al (112(32) mb [24]).

A comparison of the β-NMR amplitudes given in Fig. 3 shows no large difference between the AFP-resonance and the continuous rf result. Within the errors, both amplitudes are the same. Also for the β-NQR measurements (indicated in Fig. 4) no clear difference in amplitude exists. The expected double effect has not been observed since the AFP-technique was not optimized and, as a consequence, the exact AFP-condition was never reached.

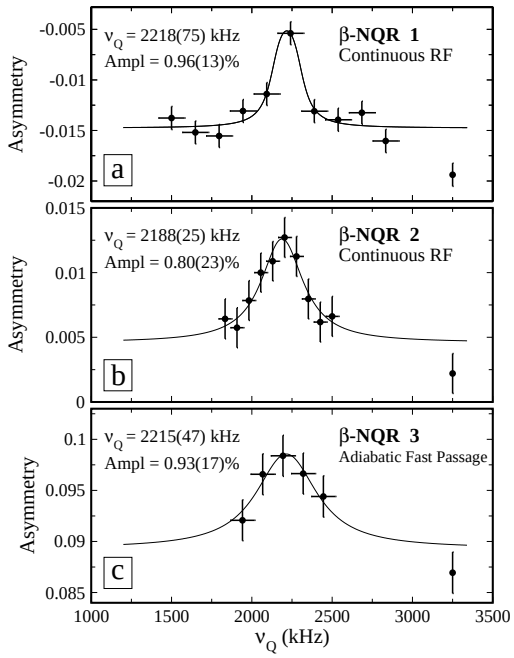

Figure 4: β-NQR resonances obtained with the continuous rf technique (a and b) and the AFP method (c).

IV. DISCUSSION

Recently, the proton core polarization charges and the electric quadrupole moments of the neutron-rich Al isotopes have been investigated in the microscopic particle-vibration coupling (PVC) model [35]. The single particle wave functions used in this model are obtained from solving the Skyrme Hartee-Fock-Bogoliubov equation self-consistently while the phonon energies are deduced from the quasiparticle-random-phase approximation. The ^{31}Al quadrupole moment was calculated for two different values of the Landau-Migdal (LM) interaction strength, resulting in $Q_{PVC}(^{31}\mathrm{Al}) = 136$ mb and 139 mb, in excellent agreement with our experimental value. By comparing the calculated single particle quadrupole moment (without coupling to E2-excitations) with the quadrupole moment calculated in the PVC model, the authors deduced a proton core polarization charge of $1.03e$ and $1.08e$ for ^{31}Al, depending on the LM interaction strength used.

In this letter, the ^{31}Al quadrupole moment is interpreted in the framework of two large-scale shell-model approaches. ANTOINE calculations [36] are performed with the sdpf residual interaction [37] and the Monte Carlo Shell Model (MCSM) [38, 39] is used with the SDPF-M interaction [40]. Both models are very efficient in

outlining the nuclear properties of isotopes that belong to the island of inversion. For the odd-mass neutron-rich Al-isotopes, four different calculations are made and presented in Fig. 5. Three of them are ANTOINE calculations: one with all neutrons confined to the sd-shell (0p-0h, squares), one with two neutrons forced into the $f_{7/2}p_{3/2}$ orbitals (2p-2h, triangles) and one without truncations in the $\nu(sdf_{7/2}p_{3/2})$ model space (free sdpf, diamonds). The fourth dataset is a MCSM calculation using the SDPF-M interaction in the $\nu(sdf_{7/2}p_{3/2})$ valence space (free SDPF-M, stars). In the ANTOINE calculations, protons are restricted to the sd-shell while the MCSM imposes no restrictions on the proton space. All calculations are performed using the standard effective charges $e_p = 1.3e$ and $e_n = 0.5e$ [41]. The experimental data (dots) are taken from this work and from Ref. [33].

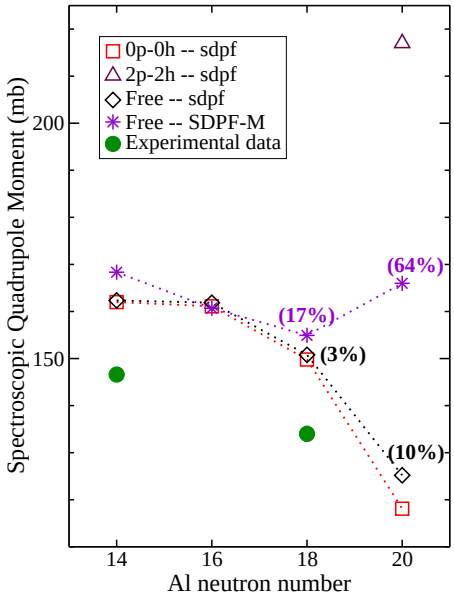

Figure 5: (Color online) An overview of the calculated and the measured quadrupole moments of the neutron-rich odd-mass Al ground-states (I=5/2$^+$). All calculations were made using **the effective charges $\mathbf{e_p = 1.3e}$ and $\mathbf{e_n = 0.5e}$**. The contribution of intruders configurations in the ground state is given between brackets (if different from zero).

For $^{27-31}$Al, 0p-0h calculations and calculations in the untruncated model space predict similar quadrupole moments. No intruder configurations are present in the ground states of $^{27-29}$Al while a minor contribution (see Fig. 5) is predicted for ^{31}Al. The theoretical Q-moments reproduce the observed trend but theory overestimates all experimental values by about 15%.

As the quadrupole moments of the odd-mass Al-isotopes are dominated by the odd $d_{5/2}$ proton hole, the proton effective charge has been rescaled to $e_p = 1.1e$ in order to obtain a quantitative agreement with the experimental value of ^{27}Al. Fig. 6 gives an overview of the experimental and rescaled theoretical Q-moments of $^{27-33}$Al, adopting the same color code as in Fig. 5.

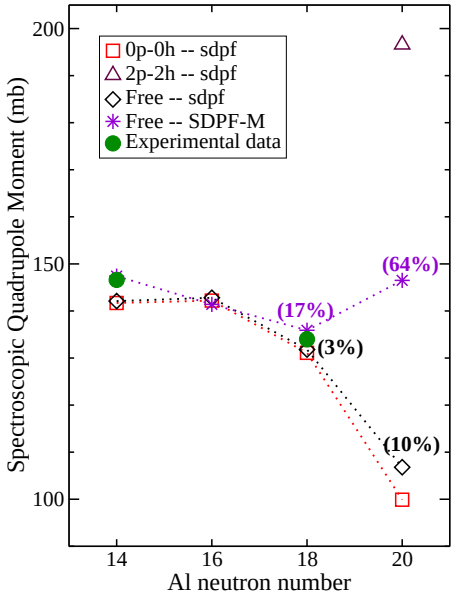

Figure 6: (Color online) An overview of the calculated and the measured quadrupole moments of the neutron-rich odd-mass Al ground-states (I=5/2$^+$). All calculations were made using **the effective charges 1.1e and 0.5e** for protons and neutrons respectively.

All theoretical predictions for ^{31}Al (N=18), calculated with the reduced effective proton charge, show a good agreement with the experimental value. Pure neutron sd-calculations as well as calculations in the untruncated model space can explain the observed Q-moment. This indicates that the ^{31}Al ground state is dominated by normal sd-configurations with a possible small admixture of intruder states.
For ^{33}Al (N=20), free ANTOINE and MCSM calculations predict an amount of 10% and 64% respectively of intruder configurations in the ground state, leading to an enhanced quadrupole moment compared to what is suggested by 0p-0h calculations. In case ^{33}Al has a pure sd ground-state configuration, a strong decrease of the quadrupole moment with respect to the ^{31}Al value should be observed, as expected for a 'normal' closed-shell nucleus. However, a recent report on the g-factor of ^{33}Al suggests a non-negligible contribution of neutron excitations across N=20 in the

ground state [19]. A measurement of the ^{33}Al quadrupole moment will therefore provide decisive information about the structure of the Al isotopes at the N=20 shell closure.

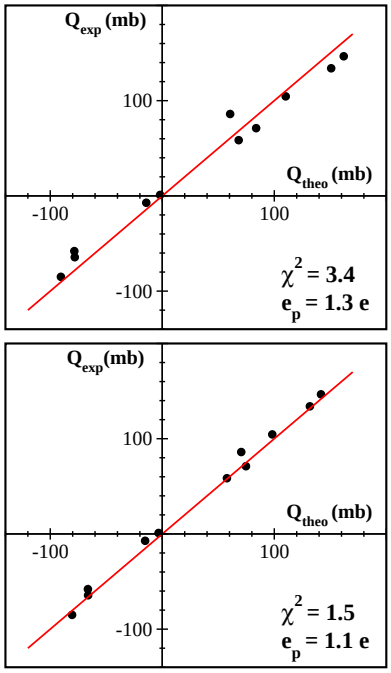

Figure 7: Known quadrupole moments of πsd-shell nuclei with odd Z and even N. The theoretical values are obtained using the sdpf residual interaction with the protons restricted to the sd-shell and the neutrons allowed in the $\mathrm{sdf_{7/2}p_{3/2}}$ space. Scattering around $Q_{exp} = Q_{theo}$ is studied. In the upper panel, Q_{theo} is calculated with $e_p = 1.3e$ while the lower panel shows Q_{theo} values determined with $e_p = 1.1e$. The experimental errors are smaller than the symbol size.

The use of the reduced effective proton charge $e_p = 1.1e$ to describe the odd-mass Al quadrupole moments can be justified in the framework of the full πsd shell. The standard effective charges $e_p = 1.3e$ and $e_n = 0.5e$ were established in 1988 by Brown and Wildenthal [41] based on a comparison of shell-model calculations with the experimental E2 γ-decay transition matrix elements and the not very precise static quadrupole moments known at that time. Since then, nine new and/or more precise static quadrupole moments of odd-Z even-N πsd-shell nuclei became available, including the present result for ^{31}Al. Isotopes with an odd proton and an even neutron number are excellent probes to define the proton effective charge used in the πsd-shell as their quadrupole moments are mainly determined by proton configurations.

In Fig. 7, each odd-Z even-N πsd-isotope for which the ground-state quadrupole moment is measured, is represented by a data point with Q_{theo} as X-coordinate and Q_{exp} as Y-coordinate. All data scatter around the $Q_{exp} = Q_{theo}$ line. In the upper panel, the quadrupole moments are calculated using the ANTOINE sdpf residual interaction with protons in the sd shell and neutrons in the $\mathrm{sdf_{7/2}p_{3/2}}$ orbits using the standard effective charges $e_p = 1.3e$ and $e_n = 0.5e$. A rather large reduced χ^2-value of 3.4 is found with respect to the $Q_{exp} = Q_{theo}$ curve. In the lower panel, Q_{theo} is determined using the reduced effective proton charge $e_p = 1.1e$. A much better agreement between experiment and theory ($\chi^2_{red} = 1.5$) is observed. The experimental data are taken from this work and from Refs. [42, 43].
Thus, based on a compilation of recent and remeasured quadrupole moments for odd-Z even-N πsd isotopes, it can be concluded that $e_p = 1.1e$ is a more realistic effective proton charge for the sd-shell than the previously adopted value $1.3e$. This conclusion offers a strong argument to justify the use of the effective proton charge $1.1e$ in the discussion of the ^{31}Al quadrupole moment.

V. SUMMARY

In conclusion, the electric quadrupole coupling constant of ^{31}Al, produced in a projectile-fragmentation reaction, was measured using two Nuclear Quadrupole Resonance techniques, one based on a continuous rf-signal, the other on a pulsed sequence. The measured values are in good agreement with each other, leading to a mean value of ν_Q=2196(21) kHz. From this, the quadrupole moment of ^{31}Al could be extracted: $\left|Q(^{31}\mathrm{Al})\right| = 134.0(16)$ mb.
The precise value of $|Q(^{31}\mathrm{Al})|$ together with other experimental quadrupole moments of odd-Z even-N sd-nuclei were used to determine the proton effective charge in the πsd-shell. Calculations performed with $e_p = 1.1e$ result in a better agreement with experiment than calculations using the standard effective proton charge $e_p = 1.3e$.
Comparison with shell-model calculations using the sdpf and SDPF-M residual interactions shows that the ground state of ^{31}Al is dominated by normal sd-shell configurations with a possible small admixture of neutron 2p-2h states. This points to a gradual transition from the deformed Mg isotopes to the normal Si ground states. A measurement of $Q(^{33}\mathrm{Al})$ would add important information to the study of the nuclear structure of the odd-mass Al-isotopes at the border of the island of inversion. The accurate value of $|Q(^{31}\mathrm{Al})|$, obtained in this work, will contribute to a correct interpretation of that new result.

We are grateful to the GANIL staff for the technical support and to Dr. E. Yagi for the useful help and advice with the X-ray diffraction analysis of the α-Al_2O_3 sample. This work has been financed by the European Community FP6 - Structuring the ERA - Integrated Infrastructure Initiative contract EURONS No. RII3-CT-2004-506065, by the FWO-Vlaanderen and by the IAP-programme of the Belgium Science Policy under grand number P6/23.

[1] C. Thibault *et. al.*, Phys. Rev. C **12**, 644 (1975)
[2] X. Campi *et. al.*, Nucl. Phys. A **251**, 193 (1975)
[3] C. Détraz *et. al.*, Phys. Rev. C **19**, 164 (1979)
[4] D. Guillemaud-Mueller *et. al.*, Nucl. Phys. A **426**, 37 (1984)
[5] B.V. Pritychenko *et. al.*, Phys. Lett. B **461**, 322 (1999)
[6] H. Iwasaki *et. al.*, Phys. Lett. B **620**, 118 (2005)
[7] M. Keim, AIP Conf. Proc. **455**, 50 (1998)
[8] M. Keim *et. al.*, Eur. Phys. J. A **8**, 31 (2000)
[9] V. Tripathi *et. al.*, Phys. Rev. Lett. **94**, 162501 (2005)
[10] T. Motobayashi *et. al.*, Phys. Lett. B **346**, 9 (1995)
[11] G. Neyens *et. al.*, Phys. Rev. Lett. **94**, 022501 (2005)
[12] O. Sorlin and M.-G. Porquet, Prog. Part. Nucl. Phys. **61**, 602 (2008)
[13] A. Watt *et. al.*, J. Phys. G **7**, L145 (1981)
[14] A. Poves and J. Retamosa, Phys. Lett. B **184**, 311 (1987)
[15] E. Caurier *et. al.*, Phys. Rev. C **58**, 2033 (1998)
[16] Y. Utsuno *et. al.*, Phys. Rev. C **60**, 054315 (1999)
[17] D. Borremans *et. al.*, Phys. Lett. B **537**, 45 (2002)
[18] H. Ueno *et. al.*, Phys. Lett. B **615**, 186 (2005)
[19] P. Himpe *et. al.*, Phys. Lett. B **643**, 257 (2006)
[20] P. Himpe *et. al.*, Phys. Lett. B **658**, 203 (2008)
[21] W. Mittig *et. al.*, Eur. Phys. J. A **15**, 157 (2002)
[22] B.V. Pritychenko *et. al.*, Phys. Rev. C **63**, 047308 (2001)
[23] D. Kameda *et. al.*, Phys. Lett. B **647**, 93 (2007)
[24] D. Nagae *et. al.*, Phys. Rev. C **79**, 027301 (2009)
[25] R. Anne *et. al.*, Nucl. Instr. Methods A **257**, 215 (1987)
[26] R. Anne *et. al.*, Nucl. Instr. Methods B **70**, 276 (1992)
[27] K. Asahi *et. al.*, Phys. Lett. B **251**, 488 (1990)
[28] R.L. Mieher , Phys. Rev. Lett. **4**, 57 (1960)
[29] A.P.M. Kentgens *et. al.*, Solid State Nucl. Magn. Reson. **3**, 315 (1994)
[30] A. Abragam, The Principles of Nuclear Magnetism, Clarendon, Oxford (1961)
[31] E. Arnold *et. al.*, Phys. Lett. B **197**, 311 (1987)
[32] D. Borremans *et. al.*, Phys. Rev. C **72**, 044309 (2005)
[33] V. Kellö *et. al.*, Chem. Phys. Lett. **304**, 414 (1999)
[34] B. Filsinger *et. al.*, J. Magn. Res. **125**, 280 (1997)
[35] K. Yoshida, http://arxiv.org/abs/0902.3054v1
[36] E. Caurier, F. Nowacki, Acta Phys. Pol. **30**, 705 (1999)
[37] S. Nummela *et. al.*, Phys. Rev. C **63**, 044316 (2001)
[38] M. Honma *et. al.*, Phys. Rev. Lett. **75**, 1284 (1995)
[39] T. Mizusaki *et. al.*, Phys. Rev. C **53**, 2786 (1996)
[40] Y. Utsuno *et. al.*, Phys. Rev. C **70**, 044307 (2004)
[41] B.A. Brown *et. al.*, Ann. Rev. Nucl. Part. Sci. **38**, 29 (1988)
[42] K. Matsuta *et. al.*, J. Phys. Conf. Ser. **20**, 169 (2005)
[43] N.J. Stone, Atomic Data and Nuclear Data Tables **90**, 75 (2005)

Chapter 6

g-factor of ^{44}Cl

In December 2007, at the start of the Cl campaign in GANIL, the ground-state g-factor of ^{44}Cl was measured. This experiment was the first in a series of three, aiming to determine the g-factors of the neutron-rich $^{41-45}$Cl isotopes using the β-NMR technique on a spin-polarized fragment beam. The g-factor study is intended to reveal the $3/2^+$ to $1/2^+$ spin change in the odd-mass Cl isotopes and to probe the increasing importance of neutron excitations across the $N = 28$ shell gap. A detailed study of the physics near $N = 28$ is presented in the first section. Section 6.2 describes the preliminary results of the β-NMR measurements on ^{41}Cl, ^{42}Cl and ^{43}Cl while the g-factor measurement on ^{44}Cl is discussed in the Physical Review C article, included at the end of this chapter.

6.1 The neutron-rich Cl isotopes: physics case

Changes in the shell-structure are encountered when studying nuclei with increasing N/Z ratio. An excellent example is found in the neutron-rich $N \simeq 28$ $\pi(sd)$-shell nuclei. In these isotopes, two structural effects play a major role.

- **Reduction of the energy spacing between the $\pi(\mathbf{1d_{5/2}}, \mathbf{2s_{1/2}}, \mathbf{1d_{3/2}})$ levels and near degeneracy of the $\pi(\mathbf{2s_{1/2}})$ and the $\pi(\mathbf{1d_{3/2}})$ effective single particle states**
  The monopole component of the residual interaction between the $\pi(1d_{3/2})$ and the $\nu(1f_{7/2})$ orbits is strongly attractive, as introduced in section 1.3 and discussed in more detail by Otsuka *et al.* and Gade *et al.* in [8, 9, 17]. The attraction results in a lowering of the $\pi(1d_{3/2})$ orbit with respect to the $\pi(2s_{1/2})$ state when neutrons are added to the $\nu(1f_{7/2})$ orbit. At $N \simeq 28$, both proton levels are nearly degenerate. Simultaneously, the $\pi(1d_{5/2})$ state is rising in energy due to the repulsive proton-neutron

force between the $\pi(1d_{5/2})$ and the $\nu(1f_{7/2})$ states. The monopole interaction thus accounts for the decrease of the $\pi(1d_{3/2}) - \pi(2s_{1/2})$ and the $\pi(1d_{3/2}) - \pi(1d_{5/2})$ splittings when the number of neutrons approaches $N = 28$. It must be underlined that it is mainly the tensor force part of the proton-neutron interaction which induces the aforementioned effects. In Fig. 6.1, an illustration is given for the Ca-isotopes.

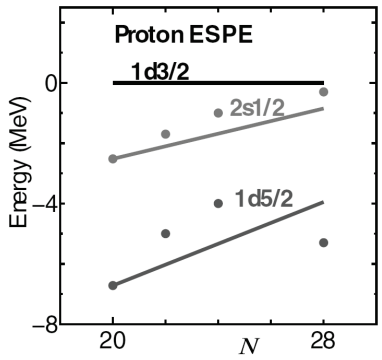

Figure 6.1: Evolution of the $\pi(sd)$ levels in Ca, relative to the $\pi(1d_{3/2})$ state, when adding neutrons to the $\nu(1f_{7/2})$ orbit. The lines show the $\pi + \rho$ tensor force calculations while the points represent the experimental data. The figure was taken from [8].

- **The reduction of the N = 28 shell gap**
  The $N = 28$ shell gap, the first shell closure arising from the spin-orbit coupling, is progressively eroded when moving away from the stability line. This erosion is mainly caused by the proton-neutron interaction and again the tensor component accounts for the largest effect [8]. When taking away protons from the $\pi(1d_{3/2})$ orbit, going from Ca to S, the strong $\pi(1d_{3/2}) - \nu(1f_{7/2})$ attraction weakens. As a consequence, the $\nu(1f_{7/2})$ level is pushed up in energy and the $N = 28$ shell gap, formed with respect to the higher lying $\nu(2p_{3/2})$ orbit, is reduced.
  Also the density dependence of the spin-orbit interaction [99] and the large neutron surface diffuseness in exotic nuclei [100, 101] can induce a smaller $N = 28$ gap. Both effects, however, are strongly model dependent and are expected to be relatively small for the $N \leq 28$ isotopes. The density dependence of the spin-orbit splitting was introduced by relativistic mean field calculations. Theoretically, it was demonstrated that the magnitude of the low-j $\nu(2p_{3/2}) - \nu(2p_{1/2})$ spin-orbit splitting depends sensitively on the proton density near the center of the nucleus and in

particular on the occupation of the $\pi(s_{1/2})$ orbits. For high-j states, such as the $\nu(1f_{7/2})$ and the $\nu(1f_{5/2})$ levels, the collapse of the spin-orbit splitting is associated with the development of a diffuse neutron-rich surface. Since the spin-orbit potential contains a surface-peaked radial derivative of the nuclear potential (see Eq. 1.4), its strength will be reduced for nuclei near the neutron drip line.

The reduction of the $Z = 16$ and $N = 28$ (sub) shell gaps plays an important role in the structure of the neutron-rich nuclei from Si ($Z = 14$) to K ($Z = 19$). For these isotopes, configuration mixing, shape coexistence and nuclear deformation have been observed. Below, the structural highlights happening in the isotopic chains of $_{20}$Ca, $_{19}$K, $_{18}$Ar, $_{17}$Cl, $_{16}$S, $_{15}$P and $_{14}$Si are presented.

6.1.1 The neutron-rich Ca isotopes ($Z = 20$)

To a large extent, the neutron-rich Ca isotopes respect the shell closures at $N = 20$ and $N = 28$. Evidence for this is found in e.g. the systematics of the first 2^+ energies in the even-even nuclei. As shown in Fig. 6.2, high $E(2_1^+)$ values, characteristic for magic nuclei, have been observed for ^{40}Ca and ^{48}Ca. The experimental data presented in Fig. 6.2 are taken from the compilation [102]. In addition, also the weak $B(E2; 0_1^+ \rightarrow 2_1^+)$ values at $N = 20, 28$ and the sharp drop of the one-neutron separation energies at $N = 21, 29$ confirm the doubly magic nature of ^{40}Ca and ^{48}Ca.

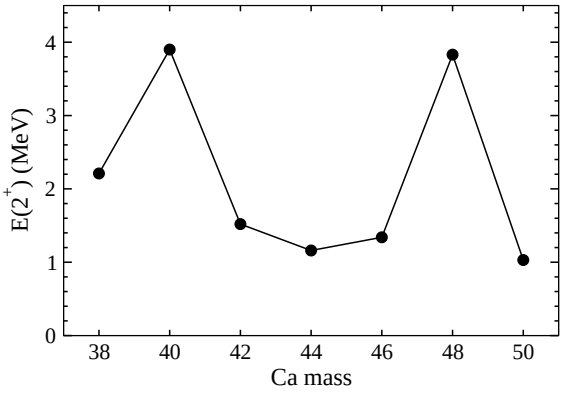

Figure 6.2: Energies of the first 2^+ state in the even-even Ca isotopes ($Z = 20$).

From the difference in binding energy of the last neutron in $^{48}Ca_{28}$ and $^{49}Ca_{29}$ [61], the $N = 28$ shell gap between the $f_{7/2}$ and $p_{3/2}$ orbits is estimated to be 4.8 MeV. As mentioned later, this $N = 28$ energy gap decreases by 330(80) keV when going from Ca to Ar ($Z = 18$), illustrating that below Ca changes in the shell structure are expected.

6.1.2 The neutron-rich K isotopes ($Z = 19$)

In the 1960's and 1970's, a large set of transfer-reaction experiments (e.g. [103–106]) revealed a $3/2^+$ to $1/2^+$ ground-state spin flip at $N = 28$ in the K isotopes. The energy difference between the $1/2^+$ and $3/2^+$ states is shown in Fig. 6.3, the negative value obtained for ^{47}K indicates the reversed order of both levels. The outcome of the ^{40,42,44,48}Ca(d, ^{3}He) one-proton pickup reactions [105, 106] is summarized in Table 6.1, providing the energies and the spectroscopic factors[A] (SF) of the $3/2^+$ and $1/2^+$ states in ^{39,41,43,47}K. As can be seen in Table 6.1, the ground states of ^{39,41,43}K and the first excited state of ^{47}K carry about the full $\pi(d_{3/2})$ strength. The strength of the $\pi(s_{1/2})$ state is divided among two or three levels per isotope but the lowest level always exhibits the largest spectroscopic factor. This implies that the first excited states of ^{39,41,43}K and the ground state of ^{47}K have a strong single-particle $\pi(s_{1/2})$ nature. However, configurations arising from the coupling of the $3/2^+$ state with the 2^+ excitation of the core also contribute to the $1/2^+$ state, especially for ^{41}K$_{22}$ where a strong fragmentation of the $\pi(s_{1/2})$ strength has been observed.

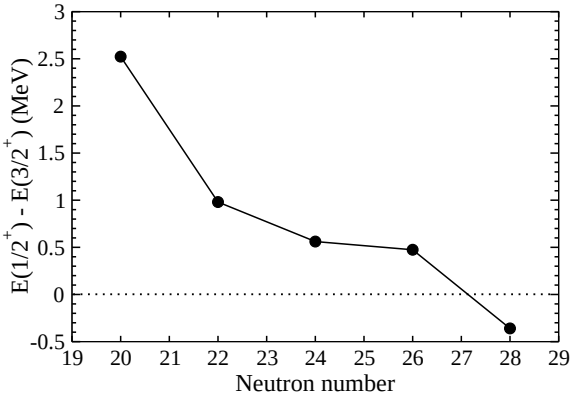

Figure 6.3: Energy difference between the $1/2^+$ and $3/2^+$ states in the odd-mass K isotopes ($Z = 19$). The negative value obtained for ^{47}K indicates the reversed order of both levels. The experimental data are taken from [107–111].

The (d, ^{3}He) transfer reactions on the neutron-rich K isotopes mentioned above reveal the reduced energy spacing of the two proton orbits $\pi(s_{1/2})$ and $\pi(d_{3/2})$ when approaching $N = 28$. The splitting vanishes completely for ^{47}K. This conclusion was confirmed by measuring the ground-state spins, magnetic moments and mean square charge radii of $^{39,41-47}$K using optical laser spectroscopy [112].

[A] The spectroscopic factor is a measure of the occupation number of the (single particle) orbit from which the picked-up nucleon originates. It indicates the single-particle nature of a nuclear state.

Table 6.1: Energies, spins, configurations and spectroscopic factors (SF) of the $1/2^+$ and $3/2^+$ states in ^{39,41,43,47}K, obtained from the ^{40,42,44,48}Ca(d, ^{3}He) pick up reactions.

Nucleus	E (MeV)	I^π	l	subshell	SF
^{39}K [105]	0	$3/2^+$	2	$d_{3/2}$	3.70
	2.52	$1/2^+$	0	$s_{1/2}$	1.65
^{41}K [105]	0	$3/2^+$	2	$d_{3/2}$	3.43
	0.98	$1/2^+$	0	$s_{1/2}$	0.77
	1.57	$1/2^+$	0	$s_{1/2}$	0.17
	2.67	$1/2^+$	0	$s_{1/2}$	0.64
^{43}K [105]	0	$3/2^+$	2	$d_{3/2}$	3.15
	0.56	$1/2^+$	0	$s_{1/2}$	1.15
	2.45	$1/2^+$	0	$s_{1/2}$	0.32
^{47}K [106]	0	$1/2^+$	0	$s_{1/2}$	1.55
	0.36	$3/2^+$	2	$d_{3/2}$	4.16
	3.80	$1/2^+$	0	$s_{1/2}$	0.28
	3.88	$3/2^+$	2	$d_{3/2}$	0.70

Interesting information regarding the change of the proton single particle states can also be obtained from $^{46}_{19}K_{27}$, which is one proton hole and one neutron hole away from the doubly magic nucleus ^{48}Ca. The nuclear structure of ^{46}K was studied in the ^{48}Ca(p,^{3}He)^{46}K [113] and ^{48}Ca(d,α)^{46}K [114, 115] reactions, revealing the spins of the ground state and the low-lying excited levels. A comparison of the experimental level schemes of ^{46}K and $^{38}_{17}Cl_{21}$ shows a significant lowering of the 3^- and 4^- states in ^{46}K while the 2^- and 5^- levels remain at about the same excitation energy in both nuclei. As the splitting between the $\pi(s_{1/2})$ and $\pi(d_{3/2})$ orbits is rather large for ^{38}Cl (see further), the 2^-, 3^-, 4^- and 5^- states in ^{38}Cl have wave functions dominated by $\pi(d_{3/2})$ $\nu(f_{7/2})$ configurations. For ^{46}K, the near degeneracy of the $\pi(s_{1/2})$ and $\pi(d_{3/2})$ orbits results in a large admixture of $\pi(s_{1/2})$ $\nu(f_{7/2})$ components in the 3^- and 4^- wave functions. Therefore, both levels are lowered in energy with respect to the 2^- and 5^- levels which remain rather pure $\pi(d_{3/2})$ $\nu(f_{7/2})$ states. Thus, in addition to the energy splitting of the $1/2^+$ and $3/2^+$ states in the odd-mass K isotopes, the level scheme of ^{46}K also probes the relative position of the proton effective single particle orbits.

6.1.3 The neutron-rich Ar isotopes ($Z = 18$)

The Ar isotopes have two proton holes in the $\pi(sd)$ shell, located in the $\pi(d_{3/2})$ orbit according to the single-particle shell model. The $E(2_1^+)$ energies and $B(E2, 0_1^+ \rightarrow 2_1^+)$ values of the even-even Ar isotopes [102] are shown in Fig. 6.4. Although less pronounced as in the Ca isotopes[A], the experimental data exhibit a typical behavior, high $E(2_1^+)$ and low $B(E2, 0_1^+ \rightarrow 2_1^+)$, at the 'magic' numbers $N = 20$ and $N = 28$ [101]. This implies that the $N = 28$ shell closure remains a valid assumption for ^{46}Ar, as mentioned explicitly in [116], even though a partial reduction of the shell gap cannot be excluded.

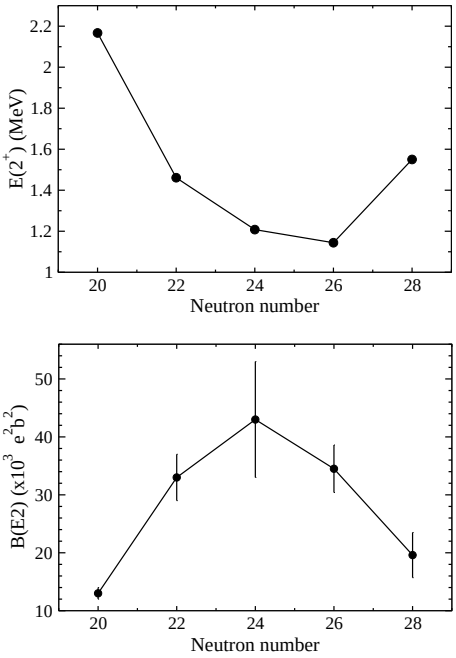

Figure 6.4: $E(2_1^+)$ energies (upper panel) and $B(E2, 0_1^+ \rightarrow 2_1^+)$ values (lower panel) of the even-even Ar isotopes ($Z = 18$). Experimental data are taken from [102]

Relativistic Mean Field (RMF) and Hartree Fock (HF) calculations performed by Werner *et al.* [117] favor oblate quadrupole deformations ($\beta_2 < -0.2$) for the neutron-rich Ar isotopes. The shape of the $^{46}Ar_{28}$ nucleus, however, is model dependent. RMF calculations predict a spherical configuration while an oblate deformation is obtained in HF calculations. The ambiguity among the

[A] Mainly the fact that the Ar isotopes do not have a magic proton number explains the reduced magicity observed for the $E(2_1^+)$ energies at $N = 20$ and $N = 28$ when compared to the Ca isotopes.

different theories and the first experimental results made it impossible in the late 1990's to draw a final conclusion on the $N = 28$ shell-gap in ^{46}Ar. Therefore, a series of high-sensitivity experiments was performed on $^{45-47}Ar_{27-29}$ in the last decade. An overview of the corresponding publications is given below.

The structure of the $^{45-46}$Ar nuclei is investigated through in-beam γ-ray spectroscopy, revealing the extended level schemes of both nuclei [118]. An excellent agreement is observed when comparing the experimental levels with large-scale shell-model calculations, as shown in Fig. 6.5. The latter also indicate that the ^{46}Ar ground-state is dominated by normal $0p-0h$ neutron configurations while the $2p-2h$ components are mainly located in the second and third excited 0^+ states. Furthermore, the positive quadrupole moment calculated for the 2_1^+ level corresponds to the excitation of an oblate ground-state, as proposed by the HF calculations in [117].

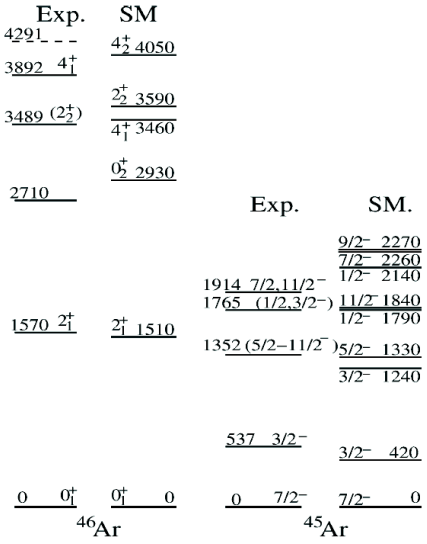

Figure 6.5: Comparison of the experimental $^{45-46}$Ar level schemes with large-scale shell-model calculations. Figure taken from [118].

Information on the ground state of ^{45}Ar is obtained from the study of the ^{9}Be(^{46}Ar, ^{45}Ar+γ)X one-neutron removal reaction in inverse kinematics [119]. The measured partial cross section corresponds to a ground-state spectroscopic factor of 4.9(7). An $l = 3$ ground-state neutron removal is observed as expected for populating a $\nu(f_{7/2})$ hole in the $N = 28$ projectile. This result was later confirmed in an experiment probing the ^{44}Ar$(d,p)^{45}$Ar neutron transfer reaction (see further).

Table 6.2: Wave-function decomposition of the ground state and lowest two excited states in $^{45}_{18}Ar_{27}$. Only configurations larger than 10% are shown.

Energy (keV)	Spin		Wave function
0	$7/2^-$	29%	$(\pi s_{1/2})^2\ (\pi d_{3/2})^2\ (\nu f_{7/2})^7$
		21%	$(\pi s_{1/2})^0\ (\pi d_{3/2})^4\ (\nu f_{7/2})^7$
		13%	$(\pi s_{1/2})^1\ (\pi d_{3/2})^3\ (\nu p_{3/2})^1$
535(5)	$3/2^-_1$	19%	$(\pi s_{1/2})^1\ (\pi d_{3/2})^3\ (\nu f_{7/2})^7$
		22%	$(\pi s_{1/2})^2\ (\pi d_{3/2})^2\ (\nu p_{3/2})^1$
		11%	$(\pi s_{1/2})^0\ (\pi d_{3/2})^4\ (\nu p_{3/2})^1$
1415(10)	$3/2^-_2$	44%	$(\pi s_{1/2})^2\ (\pi d_{3/2})^2\ (\nu p_{3/2})^1$
		15%	$(\pi s_{1/2})^0\ (\pi d_{3/2})^4\ (\nu p_{3/2})^1$
		11%	$(\pi s_{1/2})^2\ (\pi d_{3/2})^2\ (\nu p_{3/2})^2$

Based on the ^{44}Ar$(d,p)^{45}$Ar neutron transfer reaction, the excitation energies, angular momenta and spectroscopic factors of the states populated in $^{45}Ar_{27}$ are studied [120]. The angular momentum of the ^{45}Ar ground state is found to be $l = 3$, whereas the first two excited states have $l = 1$. This is in perfect agreement with the spins and wave functions calculated in the shell-model framework and summarized in Table 6.2. The values quoted in Table 6.2 are taken from [120] and only contributions larger than 10% are shown. The neutron part of the ^{45}Ar ground state ($7/2^-$) peaks at normal $(\nu f_{7/2})^7$ configurations. As the proton $\pi(s_{1/2})$ and $\pi(d_{3/2})$ orbits are quasi degenerate in energy, $(\pi d_{3/2})^2$ as well as $(\pi d_{3/2})^4$ components[A] appear in the ground state. The first excited state ($3/2^-_1$) of ^{45}Ar has a strongly mixed wave function whereas the second excited state ($3/2^-_2$) is dominated by neutron excitations to the $\nu(p_{3/2})$ orbit. The $3/2^-_2$ state at 1.42 MeV corresponds to the first excited level at 2 MeV in ^{47}Ca. Although the ground state of ^{45}Ar is dominated by $(\nu f_{7/2})^7$ configurations, the reduced excitation energy of the $3/2^-_2$ state compared to its analogue level in ^{47}Ca indicates the growing importance of neutron excitations across $N = 28$ when going to lower Z-values.

A direct measure of the $N = 28$ shell gap in $^{46}Ar_{28}$ is obtained from the ^{46}Ar$(d,p)^{47}$Ar transfer reaction [18, 121, 122]. The experimental mass excess gives rise to a $N = 28$ gap of 4.47(9) MeV which is 330(90) keV smaller than

[A] Due to the larger j-value, the pairing energy of two protons in a $d_{3/2}$ orbit is larger than in a $s_{1/2}$ state. As the $\pi(s_{1/2})$ and $\pi(d_{3/2})$ orbits are close together for $N \simeq 28$, the gain in pairing energy exceeds the energy needed to promote two protons to the $\pi(d_{3/2})$ level, giving rise to $(\pi d_{3/2})^4$ components in the ground-state wave function.

in ^{48}Ca. From the analysis of the measured spectroscopic factors and the comparison of the experimental results with shell-model calculations, it is observed that some of the $f_{7/2}$ neutrons in ^{46}Ar have moved to the $p_{3/2}$ orbital. Moreover, it is found that the spin-orbit splitting of the $\nu(f)$ and $\nu(p)$ states is reduced between ^{49}Ca and ^{47}Ar. This effect is accounted for by the proton-neutron tensor interaction for the f states and by the density dependence of the spin-orbit interaction in the interior of the nucleus for the p states. For the $N = 28$ shell gap in particular, a reduction of 10(2)% is registered.

For completeness it must be mentioned that the systematics of the Ar isotopes between the neutron shell-closures $N = 20$ and $N = 28$ has also been studied in experiments probing the nuclear moments and the charge radii [123]. The series of mean square charge radii is characterized by a parabolic trend on top of a linear increase with neutron number and a pronounced 'normal' odd-even staggering effect. Strong correlations are developed at mid-shell ($N \simeq 24$) as a rather large $< r^2 >$ is obtained for ^{42}Ar. This is confirmed for ^{43}Ar$_{25}$ which has a spin $I = 5/2$[A], a ground state dominated by anomalously coupled $(f_{7/2})^5_{5/2}$ configurations and a magnetic moment far off the Schmidt value.

6.1.4 The neutron-rich Cl isotopes ($Z = 17$)

Up to now, no firm ground-state spin and structure assignments have been made for the $^{41-45}$Cl$_{24-28}$ isotopes. A g-factor measurement on these nuclei can therefore reveal decisive information on the reduction of the $N = 28$ shell gap and on the quasi-degeneracy of the $\pi(s_{1/2})$ and $\pi(d_{3/2})$ levels. For a detailed discussion of the performed β-NMR measurements, the reader is referred to section 6.2 and to the Physical Review C article at the end of the chapter. This part only covers a selection of the publications on the neutron-rich Cl-isotopes which appeared in literature so far.

The nuclear structure of the odd-mass Cl isotopes ^{41}Cl$_{24}$, ^{43}Cl$_{26}$ and ^{45}Cl$_{28}$ is to a large extent determined by the odd proton in the $\pi(sd)$ shell. Similar as for the neutron-rich K nuclei, a $3/2^+$ to $1/2^+$ ground-state spin inversion is induced by the decreasing $Z = 16$ energy gap when approaching $N = 28$. The 'normal' $3/2^+$ ground state is determined by configurations having a single proton in the $\pi(d_{3/2})$ orbit while the $1/2^+$ spin-parity originates from an odd $\pi(s_{1/2})$ proton, obtained by promoting one proton to the $\pi(d_{3/2})$ state [B]. Deep inelastic processes suggest that the spin flip happens already at ^{41}Cl [125]. The level structure and the spins of ^{43}Cl and ^{45}Cl, obtained through in-

[A] For the odd-mass Ar isotopes with $20 \leq N \leq 28$ a ground-state spin $I = 7/2$ is expected, originating from the odd neutron in the $\nu(f_{7/2})$ state.

[B] As the pairing is stronger in a larger j-orbit, promoting one proton from the $\pi(s_{1/2})$ to the $\pi(d_{3/2})$ orbit is energetically favored when both levels are close together.

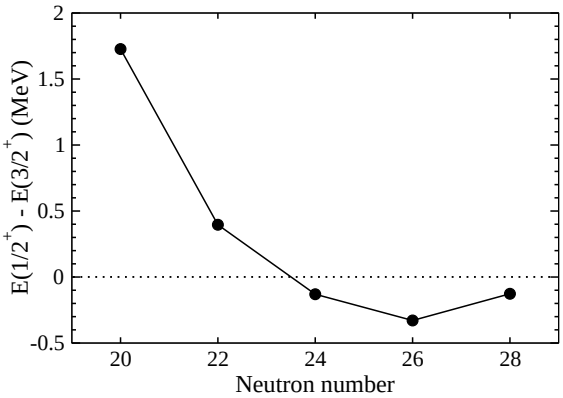

Figure 6.6: Energy difference between the $1/2^+$ and $3/2^+$ states in the odd-mass Cl isotopes ($Z = 17$). The negative value obtained for $^{41-45}$Cl indicates the reversed order of both levels. Experimental data are taken from [17, 107, 124–126].

beam γ-spectroscopy, indicate that both nuclei have a $1/2^+$ ground state [126]. Later, the systematics of the $E(1/2^+) - E(3/2^+)$ level spacing in the odd-mass Cl-isotopes was completed by a measurement of the first excited state in ^{45}Cl, using in-beam γ-spectroscopy following proton removal [17]. The energy difference between the $1/2^+$ and $3/2^+$ states is given in Fig. 6.6. Recall that, although strong arguments support the sequence of the $1/2^+$ and $3/2^+$ energies as presented in Fig. 6.6, the spin-assignments of $^{41}\mathrm{Cl}_{24}$, $^{43}\mathrm{Cl}_{26}$ and $^{45}\mathrm{Cl}_{28}$ are still preliminary.

Taking away protons from the doubly magic ^{48}Ca nucleus, results in a weakening of the $N = 28$ shell closure. Indeed, the short β-decay half life and the small β-delayed neutron-emission probability, measured for ^{45}Cl, indicate collectivity and suggest a rapid vanishing of the $N = 28$ shell strength below ^{48}Ca [127]. Extended mass measurements in the range $A = 29 - 47$ confirm that the neutron-rich Cl, S and P isotopes exhibit changes in the shell structure around $N = 28$. A comparison with shell-model calculations and relativistic mean field theory demonstrates that the observed effects arise from deformed prolate ground-state configurations associated with shape coexistence [128]. Furthermore, the single-neutron knockout reaction ^{9}Be(^{45}Cl, ^{44}Cl)X was used to directly study the ground-state composition of ^{44}Cl and ^{45}Cl [129]. The measured momentum distribution of the residual ^{44}Cl after direct population of the ground state is consistent with the removal of a $l = 1$ neutron. This implies that $p_{3/2}$ neutrons from above the $N = 28$ shell closure play an important role in the ground states of both ^{44}Cl and ^{45}Cl.

6.1.5 The neutron-rich S isotopes ($Z = 16$)

In the 1990's, the S-isotopes around $^{44}S_{28}$ provided the first evidence for the region of deformation being discussed in this literature study. The first indication was found in the experimental work performed by Sorlin *et al.*, demonstrating that the experimentally observed half life and neutron-emission probability of ^{44}S can only be obtained when assuming that the ground state is not spherical but oblate deformed [127]. Self-consistent mean field calculations strengthen this hypothesis. According to RMF calculations, ^{44}S has a well-deformed prolate ground state whereas in the HF model, ^{44}S is a γ-soft system with a small positive quadrupole deformation. In both models, however, an oblate configuration is nearly degenerate [117, 130]. Other theoretical studies also predict deformation and shape coexistence in the neutron-rich S isotopes. Shell model calculations for instance [131] give large negative spectroscopic quadrupole moments and large $B(E2)$ values for $^{40-42}$S. The quadrupole moments lead to deformation parameters which are consistent with the ones found in [117, 130]. Relativistic Hartree-Bogoliubov calculations result in an oblate ground state for ^{44}S, nearly degenerate with a prolate state at 30 keV, illustrating once more the expected shape-coexistence in the $N = 28$ nucleus [132].

Also experimentally, many efforts have been made to probe the changes in the shell structure around ^{44}S. An overview of the most important results is given below.

- Coulomb-excitation measurements on the even-even S isotopes revealed the systematics of the 2_1^+ energies and $B(E2, 0_1^+ \rightarrow 2_1^+)$ values shown in Fig. 6.7. As can be observed from Fig. 6.7, $^{36}S_{20}$ has a very high lying first 2^+ state (comparable to $E(2_1^+)$ in ^{48}Ca) and a low $B(E2)$ value, indicating that both $Z = 16$ and $N = 20$ are closed shells. Scheit *et al.* performed Coulomb-excitation experiments on $^{38}S_{22}$, $^{40}S_{24}$ and $^{42}S_{26}$ [116]. The obtained results are in agreement with the predictions of Werner *et al.* [117, 130], pointing to deformation in the ground states of ^{40,42}S and the presence of a new region of deformed nuclei near $N = 28$. The $E(2_1^+)$ and $B(E2, 0_1^+ \rightarrow 2_1^+)$ values of ^{44}S were determined by Glasmacher *et al.* [133], demonstrating that the ^{44}S ground state has a collective nature although the deformation parameter β_2 is smaller than for ^{40,42}S. A comparison with shell-model calculations suggests that the collectivity in ^{44}S has a vibrational origin while ^{40,42}S have static deformations. As can be seen in Fig. 6.7, the low $E(2_1^+)$ and high $B(E2)$ values of $^{44}S_{28}$ confirm the collapse of the $Z = 16$ sub-shell gap and they do not exclude the hypothesized reduction of the $N = 28$ major shell closure [101].

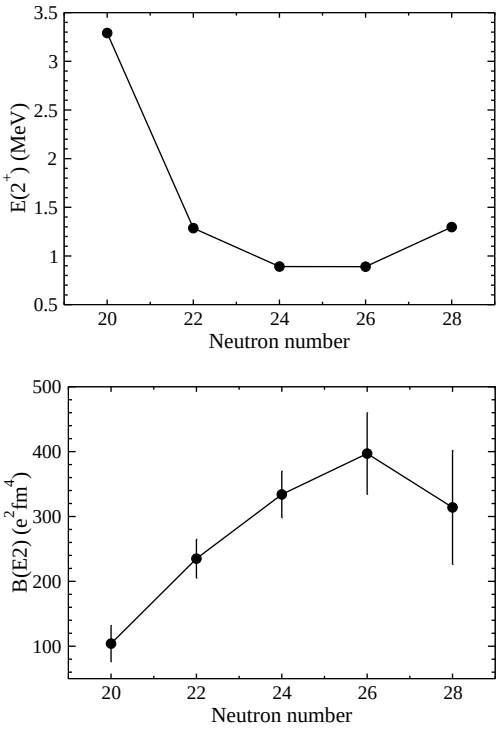

Figure 6.7: $E(2_1^+)$ energies (upper panel) and $B(E2, 0_1^+ \rightarrow 2_1^+)$ values (lower panel) of the even-even S isotopes ($Z = 16$). The experimental data are taken from [102, 116, 133].

The results of the coulomb excitation measurements on the even-odd $^{41}S_{25}$ and $^{43}S_{27}$ isotopes have been compared to particle-rotor and particle-vibrator calculations. The $B(E2)$ value and the low-energy behavior of ^{41}S can be interpreted as rotations of a prolate deformed core. For ^{43}S, a good agreement is observed for all theoretical models. The coulomb-excitation measurement is therefore not able to make the distinction between the deformed and the spherical interpretation [134].

- Decisive information on the structure of the even-even S isotopes has also been obtained from in-beam γ-ray spectroscopy experiments. Using this technique, Sohler *et al.* proposed extended level schemes and spins for the neutron-rich ^{40,42,44}S nuclei. Large-scale shell-model calculations interpret the results as an erosion of the $N = 28$ shell closure at $Z = 16$ and suggest a deformed ground state for ^{40,42}S and a spherical-deformed mixed configuration for ^{44}S [135]. The same conclusions were drawn from the work performed by Azaiez *et al.* [136]. The first experimental evidence of shape coexistence in ^{44}S, however, was obtained from the observation of an isomeric 0_2^+ state (2.3(3) μs) at 1365(1) keV. The presence of such a low-lying 0_2^+ state strongly supports the weakening of the $N = 28$ shell gap [137].

- Further strong evidence for the reduced $N = 28$ shell gap was found by performing a TDPAD experiment on the isomeric state at 320.5(5) keV in ^{43}S [138]. The measured g-factor establishes the first experimental evidence for the $7/2^-$ spin-parity of the isomer and the intruder nature of the ground state ($3/2^-$). An interpretation of these results in the shell-model framework shows that the isomer is dominated by pure $\nu(f7/2)$ configurations while the ground state wave function mainly consists of $\nu(p_{3/2})$ intruder components. This interpretation provides a direct and unambiguous evidence of the collapse of the N=28 shell closure and the coexistence of a deformed ground state and quasi-spherical isomeric state in ^{43}S.

  In addition, single-knockout reactions were used to probe the second $7/2^-$ state at 971 keV in ^{43}S [139]. This level was found to be a rotational excitation of the deformed ground state, confirming the hypothesis of shape coexistence put forward by Gaudefroy *et al* [138]. The authors of [139] also mention that the driving factor behind the deformed $3/2^-$ state becoming the ground state in ^{43}S is the gain in correlation energy when promoting a neutron to the $\nu(p_{3/2})$ state.

6.1.6 The neutron-rich P isotopes ($Z = 15$)

The neutron-rich P isotopes are again excellent test cases to probe the near degeneracy of the $\pi(s_{1/2})$ and $\pi(d_{3/2})$ orbits when approaching $N = 28$. The ground-states of the odd-mass P nuclei are expected to have spin-parity $1/2^+$, in accordance with the last proton occupying the $\pi(s_{1/2})$ state. The first excited state would be a $3/2^+$ level, formed by promoting the odd proton from the $\pi(s_{1/2})$ to the $\pi(d_{3/2})$ state. Several γ-ray spectroscopy [126, 140] and one-proton knockout reactions [141–143] revealed the $E(1/2^+) - E(3/2^+)$ systematics in the P chain and confirmed that the $s_{1/2}$ proton strength is concentrated in the ground state while the $d_{3/2}$ strength is dominating the first excited state. The energy difference between the $1/2^+$ and $3/2^+$ states is given in Fig. 6.8, illustrating that the vanishing of the $Z = 16$ sub-shell gap is very explicit in the P isotopes although no spin inversion has been observed. All conclusions are consistent with shell-model calculations.

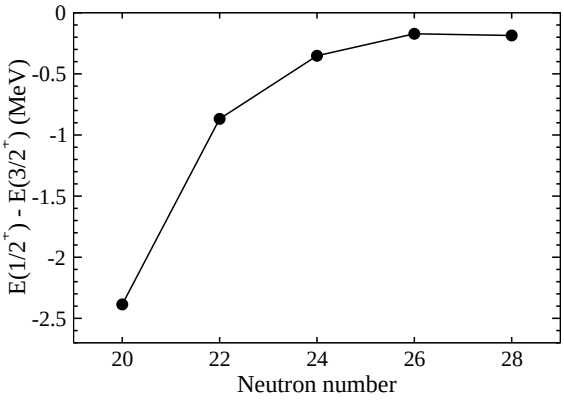

Figure 6.8: Energy difference between the $1/2^+$ ground state and $3/2^+$ first excited state in the odd-mass P isotopes. Experimental data are taken from [124, 126, 140].

Two recent experiments are worth some further attention. The first one, performed by Bastin *et al.* [140], uses in-beam γ-ray spectroscopy to probe the energies of the excited states in ^{41,43}P$_{26,28}$. The presence of excited states around 1 MeV provides additional evidence for the disappearance of the $N = 28$ shell closure, as these levels are believed to be a coupling of the odd proton in the P isotopes to the low 2^+ state in ^{40,42}Si respectively (see later).
The second experiment is a one-proton knockout reaction from ^{44}S, used to study the low-lying excited states in ^{43}P$_{28}$ [143]. The assignment of $l = 2$ to the excited states around 1 MeV is consistent with their interpretation as arising from the removal of a proton from the more deeply bound $d_{5/2}$ proton orbital in ^{44}S.

6.1.7 The neutron-rich Si isotopes ($Z = 14$)

The study of the neutron-rich Si isotopes concentrates on $^{42}Si_{28}$, trying to answer the question whether or not the magic number $N = 28$ holds for very neutron-rich nuclei. The structure of ^{42}Si has always been very controversial. On the one hand, the short β-decay lifetime of ^{40,42}Si [144] and the observation of ^{43}Si being particle-bound [145] point to a strongly (oblate) deformed ground state. Several theoretical approaches, e.g. [117, 130, 132, 146, 147], support this hypothesis. On the other hand, the small two-proton knockout cross section, observed for the ^{44}S$\rightarrow^{42}$Si reaction, favors a magic spherical nucleus with a large $Z = 14$ shell gap [141]. The same authors, however, admit that a reduction of the $N = 28$ and/or $\pi(d_{5/2}) - \pi(d_{3/2})$ gap with 1 MeV would not increase the two-proton knockout cross section significantly [142], making it a rather unsensitive probe to study changes in the shell structure.
Decisive information on the ground-state structure of ^{42}Si was obtained from an in-beam γ-ray spectroscopy measurement, revealing the energy of the first 2^+ state in ^{42}Si [140]. A very low value, $E(2_1^+) = 770(19)$ keV, was found, providing evidence for the disappearance of the $Z = 14$ and $N = 28$ spherical shell closures. In order to obtain a good agreement between shell-model calculations and experiment, the pf shell V^{nn} matrix elements and the $\pi(d_{3/2} - d_{5/2})$ splitting needed a reduction of 300 keV and 1.94 MeV respectively. A comparison with shell-model calculations also indicated that ^{42}Si is best described as a well-deformed oblate rotor. Earlier, the low $E(2_1^+)$ observed for ^{40}Si was also interpreted in the framework of a reduced $N = 28$ shell gap [148]. Figure 6.9 presents the systematics of the experimental 2^+ states in the Si isotopes and in the Ca chain for comparison. At $N = 28$, the difference between both curves underlines once more the collapse of the $\nu(f_{7/2}) - \nu(p_{3/2})$ level splitting.

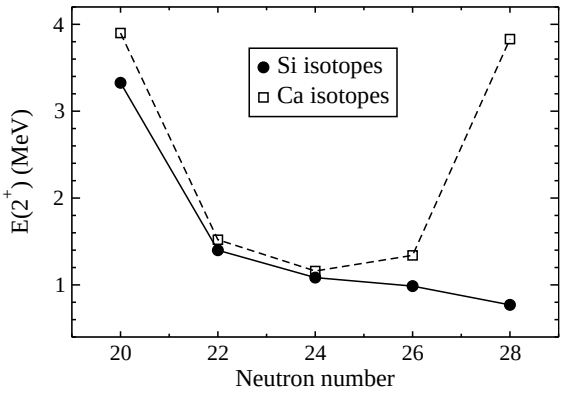

Figure 6.9: Energies of the first 2^+ states in the even-even Si ($Z = 14$) and Ca ($Z = 20$) isotopes. The experimental data for the Si chain are taken from [102, 140, 148].

6.2 β-NMR measurements on ^{41}Cl, ^{42}Cl and ^{43}Cl

In addition to the successful β-NMR results obtained for the ^{44}Cl ground state, considerable effort has been expended on measuring the g-factors of $^{41-43}$Cl. The fragment beams were produced in a projectile-fragmentation reaction induced by a ^{48}Ca primary beam (60 AMeV, 2 to 3.5 μA) on a 535 μm ^{9}Be target. After selection and purification, using a 1058 μm ^{9}Be wedge-shaped degrader (section 3.1), the beam was implanted in a NaCl crystal at the final focal point of the LISE fragment separator. For none of the three isotopes, a clear and unambiguous resonance could be observed. A compilation of the outcome of the different measurements is presented in the following three subsections, together with a record of the applied experimental parameters and encountered difficulties. All shell-model calculations quoted further in the text are made with the ANTOINE code using the SDPF-U residual interaction. The protons are restricted to the $\pi(sd)$ orbits while the neutrons are free in the full $\nu(pf)$ shell. Neutron excitations from the $\nu(sd)$ to the $\nu(pf)$ states are forbidden. The g-factors are calculated using either the free nucleon g-factors ($g_s^\nu = -3.826$, $g_l^\nu = 0$, $g_s^\pi = 5.586$, $g_l^\pi = 1$) or the effective nucleon g-factors ($g_s = 0.75\, g_s^{free}$, $g_l^\nu = -0.1$, $g_l^\pi = 1.1$) proposed in [149].

6.2.1 β-NMR on ^{41}Cl

^{41}Cl is definitely the most interesting neutron-rich Cl isotope to be studied. Experimental evidence exists that the $3/2^+$ to $1/2^+$ ground-state spin inversion in the odd-mass Cl-isotopes already takes place at ^{41}Cl. To confirm this, a ground-state spin assignment has to be made. As shell-model calculations predict a very different magnetic moment for the $3/2^+$ and $1/2^+$ state, a g-factor measurement can indirectly reveal the spin of the ground state. Fig. 6.10 shows the experimental [126, 150] and the calculated level schemes of ^{41}Cl, together with the corresponding calculated g-factors.

Measuring the g-factor of ^{41}Cl using the β-NMR technique involves two experimental challenges. The first difficulty to overcome is the long half-life of ^{41}Cl: $t_{1/2} = 38.4(8)$ s [151]. To perform a successful β-NMR measurement, the spin-lattice relaxation time T_1 of the nuclear polarization in the implantation crystal must be at least twice the half-life of the implanted nucleus. If not, most of the spin-polarization is lost before the isotope of interest decays.
In the β-NMR experiments described here, ^{41}Cl fragments are implanted in a NaCl crystal. To get an idea how the relaxation time of ^{41}Cl in NaCl compares to its half-life, the formalism developed by Yamanishi *et al.* [152] is used. Ref. [152] describes the behavior of the T_1 relaxation time as a function of the temperature T for ^{35}Cl nuclei ($3/2^+$) in a NaCl crystal. At low temperatures ($T < 400$ K), quadrupole relaxation is caused by vibrations of the crystal lattice

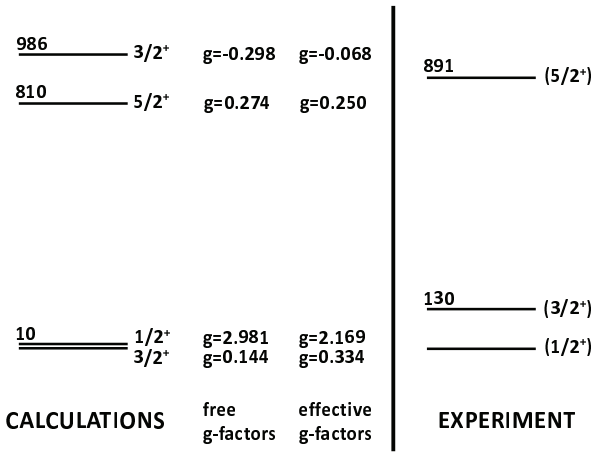

Figure 6.10: Calculated and experimental level schemes of ^{41}Cl.

while the relaxation mechanism at higher temperatures ($T > 400$ K) originates from diffusing defects. For the temperature range below room temperature, the following relation between T_1 and T is deduced:

$$\frac{1}{T_1} = A\,T^2 \tag{6.1}$$

with A an experimental constant, proportional to the spectroscopic quadrupole moment squared $(Q_s)^2$. For the reference isotope, ^{35}Cl, A equals $2.0(4) \times 10^{-6}$ s^{-1}K^{-2}. By comparing the ground-state quadrupole moment of ^{35}Cl, $|Q_s(^{35}\mathrm{Cl})| = 85.0(11)$ mb [96, 153], to the calculated value[A] for the $3/2^+$ state in ^{41}Cl, $|Q_s(^{41}\mathrm{Cl})| = 109$ mb, the relaxation time of ^{41}Cl $(3/2^+)$ at room temperature is found to be 3.5 s. When ^{41}Cl has a $3/2^+$ ground-state spin, the NaCl crystal needs cooling below 63 K to obtain a relaxation time which is twice the half-live. When the ground state spin of ^{41}Cl is $1/2^+$, the relaxation time is probably much longer as there is no spectroscopic quadrupole moment present. Crystal cooling might not be needed then but this has never been confirmed in literature.

The second experimental challenge encountered when performing a β-NMR measurement on ^{41}Cl is the ability to spin-polarize a nucleus which is most probably dominated by a $s_{1/2}$ proton configuration. Intuitively, one would expect that a preferred spin orientation cannot arise when a s-nucleon is involved.

[A] The quadrupole moment of ^{41}Cl is calculated with the effective charges $e_p = 1.1e$ and $e_n = 0.5e$ for protons and neutrons respectively.

Table 6.3: Wave-function decomposition of the lowest calculated $1/2^+$ and $3/2^+$ states in ^{41}Cl. Only configurations larger than 5% are shown.

Spin	Wave function		Spin	Wave function	
$1/2^+$	9%	$(\pi d_{3/2})^1\ (\nu f_{7/2})^4$	$3/2^+$	40%	$(\pi d_{3/2})^1\ (\nu f_{7/2})^4$
	46%	$(\pi s_{1/2})^1\ (\nu f_{7/2})^4$		15%	$(\pi s_{1/2})^1\ (\nu f_{7/2})^4$
	8%	$(\pi d_{3/2})^1\ (\nu p_{3/2})^1$		5%	$(\pi d_{3/2})^1\ (\nu p_{3/2})^2$
	6%	$(\pi s_{1/2})^1\ (\nu p_{3/2})^1$		7%	$(\pi s_{1/2})^1\ (\nu p_{3/2})^1$

Also experimentally, the magnetic moment of a $1/2^+$ state, originating from a $s_{1/2}$ configuration, has never been measured applying the β-NMR technique on a polarized fragment beam. In the participant-spectator model, which has been introduced in section 4.3, the induced spin-polarization in a projectile-fragmentation reaction is related to the total fragment spin J_f (1/2 or 3/2 for ^{41}Cl) and not to the orbital component of the nucleon that carries the spin. The model is therefore not appropriate to provide a better insight or a final conclusion on this matter.

ANTOINE calculations show that the wave functions of the $1/2^+$ and the $3/2^+$ states in ^{41}Cl are not pure single-particle configurations. A decomposition of both wave functions is given in Table 6.3, displaying only components that contribute to more than 5%. Configuration mixing is an important aspect when the polarization of a nuclear state with a dominant $|0^+ \times s_{1/2}>$ character is discussed. For ^{41}Cl, only 56% of the $1/2^+$ wave function consists of an odd $s_{1/2}$ proton coupled to a 0^+ neutron configuration. The remaining fraction, including mainly odd $\pi(d_{3/2})$ components, does allow the ground-state spin to be polarized. It is therefore not excluded that a spin-oriented ^{41}Cl$(1/2^+)$ beam can be produced, although the degree of polarization is expected to be rather low. Up to now, no theoretical model has been developed to simulate the spin-polarization in terms of the fragment wave-function components. As it is also impossible to measure the polarization directly, it remains an unknown parameter in the performed β-NMR experiments.

Even when the induced spin-polarization would be very small, a good chance exists that a β-NMR resonance is observed, thanks to the optimal production yield and the large asymmetry parameter of ^{41}Cl. A production yield of about 1.3×10^4 polarized ^{41}Cl ions per second was obtained behind the second LISE dipole for a primary beam intensity of 1 μA. The asymmetry parameter is estimated as follows. More than 80% of the ^{41}Cl β-decay proceeds to the $1/2^+$ excited state at 1868 keV in ^{41}Ar [108]. Using the formulae in Table 2.1 and assuming a single β-branch of 100% to the aforementioned level in ^{41}Ar, $A_\beta = -1$ is obtained for a $3/2^+$ ^{41}Cl ground state. Supposing a pure Gamow-Teller β-decay, $A_\beta = -0.67$ is found when the ground-state spin would be $1/2^+$.

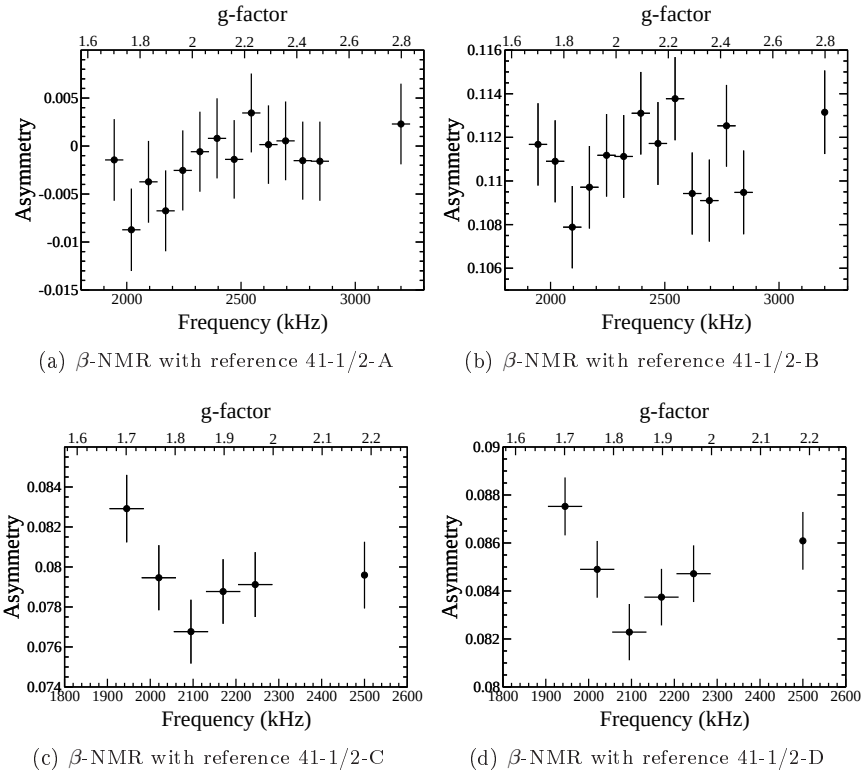

(a) β-NMR with reference 41-1/2-A

(b) β-NMR with reference 41-1/2-B

(c) β-NMR with reference 41-1/2-C

(d) β-NMR with reference 41-1/2-D

Figure 6.11: β-NMR measurements probing the lower g-factor range [1.67, 2.52] for the $1/2^+$ state in ^{41}Cl, including the value $g_{eff}(^{41}\mathrm{Cl}) = 2.17$ calculated with effective g-factors. The experimental parameters of each scan can be found in Table 6.4.

β-NMR measurements probing the $1/2^+$ state in ^{41}Cl

As can be seen from Fig. 6.10, ANTOINE calculations predict an *effective* g-factor $g_{eff}(^{41}\mathrm{Cl}) = 2.169$ for the $1/2^+$ state in ^{41}Cl. Using this as a central value, the g-factor interval $1.67 < |g| < 2.52$ was scanned. Two β-NMR measurements were performed, one applying crystal cooling (Fig. 6.11a) and one at room temperature (Fig. 6.11b). In the former case, a temperature of 15 K was achieved at the tip of the cold finger. The experimental parameters of both scans, indicated with the references 41-1/2-A and 41-1/2-B respectively, are given in Table 6.4. In the data-analysis, only coincident events were selected taking into account the full ΔE and E spectra, except for the noise peak in the beginning of each spectrum. The spectrum 41-1/2-B has a statistical accuracy of 0.19%. This implies that, when a 3σ effect is present, the resonance amplitude can be at most 0.6%.

Table 6.4: Experimental parameters for the β-NMR scans probing the $1/2^+$ state in ^{41}Cl. For each measurement, the applied frequency interval, the step between two central frequencies, the frequency modulation and the obtained statistical accuracy are given. In addition, it is indicated whether or not crystal cooling was used.

^{41}Cl – $1/2^+$ state – $1.67 < \|g\| < 2.52$ – $B_0 \simeq 0.15$ T					
Reference	Cooling	1σ (%)	Freq(kHz)	Step(kHz)	Mod(kHz)
41-1/2-A	yes	0.43	1945-2845	75	40
41-1/2-B	no	0.19	1945-2845	75	40
41-1/2-C	no	0.17	1945-2245	75	40
41-1/2-D	yes+no	0.12	1945-2245	75	40
^{41}Cl – $1/2^+$ state – $2.45 < \|g\| < 3.18$ – $B_0 \simeq 0.15$ T					
Reference	Cooling	1σ (%)	Freq(kHz)	Step(kHz)	Mod(kHz)
41-1/2-E	no	0.27	2845-3595	75	40

As Fig. 6.11b shows a weak indication for a resonance around 2095 kHz, an independent β-NMR measurement was performed, zooming in on the left wing of the frequency range. The result, indicated with reference 41-1/2-C in Table 6.4, is presented in Fig. 6.11c. Adding all the statistics of runs 41-1/2-A, 41-1/2-B and 41-1/2-C for the frequency interval they have in common, results in the spectrum 41-1/2-D shown in Fig. 6.11d. A 2.5σ effect with respect to the baseline is observed for the data point at 2095 kHz ($|g| \simeq 1.832(35)$). However, a new β-NMR measurement is needed to reproduce and confirm this indication.

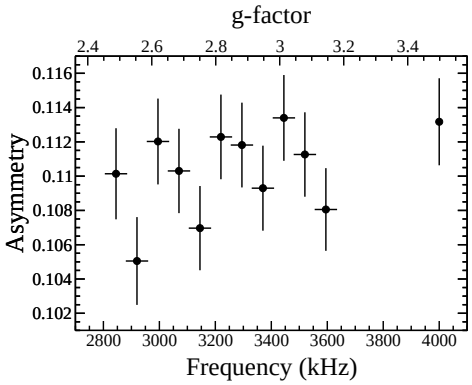

Figure 6.12: Higher g-factor range [2.45, 3.18] for the $1/2^+$ state in ^{41}Cl, corresponding to the calculation with free g-factors. Details are given in Table 6.4.

ANTOINE calculations with free nucleon g-factors predict a value $g_{free}(^{41}\mathrm{Cl}) = 2.981$ for the $1/2^+$ state in ^{41}Cl. The outcome of the β-NMR measurement, covering the g-factor interval [2.45, 3.18], is presented in Fig. 6.12. Within the errors, all data scatter around a mean value, without any pronounced resonance candidate. The statistical accuracy (0.27%) excludes a real effect larger than 0.9% (3σ level). A record of the experimental parameters was added to the lower part of Table 6.4 (reference 41-1/2-E).

β-NMR measurements probing the $3/2^+$ state in ^{41}Cl

For the $3/2^+$ state in ^{41}Cl, only one β-NMR measurement was performed in the $0.19 < |g| < 0.44$ range, including the value $g(3/2^+) = 0.334$ calculated with effective nucleon g-factors. An overview of the experimental parameters can be found in Table 6.5. As can be seen in Fig. 6.13, the error bars (1.7%) are too large to draw any conclusions, except that if a resonance is present, the effect is certainly smaller than 5%.

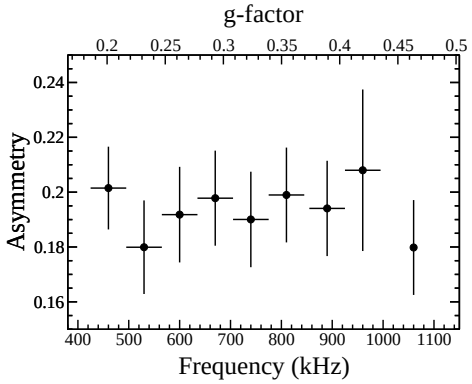

Figure 6.13: β-NMR measurement covering the g-factor range [0.19, 0.44]. The interval contains the value $g(3/2^+) = 0.33$, calculated for the $3/2^+$ state in ^{41}Cl using effective nucleon g-factors. Experimental details are given in Table 6.5.

Table 6.5: Experimental parameters for the β-NMR scan probing the $3/2^+$ state in ^{41}Cl. The applied frequency interval, the step between two central frequencies, the frequency modulation and the statistical accuracy are given.

^{41}Cl – $3/2^+$ state – $0.19 < \|g\| < 0.44$ – $B_0 \simeq 0.3$ T					
Reference	Cooling	1σ (%)	Freq(kHz)	Step(kHz)	Mod(kHz)
41-3/2-A	yes	1.7	460-940	70	35

6.2.2 β-NMR on ^{42}Cl

For the ground state of ^{42}Cl, three spin possibilities exist. Experimental results, such as the β-decay study of ^{42}S, the equal feeding of the 2^+ and 4^+ states in the β-decay of ^{42}Cl and the systematic decrease of the 3^- state when going from ^{38}Cl to ^{40}Cl favor a spin 3^- [154]. ANTOINE calculations on the other hand predict a 2^- ground-state which lies very close in energy to the 3^- and 1^- excited states. The theoretical and experimental level schemes of ^{42}Cl are depicted in Fig. 6.14, together with their corresponding calculated g-factors.

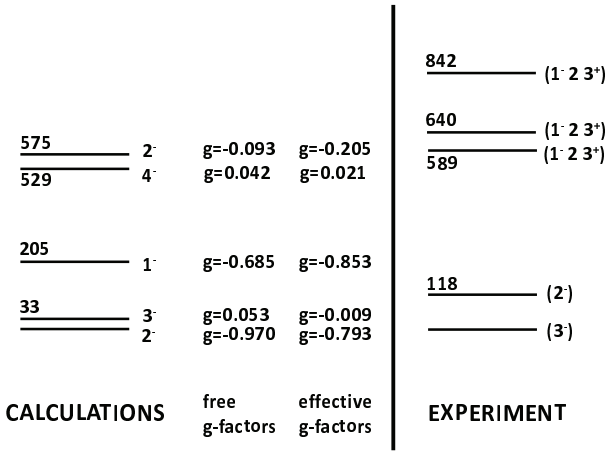

Figure 6.14: Calculated and experimental level schemes of ^{42}Cl.

A decomposition of the calculated 2^- and 3^- wave functions in terms of single particle configurations can be found in Table 6.6, reflecting the configuration mixing present in ^{42}Cl. Only configurations larger than 5% are reported. Again a g-factor measurement can decide which of both is the real ground state since shell-model calculations suggest a large difference between the g-factors of the two levels. Note however that, when a resonance would be observed in the $0.6 < |g| < 1.0$ range, a 1^- ground-state spin cannot be completely excluded. Due to the suggested configuration mixing in ^{42}Cl, the g-factors of the ground and excited states consist of many positive and negative contributions, originating from configurations such as $(\pi s_{1/2})^1\ (\nu p_{3/2})^1$ which has a positive g-factor or $(\pi d_{3/2})^1\ (\nu f_{7/2})^5$ with a negative g-factor. The admixture of positive and negative contributions results in the small g-factors predicted for the 3^- state. Note that if the ^{42}Cl g-factor is as small as the calculated 'effective' value of the 3^- state, it cannot be measured since the lowest g-factor, technically accessible with the new β-NMR/β-NQR setup, equals $|g| = 0.013$.

Table 6.6: Wave-function decomposition of the lowest calculated 2^- and 3^- states in ^{42}Cl. Only configurations larger than 5% are shown.

Spin	Wave function		Spin	Wave function	
2^-	21%	$(\pi d_{3/2})^1\ (\nu f_{7/2})^5$	3^-	21%	$(\pi d_{3/2})^1\ (\nu f_{7/2})^5$
	27%	$(\pi s_{1/2})^1\ (\nu f_{7/2})^5$		31%	$(\pi s_{1/2})^1\ (\nu f_{7/2})^5$
	8%	$(\pi d_{3/2})^1\ (\nu p_{3/2})^1$		6%	$(\pi d_{3/2})^1\ (\nu p_{3/2})^1$
	11%	$(\pi s_{1/2})^1\ (\nu p_{3/2})^1$		10%	$(\pi s_{1/2})^1\ (\nu p_{3/2})^1$

The half life of ^{42}Cl, 6.8(3) s [155], is longer than the spin-lattice relaxation time T_1=5.8 s [152] for ^{35}Cl-isotopes ($3/2^+$) in a NaCl crystal at room temperature. As T_1 was never measured for 2^- or 3^- Cl ground states, the temperature needed to preserve the spin polarization for at least two half-lives can only be roughly estimated. Assuming the same quadrupole relaxation process as for ^{35}Cl, T_1 of ^{42}Cl in NaCl is calculated based on a comparison of the spectroscopic quadrupole moments of both nuclei. $|Q_s| = 85.0(11)$ mb [96, 153] is found for ^{35}Cl while $|Q_s|$ is calculated[A] to be 125 mb and 201 mb for the 2^- and 3^- states in ^{42}Cl respectively. Applying the formula $\frac{1}{T_1} = AT^2$ [152] with rescaled A-factors gives $T_1 = 2.7$ s for the 2^- state and $T_1 = 1$ s for the 3^- state at room temperature. To obtain a spin-lattice relaxation time of 13.6 s (twice the half life of ^{42}Cl), the NaCl crystal should be cooled to 130 K for the 2^- state or to 81 K for the 3^- level.

All β-NMR measurements on ^{42}Cl, presented in this thesis work, are performed with the maximum cooling power, resulting in a temperature of about 15 K on the tip of the cold finger. On the copper crystal holder, a NaCl crystal of 2 mm was mounted and tilted over 35° with respect to the vertical axis in order to reduce the absorption and the scattering of the emitted β-particles. The data analysis was performed, selecting only coincident events but taking into account the full ΔE and E spectra avoiding the noise peak in the beginning of each spectrum. Due to the limited knowledge of the ^{42}Cl β-decay [156], the asymmetry parameter cannot be calculated. A polarized production yield of about 2.3×10^4 ^{42}Cl ions was obtained behind the second LISE dipole, using a primary beam intensity of 2 μA.

β-NMR measurements probing the 3^- state in ^{42}Cl

According to ANTOINE calculations using the free and effective nucleon g-factors, the 3^- state in ^{42}Cl has $|g_{free}(3^-)| = 0.053$ and $|g_{eff}(3^-)| = -0.009$. To cover these theoretical values, the lowest experimentally accessible g-factor

[A] Using $e_p = 1.1e$ and $e_n = 0.5e$ as effective charges for the protons and neutrons.

Table 6.7: Experimental parameters for the β-NMR scan probing the 3^- state in ^{42}Cl. The applied frequency interval, the step between two central frequencies, the frequency modulation and the statistical accuracy are given.

^{42}Cl – 3^- state – $0.0125 < \|g\| < 0.119$ – $B_0 \simeq 1$ T					
Reference	Cooling	1σ (%)	Freq(kHz)	Step(kHz)	Mod(kHz)
42-3-A	yes	0.35	150-850	100	55

range was scanned: $0.0125 < |g| < 0.119$. The result is shown in Fig. 6.15 and the experimental parameters are summarized in Table 6.7. Due to technical problems, the region has only been studied with a precision of 0.35% which is insufficient to observe an effect smaller than 1%. In case the g-factor is even smaller than 0.0125, the resonance cannot be observed with the present setup.

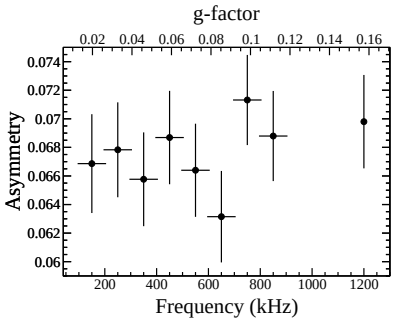

Figure 6.15: β-NMR measurement probing the $0.0125 < |g| < 0.119$ interval corresponding to the 3^- state in ^{42}Cl. Details are summarized in Table 6.7.

β-NMR measurements probing the $2^-(1^-)$ state in ^{42}Cl

In the series of β-NMR experiments presented here, the g-factor interval $0.527 < |g| < 1.162$ is studied, including all theoretical predictions for the 2^- and 1^- states in ^{42}Cl. The first broad scan, with reference 42-2-A, covers the full range in steps of 120 kHz, applying a modulation of 65 kHz. Further experimental details can be found in Table 6.8 and the outcome of the measurement is shown in Fig. 6.16a. A precision of 0.2% is achieved implying that a β-NMR effect of 0.6% or larger should have been observed if present.

In the broad scan, a hint for a resonance was found around 1790 kHz. Therefore, a zoom was made of the $|g| = 0.78 - 1.1$ interval, indicated by the dotted lines in Fig. 6.16a. All data added together result in a 0.15% accuracy for this

Table 6.8: Experimental parameters for the β-NMR measurements probing the $2^-(1^-)$ state(s) in ^{42}Cl. The applied frequency interval, the step between two central frequencies, the frequency modulation and the statistical accuracy are given.

^{42}Cl – $2^-(1^-)$ state – $0.527 < \|g\| < 1.162$ – $B_0 \simeq 0.25$ T					
Reference	Cooling	1σ (%)	Freq(kHz)	Step(kHz)	Mod(kHz)
42-2-A	yes	0.20	1070-2150	120	65
42-2-B	yes	0.15	1550-2030	120	65
42-2-C	yes	0.12	1660-1960	60	32

frequency range (β-NMR measurement 42-2-B and Fig. 6.16b). Afterwards, an even narrower g-factor range $|g| = 0.854 - 1.045$ was scanned, marked on Fig. 6.16a by two dashed lines. In the latter measurement (reference 42-2-C and Fig. 6.16c), error bars of 0.12% were achieved. Both fine scans, 42-2-B and 42-2-C, completely exclude a β-NMR resonance in their scan ranges.

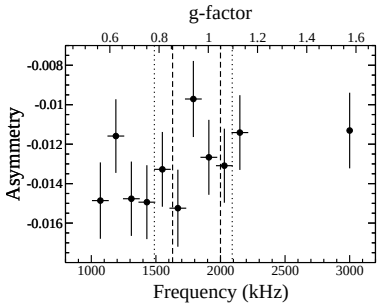

(a) β-NMR with reference 42-2-A

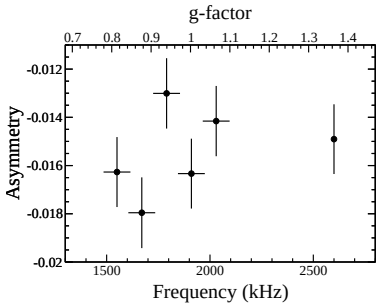

(b) β-NMR with reference 42-2-B

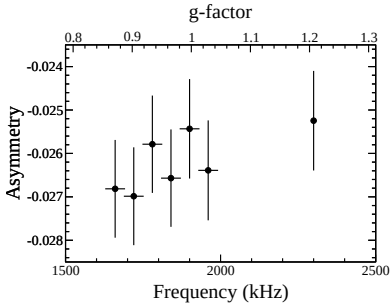

(c) β-NMR with reference 42-2-C

Figure 6.16: β-NMR measurement probing the $0.527 < |g| < 1.162$ interval corresponding to the $2^-(1^-)$ state(s) in ^{42}Cl. Experimental details are given in Table 6.8.

6.2.3 β-NMR on ^{43}Cl

The discussion of the β-NMR experiments performed on ^{41}Cl can be repeated to a large extent for ^{43}Cl. Again, a g-factor measurement can probe the spin and the structure of the ground state. Experiments [126] suggest a $1/2^+$ ground-state for ^{43}Cl dominated by odd $s_{1/2}$ proton configurations. At 330 keV, the first excited state is situated, presumably having a spin $3/2^+$ and consisting mainly of $\pi(d_{3/2})$ configurations. A decomposition of the calculated wave functions of both states is given in Table 6.9 and an overview of the experimental and theoretical level schemes can be found in Fig. 6.17.

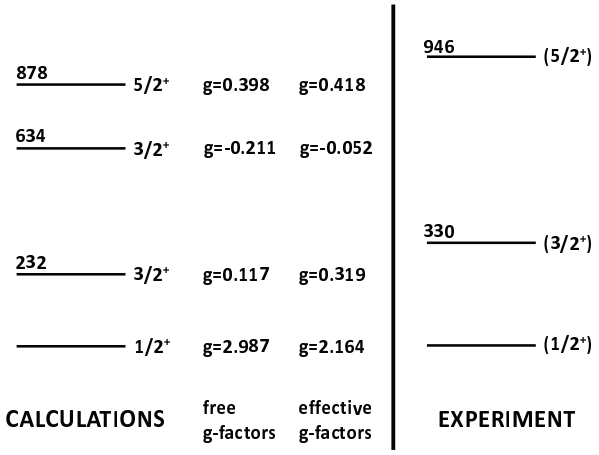

Figure 6.17: Calculated and experimental level schemes of ^{43}Cl.

The procedure to determine the spin-lattice relaxation time of the polarized ^{43}Cl nuclei in a NaCl crystal is analogous to the one applied for $^{41-42}$Cl. By comparing the calculated quadrupole moment of the $3/2^+$ state in ^{43}Cl[A] to the value obtained for ^{35}Cl $(3/2^+)$, the parameter A is rescaled and T_1 can be calculated using the relation $\frac{1}{T_1} = AT^2$ [152]. At room temperature, $T_1 = 6.3$ s is obtained. As the half-life of ^{43}Cl is 3.13(9) s [154], cooling is not absolutely necessary. Note that the magnetic moment of ^{33}Cl ($I^\pi = 3/2^+$, $t_{1/2} = 2.51$ s) has also been determined with the β-NMR technique in a NaCl-crystal at room temperature [157]. In that experiment, the relaxation time of ^{33}Cl was measured to be $5.6^{\infty}_{-3.3}$ s. When the ground-state spin of ^{43}Cl turns out to be $1/2^+$, the relaxation time cannot be calculated. But as there is no spectroscopic quadrupole moment, T_1 is expected to be very long and cooling is not needed.

[A] The calculated spectroscopic quadrupole moment of ^{43}Cl$(3/2^+)$ is 82 mb, using $e_p = 1.1$ and $e_n = 0.5$ as effective proton and neutron charges.

Table 6.9: Wave-function decomposition of the lowest calculated $1/2^+$ and $3/2^+$ states in ^{43}Cl. Only configurations larger than 5% are shown.

Spin		Wave function	Spin		Wave function
$1/2^+$	9%	$(\pi d_{3/2})^1\ (\nu f_{7/2})^6$	$3/2^+$	22%	$(\pi d_{3/2})^1\ (\nu f_{7/2})^6$
	39%	$(\pi s_{1/2})^1\ (\nu f_{7/2})^6$		15%	$(\pi s_{1/2})^1\ (\nu f_{7/2})^6$
	5%	$(\pi d_{3/2})^1\ (\nu p_{3/2})^1$		10%	$(\pi d_{3/2})^3\ (\nu f_{7/2})^6$
	7%	$(\pi s_{1/2})^1\ (\nu p_{3/2})^1$		10%	$(\pi s_{1/2})^1\ (\nu p_{3/2})^1$
	6%	$(\pi s_{1/2})^1\ (\nu p_{3/2})^2$			

The discussion of the reaction-induced spin polarization, presented earlier for ^{41}Cl, can be repeated for ^{43}Cl. As the ground-state of ^{43}Cl corresponds most probably to the earlier mentioned $1/2^+$ level dominated by $\pi(s_{1/2})$ configurations, a very small, if any, polarization is expected. Again, an accurate model is missing to simulate the exact amount. Moreover, the β-decay of ^{43}Cl is very fragmented [154] and not known to its full extent, resulting in an A_β asymmetry parameter which cannot be calculated and which is expected to be (much) smaller than for ^{41}Cl. The feasibility of a β-NMR experiment on ^{43}Cl is therefore questionable. Nevertheless, a few efforts have been made studying the g-factor range that includes the calculated g-factors of the $1/2^+$ state.

All β-NMR measurements were performed using a 1 mm NaCl implantation crystal at the final focal point of the LISE fragment separator. The crystal was mounted on the room-temperature crystal holder and tilted over $-30°$. Only coincident events were hard-ware selected and in the data-analysis the full ΔE and E spectra were taken into account, apart from the noise peak in the beginning of each spectrum. An experimental value for the production yield of ^{43}Cl has not been registered but LISE++ calculations predict it to be four times smaller than the production yield of ^{41}Cl.

Two measurements cover the interval $1.66 < |g| < 2.63$, including the g-factor $g_{eff} = 2.16$ of ^{43}Cl $(1/2^+)$ calculated with effective nucleon values. The first β-NMR scan is shown in Fig. 6.18a. This measurement studies the [1.66, 2.54] range using the experimental parameters indicated with reference 43-1/2-A in Table 6.10. To exclude that the last data point in this measurement is a potential resonance, a second β-NMR scan was performed, zooming in on the last two points and adding a third one to the right. The outcome and the details of the measurement are given in Fig. 6.18b and in Table 6.10 (reference 43-1/2-B). No (hint for a) resonance has been observed. As the statistical accuracy in both figures is below 0.2%, a β-NMR effect larger than 0.6% can be excluded.

Table 6.10: Experimental parameters for the β-NMR scans probing the $1/2^+$ state in ^{43}Cl. For each measurement, the applied frequency interval, the step between two central frequencies, the frequency modulation and the obtained statistical accuracy are given. In addition, it is indicated that no crystal cooling was used.

^{43}Cl – $1/2^+$ state – $1.66 < \|g\| < 2.63$ – $B_0 \simeq 0.15$ T					
Reference	Cooling	1σ (%)	Freq(kHz)	Step(kHz)	Mod(kHz)
43-1/2-A	no	0.2	1950-2850	100	55
43-1/2-B	no	0.17	2750-2950	100	55
^{43}Cl – $1/2^+$ state – $2.24 < \|g\| < 3.30$ – $B_0 \simeq 0.15$ T					
Reference	Cooling	1σ (%)	Freq(kHz)	Step(kHz)	Mod(kHz)
43-1/2-C	no	0.17	2630-3710	120	65

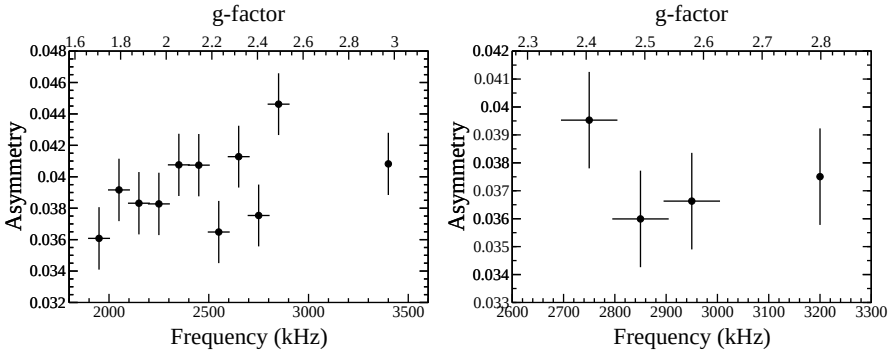

(a) β-NMR with reference 43-1/2-A (b) β-NMR with reference 43-1/2-B

Figure 6.18: β-NMR measurement probing the a) $1.66 < |g| < 2.54$ and b) $2.36 < |g| < 2.63$ intervals corresponding to the $1/2^+$ state in ^{43}Cl. Experimental details are given in Table 6.10.

Performing the same shell-model calculations using free nucleon g-factors results in $g_{free} = 2.99$ for the $1/2^+$ state in ^{43}Cl. Therefore, the interval [2.24, 3.30] was scanned in steps of 120 kHz with a frequency modulation of 65 kHz (see reference 43-1/2-C in Table 6.10). The result is shown in Fig. 6.19. Once more, no clear evidence for a resonance is found.

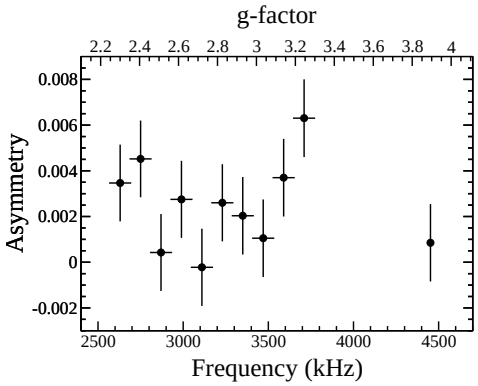

Figure 6.19: β-NMR measurement covering the g-factor range [2.24, 3.30]. The interval contains the value $g(1/2^+) = 2.99$, calculated for the $1/2^+$ state in ^{43}Cl using free nucleon g-factors. Experimental details are given in Table 6.10.

So far, no β-NMR measurements have been performed for ^{45}Cl. According to shell-model calculations, the ^{45}Cl ground state has a spin-parity $1/2^+$ with $g_{free}(1/2^+) = 2.81$ and $g_{eff}(1/2^+) = 2.20$. In that case, spin-polarization of the fragment beam is hard to obtain, as illustrated earlier for ^{41,43}Cl. Theoretically, the first excited state is predicted at 133 keV, having $g_{free}(3/2^+) = 0.09$ and $g_{eff}(3/2^+) = 0.40$. The short ^{45}Cl half-life $t_{1/2} = 413(25)$ ms makes crystal cooling unnecessary. A straightforward g-factor measurement, however, is further hindered by the low production yield which is expected to be 26 times smaller than that of ^{41}Cl and by the unknown β-asymmetry parameter.

6.2.4 Conclusions and outlook for the Cl-studies

In conclusion to this section it is stated that, in spite of the successful β-NMR measurements on ^{44}Cl which are shown and discussed in the Physical Review C article at the end of this chapter, no resonances have been observed for ^{41,42,43}Cl. However, two 'promising' cases are worth to be studied in more detail. First of all, a second evaluation is needed of the [1.67, 2.52] g-factor range, covering the calculated 'effective' g-factor of the $1/2^+$ state in ^{41}Cl. As the $3/2^+$ to $1/2^+$ ground-state spin inversion in the odd-mass Cl isotopes is predicted to happen at ^{41}Cl, this isotope is by far the most interesting nucleus to be studied. Moreover, ^{41}Cl also provides the highest probability to observe a β-NMR resonance. If any reaction-induced polarization is created, a β-NMR measurement might reveal the value of $|g(^{41}\mathrm{Cl})|$, assisted by the high ^{41}Cl production rate and the large $A_\beta(^{41}\mathrm{Cl})$ parameter. The feasibility of a similar experiment on ^{43,45}Cl is controversial since both nuclei do not bene-

fit from large production yields and known asymmetry parameters. A future β-NMR measurement might also reconsider the g-factor range corresponding to the 3^- state in ^{42}Cl. The [0.0125,0.119] g-factor interval has only been studied to a limited extent although many other experimental results favor a ^{42}Cl(3^-) ground state. In addition to the experiments mentioned above, new theoretical work is encouraged to describe the spin polarization, induced in a projectile-fragmentation reaction, in terms of the wave-function components of the created fragments. Such research would shed light on the amount of polarization that can be obtained for the odd-mass neutron-rich Cl isotopes being dominated by a $|0^+ \times s_{1/2}>$ configuration.

g factor of the ^{44}Cl ground state: probing the reduced $Z = 16$ and $N = 28$ gaps

M. De Rydt,[1] J.M. Daugas,[2] F. de Oliveira Santos,[3] L. Gaudefroy,[2] S. Grévy,[3] D. Kameda,[4] V. Kumar,[5] R. Lozeva[1*,1] T.J. Mertzimekis,[6] P. Morel,[2] T. Nagatomo,[4] G. Neyens,[1] L. Perrot,[7] O. Sorlin,[3] C. Stödel,[3] J.C. Thomas,[3] N. Vermeulen,[1] and P. Vingerhoets[1]

[1] *Instituut voor Kern- en Stralingsfysica, K.U. Leuven, Celestijnenlaan 200D, B-3001 Leuven, Belgium*
[2] *CEA, DAM, DIF, F-91297 Arpajon Cedex, France*
[3] *Grand Accélérateur National d'Ions Lourds (GANIL), CEA/DSM-CNRS/IN2P3, B.P. 55027, F-14076 Caen Cedex 5, France*
[4] *RIKEN Nishina Center, 2-1 Hirosawa, Wako, Saitama 351-0198, Japan*
[5] *Weizmann Institute of Science, Rehovot 76100, Israel*
[6] *University of Ioannina, 45110 Ioannina, Greece*
[7] *IPN, 15 Rue G. Clemenceau, F-91406 Orsay, France*

The g factor of the ^{44}Cl ground state is measured at the LISE fragment separator at GANIL using the β-Nuclear Magnetic Resonance (β-NMR) technique, resulting in $g(^{44}\mathrm{Cl}) = (-)0.2749(2)$. An analysis of the g factor value and of the theoretical level scheme in the shell-model framework reveals the presence of odd-proton $s_{1/2}$ configurations and neutron excitation across the $N = 28$ shell gap in the ground state of ^{44}Cl. In addition, the measured g factor strongly supports a 2^- spin assignment for the ^{44}Cl ground state.

PACS:25.70.Mn, 29.27.Hj, 24.70.+s

I. INTRODUCTION

Isotopes with extreme proton-to-neutron ratios attract a lot of attention since they exhibit nuclear properties that significantly differ from those near the valley of stability. Several regions on the nuclear chart are currently being explored (e.g. the island of inversion around $N = 20$, neutron rich nuclei around ^{68}Ni) revealing vanishing magic numbers and new shell gaps.
About 15 years ago, a β-decay experiment suggested a new region of deformation around $^{44}\mathrm{S}_{28}$ [1]. Since then, extensive experimental and theoretical studies have been performed to analyze the nuclear structure of the neutron-rich isotopes in the

* Present address: CSNSM, Université Paris-Sud 11, CNRS/IN2P3, F-91405 Orsay-Campus, France

vicinity of the $N = 28$ shell closure. Various observables such as masses [2–4], β-decay properties [5, 6], excitation energies and level schemes [7–10], $B(E2)$ values [11–13], spectroscopic factors [14, 15] and nuclear moments [16, 17] have been studied, yielding a large set of complementary data. In parallel, elaborate shell-model calculations [18–22] and mean-field theories [23–27] have been developed.

Both the erosion of the $N = 28$ shell-gap and the collapse of the $Z = 16$ subshell closure are responsible for the collectivity, shape coexistence and configuration mixing observed in the neutron-rich isotopes from Si ($Z = 14$) to K ($Z = 19$). Since $^{44}_{17}Cl_{27}$ has three proton holes in the $\pi(sd)$ shell, it is very sensitive to the near-degeneracy of the $\pi(s_{1/2})$ and $\pi(d_{3/2})$ levels and to the induced proton correlations. With one neutron hole in the $\nu(f_{7/2})$ state, ^{44}Cl is also an excellent probe for neutron excitations across $N = 28$.

As the nuclear g factor consists of an orbital and a spin contribution, it indicates the shell-model character of the state being studied. Therefore, a measurement of the g factor can provide crucial and decisive information on the nuclear structure of the $N \simeq 28$ isotopes.

This article reports on the ground-state g factor of ^{44}Cl which has been measured using the β-Nuclear Magnetic Resonance technique (β NMR) at the LISE fragment separator at GANIL. The experimental results are presented and compared to large-scale shell-model calculations. In order to give a correct interpretation of the $^{44}_{17}Cl_{27}$ g factor and ground state structure in terms of changing single particle orbits and enhanced correlations, the isotopic $Z = 17$ and isotonic $N = 27$ chains are discussed. This study reveals a deeper insight into the structural changes happening around the 'magic' number $N = 28$.

II. EXPERIMENTAL TECHNIQUE

Neutron-rich ^{44}Cl nuclei were produced in a projectile-fragmentation reaction of a stable $^{48}Ca^{20+}$ beam (60 AMeV) impinging on a 1212 μm rotating ^{9}Be target. The secondary beam was selected by the high-resolution fragment separator LISE at GANIL [28, 29]. The polarization necessary to perform a β-NMR measurement was obtained by putting an angle of $2(1)^\circ$ on the primary beam with respect to the forward direction. In order to get the highest polarization, a selection was made in the right wing of the longitudinal momentum distribution. This configuration led to a production yield of about 2700 ^{44}Cl-ions per second for 1 μA of ^{48}Ca. A secondary beam purity of 90% was achieved by placing a 1077 μm ^{9}Be wedge-shaped degrader in the intermediate dispersive plane and by adjusting the settings of the Wien filter in front of the β-NMR setup. The identification of the transmitted fragments was done by means of the standard energy loss versus time of flight procedure using three Si-detectors along the beam path. The characteristic γ-lines following the β-decay of the ^{44}Cl nuclei contributed to a correct identification of the produced fragments.

At the end of the LISE-separator, the β-NMR setup is installed [30]. The spin-polarized ^{44}Cl-fragments ($t_{1/2} = 0.56(11)$ s, $Q_\beta = 12.27(22)$ MeV) are implanted in a 1 mm thick NaCl crystal at room temperature. The stopper material is positioned in the center of a static magnetic field $\mathbf{B}_0$ that is oriented parallel to the vertical polarization axis. $\mathbf{B}_0$ induces a Zeeman splitting of the nuclear m quantum states. The energy difference between two successive levels, $m - 1$ and m, is proportional to

the nuclear g factor g and to the magnetic field strength B_0. It is given by:

$$\Delta E = E_m - E_{m-1} = g\mu_N B_0 \quad (1)$$

The β-particles emitted in the β-decay of ^{44}Cl are detected in two ΔE/E pairs of plastic scintillators, placed along the polarization direction. One pair is situated above the crystal, the other below. Requiring coincidences between the upper two or the lower two detectors reduces scattering and noise events. When the implanted nuclear ensemble is spin polarized, the m-states have a different occupation probability which induces an anisotropic β-decay pattern.
Perpendicular to the magnetic field, a radiofrequent (rf) field is applied in the Cu-coil placed around the crystal. By varying the rf-frequency ν, the emitted energy $h\nu$ is adjusted to match the energy difference between the m-states (Eq. 1). This induces an equal population of all quantum levels and a destruction of the polarization when the Larmor frequency $\nu_L = (g\mu_N B_0)/h$ is encountered. As a consequence, the β-decay pattern becomes isotropic and a resonance is observed when the experimental asymmetry is measured as a function of the rf-frequency. The experimental asymmetry is defined as:

$$\text{Asymmetry} = \frac{N_{up} - N_{down}}{N_{up} + N_{down}} \simeq \frac{v_\beta}{c} A_\beta P \quad (2)$$

The number of coincident events in the upper and the lower detectors is given by N_{up} and N_{down} respectively. A_β is the asymmetry parameter which depends on the β-decay properties and the spin of ^{44}Cl. P is the polarization induced in the projectile-fragmentation reaction and v_β/c, the ratio of the velocity of the β-particles to the speed of light, is assumed to be one since ^{44}Cl has a high Q_β.
The variation of the rf-frequency is performed in discrete steps, all characterized by a central frequency. In parallel to the continuous β-detection, each central frequency is applied and modulated simultaneously during several seconds up to minutes depending on the lifetime of the nucleus. The modulation range covers at least one half of the interval between two subsequent central frequencies and has a repetition rate of 100 Hz. After applying the last central frequency, data without rf-field are collected as a reference before starting the next scan.

III. RESULTS

The first indication of the ^{44}Cl β-NMR resonance was found in a broad scan, covering a 2 MHz wide frequency range in steps of 200 kHz using a large frequency modulation of 110 kHz. A preliminary Larmor frequency $\nu_{L,1}(^{44}\text{Cl}) = 2126(110)$ kHz could be deduced. Starting from this result, four fine scans were performed, gradually reducing the scan range and the frequency modulation until an accurate β-NMR curve and a precise Larmor frequency $\nu_{L,5}(^{44}\text{Cl}) = 2096.5(2)$ kHz were obtained. Table I gives the scanned frequency range, the step between two central values, the applied frequency modulation and the deduced Larmor frequency for the subsequent β-NMR measurements.
Two fine scan examples with a frequency modulation of 17 kHz and 0.6 kHz respectively are shown in Fig.1. The outer right point represents the data collected without rf-field. In several measurements, including the ones presented in Fig.1, two frequencies are added on either side of the resonance region to emphasize the baseline. The

Table I: The scanned frequency range, the interval between two central frequencies, the applied frequency modulation and the obtained Larmor frequency for the five ^{44}Cl β-NMR measurements, performed for $B_0 = 1.0001(7)$ T.

$B_0 = 1.0001(7)$ T			
Range (kHz)	Step (kHz)	Modulation (kHz)	ν_L (kHz)
850-2850	200	110	2126(110)
1800-2300	30	17	2097(4)
2070-2122	4	1.6	2098(2)
2085-2110	1	0.01	2096.1(3)
2085-2110	1	0.6	2096.5(2)

β-NMR curves are fitted with a function that includes the Lorentzian line shape and the frequency modulation [31]. The weighted mean of the five ν_L's is calculated to be $\nu_L(^{44}\mathrm{Cl})_{1T} = 2096.4(2)$ kHz.
All aforementioned β-NMR measurements were performed for a magnetic field $B_0 = 1.0001(7)$ T. During the run, the field was continuously monitored by the hall probe positioned at 7 cm behind the implantation crystal. From the measured field value, the magnetic field in the center could be calculated, relying on the field calibrations made before and after the experiment.
During the calibration process, a complete and stable hysteresis curve was measured in steps of 0.5 A. This procedure was performed in the center and at the position of the hall probe, firmly establishing the relation between both. The total error on B_0 consists of two contributions, added in quadrature. The statistical contribution (0.15 mT) is the smallest and originates from the linear relation between the measured and the central magnetic field. It includes the uncertainty on the hall probe readout and the errors on the slope and the intercept of the calibration function. The largest contribution (0.66 mT) is a systematic effect, linked to the fact that the field calibration around 1 T can only be reproduced with an accuracy of 0.66 mT.
From the weighted mean of the individual Larmor frequencies and the calculated magnetic field value B_0, the g factor of the ^{44}Cl ground state can be deduced: $|g(^{44}\mathrm{Cl})|_{1T} = 0.2750(2)$.

Table II: The scanned frequency range, the interval between two central frequencies, the applied frequency modulation and the obtained Larmor frequency for the β-NMR measurement performed for $B_0 = 0.5001(4)$ T.

$B_0 = 0.5001(4)$ T			
Range (kHz)	Step (kHz)	Modulation (kHz)	ν_L (kHz)
1035-1061	2	1.5	1047.0(5)

In order to check this result, an extra β-NMR scan was performed at a different magnetic field. The experimental details and the observed Larmor frequency can be

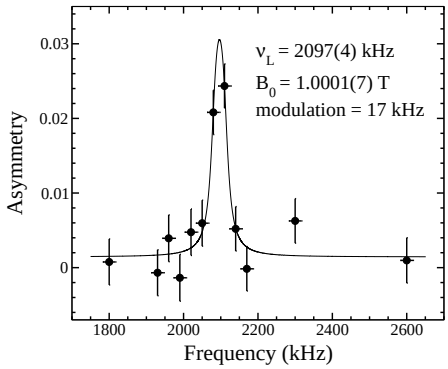

(a)Fine scan on ^{44}Cl with 17 kHz modulation

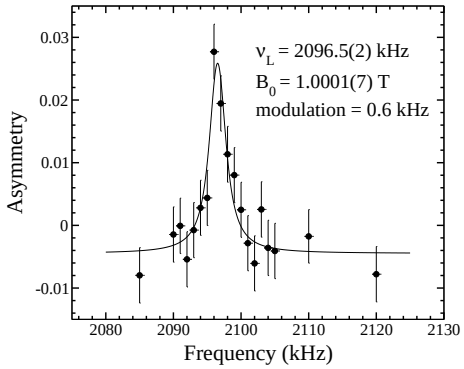

(b)Fine scan on ^{44}Cl with 0.6 kHz modulation

Figure 1: Two ^{44}Cl fine scans for B_0=1.0001(7)T. The NMR in Fig. 1(a) has a frequency step of 30 kHz and a modulation of 17 kHz. Fig. 1(b) shows a scan performed with frequencies that are only 1 kHz apart and a modulation of 0.6 kHz.

found in Table II. The β-NMR resonance is plotted in Fig. 2. A static magnetic field B_0 = 0.5001(4) T was applied, the error being mainly determined by the 0.36 mT divergence observed for repeated calibrations around 0.5 T. Based on the measured Larmor frequency ν_L = 1047.0(5) kHz and the calibrated magnetic field, an independent value for the g factor of the ^{44}Cl ground state could be deduced. The result, $|g(^{44}\mathrm{Cl})|_{0.5T}$ = 0.2747(3), is in good agreement with the g factor observed for the double field value.

The experimentally determined g factor of the ^{44}Cl ground state is the weighted mean of the g factors observed at 1 T and at 0.5 T and is calculated to be $|g(^{44}\mathrm{Cl})|$ = 0.2749(2).

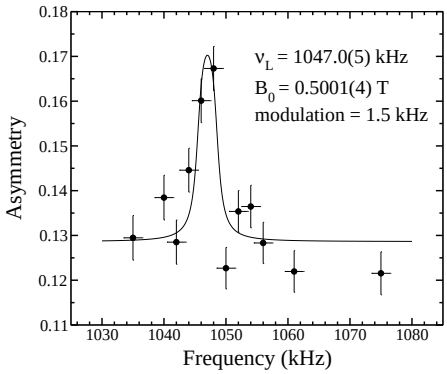

Figure 2: ^{44}Cl scan for a magnetic field of 0.50010(4) T.

IV. DISCUSSION

Being an odd-proton isotope, $^{44}_{17}$Cl is very sensitive to the near-degeneracy of the $\pi(s_{1/2})$ and the $\pi(d_{3/2})$ levels [9, 32–34]. Having 27 neutrons, ^{44}Cl is also an excellent probe to study the reduction of the $N = 28$ shell gap, which has been observed in the neighboring ^{43}S [17] and ^{45}Ar [15] isotones. Prior to the discussion of the ^{44}Cl ground-state structure, the above effects are addressed from an experimental and a theoretical point of view. The entire discussion is performed in the shell-model framework and the calculations are made using the ANTOINE code [35] with the most recent *sdpf* residual interaction (SDPF-U) [22]. The protons are confined to the $\pi(sd)$ orbits while the valence neutrons occupy the full $\nu(pf)$ shell.

The degeneracy of the $\pi(s_{1/2})$ and $\pi(d_{3/2})$ levels is to a large extent caused by the proton-neutron tensor force [36, 37] which works attractively on the $\pi(d_{3/2})$ state, lowering it in energy with respect to the $\pi(s_{1/2})$ level when the $\nu(f_{7/2})$ orbit is filled. When both proton levels come close together, ground-state configurations with an odd $s_{1/2}$ proton are energetically favored as the energy gain by pairing two protons in the $\pi(d_{3/2})$ level overcomes the energy needed to excite a proton. As a consequence, a ground-state spin change is predicted in the odd-mass Cl isotopes, similar to the spin flip observed in the K isotopes [38]. Going towards ^{45}Cl, a decrease of the energy difference between the 'normal' $3/2^+$ ground state and the first excited state with spin $1/2^+$ is observed. The inversion of both states is suggested to happen at $^{41}_{17}$Cl$_{24}$ [9, 39]. The calculated and experimental level schemes, including only the lowest two states of $^{39-45}$Cl, are given in Fig. 3. The experimental data are taken from Refs. [9, 39–42]. A good agreement between theory and experiment is observed.

$^{43}_{17}$Cl$_{26}$ and $^{45}_{17}$Cl$_{28}$ are predicted to have a $1/2^+$ ground-state spin and a wave function dominated by configurations with an odd $s_{1/2}$ proton (59% for ^{43}Cl and 65% for ^{45}Cl). This provides a strong indication that also in the ground state of ^{44}Cl, $\pi(s_{1/2})$ configurations are favored.

The second structural change, relevant for the study of ^{44}Cl, comprises the vanishing of the $N = 28$ shell closure and is also induced by the proton-neutron (tensor) interac-

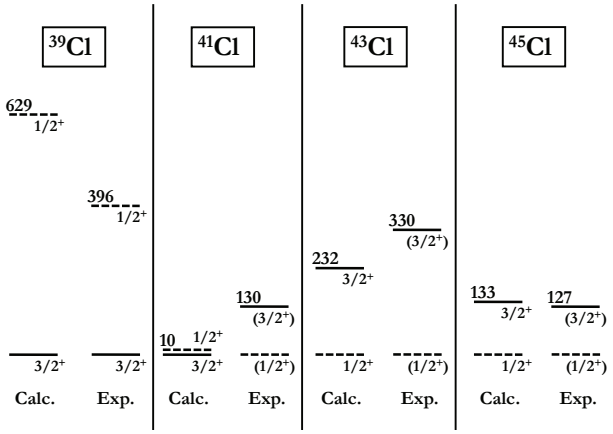

Figure 3: Calculated and experimental level schemes of the odd-mass neutron-rich $^{39-45}Cl_{22-28}$ isotopes.

tion. Taking away protons from the ^{47}Ca-nucleus weakens the attraction between the $\nu(f_{7/2})$ and the $\pi(d_{3/2})$ level, which leads to enhanced cross-shell excitations to the $\nu(p_{3/2})$ level. Fig. 4 shows the experimental level schemes and the known g factors of the odd-mass $N = 27$ isotones, from ^{47}Ca down to ^{43}S [2, 8, 13, 15, 17, 43–46]. Nuclear states with a calculated or observed dominating single-particle nature are indicated with a full line, dashed-dotted lines define strongly mixed states. The $7/2^-$ ground state of ^{47}Ca originates from the odd-neutron hole in the $\nu(f_{7/2})$ orbital. Promoting one neutron across the $N = 28$ shell gap to the $\nu(p_{3/2})$ level gives the $3/2^-$ first excited state. Both configurations are also present in the level scheme of ^{45}Ar. The lower excitation energy of the $3/2^-$ state already indicates the weakening of the $N = 28$ shell gap. In addition, a collective $3/2^-$ state appears at 535 keV. When going to ^{43}S, the intruder $3/2^-$ level with a neutron configuration dominated by np-nh excitations across $N = 28$ is suggested to replace the 'single-particle' $7/2^-$ level as the ground state. An extensive discussion of this structural change can be found in Refs. [15, 17, 46]. Note that for the $N = 27$ isotones a good agreement between the experimental and calculated g factors is obtained, using the effective nucleon g factors proposed in [47] ($g_l^\pi = 1.1$, $g_l^\nu = -0.1$ and $g_s = 0.75\ g_s^{free}$).

As $^{44}_{17}Cl_{27}$ is situated between $^{45}_{18}Ar_{27}$ and $^{43}_{16}S_{27}$, $\nu(p_{3/2})$ configurations are expected to contribute to the ground-state wave function. Experimentally, this was confirmed by Riley *et al.* who measured the momentum distribution of the ^{44}Cl nuclei in the single-neutron knockout reaction ^{9}Be(^{45}Cl, ^{44}Cl)X [48]. From the obtained results, it was concluded that the $\nu(p_{3/2})$ configurations play a prominent role in the ^{44}Cl ground state and that the collapse of the $N = 28$ shell closure, earlier observed in ^{43}S [17], persists in ^{44}Cl.

Let us now combine both effects, the degeneracy of the $\pi(s_{1/2})$ and $\pi(d_{3/2})$ levels and the reduced $N = 28$ shell gap, in the odd-odd nuclei. The theoretical and (known)

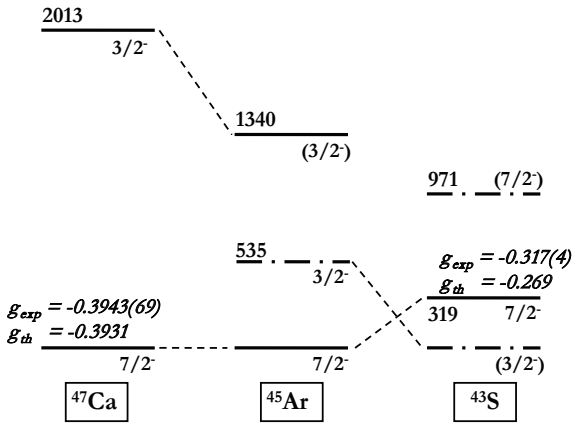

Figure 4: Experimental level schemes and known g factors of the $N = 27$ isotones (^{47}Ca, ^{45}Ar and ^{43}S). Nuclear states with a dominating single-particle nature are indicated with a full line, dashed-dotted lines define strongly fragmented states.

experimental level schemes of $^{46}_{19}K_{27}$ and $^{44}_{17}Cl_{27}$ are presented in Fig. 5, together with the calculated and measured ground-state g factors. The experimental data are taken from this work and from [38, 49]. Near the stability line, in $^{46}_{19}K_{27}$, one would naively expect to have an unpaired neutron in the $\nu(f_{7/2})$ orbit and an odd proton in the $\pi(d_{3/2})$ state. This configuration gives rise to the 2^- ground state and the 3^-, 4^- and 5^- levels at low excitation energies. The decomposition of the calculated wave functions of these states is shown in Table III. Only contributions larger than 10% are reported.

As the $\pi(s_{1/2})$ and $\pi(d_{3/2})$ single-particle states are nearly degenerate in the neutron-rich K isotopes around $^{47}_{19}K_{28}$, $(\pi s_{1/2})^1$ $(\nu f_{7/2})^7$ configurations should be taken into account in the wave function of ^{46}K. They induce a significant configuration mixing in the aforementioned 3^- and 4^- excited states, as shown in Table III. When considering the higher lying states, the 0^- and 1^- spins can only be formed by coupling a proton to a $p_{3/2}$ neutron. This hypothesis is confirmed by the calculations in Table III.

As observed in Fig. 5, the calculated level scheme of ^{44}Cl is much more compressed in energy than that of ^{46}K. The main difference between both is the position of the 0^-, 1^- multiplet, related to neutron excitations across $N = 28$. In ^{44}Cl, it dropped by about 1.5 MeV as compared to ^{46}K, indicating the collapse of the $N = 28$ shell gap and the grown importance of $\nu(p_{3/2})$ configurations in the ground state and low-lying excited states of ^{44}Cl. Moreover, the ^{44}Cl wave functions shown in Table III appear to be very fragmented, providing a strong indication for the development of correlations and collectivity as observed in the even-odd $N = 27$ isotones.

Independent of the nuclear level schemes, also the g-factor values reflect the increasing amount of $\nu(p_{3/2})$ and $\pi(s_{1/2})$ configurations. As the ground state of ^{46}K is dominated by $(\pi d_{3/2})^3$ $(\nu f_{7/2})^7$ configurations, its g factor $g_{exp}(^{46}\mathrm{K}) = -0.526(3)$ [38] can

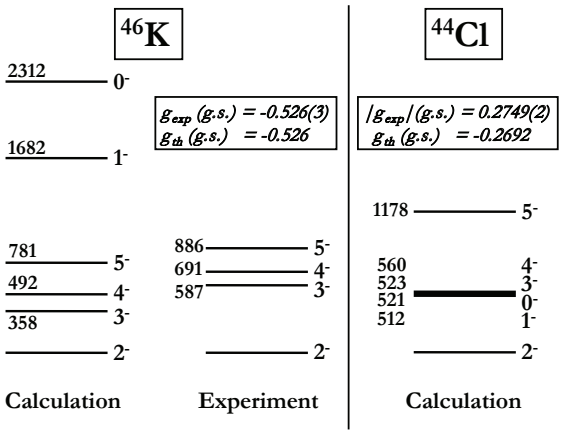

Figure 5: Calculated and experimental (if known) level schemes of ^{46}K and ^{44}Cl. The experimental spin assignments for ^{46}K are the ones adopted in [49] and the measured ground-state (g.s) g factors are taken from this work and [38].

be compared to the value $g_{pure} = -0.98$ of a pure $(\pi d_{3/2})^3$ $(\nu f_{7/2})^7$ state, calculated with effective nucleon g factors. For the ^{44}Cl ground state however, ANTOINE calculations suggest a highly fragmented wave function with $(\pi d_{3/2})^3$ $(\nu f_{7/2})^7$ and $(\pi s_{1/2})^1$ $(\nu p_{3/2})^1$ as main components. Since the $(\pi s_{1/2})^1$ $(\nu p_{3/2})^1$ contribution has a g factor with a positive sign, $g_{pure} = 0.28$, the total value of the ^{44}Cl g factor is reduced when both configurations are mixed. The experimentally observed value $g(^{44}\mathrm{Cl}) = (-)0.2749(2)$ (sign adopted from theory) confirms this argument: additional components in the wave function due to configuration mixing lower the g factor with respect to the value observed for a single-particle configuration.
An excellent agreement is observed between the experimental and calculated 'effective' g factors of the $N = 27$ isotones ^{47}Ca, ^{43}S^m, ^{46}K and ^{44}Cl. The measured ^{44}Cl g factor, presented in this work, therefore strongly supports the 2^- spin assignment for the ground state of ^{44}Cl, consistent with the conclusion drawn in Ref. [48].
In conclusion, the ^{44}Cl ground state and g factor are very sensitive to the subtle interplay between proton configurations originating from the collapse of the $Z = 16$ sub-shell closure and neutron excitations across the reduced $N = 28$ shell gap. From the comparison of the ^{44}Cl level scheme and g factor with calculated and experimental values in neighboring nuclei, it is deduced that both effects play a major role in the ground state of ^{44}Cl.

V. SUMMARY

The g factor of the ^{44}Cl ground state was studied using the β-NMR technique at the LISE fragment separator at GANIL. Several measurements at two different magnetic field values were performed, leading to the final value $g(^{44}\mathrm{Cl}) = (-)0.2749(2)$.

Table III: Main calculated wave-function components of the ground state and low lying excited states in ^{46}K and ^{44}Cl. Only contributions larger than 10% are reported.

J^π	^{46}K configuration	J^π	^{44}Cl configuration
2^-	71% $(\pi d_{3/2})^3\ (\nu f_{7/2})^7$	2^-	24% $(\pi d_{3/2})^3\ (\nu f_{7/2})^7$
			18% $(\pi s_{1/2})^1\ (\nu p_{3/2})^1$
3^-	35% $(\pi d_{3/2})^3\ (\nu f_{7/2})^7$	1^-	16% $(\pi d_{3/2})^1\ (\nu p_{3/2})^1$
	32% $(\pi s_{1/2})^1\ (\nu f_{7/2})^7$		27% $(\pi s_{1/2})^1\ (\nu p_{3/2})^1$
	15% $(\pi d_{3/2})^3\ (\nu p_{3/2})^1$		
4^-	16% $(\pi d_{3/2})^3\ (\nu f_{7/2})^7$	0^-	20% $(\pi d_{3/2})^1\ (\nu p_{3/2})^1$
	61% $(\pi s_{1/2})^1\ (\nu f_{7/2})^7$		22% $(\pi s_{1/2})^1\ (\nu p_{3/2})^1$
5^-	77% $(\pi d_{3/2})^3\ (\nu f_{7/2})^7$	3^-	13% $(\pi d_{3/2})^1\ (\nu f_{7/2})^7$
			22% $(\pi s_{1/2})^1\ (\nu f_{7/2})^7$
			11% $(\pi s_{1/2})^1\ (\nu p_{3/2})^1$
1^-	63% $(\pi d_{3/2})^3\ (\nu p_{3/2})^1$	4^-	10% $(\pi d_{3/2})^1\ (\nu f_{7/2})^7$
			35% $(\pi s_{1/2})^1\ (\nu f_{7/2})^7$
0^-	64% $(\pi d_{3/2})^3\ (\nu p_{3/2})^1$	5^-	12% $(\pi d_{3/2})^1\ (\nu f_{7/2})^7$
			12% $(\pi s_{1/2})^1\ (\nu f_{7/2})^7$
			29% $(\pi d_{3/2})^3\ (\nu f_{7/2})^7$
			10% $(\pi s_{1/2})^1\ (\nu p_{3/2})^1$

Comparison of this result with large-scale shell-model calculations using the ANTOINE code with the SDPF-U residual interaction and effective nucleon g factors favors 2^- as the ground-state spin of ^{44}Cl. The analysis of the g-factor value and the comparison of the theoretical ^{44}Cl level scheme with observations in the neighboring $N = 27$ and $Z = 17$ nuclei, reveal the presence of odd $s_{1/2}$ proton configurations and neutron excitations across $N = 28$ in the ground state of ^{44}Cl.

[1] O. Sorlin *et al.*, Phys. Rev. C **47**, 2941 (1993).
[2] F. Sarazin *et al.*, Phys. Rev. Lett. **84**, 5062 (2000).
[3] Z. Dlouhý *et al.*, Nucl. Phys. **A 701**, 189c (2002).
[4] B. Jurado *et al.*, Phys. Lett. **B 649**, 43 (2007).
[5] S. Grévy *et al.*, Phys. Lett. **B 594**, 252 (2004).
[6] J.A. Winger, P.F. Mantica and R.M. Ronningen, Phys. Rev. C **73**, 044318 (2006).
[7] D. Sohler *et al.*, Phys. Rev. C **66**, 054302 (2002).
[8] Zs. Dombrádi *et al.*, Nucl. Phys. **A 727**, 195 (2003).
[9] A. Gade *et al.*, Phys. Rev. C **74**, 034322 (2006).
[10] B. Bastin *et al.*, Phys. Rev. Lett. **99**, 022503 (2007).
[11] H. Scheit *et al.*, Phys. Rev. Lett. **77**, 3967 (1996).

[12] T. Glasmacher *et al.*, Phys. Lett. **B 395**, 163 (1997).
[13] R.W. Ibbotson, T. Glasmacher, P.F. Mantica, H. Scheit, Phys. Rev. C **59**, 642 (1999).
[14] L. Gaudefroy *et al.*, Phys. Rev. Lett. **97**, 092501 (2006).
[15] L. Gaudefroy *et al.*, Phys. Rev. C **78**, 034307 (2008).
[16] K. Blaum, W. Geithner, J. Lassen, P. Lievens, K. Marinova, R. Neugart, Nucl. Phys. **A 799**, 30 (2008).
[17] L. Gaudefroy *et al.*, Phys. Rev. Lett. **102**, 092501 (2009).
[18] J. Retamosa, E. Caurier, F. Nowacki and A. Poves, Phys. Rev. C **55**, 1266 (1997).
[19] D.J. Dean, M.T. Ressell, M. Hjorth-Jensen, S.E. Koonin, K. Langanke, A.P. Zuker, Phys. Rev. C **59**, 2474 (1999).
[20] E. Caurier, F. Nowacki and A. Poves, Eur. Phys. J. A **15**, 145 (2002).
[21] E. Caurier, F. Nowacki and A. Poves, Nucl. Phys. **A 742**, 14 (2004).
[22] F. Nowacki and A. Poves, Phys. Rev. C **79**, 014310 (2009).
[23] T. R. Werner, J.A. Sheikh, W. Nazarewicz, M.R. Strayer, A.S. Umar, M. Misu, Phys. Lett. **B 335**, 259 (1994).
[24] T. R. Werner, J.A. Sheikh, M. Misu, W. Nazarewicz, J. Rikovska, K. Heeger, A.S. Umar, M.R. Strayer, Nucl. Phys. **A 597**, 327 (1996).
[25] G.A. Lalazissis, D. Vretenar, P. Ring, M. Stoitsov and L.M. Robledo, Phys. Rev. C **60**, 014310 (1999).
[26] S. Péru, M. Girod and J.F. Berger, Eur. Phys. J. A **9**, 35 (2000).
[27] R. Rodríguez-Guzmán, J.L. Egido and L.M. Robledo, Phys. Rev. C **65**, 024304 (2002).
[28] R. Anne *et al.*, Nucl. Instr. Methods A **257**, 215 (1987).
[29] R. Anne *et al.*, Nucl. Instr. Methods B **70**, 276 (1992).
[30] M. De Rydt *et al.*, doi:10.1016/j.nima.2009.09.125 (2009).
[31] D. Yordanov, PhD in Physics, Instituut voor Kern- en Stralingsfysica, K.U.Leuven, Celestijnenlaan 200D B-3001 Leuven, Belgium (2007), unpublished.
[32] P.D. Cottle and K.W. Kemper, Phys. Rev. C **58**, 3761 (1998).
[33] P.D. Cottle and K.W. Kemper, Phys. Rev. C **66**, 061301(R) (2002).
[34] J. Fridmann *et al.*, Phys. Rev. C **74**, 034313 (2006).
[35] E. Caurier, F. Nowacki, Acta Phys. Pol. **30**, 705 (1999).
[36] T. Otsuka, R. Fujimoto, Y. Utsuno, B.A. Brown, M. Honma and T. Mizusaki, Phys. Rev. Lett. **87**, 082502 (2001).
[37] T. Otsuka, T. Suzuki, R. Fujimoto, H. Grawe and Y. Akaishi, Phys. Rev. Lett. **95**, 232502 (2005).
[38] F. Touchard *et al.*, Phys. Lett. **108B**, 169 (1982).
[39] O. Sorlin *et al.*, Eur. Phys. J **22**, 173 (2004).
[40] B. Singh and J.A. Cameron, Nucl. Data Sheets **107**, 225 (2006).
[41] X. Liang *et al.*, Phys. Rev. C **66**, 037301 (2002).
[42] J. Ollier *et al.*, Phys. Rev. C **67**, 024302 (2003).
[43] J.H. Bjerregaard, O. Hansen and G. Sidenius, Phys. Rev **138**, B 1097 (1965).
[44] J. Mrazek *et al.*, Nucl. Phys. A **734**, E65 (2004).
[45] A. Andl, K. Bekk, S. Göring, A. Hanser, G. Nowicki, H. Rebel, G. Schatz and R.C. Thompson, Phys. Rev C **26**, 2194 (1982).
[46] L.A. Riley *et al.*, Phys. Rev. C **80**, 037305 (2009).
[47] E. Caurier, G. Martínez-Pinedo, F. Nowacki, A. Poves, A. P. Zuker, Rev. Mod. Phys. **77**, 427 (2005).

[48] L.A. Riley *et al.*, Phys. Rev. C **79**, 051303(R) (2009).
[49] S. Angelo, A.A. Pilt and J.A. Kuehner, Phys. Rev C **22**, 427 (1980).

Conclusions and outlook

This PhD thesis discusses the technical and scientific aspects of the nuclear moment measurements performed on the light neutron-rich $^{17-18}$N isotopes, the ^{31}Al nucleus at the border of the island of inversion and the neutron-rich $^{41-44}$Cl isotopes in the vicinity of the $N = 28$ shell closure. All experiments were accomplished using a newly designed β-NMR/β-NQR setup at the LISE fragment separator at GANIL.

A detailed description of the new setup is given, including extensive field-profile measurements and GEANT4 simulations. In order to achieve accurate and reliable β-NMR/β-NQR results an electromagnet is installed, providing a homogeneous magnetic field up to 1.02 T across the implantation crystal. A special type of amplifier, designed for variable impedance circuits, is connected to the rf-coil, making it possible to apply a broad frequency range of strong rf fields. From the GEANT4 simulations the ideal β-NMR/β-NQR conditions can be deduced, demonstrating that a high Q_β value and a thin tilted implantation crystal strongly improve the detection efficiency and the sensitivity to observe a resonant change in the β-asymmetry.

When the installation of the setup was completed, a test experiment was performed probing the g-factors of $^{17-18}$N. For the ^{17}N ground state, the magnetic moment $|\mu(^{17}\mathrm{N})| = 0.3551(4)\ \mu_N$ was found. This result is in agreement with and five times more accurate than the earlier published value, illustrating that the newly designed β-NMR/β-NQR setup is suited for precision measurements of nuclear moments. The ^{18}N nucleus, on the other hand, provides an excellent physics case as two conflicting magnetic moments exist in literature. In the present experiment, three β-NMR measurements with different initial polarizations resulted in $|\mu(^{18}\mathrm{N})| = 0.3273(4)\mu_N$, confirming the magnetic moment published by Ogawa *et al.* [1]. A future g-factor measurement around $|g| = 0.135(15)$ should further examine the result from Neyens *et al.* [2].

As nuclear moments are excellent tools to probe changes in the shell structure, they have been frequently used to study nuclei in and near the island of inversion. This region, including the $_{10}$Ne, $_{11}$Na and $_{12}$Mg isotopes with neutron number around $N = 20$, is characterized by the dominance of neutron excita-

tions from the *sd* to the *pf*-orbits in the ground state. In order to determine the influence of intruder configurations in the neutron-rich $_{13}$Al isotopes, the quadrupole moment of ^{31}Al is studied using the multiple-rf β-NQR technique. A precise value for the quadrupole moment of ^{31}Al is deduced: $|Q(^{31}\mathrm{Al})| = 134.0(16)$ mb. Comparison of this value with large-scale shell-model calculations in the *sd* and *sdpf* valence spaces suggests that the ^{31}Al ground state is dominated by normal *sd*-shell configurations with a possible small contribution of intruder states. Furthermore, a compilation of measured quadrupole moments of odd-Z even-N isotopes in comparison with shell-model calculations shows that the proton effective charge $e_p = 1.1e$ provides a much better description of the nuclear properties in the *sd*-shell than the adopted value $e_p = 1.3e$. In addition, a detailed analysis of the physics behind the Adiabatic Fast Passage and Continuous rf β-NMR techniques is given.
Another region of exotic nuclei, exhibiting structural changes, is situated around $N = 28$. Both the erosion of the $N = 28$ shell gap and the collapse of the $Z = 16$ sub-shell closure are responsible for the collectivity, shape coexistence and configuration mixing observed in the neutron-rich isotopes from $_{14}$Si to $_{19}$K. As the Cl isotopes have three proton holes in the $\pi(sd)$ shell, they are very sensitive to the near-degeneracy of the $\pi(s_{1/2})$ and $\pi(d_{3/2})$ levels and to the induced proton correlations. The neutron-rich Cl isotopes are also excellent probes to study neutron excitations across $N = 28$. A measurement of the ^{44}Cl g-factor, resulting in $g(^{44}\mathrm{Cl}) = (-)0.2749(2)$, showed that both effects play an important role in the ground state of this nucleus. The experimental g-factor also strongly supports a 2^- spin assignment for ^{44}Cl. Additionally, β-NMR measurements were performed on the $^{41-43}$Cl ground states, so far without any result.

Studying nuclear structure is one of the major pillars in today's scientific research. Exploring exotic regions of the nuclear chart sheds light on the fundamental interactions in nature and on the way matter is created in the universe. This PhD thesis offers a small contribution to this enormous work which has by far not been completed. Even the results obtained in this work are calling for further investigations and experiments. A few examples are given. In order to extend the systematics of the neutron-rich Al and Cl isotopes, new nuclear moment measurements on ^{33,34}Al and $^{41-43,45}$Cl are needed. A theoretical study of the polarization obtained in $s_{1/2}$ nuclei using projectile fragmentation reactions can solve the polarization problems encountered in this thesis. More experimental data are needed to establish the role of frequency modulation on the β-NMR line-shape and a new β-NMR experiment on ^{18}N would clarify why two resonances were observed earlier. In conclusion, this thesis provides new physical insights in the current nuclear structure debate but at the same time it opens other questions for future research.

Bibliography

[1] H. Ogawa *et al.*, Phys. Lett. **B 451**, 11 (1999).

[2] G. Neyens *et al.*, Phys. Rev. Lett. **82**, 497 (1999).

[3] K. Heyde, *The Nuclear Shell Model* (Springer-Verlag, 1990).

[4] R. Casten, *Nuclear Structure from a Simple Perspective* (Oxford University Press, 2000).

[5] K. Krane, *Introductory Nuclear Physics* (John Wiley and Sons, New York, Chichester, Brisbane, Toronto, Singapore, 1988).

[6] H. Grawe, Lect. Notes Phys. **651**, 33 (2004).

[7] T. Otsuka *et al.*, Lect. Notes Phys. **764**, 1 (2009).

[8] T. Otsuka, T. Suzuki, R. Fujimoto, H. Grawe and Y. Akaishi, Phys. Rev. Lett. **95**, 232502 (2005).

[9] T. Otsuka, R. Fujimoto, Y. Utsuno, B.A. Brown, M. Honma and T. Mizusaki, Phys. Rev. Lett. **87**, 082502 (2001).

[10] A. de Shalit and I. Talmi, *Nuclear Shell Theory* (Academic Press, New York and London, 1963).

[11] E. Caurier and F. Nowacki, Acta Phys. Pol. **30**, 705 (1999).

[12] S. Nummela *et al.*, Phys. Rev. C **63**, 044316 (2001).

[13] F. Nowacki and A. Poves, Phys. Rev. C **79**, 014310 (2009).

[14] B.H. Wildenthal, Prog. Part. Nucl. Phys. **11**, 5 (1984).

[15] A. Poves and A. Zuker, Phys. Rep. **70**, 4 (1981).

[16] S. Kahana, H.C. Lee and C.K. Scott, Phys. Rev. **180**, 956 (1969).

[17] A. Gade *et al.*, Phys. Rev. C **74**, 034322 (2006).

[18] L. Gaudefroy *et al.*, Phys. Rev. Lett. **97**, 092501 (2006).

[19] L. Armstrong, *Theory of the Hyperfine Structure of Free Atoms* (John Wiley and Sons, 1971).

[20] C. Schwartz, Phys. Rev. **97**, 380 (1955).

[21] P.J. Mohr and B.N. Taylor, Rev. Mod. Phys. **72**, 351 (2000).

[22] S. Cottenier and M. Rots, *Hyperfine Interactions and their Applications in Nuclear Condensed Matter Physics: a Microscopic Introduction* (unpublished lecture notes Katholieke Universiteit Leuven, 2005).

[23] B. Castel and I. Towner, *Modern Theories of Nuclear Moments* (Clarendon Press - Oxford, 1990).

[24] R. Neugart and G. Neyens, Lect. Notes Phys. **700**, 135 (2006).

[25] E. Matthias, B. Osen, D.A. Shirley, J.E. Templeton and R.M. Steffen, Phys. Rev. A **4**, 1626 (1971).

[26] G. Neyens, Rep. Prog. Phys. **66**, 633 (2003).

[27] N. Stone and H. P. (Eds.), *Low-Temperature Nuclear Orientation* (Elsevier, Amsterdam, 1986), chapters 1-3.

[28] R. Steffen and K. Alder, *The Electromagnetic Interaction in Nuclear Spectroscopy (edit. W.D. Hamilton)* (North-Holland, Amsterdam - Oxford, 1975), chapter 12, Appendix 3.

[29] A. Abragam, *The Principles of Nuclear Magnetism* (Oxford at the Clarendon Press, 1973).

[30] M. De Rydt *et al.*, Nucl. Instrum. Meth. A **612**, 112 (2009).

[31] R. Anne, D. Bazin, A.C. Mueller, J.C. Jacmart and M. Langevin, Nucl. Instrum. Methods A **257**, 2151 (1987).

[32] R. Anne and A.C. Mueller, Nucl. Instrum. Methods B **70**, 276 (1992).

[33] `http://groups.nscl.msu.edu/lise/lise.html`.

[34] O.B. Tarasov and D. Bazin, Nucl. Instrum. Methods B **266**, 4657 (2008).

[35] S. Agostinelli *et al.* (GEANT collaboration), Nucl. Instrum. Methods A **506**, 250 (2003).

[36] `http://www.ge.infn.it/geant4/lowE/`.

[37] D.H. Wilkinson, Nucl. Instrum. Methods A **275**, 378 (1989).

[38] D.H. Wilkinson, Nucl. Instrum. Methods A **290**, 509 (1990).

[39] D.H. Wilkinson, Nucl. Instrum. Methods A **335**, 305 (1993).

[40] D.H. Wilkinson, Nucl. Instrum. Methods A **365**, 203 (1995).

[41] D.H. Wilkinson, Nucl. Instrum. Methods A **365**, 497 (1995).

[42] H. Ueno *et al.*, Phys. Rev. C **53**, 2142 (1996).

[43] M. De Rydt *et al.*, Phys. Rev. C **80**, 037306 (2009).

[44] O. Sorlin and M.G. Porquet, Prog. Part. Nucl. Phys. **61**, 602 (2008).

[45] E. Sauvan *et al.*, Phys. Lett. **B 491**, 1 (2000).

[46] V. Maddalena *et al.*, Phys. Rev. C **63**, 024613 (2001).

[47] M. Wiedeking *et al.*, Phys. Rev. C **77**, 054305 (2008).

[48] K. Asahi *et al.*, *CP570, SPIN 2000, 14th International Spin Symposium* (American Institute of Physics 0-7354-0008-3, 2001).

[49] Zs. Dombrádi *et al.*, Phys. Lett. **B 621**, 81 (2005).

[50] K. Matsuta *et al.*, Phys. Rev. Lett. **86**, 3735 (2001).

[51] M. Wiedeking *et al.*, Phys. Rev. Lett. **94**, 132501 (2005).

[52] G.D. Putt, L.K. Fifield, M.A.C. Hotchkis, T.R. Ophel and D.C. Weisser, Nucl. Phys. **A 399**, 190 (1983).

[53] M.S. Pravikoff *et al.*, Nucl. Phys. **A 528**, 225 (1991).

[54] K. Asahi *et al.*, Phys. Lett. **B 251**, 488 (1990).

[55] H. Okuno *et al.*, Phys. Lett. **B 335**, 29 (1994).

[56] D.E. Groh, J.S. Pinter, P.F. Mantica, T.J. Mertzimekis, A.E. Stuchbery and D.T. Khoa, Phys. Rev. C **76**, 054608 (2007).

[57] K. Turzó *et al.*, Phys. Rev. C **73**, 044313 (2006).

[58] G.A. Souliotis, D.J. Morrissey, N.A. Orr, B.M. Sherrill and J.A. Winger, Phys. Rev. C **46**, 1383 (1992).

[59] R. Pfaff *et al.*, Phys. Rev. C **51**, 1348 (1995).

[60] M. De Rydt *et al.*, Phys. Lett. **B 678**, 344 (2009).

[61] G. Audi, A.H. Wapstra and C. Thibault, Nucl. Phys. **A 729**, 337 (2003).

[62] D. Guillemaud-Mueller, C. Detraz, M. Langevin, F. Naulin, M. de Saint-Simon, C. Thibault, F. Touchard and M. Epherre, Nucl. Phys. A **426**, 37 (1984).

[63] Y. Yanagisawa *et al.*, Phys. Lett. **B 566**, 84 (2003).

[64] J.A. Church *et al.*, Phys. Rev. C **72**, 054320 (2005).

[65] S. Grévy *et al.*, Nucl. Phys. A **734**, 369 (2004).

[66] M. Keim, *Recent Measurements of Nuclear Moments far from Stability* (CP455 p.50, ENAM98: Exotic Nuclei and Atomic Masses, The American Institute of Physics (Eds. B.M. Sherrill, D.J. Morrissey and C.N. Davids), 1998).

[67] M. Keim, U. Georg, A. Klein, R. Neugart, M. Neuroth, S. Wilbert, P. Lievens, L. Vermeeren and B.A. Brown, Eur. Phys. J. A **8**, 31 (2000).

[68] G. Neyens *et al.*, Phys. Rev. Lett. **94**, 022501 (2005).

[69] D.T. Yordanov, M. Kowalska, K. Blaum, M. De Rydt, K.T. Flanagan, P. Lievens, R. Neugart, G. Neyens and H.H. Stroke, Phys. Rev. Lett. **99**, 212501 (2007).

[70] K. Heyde and J.L. Wood, J. Phys. G: Nucl. Part. Phys. **17**, 135 (1991).

[71] Y. Utsuno, T. Otsuka, T. Mizusaki and M. Honma, Phys. Rev. C **60**, 054315 (1999).

[72] P. Himpe, PhD in Physics, Instituut voor Kern- en Stralingsfysica, K.U.Leuven, Celestijnenlaan 200D B-3001 Leuven, Belgium (2006).

[73] W. Geithner *et al.*, Phys. Rev. C **71**, 064319 (2005).

[74] B.A. Brown and B.H. Wildenthal, Annu. Rev. Nucle. Part. Sci. **38**, 29 (1988).

[75] Y. Utsuno, T. Otsuka, T. Glasmacher, T. Mizusaki and M. Honma, Phys. Rev. C **70**, 044307 (2004).

[76] M. Kowalska, D.T. Yordanov, K. Blaum, P. Himpe, P. Lievens, S. Mallion, R. Neugart, G. Neyens and N. Vermeulen, Phys. Rev. C **77**, 034307 (2008).

[77] S. Nummela *et al.*, Phys. Rev. C **64**, 054313 (2001).

[78] V. Tripathi *et al.*, Phys. Rev. Lett. **101**, 142504 (2008).

[79] D.T. Yordanov, K. Blaum, M. De Rydt, M. Kowalska, R. Neugart, G. Neyens and I. Hamamoto, Submitted to Phys. Rev. Lett. (2009), comment on 'Intruder Configurations in the A=33 isobars ^{33}Mg and ^{33}Al'.

[80] B.V. Pritychenko *et al.*, Phys. Rev. C **65**, 061304(R) (2002).

[81] Z. Elekes *et al.*, Phys. Rev. C **73**, 044314 (2006).

[82] D. Borremans *et al.*, Phys. Lett. **B 537**, 45 (2002).

[83] P. Himpe *et al.*, Phys. Lett. **B 643**, 257 (2006).

[84] P. Himpe *et al.*, Phys. Lett. **B 658**, 203 (2008).

[85] H. Ueno *et al.*, Phys. Lett. **B 615**, 186 (2005).

[86] D. Nagae *et al.*, Phys. Rev. C **79**, 027301 (2009).

[87] D. Kameda *et al.*, Phys. Lett. **B 647**, 93 (2007).

[88] C. Slichter, *Principles of Magnetic Resonance* (Springer-Verlag Berlin Heidelberg New York, 1978).

[89] R. Barlow, *Statistics - A Guide to the Use of Statistical Methods in the Physical Sciences* (John Wiley and Sons, 1989).

[90] D. Schwalm, E.K. Warburton and J.W. Olness, Nucl. Phys. **A 293**, 425 (1977), table 10.

[91] M.A. Schumaker *et al.*, Eur. Phys. J. **A** (2009), doi: 10.1140/epja/i2009-10816-4.

[92] N.J. Stone, At. Data Nucl. Data Tables **90**, 75 (2005).

[93] V. Kellö and A.J. Sadlej, Phys. Rev. A **60**, 3575 (1999).

[94] K. Matsuta *et al.*, J. Phys. Conf. Ser. **20**, 169 (2005).

[95] V. Kellö, A.J. Sadlej, P. Pyykkö, D. Sundholm and M. Tokman, Chem. Phys. Lett. **304**, 414 (1999).

[96] R.E. Alonso, A. Svane, C.O. Rodríguez and N.E. Christensen, Phys. Rev. B **70**, 119901(E) (2004).

[97] D. Sundholm and J. Olsen, J. Chem. Phys. **98**, 7152 (1993).

[98] V. Kellö and A.J. Sadlej, Chem. Phys. Lett. **292**, 403 (1998).

[99] B.G. Todd-Rutel, J. Piekarewicz and P.D. Cottle, Phys. Rev. C **69**, 021301(R) (2004).

[100] G.A. Lalazissis, D. Vretenar, W. Pöschl and P. Ring, Phys. Lett. **B 418**, 7 (1998).

[101] P.D. Cottle and K.W. Kemper, Phys. Rev. C **66**, 061301 (2002).

[102] S. Raman, C.W. Nestor, P. Tikkanen, At. Data Nucl. Data Tables **78**, 1 (2001).

[103] R. Santo, R. Stock, J.H. Bjerregaard, O. Hansen, P. Nathan, R. Chapman and S. Hinds, Nucl. Phys. **A 118**, 409 (1968).

[104] P. Martin, M. Buenerd, Y. Dupont and M. Chabre, Nucl. Phys. **A 185**, 465 (1972).

[105] P. Doll, G.J. Wagner, K.T. Knöpfle and G. Mairle, Nucl. Phys. **A 263**, 210 (1976).

[106] S.M. Banks *et al.*, Nucl. Phys. **A 437**, 381 (1985).

[107] B. Singh and J.A. Cameron, Nucl. Data Sheets **107**, 225 (2006).

[108] J.A. Cameron and B. Singh, Nucl. Data Sheets **94**, 429 (2001).

[109] J.A. Cameron and B. Singh, Nucl. Data Sheets **92**, 783 (2001).

[110] T.W. Burrows, Nucl. Data Sheets **109**, 171 (2008).

[111] T.W. Burrows, Nucl. Data Sheets **108**, 923 (2007).

[112] F. Touchard *et al.*, Phys. Lett. **B 108**, 169 (1982).

[113] W.W. Daehick and R. Sherr, Phys. Rev. C **7**, 150 (1973).

[114] W.W. Daehick, J.H. Orloff, T. Canada and T.S. Bhatia, Phys. Rev. C **10**, 136 (1974).

[115] S. Angelo, A.A. Pilt and J.A. Kuehner, Phys. Rev. C **22**, 427 (1980).

[116] H. Scheit *et al.*, Phys. Rev. Lett. **77**, 3967 (1996).

[117] T.R. Werner, J.A. Sheikh, M. Misu, W. Nazarewicz, J. Rikovska, K. Heeger, A.S. Umar and M.R. Strayer, Nucl. Phys. **A 597**, 327 (1996).

[118] Zs. Dombrádi *et al.*, Nucl. Phys. **A 727**, 195 (2003).

[119] A. Gade *et al.*, Phys. Rev. C **71**, 051301(R) (2005).

[120] L. Gaudefroy *et al.*, Phys. Rev. C **78**, 034307 (2008).

[121] A. Signoracci and B.A. Brown, Phys. Rev. Lett. **99**, 099201 (2007).

[122] L. Gaudefroy *et al.*, Phys. Rev. Lett. **99**, 099202 (2007).

[123] K. Blaum, W. Geithner, J. Lassen, P. Lievens, K. Marinova and R. Neugart, Nucl. Phys. **A 799**, 30 (2008).

[124] P.M. Endt and R.B. Firestone, Nucl. Phys. **A 633**, 1 (1998).

[125] X. Liang *et al.*, Phys. Rev. C **66**, 037301 (2002).

[126] O. Sorlin *et al.*, Eur. Phys. J. **A 22**, 173 (2004).

[127] O. Sorlin *et al.*, Phys. Rev. C **47**, 2941 (1993).

[128] F. Sarazin *et al.*, Phys. Rev. Lett. **84**, 5062 (2000).

[129] L.A. Riley *et al.*, Phys. Rev. C **79**, 051303(R) (2009).

[130] T.R. Werner, J.A. Sheikh, W. Nazarewicz, M.R. Strayer, A.S. Umar and M. Misu, Phys. Lett. **B 335**, 259 (1994).

[131] J. Retamosa, E. Caurier, F. Nowacki and A. Poves, Phys. Rev. C **55**, 1266 (1997).

[132] G.A. Lalazissis, D. Vretenar, P. Ring, M. Stoitsov and L.M. Robledo, Phys. Rev. C **60**, 014310 (1999).

[133] T. Glasmacher *et al.*, Phys. Lett. **B 395**, 163 (1997).

[134] R.W. Ibbotson, T. Glasmacher, P.F. Mantica and H. Scheit, Phys. Rev. C **59**, 642 (1999).

[135] D. Sohler *et al.*, Phys. Rev. C **66**, 054302 (2002).

[136] F. Azaiez *et al.*, Eur. Phys. J. A **15**, 93 (2002).

[137] S. Grévy *et al.*, Eur. Phys. J. A **25**, 111 (2005).

[138] L. Gaudefroy *et al.*, Phys. Rev. Lett. **102**, 092501 (2009).

[139] L.A. Riley *et al.*, Phys. Rev. C **80**, 037305 (2009).

[140] B. Bastin *et al.*, Phys. Rev. Lett. **99**, 022503 (2007).

[141] J. Fridmann *et al.*, Nature **435**, 922 (2005).

[142] J. Fridmann *et al.*, Phys. Rev. C **74**, 034313 (2006).

[143] L.A. Riley *et al.*, Phys. Rev. C **78**, 011303(R) (2008).

[144] S. Grévy *et al.*, Phys. Lett. **B 594**, 252 (2004).

[145] M. Notani *et al.*, Phys. Lett. **B 542**, 49 (2002).

[146] S. Péru, M. Girod and J.F. Berger, Eur. Phys. J. A **9**, 35 (2000).

[147] R. Rodríguez-Guzmán, J.L. Egido and L.M. Robledo, Phys. Rev. C **65**, 024304 (2002).

[148] C.M. Campbell *et al.*, Phys. Rev. Lett. **97**, 112501 (2006).

[149] E. Caurier, G. Martínez-Pinedo, F. Nowacki, A. Poves and A.P. Zuker, Rev. Mod. Phys. **77**, 427 (2005).

[150] J. Ollier *et al.*, Phys. Rev. C **67**, 024302 (2003).

[151] A. Huck, G. Klotz, A. Knipper, C. Miehe, C. Richard-Serre and G. Walter, Proc. Int. Conf. Nuclei Far from Stability, Helsingor, Denmark **2**, 378 (1981).

[152] T. Yamanishi, T. Kanashiro, Y. Michihiro, Y. Kishimoto and T. Ohno, J. Phys. Soc. Japan **64**, 643 (1995).

[153] R.E. Alonso, A. Svane, C.O. Rodríguez and N.E. Christensen, Phys. Rev. B **69**, 125101 (2004).

[154] J.A. Winger, P.F. Mantica and R.M. Ronningen, Phys. Rev. C **73**, 044318 (2006).

[155] B. Vosicki, T. Bjornstad, L.C. Carraz, J. Heinemeier and H.L. Ravn, Nucl. Instrum. Meth. **186**, 307 (1981).

[156] J.A. Cameron and B. Singh, Nucl. Data Sheets **92**, 1 (2001).

[157] K. Matsuta *et al.*, Nucl. Phys. **A 746**, 493c (2004).

Publication List

- **A new dedicated β-NMR/β-NQR setup for LISE-GANIL**
  M. De Rydt, R. Lozeva, N. Vermeulen, F. de Oliveira Santos, S. Grévy, P. Himpe, C. Stödel, J.C. Thomas, P. Vingerhoets and G. Neyens
  Nuclear Instruments and Methods in Physics Research A ***612*** *(2009) 112*

- **g factors of ^{17}N and ^{18}N remeasured**
  M. De Rydt, D.L. Balabanski, J.M. Daugas, P. Himpe, D. Kameda, R. Lozeva, P. Morel, L. Perrot, K. Shimada, C. Stödel, T. Sugimoto, J.C. Thomas, H. Ueno, N. Vermeulen, P. Vingerhoets, A. Yoshimi and G. Neyens
  Physical Review C ***80*** *(2009) 037306*

- **Precision measurement of the electric quadrupole moment of ^{31}Al and determination of the effective proton charge in the sd-shell**
  M. De Rydt, G. Neyens, K. Asahi, D.L. Balabanski, J.M. Daugas, M. Depuydt, L. Gaudefroy, S. Grévy, Y. Hasama, Y. Ichikawa, P. Morel, T. Nagatomo, T. Otsuka, L. Perrot, K. Shimada, C. Stödel, J.C. Thomas, H. Ueno, Y. Utsuno, W. Vanderheijden, N. Vermeulen, P. Vingerhoets, A. Yoshimi
  Physics Letters ***B 678*** *(2009) 344*

- **g factor of the ^{44}Cl ground state: probing the reduced $Z = 16$ and $N = 28$ gaps**
  M. De Rydt, J.M. Daugas, F. de Oliveira Santos, L. Gaudefroy, S. Grévy, D. Kameda, V. Kumar, R. Lozeva, T.J. Mertzimekis, P. Morel, T. Nagatomo, G. Neyens, L. Perrot, O. Sorlin, C. Stödel, J.C. Thomas, N. Vermeulen, P. Vingerhoets
  submitted to Physical Review C (2009)

- **g factors of ^{31,32,33}Al: Indication for intruder configurations in the ^{33}Al ground state**
  P.Himpe, G. Neyens, D.L. Balabanski, G. Belier, D. Borremans, J.M.

Daugas, F. de Oliveira Santos, **M. De Rydt**, K. Flanagan, G. Georgiev, M. Kowalska, S. Mallion, I. Matea, P. Morel, Yu. E. Penionzhkevich, N.A. Smirnova, C. Stödel, K. Turzo, N. Vermeulen, D. Yordanov
Physics Letters ***B 643****(2006) 257*

- **The quadrupole moment of the 8^+ yrast state in ^{84}Kr**
R. Schwengner, D.L. Balabanski, G. Neyens, N. Benouaret, D. Borremans, N. Coulier, **M. De Rydt**, G. Georgiev, S. Mallion, G. Rainovski, G. Rusev, S. Teughels, K. Vyvey
Physical Review C ***74*** *(2006) 034309*

- **The 'island of inversion' from a nuclear moments perspective and the g-factor of ^{35}Si**
G. Neyens, P.Himpe, D.L. Balabanski, **M. De Rydt**, P. Morel, L. Perrot, I. Stefan, C. Stödel, J.C. Thomas, N. Vermeulen, D.T. Yordanov
European Physical Journal Special Topics ***150*** *(2007) 149*

- **Spin and Magnetic Moment of ^{33}Mg: Evidence for a Negative-Parity Intruder Ground State**
D.T. Yordanov, M. Kowalska, K. Blaum, **M. De Rydt**, K.T. Flanagan, P. Lievens, R. Neugart, G. Neyens, H.H. Stroke
Physical Review Letters ***99*** *(2007) 212501*

- **g factors of the exotic $N = 21$ isotope ^{34}Al: probing the $N = 20$ and $N = 28$ shell gaps at the border of the 'island of inversion'**
P.Himpe, G. Neyens, D.L. Balabanski, G. Belier, J.M. Daugas, F. de Oliveira Santos, **M. De Rydt**, K. Flanagan, I. Matea, P. Morel, Yu. E. Penionzhkevich, L. Perrot, N.A. Smirnova, C. Stodel, J.C. Thomas, N. Vermeulen, D. T. Yordanov, Y. Otsuno, T. Otsuka
Physics Letters ***B 658****(2008) 203*

- **New sub-μs isomers in ^{125,127,129}Sn and isomer systematics of $^{124-130}$Sn**
R. L. Lozeva, G. S. Simpson, H. Grawe, G. Neyens, L. A. Atanasova, D. L. Balabanski, D. Bazzacco, F. Becker, P. Bednarczyk, G. Benzoni, N. Blasi, A. Blazhev, A. Bracco, C. Brandau, L. Cáceres, F. Camera, S. K. Chamoli, F. C. L. Crespi, J.-M. Daugas, P. Detistov, **M. De Rydt**, P. Doornenbal, C. Fahlander, E. Farnea, G. Georgiev, J. Gerl, K. A. Gladnishki, M. Górska, J. Grebosz, M. Hass, R. Hoischen, G. Ilie, M. Ionescu-Bujor, A. Iordachescu, J. Jolie, A. Jungclaus, M. Kmiecik, I. Kojouharov, N. Kurz, S. P. Lakshmi, G. Lo Bianco, S. Mallion, A. Maj, D. Montanari, O. Perru, M. Pfützner, S. Pietri, J. A. Pinston, Zs. Podolyák, W. Prokopowicz, D. Rudolph, G. Rusev, T. R. Saitoh, A. Saltarelli, H. Schaffner, R. Schwengner, S. Tashenov, K. Turzy, J. J. Valiente-Dobón,

N. Vermeulen, J. Walker, E. Werner-Malento, O. Wieland, and H.-J. Wollersheim
Physical Review C ***77*** *(2008) 064313*

- **Spins and Magnetic Moments of ^{71,73,75}Cu: Inversion of $\pi(2p_{3/2})$ and $\pi(1f_{5/2})$ levels in ^{75}Cu**
K.T. Flanagan, P. Vingerhoets, M. Avgoulea, J. Billowes, M.L. Bissell, K. Blaum, B. Cheal, **M. De Rydt**, V.N. Fedosseev, D.H. Forest, Ch. Geppert, U. Koster, M. Kowalska, J. Kramer, K.L. Kratz, A. Krieger, E. Mane, B.A. Marsh, T. Materna, L. Mathieu, P.L. Molkanov, R. Neugart, G. Neyens, W. Nortershauser, M.D. Seliverstov, O. Serot, M. Schug, M.A. Sjoedin, J.R. Stone, N.J. Stone, H.H. Stroke, G. Tungate, D.T. Yordanov and Yu. M. Volkov
Physical Review Letters ***103*** *(2009) 142501*

- **Nuclear Ground-State Spin and Magnetic Moment of ^{21}Mg**
J. Kramer, K. Blaum, **M. De Rydt**, K. T. Flanagan, Ch. Geppert, M. Kowalska, P. Lievens, R. Neugart, G. Neyens, W. Nortershauser, H. H. Stroke, P. Vingerhoets, D. T. Yordanov
Physics Letters ***B 678*** *(2009) 465*

- **Comment on 'Intruder Configurations in the $A = 33$ Isobars: ^{33}Mg and ^{33}Al**
D. T. Yordanov, K. Blaum, **M. De Rydt**, M. Kowalska, R. Neugart, G. Neyens, and I. Hamamoto
Submitted to Physical Review Letters (2009)